



## City Research Online

### City, University of London Institutional Repository

---

**Citation:** Gates, J. A. (1984). Solid state properties of inorganic iodides. (Unpublished Doctoral thesis, The City University)

This is the accepted version of the paper.

This version of the publication may differ from the final published version.

---

**Permanent repository link:** <https://openaccess.city.ac.uk/id/eprint/34962/>

**Link to published version:**

**Copyright:** City Research Online aims to make research outputs of City, University of London available to a wider audience. Copyright and Moral Rights remain with the author(s) and/or copyright holders. URLs from City Research Online may be freely distributed and linked to.

**Reuse:** Copies of full items can be used for personal research or study, educational, or not-for-profit purposes without prior permission or charge. Provided that the authors, title and full bibliographic details are credited, a hyperlink and/or URL is given for the original metadata page and the content is not changed in any way.

Solid State Properties of Inorganic Iodides

by

Josephine Ann Gates

A Thesis submitted for the degree of  
Doctor of Philosophy

Department of Chemistry  
The City University, London.

August 1984.

## Contents

		<u>Page</u>
Chapter 1	Introduction	1
Chapter 2	Theoretical Background to Techniques Used	31
Chapter 3	Design and Construction	94
Chapter 4	Simple Iodide Systems	129
Chapter 5	Mixed Metal Iodide Systems	196
Chapter 6	Discussion	268

## Acknowledgements

I would like to extend my sincere appreciation and gratitude to Dr. S. J. Clark for his personal supervision and continued interest throughout the course of this study. I am also grateful to the technical staff of the Chemistry Department for all their help over the past three years. To my colleagues for all their help, encouragement and useful discussion.

Finally to my supervisor Professor J. D. Donaldson.

I would like to thank the S. E. R. C. for their support during the course of this study.

## ABSTRACT

The electronic processes responsible for the observed semiconducting properties in various main group chlorides, bromides and iodides is studied. Particular attention is paid to compounds containing iodide and a main group element in its lower oxidation state and therefore containing a non - bonding electron pair.

The design and construction of apparatus to measure the effect of temperature on electrical conductivity and photoconductivity is presented.

Materials of the type  $MI_x$  ( $x = 2$  to  $4$ ) and  $CsM'_{.5}M''_{.5}X_3$  where ( $M'$  and  $M'' = Sn^{II}, Pb^{II}, Cd^{II}, X = I, Br, Cl$ ) and  $Cs_2NaA^{III}_{.5}B^{III}_{.5}X_6$  ( $A, B = As^{III}, Sb^{III}, Bi^{III}, X = I, Br, Cl$ ) are prepared and characterised. The optical properties, bulk and surface electrical conductivities and photoconductivities of the phases are measured and the results related to compositions of phases and their electronic structure. The room temperature absorption and reflectance data for all phases studied gave absorption edges and are attributed to band-to-band rather than atomic transitions. The optical and electrical properties of the iodide systems studied are indicative of a cationic mechanism with the exception of the  $Cs_2NaSb_xBi_{1-x}I_6$  system where impurities are definitely involved all other systems can be explained in terms of donation of main-group  $ns^2$  electrons to a conduction band formed by overlap of empty halide orbitals. A mechanism involving population of empty solid state bands by iodine electrons themselves cannot account for any of the experimental data for compounds containing  $ns^2$  elements. The mechanism of halide band formation and reduction of the distorting effects of the lone-pair electrons is described in terms of orbital energy matching.

## Chapter One

### Introduction

	<u>Page</u>
1.1. Introduction	2
1.2. The Chemistry of Group IV and Group V Elements	3
1.2.2. Metal IV and Metal V Compounds	4
1.3. The Lone Pair Effect	10
1.4. Simple and Complex Iodides of Group IV and V	12
1.4.1. Tin (II) and Lead (II)	13
1.4.2. Arsenic (III), Antimony (III), Bismuth (III)	17
1.5. Band Theory	19
1.6. Summary	24

Semiconduction in main group elements is normally associated with those elements in Groups III - VII, enclosed by the lines in Fig 1.1., and with phases formed by reaction between these elements.

III	IV	V	VI	VII
B	C	N	O	F
Al	Si	P	S	Cl
Ga	Ge	As	Se	Br
In	Sn	Sb	Te	I
Tl	Pb	Bi	Po	At

Fig 1.1.

Silicon and germanium are the semiconductor elements that have received most attention because of their technical importance, particularly in the electronics industry. The mechanisms of conduction in these elements and phases are well documented<sup>(1)</sup>. There are, however, some types of compounds of the main group elements that have <sup>optical and</sup> electrical properties that cannot be explained in terms of these mechanisms. The types of compound that show <sup>such</sup> optical and conducting properties are those that contain approximately closed-packed heavy halogen or chalcogen lattices to provide acceptor bands and non-bonding electron pairs to

provide donor electrons. Optical colouration and conductivity in high symmetry iodides containing main-group elements in their lower oxidation states can, for example, arise from effects associated with the main group elements and or with the iodide sub-lattice. The main aim of the work described in this thesis is to study solid state iodide compounds with a view to elucidating the electronic transitions responsible for the observed properties. The factors of particular interest are the possible use of non-bonding electron pairs as donors and the formation of solid state bands in iodide lattices.

This introductory chapter contains a summary of the relevant previous work on lone pair effects in main group compounds, on Group IV and Group V iodides and provides an introduction to the band theories required to describe optical colouration and conductivity in solid iodides. This part of the thesis is followed by chapters dealing with the theories of techniques used: the design and construction of equipment: studies on single metal phases and on mixed metal phases.

## 1.2. The Chemistry of Group IV and Group V Elements

In this section the structural and bonding aspects of Group IV and Group V metalloid elements are introduced. The stereochemistry of compounds of these elements in their



lower oxidation state is greatly affected by the presence on the non-bonding lone pair of electrons.

The elements of interest in the present work on main group iodides are in Group IV, (namely tin and lead) and in Group V (arsenic, antimony and bismuth). The Group IV elements have an outer electronic configuration  $ns^2 np^2$  and can form compounds in either the IV+ or II+ oxidation state, while  $ns^2 np^3$  electronic configuration of Group V elements permits the formation of V+ and III+ valencies. The redox potentials show that the stability of the lower oxidation states increases with atomic number. Thus As(V) dominates arsenic chemistry, the lower oxidation state being much less stable. However, in lead and bismuth chemistries the lower oxidation state predominates and the few known compounds of Pb(IV) and Bi(V) are strong oxidising agents. Tin and antimony exhibit intermediate behaviour forming compounds in both oxidation states. The lower oxidation states, however, are reducing agents and metastable with respect to the  $Sn^{4+}$  and  $Sn^{5+}$  moieties.

### 1.2.2. Metal IV and Metal V Compounds

Derivatives of the elements in their higher oxidation states could be formed in three ways:-

- 1) By loss of all valence electrons to form  $M^{4+}$  and  $M^{5+}$  ions respectively.
- 2) By hybridization of available orbitals in a suitable

environment to form four (Group IV) or five (Group V) covalent bonds.

3) By complex formation, i.e. making use of empty  $nd$  - orbitals which are of similar energy to the outer  $ns$  and  $np$  orbitals.

Distinct geometries are predicted by these extreme views of bonding viz: a spherical ion for ionic bonding, tetrahedral (Group IV) or trigonal bipyramidal (Group V) geometries in covalent bonding and octahedral coordination in complex ions and adducts.

Because of the energy required to remove five electrons the formation of an ionic  $M^{5+}$  ion is not possible but,  $M^{4+}$  ions are said to exist in, for example tin (IV) oxide and lead (IV) oxide <sup>(2)</sup>, although appreciable covalent character in the tin-oxygen bonding has been reported <sup>(3)</sup>. Tin (IV) sulphide and tin (IV) selenide, which have the layered  $CdI_2$  structure, are also said to contain  $Sn^{4+}$  ions in octahedral sites within the chalcogenide lattice. A tetrahedral configuration based on  $sp^3$  hybridization is formed in the covalent halides of Group IV elements in the vapour phase. The structure and bonding in tin (IV) bromide <sup>(4)</sup>, lead (IV) chloride and many organo metal (IV) compounds <sup>(5-8)</sup> can be explained in these terms. Ternary tin compounds of the type  $(II - IV - V_2)$  crystallize in either the tetragonal chalcopyrite or cubic zincblende structures depending on the rate of cooling <sup>(9-11)</sup>. In both cases each cation is surrounded by four anions and

each anion by four cations, the major difference between the structures being the fact that the tetrahedra in the zincblende form are regular while those in the chalcopyrite form are distorted. As these tin compounds contain an average valence electron concentration of four, the coordination may be described, as a first approximation, in terms of  $sp^3$  - hybrid orbitals<sup>(12)</sup>.

The covalent state based on  $sp^2 + pd$  hybridization leads to a trigonal bipyramidal configuration for the Group V elements.  $AsF_5$  and a considerable number of mixed halides, such as  $SbCl_3F_2$  -  $SbCl_2F_3$ ,  $SbCl_4F$  are known, as well as mixed organo halides,  $BiPH_3Cl_2$ ,  $SbPh_5$ ,  $SbPh_3Cl_2$ , to have the trigonal bipyramidal structure<sup>(13-15)</sup>. These compounds strictly follow the rule that equatorial positions are preferred by less electronegative substituents.

For most compounds in the solid state the nature of the bonding can be described in terms of the ionic or covalent extremes.

The formal representation of complex formation is the overlap of empty orbitals on the metal with filled orbitals of a suitable ligand. In Group IV elements the use of one d-orbital to form  $sp^3 d$  hybrids leads to a trigonal bipyramidal configuration e.g.  $(CH_3)_3SnCl.NC_5H_5$ <sup>(16)</sup>. whereas the use of two d-orbitals in the formation of  $sp^3 d^2$  hybrids results in octahedral complexes e.g.  $SnCl_6^{2-}$ <sup>(17)</sup>. Octahedral complexes, such as  $SbF_6^-$ ,  $AsCl_6^-$  in Group V are due to  $sp^3 d^2$  hybrid orbitals.

## METAL II AND METAL III COMPOUNDS

In his review of bivalent tin chemistry, Donaldson<sup>(18,19)</sup> discussed four possible methods of bond formation:

- 1) Loss of two 5p-electrons to form  $\text{Sn}^{2+}$  ions.
- 2) Use of the two 5p-electrons to form covalent bonds.
- 3) Complex formation using empty 5p and possibly the 5p orbitals to form hybrid acceptor orbitals.
- 4) Lone pair donation to an acceptor species.

These arguments can be used to describe the chemistry of lead(II) and similar arguments extended to describe the chemistry of As(III), Sb(III) and Bi(III). Lead and bismuth have a greater tendency to form discrete ions than any other member in their respective groups.

The ease with which the Group IV and V elements can lose their outer np-electrons to leave an outer electronic configuration of  $ns^2$  is shown by their ionization potentials (Table 1.1). The non-bonding pair of electrons beyond a completed shell can have considerable effect on the stereochemistry. This is discussed in greater detail in Section 1.3.

Table 1.1 First two Ionization Potentials of Tin and Lead, and First three Ionization Potentials of Arsenic, Antimony and Bismuth.

<u>Element</u>	Ionization Potentials (eV)		
	<u>1st</u>	<u>2nd</u>	<u>3rd</u>
Sn	7.33	14.63	-
Pb	7.42	15.03	-
As	9.81	18.63	28.35
Sb	8.64	16.53	25.3
Bi	7.29	16.69	25.56

The formation of covalent bonds, involving essentially  $sp$  hybridization, is of greatest importance in the vapour state. The angular geometries of tin (II) and lead (II)<sup>(5)</sup> halides in the vapour phase and the trigonal pyramidal geometries of the arsenic (III), antimony (III) and bismuth (III), halides<sup>(20)</sup> in the vapour state certainly support this assumption.

Group IV, compounds formed by  $sp^2$  hybridization have an empty  $p$  orbital and similar energy to the orbitals used in bonding, and can therefore act as monofunctional acceptors to give complexes based on  $sp^3$  hybridization.

The halides readily dissolve in donor solvents such as acetone, pyridine or DMSO, and pyramidal adducts,  $\text{SnX}_2\text{L}$ , are formed<sup>(21, 22)</sup>. The lone-pair in  $\text{SnCl}_2\text{L}$  or  $\text{SnCl}_3$  can be used as a donor orbital and numerous transition-metal complexes with tin (II) chloride or the trichlorostannate (II) ion as ligand are known<sup>(23)</sup>. Most Lewis acid-Lewis base complexes of Sn (II) compounds show preference for 1:1 complex formation with monodentate ligands<sup>(24)</sup>.

The lone-pair distorted compounds of lead (II), such as lead (II) chloride and lead (II) oxide<sup>(25)</sup> can be described in either electrostatic or covalent terms. Pyramidal ions based on  $\text{sp}^3$  hybridization of lead (II) orbitals are not only very stable in solution<sup>(26)</sup> but also exist in solid materials of the type  $\text{MPbX}_3$ <sup>(29)</sup>. The Lewis acid-Lewis base complexes such as  $\text{PhBr}_2\text{:NH}_3$  and  $\text{Pb}(\text{NO}_3)_2\cdot\text{NH}_3$ <sup>(28)</sup> are also known and show the tendency of lead (II) to form covalent bonds.

$\text{sp}^3 \text{d}^2$  hybridization in Group V elements allows covalent adducts and complex ions to be formed. Complexes of this type formed with  $\text{PhNH}_2$  have structure with relatively weak N-Sb bonds and a stereochemically active lone pair. Tartrate acts as a bidentate ligand with antimony (III) and the potassium, ammonium and  $(\text{Fe}(\text{phen})_3)^{2+}$  salts are known to have a binuclear structure with tartrate bridges<sup>(29)</sup> between two antimony moieties. Similar coordination<sup>(30)</sup> is found in the complex,  $\text{K}(\text{As}(\text{C}_6\text{H}_4\text{O}_2)_2)_3$ ,

derived from pyrocatechol. A great many lone-pair distorted compounds with stoichiometry  $M^I SbX_4$  or  $M^I SbX_3Y$  have been prepared and spectroscopic evidence for  $SbX_4^-$  or  $SbX_3Y^-$  ions have been reported (31). Derivatives of the complex ions  $SbCl_5^{2-}$  and  $SbCl_6^{3-}$  have also been reported.  $SbCl_5^{2-}$  ion in  $(NH_4)_2SbCl_5$  is a discrete anion with a distorted square-pyramidal structure (32). The  $SbCl_6^{3-}$  ion however, is said to have  $O_h$  symmetry in aqueous solution but to be distorted in  $M_3^I SbCl_6$  crystals (33). The lone pair in  $MX_3$  moieties can act as a donor orbital and numerous transition metal complexes with  $M^{III}X_3$  ligands are known.

Bismuth (III) forms halo complexes that are similar to those of Sb (III). Various solids with stoichiometries such as  $M^I BiX_4$  have been isolated but have not been characterised structurally.

### 1.3. The Lone Pair Effect

Many p-block subgroup metals exhibit a stable valency two smaller than the group valency. This tendency is most pronounced for thallium, lead and bismuth and is also important for many lighter elements such as tin and antimony. The stereochemistry of molecules and solids containing ions in these valencies is often complicated.

The free ions corresponding to the lower valencies all have electronic configurations consisting of closed shells followed by a pair of s electrons; 6s for  $Tl^+$ ,  $Pb^{++}$

and  $\text{Bi}^{+++}$ ; 5s for  $\text{In}^+$ ,  $\text{Sn}^{++}$  and  $\text{Sb}^{+++}$  etc. It is generally recognised that the unusual stereochemistry of these ions is connected with the pair of electrons outside a closed shell, but various views have been expressed as to the precise way in which the unshared electrons exert their influence.

The VSEPR theory of Gillespie<sup>(34)</sup> predicts that the presence of a lone pair leads to a non-spherical charge distribution about the central  $ns^2$  ion resulting in distortion of the regular octahedra. Orgel<sup>(35)</sup> considered the effect of the regular approach of an octahedral field of ligands toward the central ion. Basing his arguments on crystal field effects he predicted a distorted environment for the central ion. If the centre of symmetry were retained, a symmetrical distortion of the ligands would favour s-d mixing, but this is energetically improbable. Distortion of the regular octahedral environment of the  $ns^2$  ions should therefore occur when the stabilization energy gained from the population of s-p excited states is greater than the energy holding the regular octahedra together.

Both of these theories explain and predict a distorted environment for the central  $ns^2$  ion. However hexachloro-, and hexabromo-selenium (IV) and tellurium (IV) anions which have six bonded pairs and one lone pair of electrons and would therefore be expected to have distorted octahedral structures, are in fact both regular octahedra in the solid and solution<sup>(36)</sup>. Similarly for  $\text{CsSnBr}_3$ ,  $\text{CsPbBr}_3$ ,  $\text{CsGeCl}_3$ .



Urch<sup>(37)</sup> used molecular orbital theory to explain the octahedral symmetry of these compounds. He suggested that as  $ns^2$  electrons play little part in bonding they could be accommodated in  $a_{1g}$  antibonding orbitals without distorting the  $O_h$  symmetry. This theory assumes that the stereochemistry of such species is governed solely by valence electron atomic orbitals even in the solid, neglecting crystal packing effects and solid state bands.

Donaldson<sup>(38)</sup> has suggested that the pseudo metallic conducting properties and  $^{119}\text{Sn}$  Mössbauer data of  $\text{CsSnBr}_3$  can be explained by the population of conduction bands in the solid by the tin  $5s^2$  - electrons. These bands would arise from the mutual overlap of empty bromine  $t_2$ , 4d- orbitals which would be at a maximum in the undistorted perovskite lattice. Taking into account exact details of the orbital electronegativities of the elements involved in bonding in any given compound, this model explains the colours and properties of compounds with high symmetry  $ns^2$ - element environments better than any previous model.

#### 1.4. Simple and Complex Iodides of Group IV and V.

The simple and complex iodides of Group IV and V elements in their lower oxidation states are reviewed briefly in this section, with emphasis on colour, structure and other relevant properties.

1.4.1.

Tin (II) and Lead (II)

The solid state structural chemistry of tin (II) is complex, and it is evident that the structures of even the stannous halides are not those of simple ionic compounds.

Orange  $\text{SnI}_2$  is a unique  $\text{AX}_2$  structure <sup>(39)</sup> of unexpected complexity which is shown in projection in Fig 1.2.

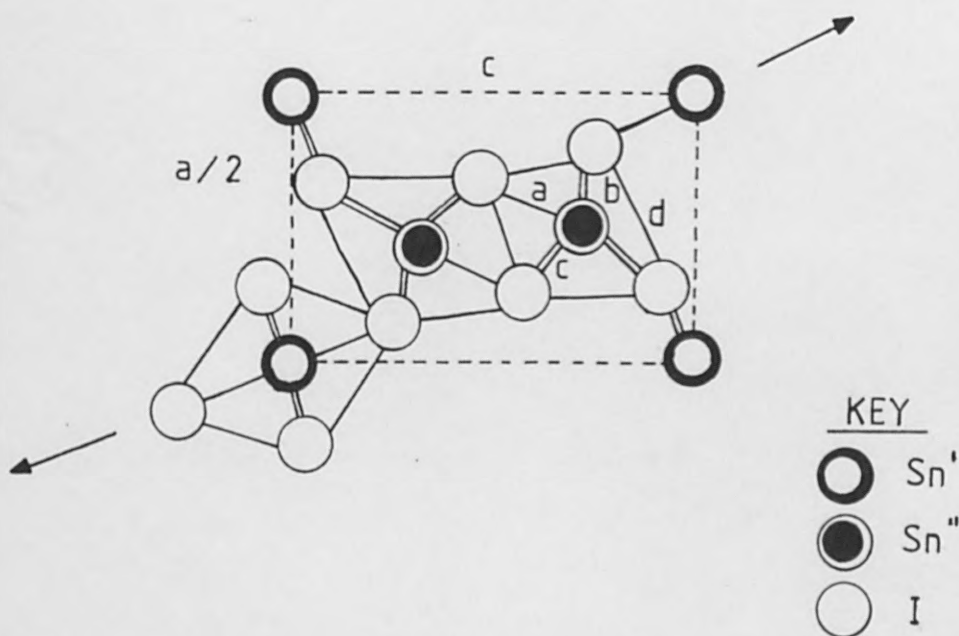


Fig 1.2. Projection of one half of a unit cell of the crystal structure of  $\text{SnI}_2$ .

One-third of the Sn atoms ( $\text{Sn}'$ ) are in positions of nearly regular octahedral coordination in rutile-like chains which are cross-linked by double chains containing the remaining metal atoms.

The latter (Sn'') form 5 shorter and 2 longer bonds to I atoms:

Sn'' - I	(a	3.00	Å)	mean	3.18	Å	Sn' - I	6	at	3.16	Å
	(2b	3.20	Å)								
	(2c	3.25	Å)								
	2d	3.72	Å								

The bonds b link the double chains in the rutile-like chains to form layers in the direction of the arrows (Fig 1.2). These layers are linked by the weaker d bonds into a 3D structure. All five of the shorter bonds lie to one side of Sn''. The coordination of Sn'' may be described as monocapped trigonal prismatic, the two longer bonds going to atoms of one edge.

The electronic band structure of tin (II) iodide has been compiled by the overlap reduced semiempirical tight-binding method<sup>(40)</sup>. The band structure obtained by this simple model indicates, in accordance with the experimental absorption spectrum, that SnI<sub>2</sub> has an indirect fundamental gap of about 2.1eV, followed by a region of direct weak transitions and then by a strong excitonic series.

In the absence of air equimolar ratios of RbI and SnI<sub>2</sub> react to form yellow needles of RbSnI<sub>3</sub>. Excess tin (II) iodide results in the formation of orange/yellow cubic crystals of RbSn<sub>2</sub>I<sub>5</sub>. Similar compounds CsSnI<sub>3</sub> and CsSn<sub>2</sub>I<sub>5</sub><sup>(41)</sup> the halogenostannates (II) have been characterised by

diffraction methods, and a systematic comparison of crystal structures of these compounds is not yet possible. The structures of the long thin yellow needles of  $\text{CsSnI}_3$  has been determined<sup>(42)</sup>, and found to be orthorhombic, isomorphous with  $\text{RbPbI}_3$ <sup>(43)</sup> and  $\text{CsPbI}_3$ <sup>(44)</sup>. The structure of  $\text{CsSnI}_3$  is characterised by parallel double chains of distorted  $\text{SnI}_6$  octahedra. Each octahedron shares opposite edges of the equatorial plane with two neighbouring octahedra, thereby forming a chain. This chain shares two edges with two octahedra of a parallel chain forming a double chain. The caesium atoms are situated at the centre of nearly equilateral triangle of iodine atoms, and link three double chains. There is no evidence for lone pair distortion in  $\text{CsSnI}_3$ .

The layer structure of  $\text{PbI}_2$  is well known, and there are reports on its behaviour as a semiconductor. The electrical conductivity has been shown to become more electrolytic and less metallic as the temperature rises in fused pulverulent<sup>(45)</sup> and thin film<sup>(46)</sup> samples of  $\text{PbI}_2$ . More recent investigations include edge and above edge luminescence<sup>(47)</sup> and photoconductivity<sup>(48)</sup> studies. The photoconductivity of  $\text{PbI}_2$  single crystals shows a band at 510 nm (2.43eV), attributed to localized excitons, and a band at 670 nm (1.85eV) due to  $\text{Pb}^{2+}$  vacancies.

Lead diiodide has long been known to form coloured complexes of the type  $\text{M}^{\text{I}}\text{PbI}_3$  and  $\text{M}^{\text{II}}_2\text{PbI}_6$  e.g.  $\text{CsPbI}_3$ <sup>(49)</sup>;  $\text{RbPbI}_3$ <sup>(49)</sup>;  $\text{NaPbI}_3$ <sup>(50)</sup>;  $\text{Mg}_2\text{PbI}_6$ <sup>(51)</sup>;  $\text{Zn}_2\text{PbI}_6$ <sup>(52)</sup> and

$\text{TlPbI}_3$ <sup>(52)</sup> all of which are yellow. A series of coloured hydrated compounds are formed with transition metal iodides<sup>(53)</sup> viz. yellow/green needles of  $\text{Cr}_2\text{PbI}_6 \cdot 3\text{H}_2\text{O}$ ; reddish brown crystals of  $\text{Mn}_2\text{PbI}_6 \cdot 3\text{H}_2\text{O}$  and green needles of  $\text{Co}_2\text{PbI}_6 \cdot 3\text{H}_2\text{O}$  and  $\text{Ni}_2\text{PbI}_6 \cdot 3\text{H}_2\text{O}$  the latter being yellow in its anhydrous form.

In  $\text{PbI}_2$  and in many complex halides lead (II) is octahedrally coordinated and the compounds are often isostructural with cadmium salts,<sup>(54)</sup>  $\text{CsPbI}_3$  for example is reported to have the  $\text{NH}_4\text{CdCl}_3$ <sup>(55)</sup> structure. The yellow orthorhombic crystals of  $\text{CsPbI}_3$ <sup>(44)</sup>, obtained from aqueous solution, belong to the space group  $\text{Pmnb}$ . The distorted  $\text{PbI}_6^{4-}$  octahedra share I- atoms to form a one-dimensional polynuclear complex ion,  $(\text{PbI}_3^-)_n$ , running parallel to the a-axis. Nine iodine atoms belonging to three different complex ions of this type are nearly di-trigonally arranged around each Cs-atom. If this material is heated to  $305 - 308^\circ\text{C}$  it is transformed into a black modification which has a monoclinically distorted perovskite-like structure.

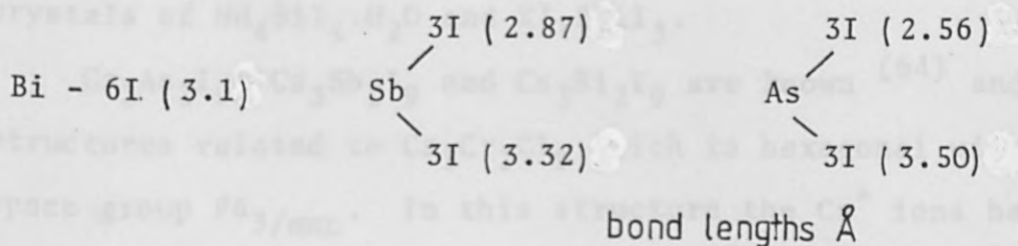
Møller<sup>(56)</sup> has reported that the perovskite phase of  $\text{CsPbI}_3$  is photoconductive with a maximum sensitivity in the region of the absorption edge i.e. in the red. The width of the forbidden gap obtained from these measurements being  $1.7 - 1.8 \text{ eV}$ .

The related compounds,  $\text{TlPbI}_3$ ,  $\text{Tl}_3\text{PbI}_5$ ,  $\text{TlSnI}_3$  and  $\text{Tl}_3\text{SnI}_5$  have been prepared and their electrical conductivities, photoconductivities and band gaps determined.<sup>(57)</sup>

The conductivities are said to be dominated by impurity contributions because they increase with temperature. The conductivity activation energies are 0.07 - 0.71 eV, while the band gaps are in the range 2.0 - 3.2 eV.

1.4.2. Arsenic (III), Antimony (III), Bismuth (III).

Arsenic, antimony and bismuth triiodides are red hexagonal platelets belonging to the space group  $\bar{R}3$ . (58) The metal occupies octahedral interstices between hexagonal close packed iodine atoms. However, the metal is progressively further from the centre of the  $I_6$  octahedron in the series  $BiI_3$ ,  $SbI_3$ ,  $AsI_3$ .



These figures show that bismuth is at the centre of the  $I_6$  octahedron, with no evidence for lone pair distortion. Antimony is significantly displaced from the centre of the octahedron and is intermediate between a molecular crystal, as found in  $AsI_3$  which forms discrete molecules, and the ionic arrangement found in  $BiI_3$ . All the trihalides have approximately hexagonal close-packed lattices.

The group V metal trichlorides and tribromides on reaction with alkali halides form crystals with the formula  $A_3B_2X_9$ . The structures of  $Cs_3As_2Cl_9$ ,<sup>(59)</sup>  $Cs_3Sb_2Cl_9$ <sup>(60)</sup>,  $Cs_3Bi_2Cl_9$ <sup>(60)</sup> and the corresponding bromides are known<sup>(61)</sup>, and the electrical conductivities, absorption spectra and Mössbauer data have been reported.<sup>(62)</sup>

Nickles<sup>(63)</sup> studied the action of  $AsI_3$  on alkali halides, but found that the complexes formed were, in general, unstable. Many of the early reports of "complex" iodides of antimony triiodide were with alkali iodides and were hydrated e.g. red trigonal prisms of  $NH_4SbI_4 \cdot 2H_2O$ , black  $4 NH_4I, SbI_3 \cdot 3H_2O$ , brown  $Na_3Sb_2I_9 \cdot 12H_2O$  and red prisms of  $KI, SbI_3 \cdot nH_2O$ . A series of red or brownish red crystals are formed by complexes of  $BiI_3$  with ammonium and metal iodides e.g. black rhombic needle crystals of  $NH_4BiI_4 \cdot H_2O$  and  $KI, 2BiI_3$ .

$Cs_3As_2I_9$ ,  $Cs_3Sb_2I_9$  and  $Cs_3Bi_2I_9$  are known<sup>(64)</sup> and have structures related to  $Cs_3Cr_2Cl_9$  which is hexagonal with space group  $P6_3/mmc$ . In this structure the  $Cs^+$  ions have twelve  $I^-$  nearest neighbours and the  $As^{3+}$ ,  $Sb^{3+}$  or  $Bi^{3+}$  ions are in distorted octahedral sites occupying two-thirds of the available octahedral voids in the close packed structure. Rubidium iodide forms related complexes with arsenic (III) iodide and antimony (III) iodide. The reported optical band gap, electrical conductivities and  $^{121}Sb$  Mössbauer data of  $M_3^I SbM^{III} X_9$  ( $M^I = Cs$  or  $Rb$ ,  $M^{III} = Bi$ ) have been explained in terms of donation of antimony 5s-electron density to the conduction band<sup>(62)</sup>.

In order to understand the properties of crystalline solids a knowledge of band theory is required.

The earliest theory was the 'free-electron theory' of metals developed by Drude<sup>(65)</sup> and Lorentz<sup>(66)</sup>. They assumed that electrons are classical particles, which, when in thermal equilibrium obey Maxwell-Boltzmann statistics. Sommerfield improved the theory by the application of Fermi-Dirac statistics. This model cannot explain conduction in non-metals since the electron behaviour is independent of the crystal structure.

The periodic potential of the crystal lattice clearly results in departures from ideal 'free' behaviour. The solution of Schrödinger's equation 1.1. for a single electron in this potential provides a set of one electron states which the electron may occupy.

$$-\frac{\hbar^2}{2m} \left( \frac{\partial^2 \psi}{\partial^2 r} \right) + V(r)\psi = E\psi \quad 1.1.$$

Eq 1.1. is often referred to as the Bloch<sup>(67)</sup> equation.  $V(r)$  is a periodic function which has the same periodicity as the crystal lattice, i.e.  $V(r) = V(na + r)$ , where  $a$  is the lattice constant and  $n$  an integer.

The most important difference between the quasi-free electron theory and the free electron theory is that the relationship between  $E$  and  $\underline{k}$  (the momentum of the electron)



is no longer a simple parabolic function. Instead the function is multivalued and there are certain values of energy which are not possible for the electrons as no permitted  $\underline{k}$  states exist for them. It is possible to plot a curve showing the energy,  $E$ , as a function of  $\underline{k}$  (Fig 1.3), this is known as the extended zone scheme. It can be seen that for large energies the function  $E(\underline{k})$  approaches the free electron relation  $E = \hbar^2 k^2 / 2m$  (shown dotted line Fig 1.3) quite closely within the allowed energy band.

Since  $\underline{k}$  is a vector the edges of the bands should be described by the boundaries of a three-dimensional shape in  $\underline{k}$ -space. Such a figure is called a Brillouin zone. Its shape is determined by the geometrical structure of the translation lattice and its dimensions depend on the lattice constant  $a$ . Similar extended zone diagrams can be drawn in two or three dimensions, the discontinuities in energy appearing all over the zone boundaries.

The difference between metals, semiconductors and insulators can be explained by the quasi-free electron theory. The number of permitted values of the wave vectors,  $\underline{k}$ , is equal to  $N_i$ ; the number of ions in the crystal. In accordance with the Pauli Principle each  $\underline{k}$  state may be associated with two electron spin states and so the total number of electrons in each zone is  $2N_i$ . For a monovalent metal only half of a zone is occupied and the energy distribution is approximately the same for the free-electron or band theory models. When there are an even number of

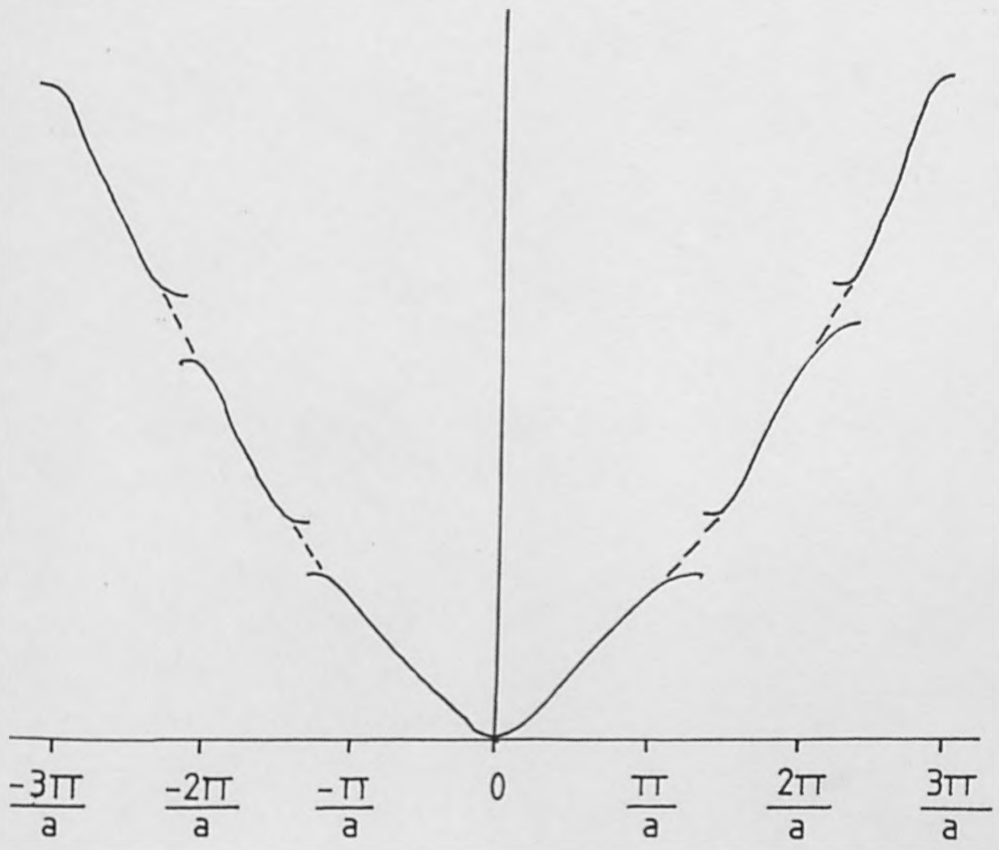


Fig. 1.3. Energy curves for a nearly free electron model in one dimension. The dotted line curve is the free electron case  $E = \hbar^2 k^2 / 2m$ .

(a)

electrons these occupy an integral number of zones. If the gap between adjacent zones is sufficiently small i.e.  $\sim kT$  the material is a semiconductor, as a few electrons can be excited across the gap at room temperature. If the gap is  $\geq kT$  excitation to the next band cannot occur and the material is an insulator.

The quasi-free electron theory stresses the plane wave part of the Bloch function but neglects the atomic part. An alternative approach is to assume that the crystal is formed by bringing the individual atoms close together, i.e. stress the Bloch function near the nucleus. When the atoms are well separated, so that each is an isolated system, the equivalent energy levels on each atom will be exactly the same (Fig 1.4(a)). When the atoms are brought sufficiently close together there is an interaction between each atom and its neighbours and they must all be considered as parts of a single system. The original equivalent energy states must shift relative to one another so that the Pauli exclusion principle is not violated. The closer the atoms are together the greater the shift energy. If there are  $N_i$  atoms, each electron state for a single atom will spread into  $N_i$  levels. Thus the 3s outer level of sodium which can contain two electrons will spread into a band containing  $2N_i$  discrete levels. Above this the unoccupied 3p sodium states will spread into another band (Fig 1.4.(b)). This treatment is called the tight binding approximation because the outer electrons are assumed initially to be closely associated with their atoms.

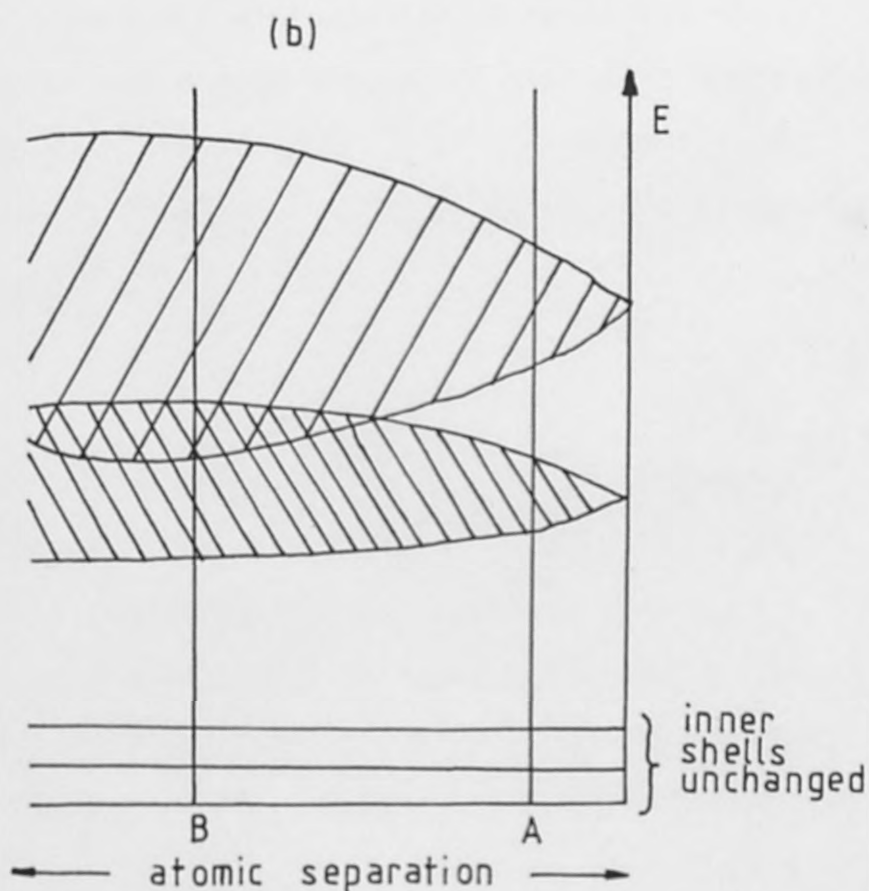
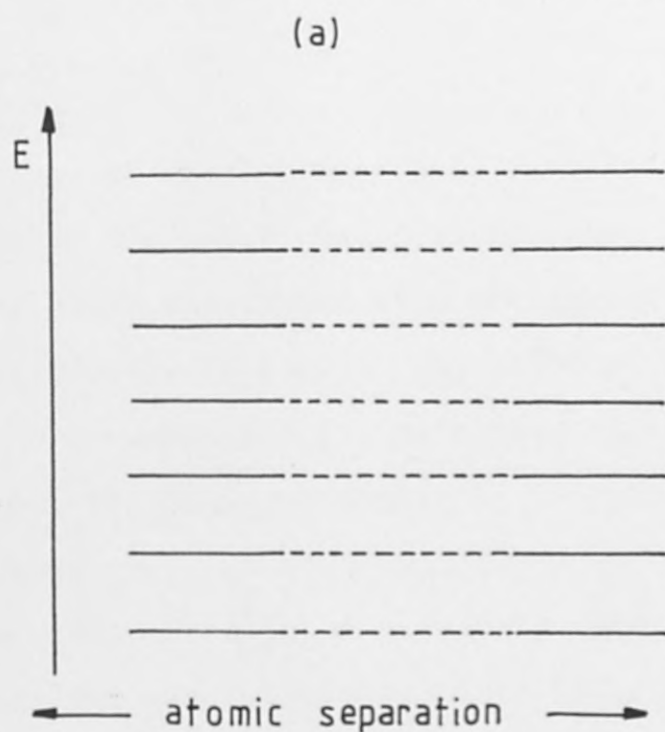


Fig.1.4. (a) sharp levels when atoms well separated  
 (b) energy levels as a function of separation, showing how they broaden (A) and overlap (at B) as atoms brought closer together. This demonstrates the formation of energy bands, band gaps and overlapping bands.

It shows that; perovskite lattice at room temperature (69)

- 1) The presence of band gaps or band overlap depends very much on the individual crystal, and
- 2) since the bands are formed from the spreading of the different electronic levels, the shape of a higher band is not necessarily the same as that of the lower band, nor need the number of permitted states be the same.

The second consequence is of particular importance in band calculations for semiconductors since it is not possible to describe either of these effects in the periodic potential band theory.

The two approximations discussed over-emphasise the free electron aspect and atomic aspect of band wave functions, respectively. However, in doing so they draw attention to the essential factors which are included in more comprehensive theories (68).

#### 1.6. Summary

The stereochemistry of most p-block elements in lower oxidation states is dominated by the presence of filled non-bonding lone pair orbitals. The environments of these elements in many compounds of tin (II), lead (III), arsenic (III), antimony (III), bismuth (III), selenium (IV), tellurium (IV) and polonium (IV) are distorted by the presence of lone pair orbitals. There are, however, a number of compounds in which these elements are found in regular octahedral sites,  $\text{CsSnBr}_3$ , for instance, is black with a metallic lustre and

has an ideal perovskite lattice at room temperature <sup>(69)</sup>. The existence of these regular environments has been explained either in terms of the accommodation of the  $ns^2$  electrons in  $a_1$  anti-bonding orbitals <sup>(35)</sup> or in terms of the absence of distorting crystal field effects <sup>(37)</sup>. All the solid compounds containing  $ns^2$  electrons in high symmetry sites are coloured and many show metallic or semiconducting properties. It has been suggested that the pseudo-metallic conducting properties and the Mössbauer data of  $CsSnBr_3$  can be explained by the population of conduction bands, in the solid, by the  $5s^2$  electrons of tin. These bands would arise from the mutual overlap of empty bromine  $t_2$ , 4-d orbitals which would be at a maximum in the undistorted perovskite structure. It is possible, however, that iodine electrons in iodine sub-lattices are sufficiently mobile to be promoted to a conduction band, produced by overlapping empty iodine orbitals to give semiconducting properties.

In evaluating the role of the main group  $ns^2$  electrons and of the iodide electrons in this study, much use was made of structural inorganic chemistry and solid state physics. Solid state chemistry may be defined as the study of reactions in solids and of the factors which may affect the reactivity of the solids with other solids and with ligands or gases. Changes in reactivity of solids may be due to a number of factors, including:

- 1) structural defects, such as lattice defects, and

phase changes, impurities and non-stoichiometry.

- 2) chemical reaction and corrosion
- 3) surface effects, such as adsorption and catalysis
- 4) absorption of electromagnetic radiation
- 5) changes in electronic and magnetic states

The techniques of solid state chemistry can be used to study the physical properties and the structure of the materials. The physical properties of materials may be divided into five classes:

- 1) electronic properties, such as electrical conductivity, photoemission and photoconductivity.
- 2) magnetic properties, including magnetic susceptibility, ferro and antiferro-magnetism
- 3) optical properties, such as refractive index and optical activity
- 4) thermal properties, such as thermal conductivity, heat capacity, thermoelectric effect and thermal expansion
- 5) mechanical properties

The research described in this work on the electronic structures of simple iodides and of a series of coloured lead (II), tin (II), antimony (III) and bismuth (III) compounds makes use of the techniques and theories of solid state chemistry and physics to provide a greater depth of understanding of the properties of the solids prepared.

## References

1. H. M. Rosenberg, "The Solid State", Clarendon Press, Oxford, 1975.
2. W. H. Bauer, Acta Cryst., 1956, 9, 515.
3. M. F. C. Ladd, J. Chem. Phys., 1974, 60, 1954.
4. P. Brand, H. Sachmann, Acta Cryst., 1963, 16, 446.
5. M. W. Lister, L. E. Sutton, Trans. Faraday Soc., 1941, 37, 393.
6. R. N. Ingham, S. D. Rosenberg, H. Gilman, Chem Rev., 1960, 60, 459.
7. G. H. Wong, V. Schomaker, J. Chem. Phys., 1958, 28, 1007.
8. P. C. Chiech, J. Trotter, J. C. S. (A), 1970, 911.
9. N. A. Goryenova, M. L. Belle, L. B. Zlatkin, G. V. Lashkova, A. S. Popavnoi, V. A. Challdgshev, Soviet Phys. Semicond., 1969, 2, 1126.
10. A. A. Vaipdin, F. P. Kesamanly, Yu. V. Rud, Izv. Akad. Nauk. S. S. S. R. Neorg. Mater, 1967, 3, 974.
11. N. A. Goryenova, F. P. Kesamanly, C. V. Lushakova, Fiz. Tekh. Poluprov. 1967, 1, 1010.
12. W. E. Howard, R. Tsu, P. J. Stiles, Proc. Int. Conf. Phys. Semicond. 9th, 1968, 29, 163.
13. J. Goubeau, R. Baumgarten, H. Weiss, Z. Anorg. Chem. 1966, 348, 286.
14. P. Reich, H. Reiss, Z. Chem., 1967, 7, 115.
15. W. Wieker, A-R. Grimmes, Z. Naturforsch, 1967, 22b, 257 & 1220.



16. R. Hulme, J. Chem. Soc., 1963, 1524.
17. L. A. Woodward, L. E. Anderson, J. Chem. Soc., 1957  
1284.
18. J. D. Donaldson, Prog. Inorg. Chem., 1967, 8, 287.
19. J. D. Donaldson, "A Review of the Chemistry of Sn(II) Compounds", 1964, Tin Research Institute, Publication No. 348.
20. J. F. Young, Adv. Inorg. Chem. Radiochem., 1965, 8,  
14, and I. Lindquist, A. Niggler, J. Inorg. Nucl. Chem.,  
1956, 2, 345.
21. J. D. Donaldson, D. G. Nicholson, B. J. Senior,  
J. Chem. Soc (A), 1968, 2928.
22. R. J. H. Clark, L. Maresca, P. J. Smith, J. Chem.  
Soc. (A), 1970, 2687.
23. J. F. Young, Adv. Inorg. Chem. Radiochem., 1968, II, 92.
24. D. G. Nicholson, Phd Thesis, London, 1969.
25. W. J. Moore, L. Pauling, J. Am. Chem. Soc., 1941, 63,  
1392.
26. L. G. Sillen, A. E. Martell "Stability Constants of  
Metal-ion Complexes", Chem Soc. (London). Spec  
Publ. 17, 1964.
27. V. E. Mironov, Zh. Neorg. Khim, 1961, 6, 415 & 897.
28. W. Blitz, Z. Anorg. Allgem. Chem., 1922, 124, 230.
29. R. E. Tapscott, R. L. Belford, I. C. Paul,  
Coordination Chem. Rev., 1969, 4, 323.
30. A. C. Skapski, Chem. Comm., 1966, 10.
31. G. Y. Ahlyah, M. Goldstein, J. Chem. Soc., A, 1970,  
1356.

32. M. Webster, S. Keats, J. Chem. Soc., A, 1971, 298.
33. E. Martineau, J. B. Milne, J. Chem. Soc., A, 1970, 2971.
34. R. J. Gillespie, J. Chem. Educ., 1970, 47, 18.
35. L. E. Orgel, J. Chem. Soc., 1959, 3815.
36. E. Martineau, J. B. Milne, J. Chem. Soc., (A), 1970, 2971.
37. D. S. Urch, J. Chem. Soc., 1964, 5775.
38. J. D. Donaldson, J. Silver, Inorg. Nucl. Chem. Lett.,  
1974, 10, 537.
39. R. A. Howie, W. Moser, I. C. Trevena, Acta. Cryst.,  
1972, B28, 2965.
40. E. Doni, G. Grosso, I. Ladiana, Physica, 1980, 99B,  
281.
41. V. Auger, T. Karontassis, Compt. Rend., 1925, 181, 665.
42. P. Mauersberger, F. Huber, Acta Cryst., 1980,  
B36, 683.
43. H. J. Haupt, F. Huber, H. Preut, Z. Anorg. Allgem  
Chem., 1974, 408, 209.
44. C. K. Møller, Mat. Fys. Medd. Dan. Vidensk. Selsk.  
1959, 32, 1.
45. W. Hampe, Ber., 1888, 21, 161.
46. G. Tamman, H. Bredmeier, Z. Anorg. Chem., 1925,  
144, 64.
47. V. G. Plekhanov, I. Kuusmann, Tr. Inst. Fiz. Akad.  
Nauk. Est., S. S. S. R., 1976, 46, 81
48. M. Constantinescu, I. Baltog, C. Ghita, L. Ghita,  
Rev. Roum. Phys., 1978, 23, 31.
49. H. L. Wells, Amer. J. Sciences, 1893, 45, 121.

50. C. H. Herty, Amer. Chem. J., 1892, 14, 126.
51. A. Mosnier, Compt. Rend., 1895, 120, 416 & 444.
52. J. Barlot. Amer. Chem. J., 1898, 72, 1,21
53. A. Mosnier, Ann. Chem. Phys., 1897, 12, 378.
54. A. F. Wells, "Structural Inorganic Chemistry", 4th Ed., Oxford University Press, London, 1975.
55. H. Brasseur, L. Pauling, J. A. C. S., 1938, 60, 2886.
56. C. K. Møller, Nature, 1958, 182, 1436.
57. V. V. Tsigita, E-Yu. Peresh, V. B. Lazarer, A. A. Kikineshi, K. A. Batori, V. I. Starosta, Izv. Akad. Nauk. S. S. S. R., Neorg. Mater, 1981, 17, 970.
58. J. Trotter, T. Zobel, Z. Kristallographic, 1966, 123, 67.
59. J. L. Hoard, L. Goldstein, J. Chem. Phys. 1935 3, 117.
60. K. Kihara, T. Sudo, Acta Cryst., 1974, B30, 1088.
61. F. Lazamini, Acta Cryst, 1977, B33, 2961.
62. M. J. K. Thomas, Phd Thesis, London, 1980.
63. J. Nickles, J. Pharm. Chim., 1862, 41, 147.
64. B. Chabot, Acta Cryst., 1978, B34, 645.
65. P. Drude, Ann. Physik, 1900, 1, 566.
66. H. A. Lorentz, "The Theory of Electrons", Teubner Verlag, Leipzig, 1909.
67. F. Bloch, Z. Physik, 1928, 52, 555.
68. R. J. Elliott, A. F. Gibson, "An Introduction to Solid State Physics". McMillan, 1974.
69. J. D. Donaldson, J. Chem. Soc., 1975, 1500.

## Chapter Two

### Theoretical Background to Techniques Used.

	<u>Page</u>
2.1. Optical Spectroscopy	33
2.1.1. Photon Absorption Processes in Solids	33
2.1.2. Optical Emission from Solids	35
2.1.3. Excited State Luminescence	36
2.1.4. Interband Luminescence	38
2.2. Conductivity	41
2.2.1. Conductivity:Temperature Dependence	46
2.2.2. Thermal Conductivity	47
2.3. Photoconductivity	48
2.3.1. General Concepts	48
2.3.2. Lifetime	50
2.3.3. Photoexcitation Dependence of Mobility	51
2.3.4. Photosensitivity	51
2.3.5. Spectral Response	52
2.3.6. Recombination Mechanisms	54
2.4. Contacts	57
2.4.1. Rectifying Contacts	57
2.4.2. Ohmic Contacts	60
2.5. Theory of Crystal Structure Determination	63
2.5.1. Data Reduction	65
2.6. Crystal Structure Determination	66

	<u>Page</u>
2.6.1. Fourier Synthesis	66
2.6.2. Patterson Function and the Heavy Atom Method	67
2.6.3. The Difference Fourier	68
2.6.4. Least Squares Refinement	69
2.7. Computer Programs used in X-Ray Crystallography	70
2.7.1. SHELX-76	70
2.7.2. Powder and Powref	70
2.7.3. X-RAY - 72	71
2.7.4. Cellplot	71
2.8. Mössbauer Spectroscopy	71
2.8.1. Introduction	71
2.8.2. Fundamental Features	72
2.8.3. Hyperfine Interactions	76
2.8.4. The Chemical Shift	77
2.8.5. Quadrupole Splitting	79
2.8.6. Magnetic Hyperfine Splitting	80
2.8.7. Combined Magnetic and Quadrupole Interactions	82
2.8.8. The Mössbauer Spectra of Tin	84
2.8.9. The Mössbauer Spectra of Antimony	86

## 2.1.

## Optical Spectroscopy

### 2.1.1.

### Photon Absorption Processes in Solids

Fig (2.1) shows the absorption spectrum of a hypothetical solid: it is a semiconductor to which a magnetic field may be applied and it is antiferromagnetic at some low temperature.

Semiconductors show all the optical properties of insulators and metals though not, of course, to the same degree. The main features are as follows:

- (a) In the ultraviolet, and sometimes extending into the visible and infrared is a region of intense absorption which arises from electronic transitions between the valence and conduction bands. Such transitions generate mobile electrons and holes, resulting in photoconductivity. The absorption coefficient is typically in the range  $10^5$  to  $10^6$   $\text{cm}^{-1}$  but some structure is normally observable in reflection measurements. On the high energy side of this band (typically around 20eV) there is often a smooth fall in absorption over a range of several electron volts. On the low energy side, on the other hand, the absorption coefficient falls more rapidly and may fall by as much as six orders of magnitude within a few tenths of an eV. In semiconductors this low energy boundary of the fundamental absorption is often the most striking feature of the spectrum and is referred to as the absorption edge.
- (b) The limit of the absorption edge corresponds to the

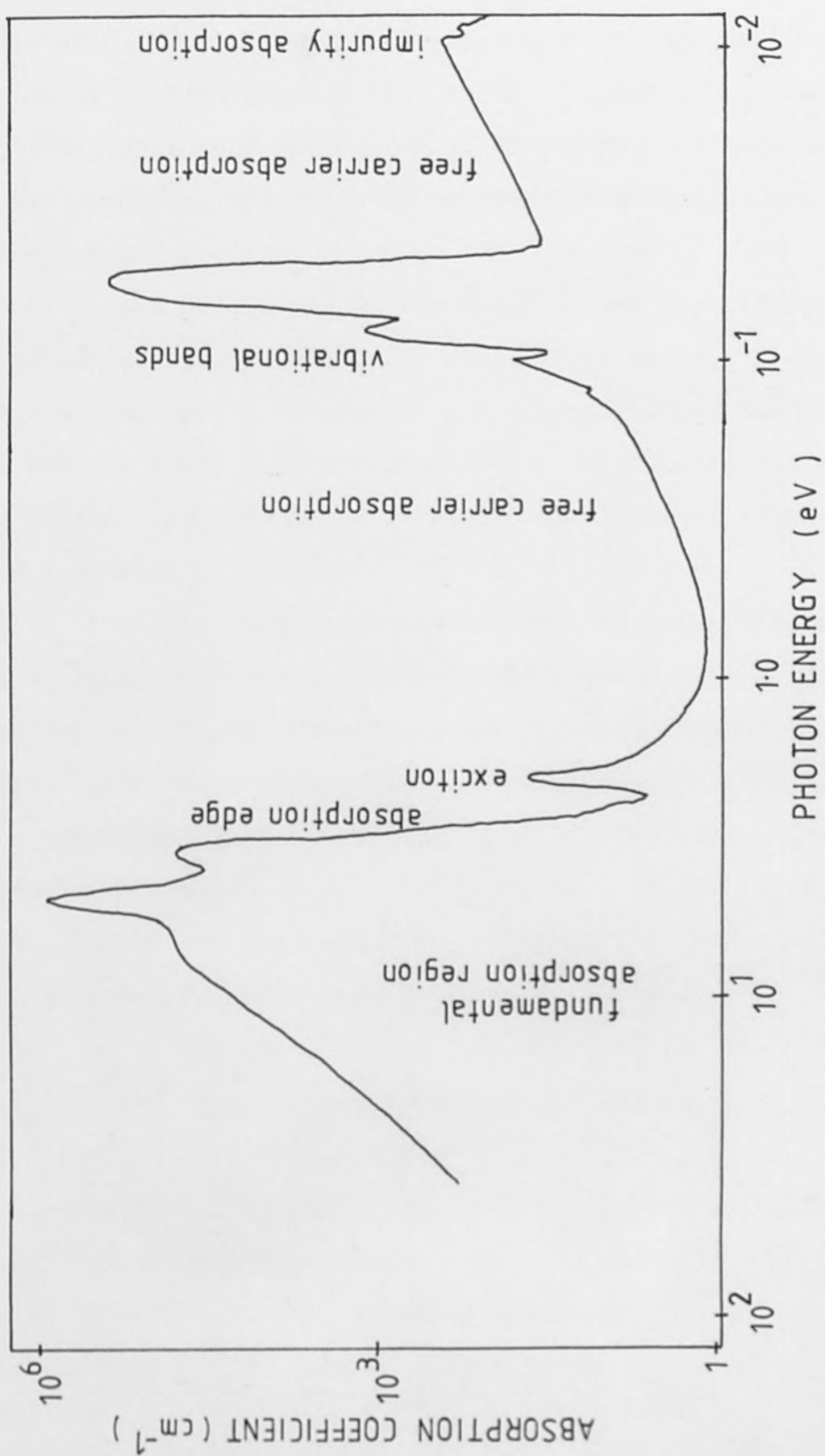


Fig. 2.1. Absorption Spectra of a Hypothetical Semiconductor

photon energy required to promote electrons across the minimum energy gap,  $E_g$ . The edge region often shows some structure, in particular that due to excitons. Exciton absorption is more pronounced in insulators, particularly ionic crystals, and can lead to strong narrow-line absorption as in atomic spectra.

(c) As the wavelength is increased beyond the absorption edge the absorption starts to rise slowly again. This increase is due to electronic transitions within the conduction or valence bands and is referred to as free carrier absorption. It extends throughout the infrared and microwave regions of the spectrum.

(d) At photon energies between 0.0eV and 0.05eV (50 to 20 nm wavelength) a new set of absorption peaks appear. These are due to interaction between the incident photons and the vibrational modes of the lattice. If the crystal is ionic the absorption coefficient may reach  $10^5 \text{ cm}^{-1}$  and strong reflection occurs.

(e) Impurities give rise to additional absorption and these are included in the figure only for completeness.

### 2.1.2. Optical Emission From Solids

Optical excitation of a sample creates electron-hole pairs called excitons. The lifetime of the excitons depends on the crystal lattice, impurity concentration and type, dislocations and so forth. Eventually the excitons will



deactivate either radiatively or non-radiatively. The former process accompanied by photon emission is termed photoluminescence, and is of primary interest since it is observable with higher sensitivity. Unlike absorption spectra, which are due to properties of the bulk material, emission spectra are strongly affected by small traces of impurities which can give rise to their own luminescence spectra or modify the band structure of the host lattice.

Luminescence is a two stage process: first, electrons are excited to higher energy states with the subsequent reemission of energy by the excited electrons in the form of electromagnetic radiation on the low energy side of the absorption band. When the excitation process involves light from the visible or near visible region of the spectrum this is known as photoluminescence.

There are two basic types of luminescence: luminescence from the excited state of a molecule or ion to its ground state, and interband luminescence.

### 2.1.3. Excited State Luminescence

The configuration coordination model of Seitz and Mott (2,3), (Fig 2.2) may be used to describe the emission process occurring at a luminescent centre. The model describes the overall geometrical configuration of the nuclei surrounding the luminescent centre and explains the red shift of the luminescent band relative to the corresponding absorption

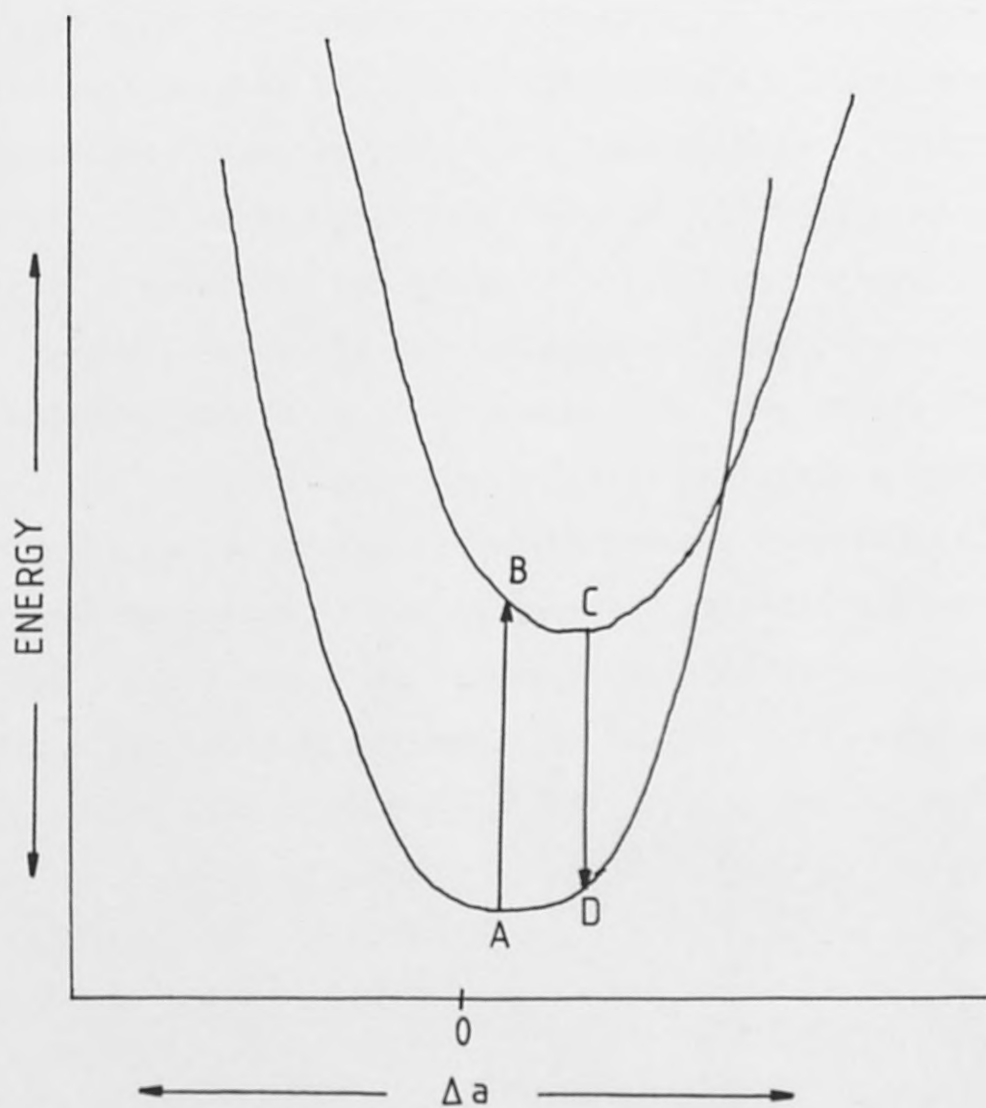


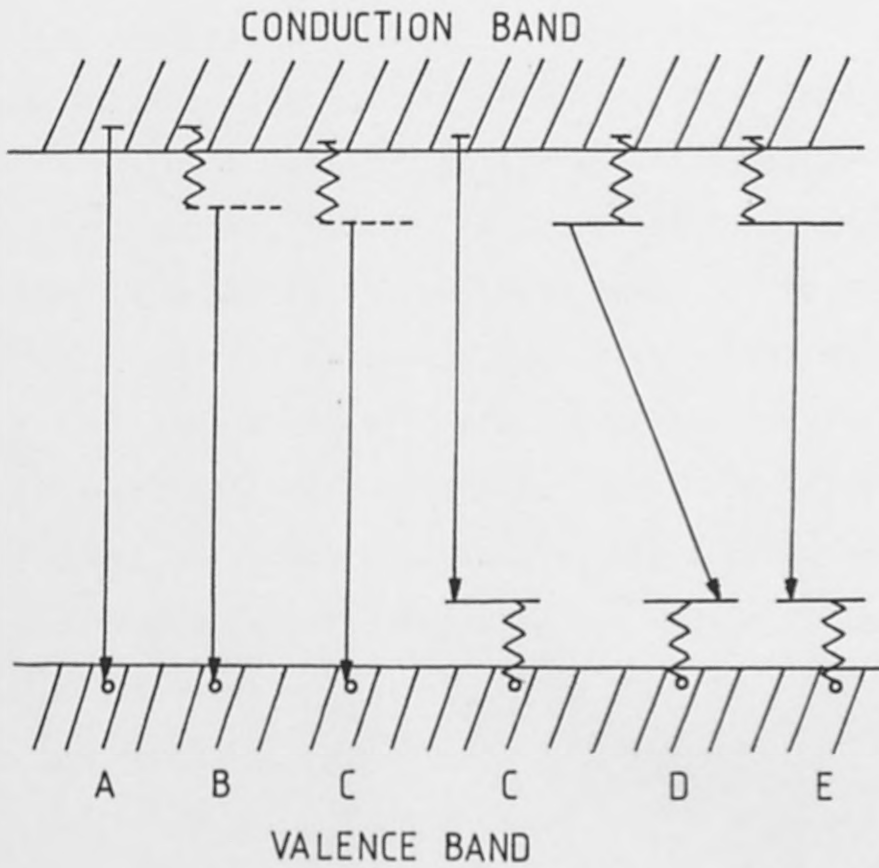
Fig. 2.2. Configuration Coordinate Diagram of Luminescence showing the origin of the Stokes Shift.

band, known as the Stokes Shift. For absorption spectra the Franck-Condon principle means that the electronic transitions occur at energies corresponding to the energy difference between the electronic states at ground state internuclear distance (AB). For luminescence to occur however, the lifetime of the emitting state must be long compared with that of a molecular vibration if significant emission is to be observed, hence the excited electron equilibrates prior to emission (CD) at a lower energy than that of the absorption band. In addition to photon emission the excited electrons can lose energy by non-radiative thermal de-excitation. As the temperature of the luminescent material increases more of the excited electrons become de-excited in this manner and the intensity of the emission falls. At a critical temperature characteristic of the material and emission band the luminescence is thermally "quenched" and no luminescence is observed, this quenching temperature is highest for a rigid lattice and small Stokes Shift.

#### 2.1.4.

#### Interband Luminescence

In addition to localised luminescence, interband luminescence can occur i.e. an electron excited into the conduction band of a semiconductor or insulator will recombine with a hole in the valence band. The photon emission processes which may occur in interband luminescence are illustrated in (Fig 2.3) using the band model of Richl and Shön<sup>(4,5)</sup>



- A. Conduction Band to Valence Band
- B. Recombination via Exciton Levels
- C. Donor Level to Valence Band and Conduction Band
- D. Donor Level to Acceptor Level
- E. Recombination via Impurity Excited States

Fig. 2.3. Photon Emission Process in Solids.

and Johnson<sup>(6)</sup>.

Process A shows direct interband recombination of electrons and holes with photon emission, which is the reverse of the absorption edge. Compared with other, competing processes it is, however, relatively unlikely and only observed in high purity, high quality crystals and is rarely seen in materials with small effective masses owing to the large electron orbital radii. If recombination occurs via exciton states (Process B) the observed bands are narrower than and slightly shifted in energy from their predicted values. The two processes shown by C are due to excitons bound to shallow donors and free-electron-to-acceptor transitions respectively. These may be phonon assisted and the binding energy of the donors and acceptors determine the energy of the emitted radiation. Process D would give rise to a series of lines in the spectrum, while Process E is the localised luminescence described in the previous section. An impure solid would be expected to show any of the transitions processes C-E.

When an electron is excited into the conduction band, any excess vibrational energy will be lost before emission (i.e. the electron will "thermalize") so that the electrons will lie in a band  $kT$  wide at the bottom of the conduction band (and the electron holes will lie within  $kT$  of the top of the valence band) and give rise to an emission band of width  $kT$  as opposed to the narrow lines expected from well defined localised levels. As in the case of localised emission non-radiative de-excitation increases with increasing

temperature.

## 2.2.

## Conductivity

The conduction of direct electric current in a material medium can be explained in terms of the band theory.

The band theory considers motion of electrons in an infinite three dimensional field. Fermi-Dirac statistics are used to deal with the large number of electrons involved and to take into account the discrete energy levels required by quantization and the Pauli Principle. This leads to the concept that electrons occupy bands which are formed in crystals by orbital overlap when the nuclei are within a certain minimum distance, the maximum number of electrons that can be accommodated in the band being determined by the Pauli Principle, taking into account the number of energy levels forming the band. Electrical conduction occurs by movement of electrons within the bands of the crystal.

As the core orbitals of atoms contain their full complements of electrons the inner, core, bands around the nuclei within crystals are also completely filled prohibiting the movement of electrons within the band. The higher valence bands may be filled or partially filled depending on the number of valence electrons available.

The differences among metals, semiconductors and insulators can be described in terms of energy-band diagrams. In metals, or conductors, there is either an empty band or a partially filled valence band which overlaps a filled

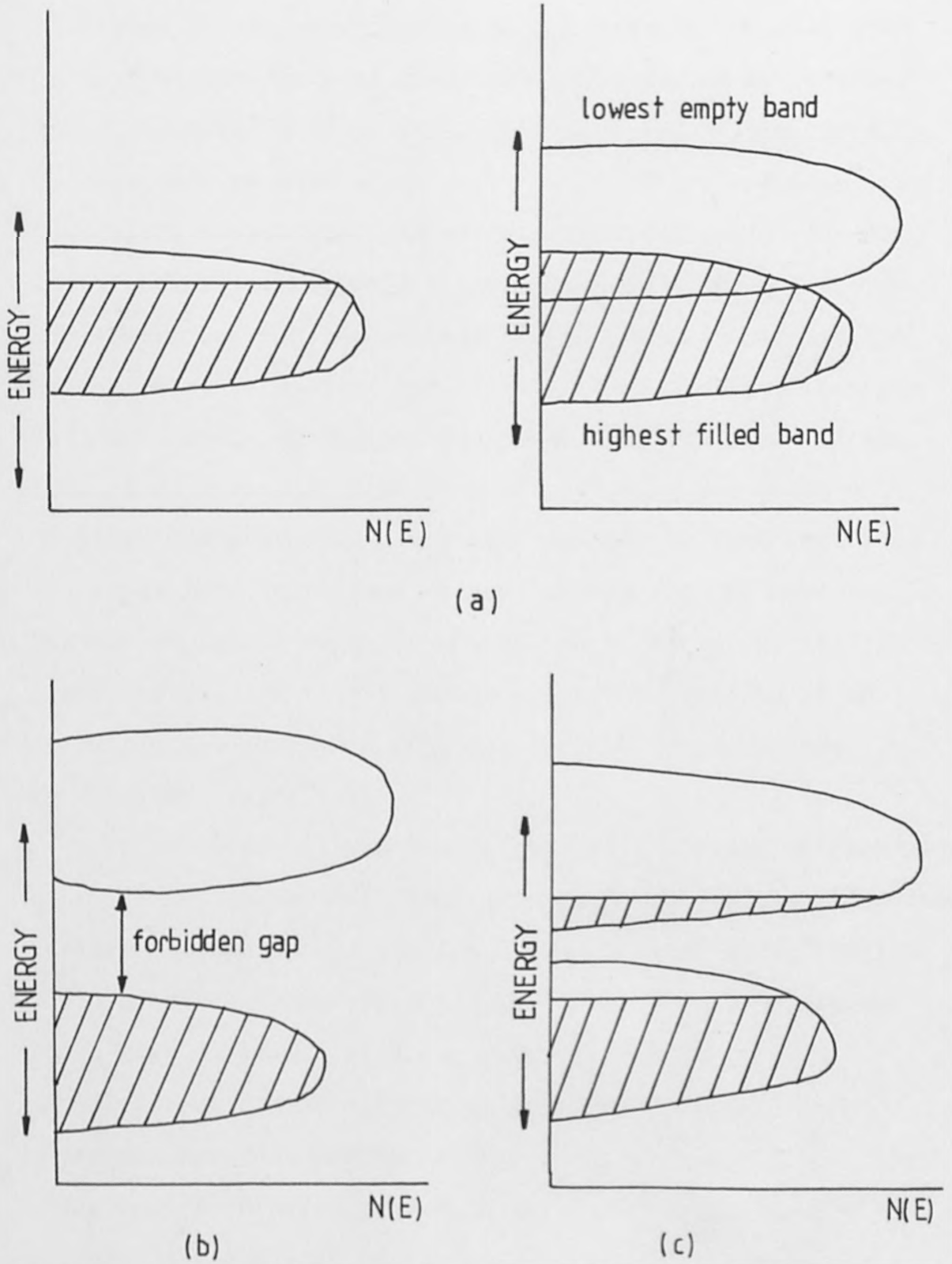


Fig. 2.4. Energy Diagrams (a) Conductor (b) Insulator  
(c) Intrinsic Semiconductor

valence band (Fig 2.4(a)), at all temperatures including  $0^{\circ}\text{K}$ . Electrons in the upper levels of the valence band are free to move within the band under the influence of an external field, hindered only by collisions with impurities, lattice defects, and phonons which slow the electrons and result in electrical resistance. In an insulator the conduction band is essentially empty at all temperatures, since the energy difference between the highest filled valence band and the lowest empty conduction band is such that the forbidden gap is inaccessible to thermal electrons (Fig 2.4(b)). In semiconductors the conduction band is partially populated at "higher" temperatures, since the band gap is such that some electrons have sufficient thermal energy ( $kT$ ) to cross it, but is completely empty at  $0^{\circ}\text{K}$  or, more generally, at "low" temperatures. In this case the crystal is said to be an intrinsic semiconductor and, for example germanium has  $E_g = 0.67\text{eV}$  (Fig 2.4(c)).

While metals differ from the other two types of materials in the occupancy of the conduction band states, the difference between semiconductors and insulators is much less definite. It is possible to modify the properties of a semiconductor or to make an insulator a semiconductor by introducing impurities or non-stoichiometry into the lattice. Such materials are then extrinsic semiconductors (Fig 2.5). The defects or impurities produce localised energy levels which lie within the forbidden region. These levels are either full, in which case they lie just below the conduction band



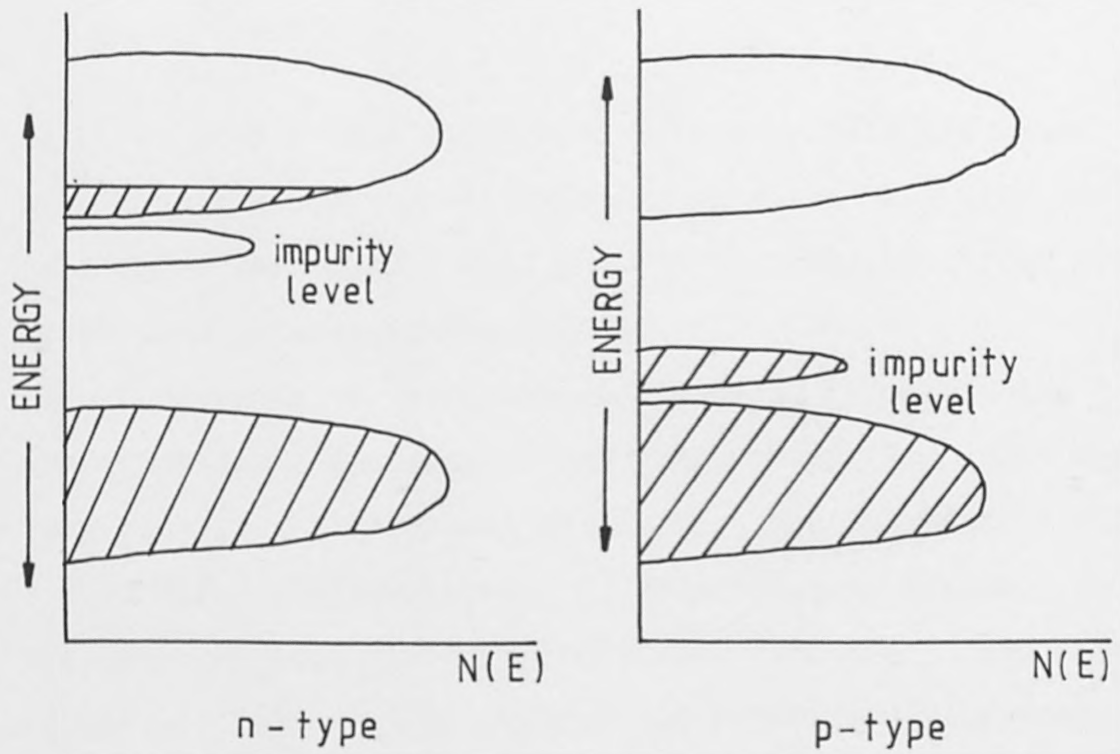


Fig. 2.5. Energy diagrams for an extrinsic semiconductor.

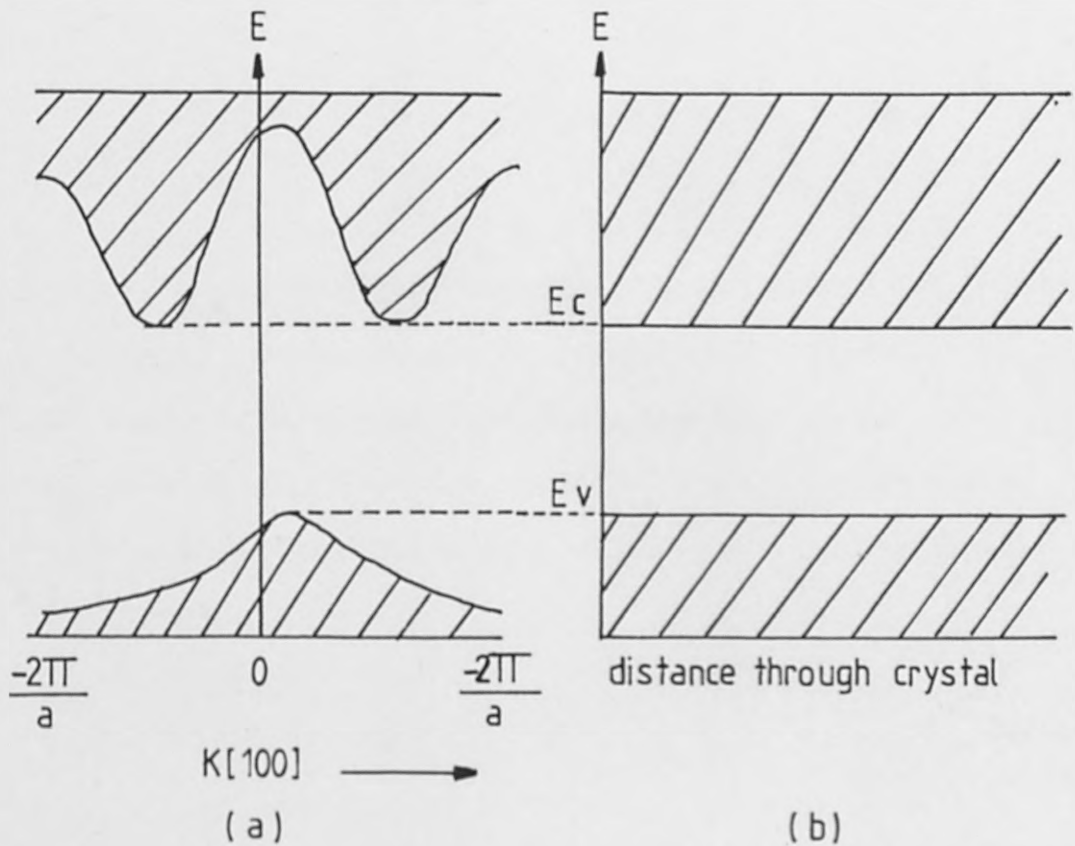


Fig. 2.6. (a) Variation of energy levels with direction in a Si Crystal (b) Representation terms of a conventional band model.

to which they donate electrons; such materials are known as n-type semiconductors; or empty in which case they lie just above the valence band and can withdraw electrons from it to give p-type semiconduction.

Because of the periodic potential in crystals, the energy maxima and minima of the valence and conduction bands vary with crystallographic direction, this is shown in Fig 2.6(a) for a silicon crystal<sup>(7)</sup>. In the qualitative treatment of band theory a conventional band model (Fig 2.6b) is used to represent an average direction in the crystal, so the minimum energy of the conduction band and the maximum energy of the valence band are constant throughout the crystal.

For a semiconductor it can be shown that<sup>(8)</sup>

$$np = 4 \left( \frac{kT}{2\pi\hbar^2} \right)^3 (m_e m_h)^{3/2} \exp - \left( \frac{E_g}{kT} \right) \quad (2.1.)$$

where  $n$ ,  $p$  are respectively the concentrations of electrons and holes of masses  $m_e$  and  $m_h$  assuming the distance of the Fermi level from the edge of both bands is large compared with  $kT$ . Conductivity is proportional to the carrier concentration, so for an intrinsic semiconductor,  $n = p$ , then

$$\sigma = A (T)^3 \exp - \left( \frac{E_g}{2kT} \right) \quad (2.2.)$$

where the exponential term is dominant i.e.  $\log \sigma = -E_g/2kT + \text{constant}$ .

The width of the forbidden band may be determined directly by optical methods provided a direct optical transition exists, or by variable temperature conductivity measurements.

### 2.2.1. Conductivity: Temperature Dependence

The differences shown in Fig 2.4 and described in the previous section indicate the reasons for different conductivity variations with changing temperature in metals and semiconductors. Using the free electron relationship for the specific conductivity,  $\sigma = ne\mu$ , it is apparent that  $\sigma$  depends on both  $n$  and  $\mu$ . The temperature dependence of  $\sigma$  stems from the variations of  $n$  or  $\mu$  or a combination of the two, with temperature.

In the case of metals, the temperature dependence of conductivity depends on the electron mobility,  $\mu$ , since the free electron concentration,  $n$ , remains essentially constant at all temperatures below the melting point. An increase in the temperature increases the thermal vibrations of the metal ions at the lattice sites. The conduction electrons interact more strongly with the more vigorously vibrating positive ions and are scattered more often from their straight-line motion and pathway. These scattering processes<sup>(9)</sup>, decrease the electron mobility and, consequently, the conductivity as the temperature is increased. Above the Debye temperature the mobility and

conductivity are proportional to  $1/T$ .

For semiconductors, the situation is quite different since,  $n$  can change as the temperature is varied. The production of charge carriers follows an exponential dependence on temperature, the number of conduction electrons,  $n$ , being given by:-

$$n = n_0 e^{-E_g/kT} \quad (2.3.)$$

where  $n_0$  is the concentration of atoms at lattice sites and  $E_g$  is the band gap energy. The conductivity relationship then becomes:-

$$\sigma = (n_0 e^{-E_g/kT}) e \mu \quad (2.4.)$$

Since  $\mu$  varies approximately as  $1/T$  the major temperature variation in the conductivity of a semiconductor is caused by the dependence on carrier concentration,  $n$ . The measurement of  $\sigma$  as a function of temperature will, therefore, permit an approximate calculation of the band gap energy,  $E_g$ , of a semiconducting material.

### 2.2.2.

### Thermal Conductivity

At normal temperatures heat is transferred through a solid primarily by phonons, i.e. lattice vibrations, and

by free charge carriers (electrons or holes). The thermal conductivity  $\sigma_T$  is a measure of the ease of heat transfer of a particular solid when the solid is placed in a thermal gradient<sup>(10)</sup>. If the heat flux  $Q$  is defined as the calorie flow per second across a unit cross section then  $\sigma_T$  is given by:-

$$Q = -\sigma_T \frac{dT}{dx} \quad \text{or} \quad \sigma_T = - \frac{Q}{(dT/dx)} \quad (2.5.)$$

The relative importance of phonons and free electrons in determining the thermal conductivity, of any particular solid, depends on the presence of free carriers and also on the mean free path of the moving particles, whether phonons or electrons.

### 2.3. Photoconductivity

#### 2.3.1. General Concepts

For an insulator or semiconductor with no impurity or other energy levels in the band gap the number of electrons in the conduction band will equal the number of holes in the valence band, and this will remain constant at a given temperature. Electrons are thermally promoted from the valence to the conduction band leaving positively charged holes in the valence band, and it is these charge carriers which are responsible for intrinsic conductivity.

Illumination of the material with light of frequency such that  $h\nu_0$  equals or exceeds the forbidden energy gap,  $E_g$ , creates further electron-hole pairs which then contribute to the conductivity. In semiconductors the band gap varies from 0.2 to 2.5 eV for which the threshold wavelengths for intrinsic photoconductivity are 6.2 and 0.5 microns. This enhancement in the number of charge carriers increases the conductivity of the material and the phenomena is called photoconductivity.

Suppose that such a material has a dark conductivity

$$\sigma_0 = n_0 e \mu_0 \quad (2.6.)$$

where for simplicity the conductivity of the material is dominated by electrons in both the light and dark, e.g. the photoexcited holes are captured by imperfection much more rapidly than electrons. In the presence of photoexcitation

$$\sigma = n e \mu \quad (2.7.)$$

where  $\sigma = (\sigma_0 + \Delta\sigma)$ ,  $n = (n_0 + \Delta n)$  and  $\mu = (\mu_0 + \Delta\mu)$ .

By substituting these expressions into Eq.(2.7), we obtain, for the photoconductivity:-

$$\Delta\sigma = \sigma - \sigma_0 = e\mu_0\Delta n + ne\Delta\mu \quad (2.8.)$$

Mechanisms exist for both changes in carrier density  $\Delta n$ , and changes in carrier mobility  $\Delta \mu$  with photoexcitation.

2.3.2.

Lifetime

The change in carrier density  $\Delta n$  with excitation intensity  $f$  is expressed per unit volume per seconds in terms of lifetime

$$\Delta n = f \tau n \quad (2.9.)$$

This relationship is in the form of a general logical statement: the steady state quantity is equal to the generation rate times the average lifetime. The actual magnitude and variation of the lifetime can be calculated on the basis of models of photoconductivity in specific cases.

If we substitute Eq(2.9) into Eq(2.8) we obtain the following expression for the photoconductivity:-

$$\Delta \sigma = fe \tau n \mu_0 + ne \Delta \mu \quad (2.10.)$$

Since in real materials the term  $fe \tau n \mu_0$  nearly always dominates, it is evident that the magnitude of the photoconductivity for a given excitation intensity is proportional to  $\tau n \mu_0$ .

### 2.3.3. Photoexcitation Dependence of Mobility

There are three simple processes by which the mobility can be a function of photoexcitation. The first of these is for photoexcitation to remove the charge on charged impurity centres dominating the scattering of free carriers. Mobility changes of a factor of 2 or less are common under photoexcitation intensities which change the free carrier density by many orders of magnitude in high resistivity semiconductors or insulators.

A second process might involve the excitation of carriers from a low-mobility band to a high-mobility band, thus producing photoconductivity though  $\Delta n = 0$ .

Finally a change in  $\mu$  may be considered to result from a photoexcitation reduction of barrier heights to free-carrier flow in an inhomogenous material.

### 2.3.4. Photosensitivity

Three different ways of describing photosensitivity are commonly used. The first, of these, describes the photosensitivity as a materials property in terms of the  $\tau\mu$  product. It is comparable to considering the photosensitivity to be related to the change in conductivity per photon absorbed.

The second way of describing photosensitivity has been given the technical name "detectivity". Detectors designed

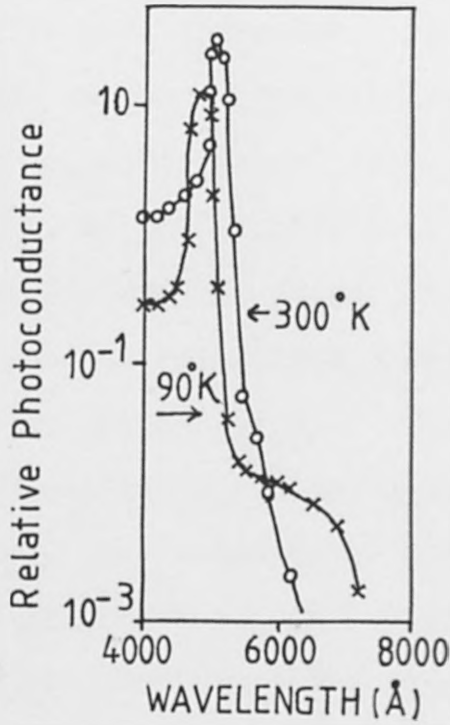


to measure small signals in the infrared are small-band gap semiconductors with high dark conductivity. Their utility as photodetectors depends ultimately on how small a signal they can detect, and this depends in turn on the signal to noise ratio. The detectivity is a measure of the radiation power needed to give a signal equal to the noise. It is comparable to considering the photosensitivity to be related to the ratio of the photoconductivity to the dark conductivity.

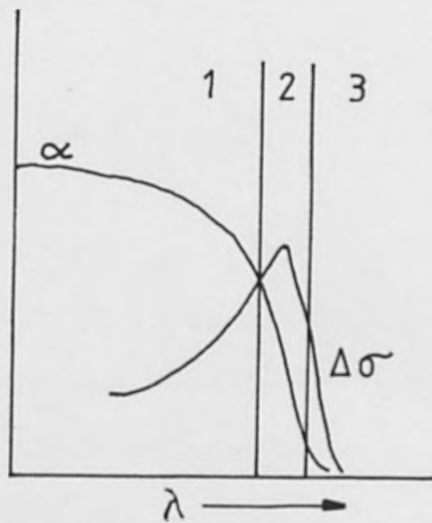
A third way of describing photosensitivity is that of gain. The gain of a photoconductor is defined as the number of charge carriers passing between the electrodes per photon absorbed. It depends on the applied voltage and on the electrode spacing, as well as on the  $\tau\mu$  product, and is thus a combination of materials and device properties.

#### 2.3.5. Spectral Response

Spectral response curves for photoconductivity in a "pure" CdS crystal are shown in Fig 2.7, together with an interpretive diagram. The spectral response curve consists of three parts. For wavelengths much less than the absorption edge of the material, absorption is very strong and occurs near the surface of the crystal. In this range the photosensitivity is limited by the lifetime for recombination at the surface, which may be appreciably



(a)



(b)

Fig. 2.7. (a) Photoconductivity excitation spectra of "pure" CdS crystal at 90 and 300°K (after R. H. Bube, L. A. Barton, *P. C. A. Rev.*, 20 564, (1959)) (b) Illustrative comparison of the shape of the photoconductivity excitation spectrum and the absorption edge of the material, defining three characteristic regions.

smaller than in the volume due to the greater imperfection density at the surface. For wavelengths near the absorption edge, appreciable penetration of photoexcitation into the volume of the crystal occurs. The maximum photoconductivity usually occurs for that wavelength corresponding to an absorption coefficient approximately equal to the reciprocal of the thickness of the crystal, i.e., when  $(|\tau - a|/e)$  of the incident radiation is absorbed in the crystal. For wavelengths much longer than the absorption edge, the incident radiation is only weakly absorbed and the resulting photoconductivity decreases rapidly. The shape of the spectral response curve in the neighbourhood of the absorption edge depends critically on the relative magnitudes of the surface and volume recombination lifetime.

#### 2.3.6. Recombination Mechanisms

It is the energy-transfer process by which an excited carrier gives up its energy in order to recombine with a carrier of opposite type that determines the capture coefficients. There are essentially three processes for energy dissipation:-

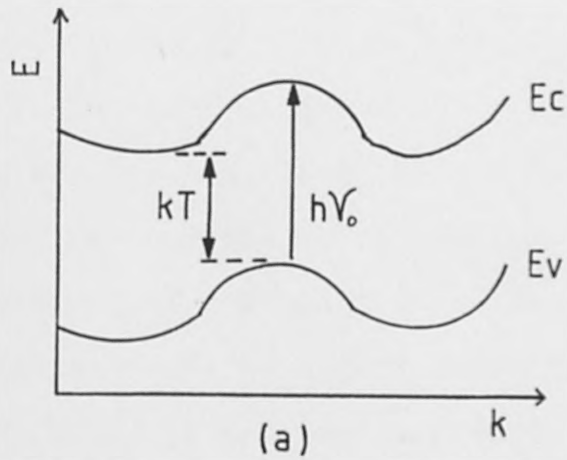
- a) emission of photons (radiative recombination), where free electrons in the conduction band are recombining with free holes in the valence band with the emission of photons.

- b) emission of phonons (non-radiative recombination)
- c) increase energy of another free carrier (Auger recombination)

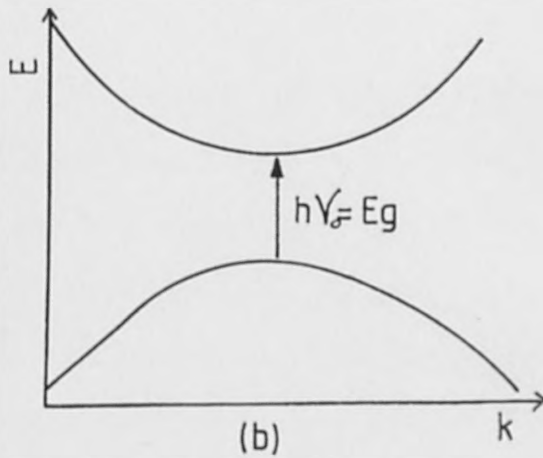
Since Auger recombination is a three-body process, its occurrence requires high densities of free carriers, and is likely to be of importance only in small-bandgap or highly imperfect semiconductors. Radiative recombination is less probable, and occurs mainly when a mechanism for dissipating the energy by phonon emission is absent; the probability of radiative recombination increases in general as the energy to be dissipated increases.

Photoconductivity measurements used together with absorption spectroscopy gives more information for interpretation of the nature of transitions resulting in the absorption spectrum. When  $E_g = kT \neq h\nu_0$  the transition is indirect (Fig (a)) and no photoconductivity will be observed. If, however,  $E_g = h\nu_0 = kT$ , the transition is direct to the conduction band or from the valence band (Fig (b)) and a photoconductive response is obtained. When  $h\nu_0 < E_g$  the current measurement observed is due to thermal electrons only, but when  $h\nu_0 \geq E_g$  the electrons are promoted to the conduction band by photons and the current rises with the onset of photoconductivity.

Photoconductivity can therefore be used to supplement absorption spectra to determine the exact values of the width of the forbidden gap and of the energy separations of impurity or imperfection levels from the valence and/or



$$E_g = kT + h\nu_0$$



$$E_g = h\nu_0 = kT$$

Diagrams to illustrate an indirect transition (a) when no photoconductive response is observed and a direct transition (b) when a photoconductive response is obtained.

conduction band edges.

## 2.4.

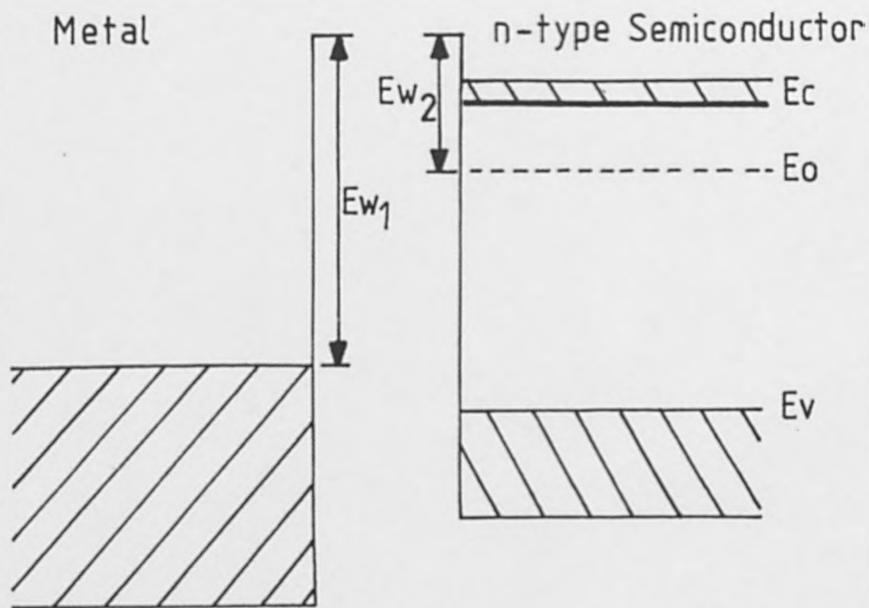
### Contacts

It is necessary to make electrical contact to semiconductor crystals or pellets by means of metallic conductors in order to carry out electrical measurements. The junction between the metal and the semiconductor determines the current which can flow into the semiconductor. The properties of the junction can be understood in terms of energy level diagrams similar to those discussed in the previous section, 2.2.

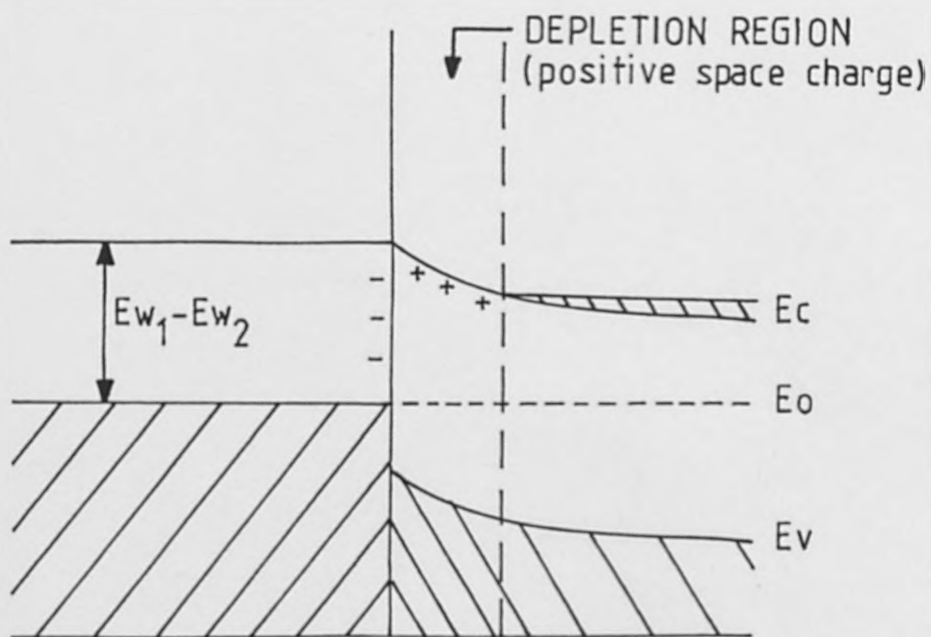
#### 2.4.1.

##### Rectifying Contacts

The energy-band models of a metal and an n-type semiconductor are shown in Fig 2.8a. The quantities  $E_{w_1}$  and  $E_{w_2}$  are the work functions of the solids and are the difference between the critical positions of the Fermi level and the height of the surface potential barrier. In Fig 2.8a the work function of the metal  $E_{w_1}$  is greater than that of the semiconductor  $E_{w_2}$ , so that, upon contact, electrons flow from the semiconductor to the metal until the negative charge on the metal builds up sufficiently to reduce the flow and make the Fermi level continuous. This is illustrated in Fig 2.8b and results in a space-charge layer in the semiconductor. An analogous situation occurs

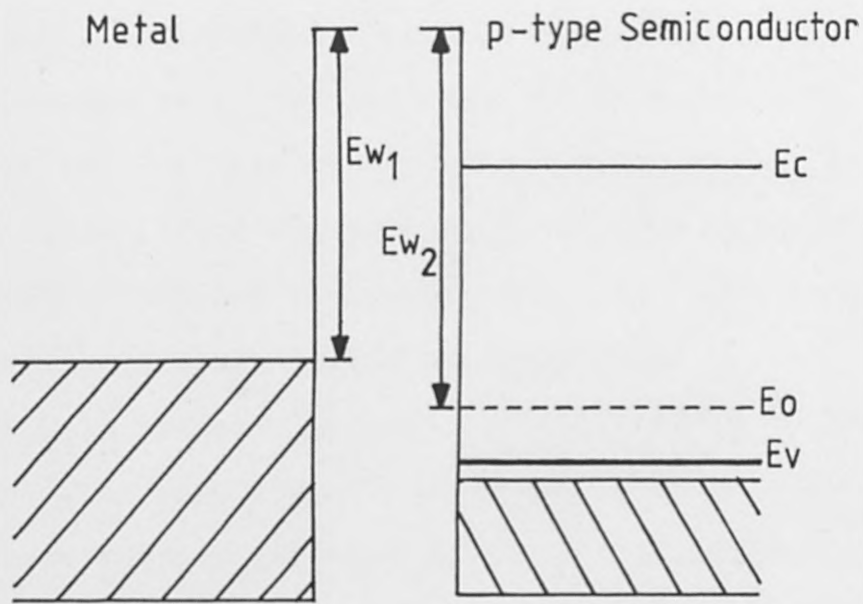


(a)

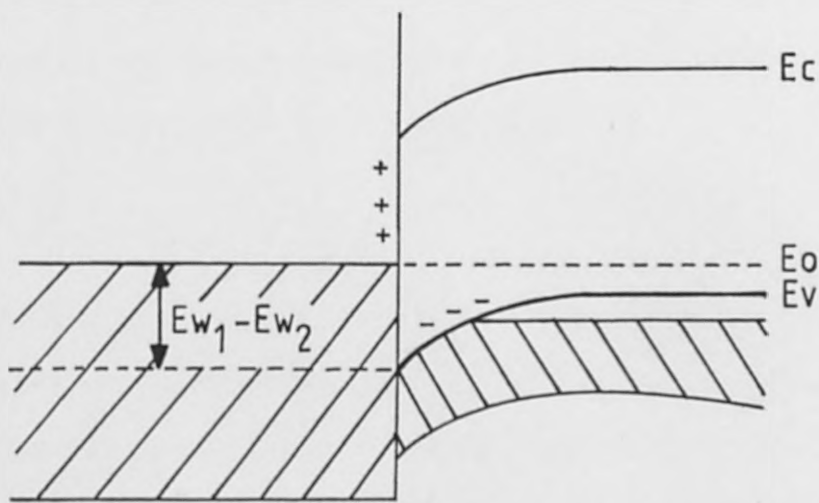


(b)

Fig. 2.8. Energy level diagram of the junction between metal and an n-type semiconductor when  $E_{w1} > E_{w2}$  (a) before contact (b) after contact



(a)



(b)

Fig. 2.9. Energy level diagram showing the space - charge layer that forms at a metal - semiconductor junction for p- type semiconductor when  $E_{w1} < E_{w2}$  (a) before contact (b) after contact



for a metal-semiconductor contact when the semiconductor is p-type and when the work function of the metal is smaller than that of the semiconductor, as shown in Fig 2.9a. Since  $E_{w_1} < E_{w_2}$  electron flow takes place from the metal to the semiconductor, and this again results in a space-charge layer in the semiconductor.

In both cases, a potential barrier forms at the metal-semiconductor junction, whose height is determined by the difference between the work functions. The potential barrier impedes the flow of charge across the junction more in one direction, than in the other, and such contacts are said to be rectifying. Although rectifying contacts are used in semiconductor devices, it is necessary to avoid them when the electrical properties of the semiconductor are being measured, lest the current flow be more a property of the junction than of the bulk crystal.

#### 2.4.2.

#### Ohmic Contacts

If the work function of an n-type semiconductor is greater than that of the metal, electron flow from the metal to the semiconductor makes the surface of the latter more n-type, as indicated in Fig 2.10a. The reverse is true for a p-type semiconductor when its work function is smaller than that of the metal (Fig 2.10b). These cases are examples of ohmic contacts since no barrier exists for the flow of electrons in either direction for n-type

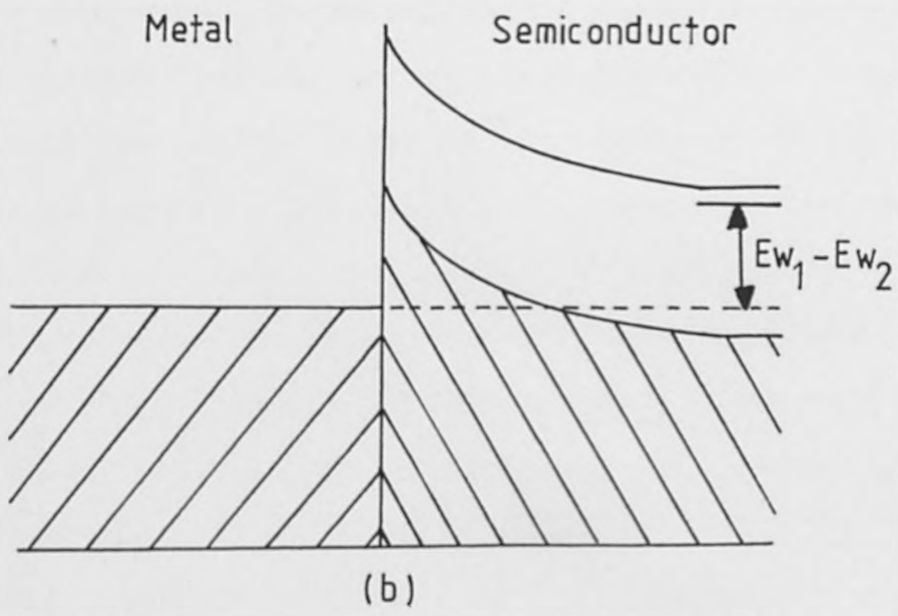
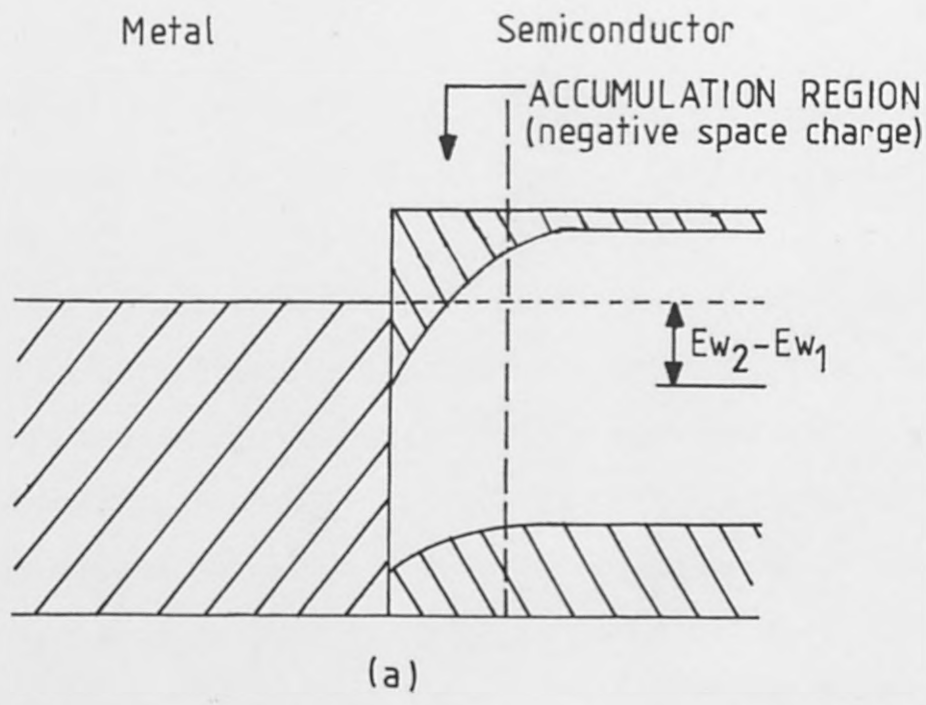


Fig. 2.10. Energy level diagrams of ohmic contacts to  
 (a) n-type and (b) p-type semiconductors.

material or for holes in either direction for p-type specimens, as can be seen in the energy level diagrams of Fig 2.10.

These considerations imply that the height of the barrier is determined by the relative work functions of the metal and semiconductor. It is often observed experimentally, however, that the height of the barrier does not depend on the work function of the metal. The reason for this is that the properties of contacts are governed mainly by surface states,<sup>(12)</sup> which determine the difference in the work functions between the contact and the substance, and therefore the energy required to pass a carrier from the contact into the substance and visa versa. If the surface state density is large enough, the barrier is regulated primarily by occupancy of the surface states. In this case, contact with a metal causes electron exchange between the metal and the surface states rather than the bulk semiconductor, so that the surface space-charge layer is not greatly altered. Specifically, this means that, in order to obtain ohmic contacts, it is necessary to remove as many of the surface states as possible before applying the metal contact.

## 2.5. Theory of Crystal Structure Determination

All crystalline materials diffract x-rays in discrete directions in accordance with Bragg's Law. The positions and absences of reflections give information on the space group and by measuring the intensities of the reflections it is possible to obtain the electron density distribution in the crystal unit cell.

The most important quantity derived from the intensities is the structure factor,  $F(hkl)$ . The relationship between the structure factor and the intensity is:-

$$I_{hkl} \propto F^2(hkl) \quad (2.11.)$$

The structure factor is the resultant of  $j$  waves scattered in the direction of the reflection  $hkl$  by  $j$  atoms in the unit cell. For the  $j^{\text{th}}$  atom at coordinates  $x_j, y_j, z_j$  with atomic scattering factor  $f_j$ , the structure factor may be related to the atomic positions by the equation:-

$$F(hkl) = \sum_j f_j(hkl) \exp 2\pi i (hx_j + ky_j + lz_j) \quad (2.12.)$$

the summation being carried out over all atoms.

This normal scattering factor equation is derived on the basis of the electron distribution about a stationary atom, however, the atoms in a crystal are always vibrating

about their rest positions. The magnitude of the vibration depends on temperature, the mass of the atoms and the firmness with which the atom is held in the lattice. The effect of such thermal motion<sup>(13)</sup> is to spread the electron cloud over a larger volume than assumed in the ideal stationary case and the scattering power of the atom is reduced. To account for the effect of temperature the atomic scattering factor  $f_j$  is multiplied by:  
 $\exp(-B \sin^2 \theta / \lambda^2)$  if the vibrations are isotropic, where  $B = 8\pi^2 u$ , and is known as the isotropic temperature factor and  $u$  is  $\bar{u}$  the mean square amplitude of vibration in any direction. However, in practice the vibrations are anisotropic and  $T$  is given by:-

$$T = \exp - (b_{11}h^2 + b_{22}k^2 + b_{33}l^2 + 2b_{12}hk + 2b_{13}hl + 2b_{23}kl)$$

where  $b_{11} = 2\pi^2 a^{*2}U_{11}$ ,  $b_{12} = 2\pi^2 a^* b^* U_{12}$  etc. (2.13)

$U_{11}$  is the vibration component in the (100) direction parallel to  $a^*$  with units of  $\text{\AA}^2$ ,  $b_{ij}$  are the anisotropic temperature factors. Thus equation(2.12) becomes:-

$$F_T(hkl) = \sum_j f_j(hkl) T_j(hkl) \exp 2\pi i (hx_j + ky_j + lz_j) \quad (2.14)$$

### 2.5.1.

### Data Reduction

The observed reflection intensities are influenced by the time over which the crystal plane will give diffraction (Lorentz factor), polarisation of the x-ray beam and the absorption of x-radiation by the crystal. The measured intensities can therefore be corrected by data reduction to give the modulus of the structure factor.

The Lorentz factor is a correction made to allow for the time spent by each plane in passing through the Bragg condition, and depends on the method of recording the reflections. For data collected on a diffractometer the Lorentz correction (L) is  $(\sin 2\theta)^{-1}$ . The polarisation factor (p) corrects for the partial plane polarisation of the x-ray beam on reflection off the lattice planes and is given by:-

$$p = \frac{1}{2} (1 + \cos^2 2\theta) \quad (2.15.)$$

When a beam of monochromatic x-radiation passes through a crystal of thickness  $t$ , it is found that the intensity,  $I$ , of the transmitted radiation is related to the intensity,  $I_0$ , of the incident radiation by  $I = I_0 \exp(-\mu t)$  where  $\mu$ , the linear absorption coefficient, is a constant for the crystalline material and may be calculated <sup>(14)</sup>. If the thickness of the crystal is less than the optimum thickness,  $t_{opt} = 2/\mu$ ,

then the absorption correction(A) is not necessary and may be neglected in all but the most precise determinations.

The final intensity equation is therefore:-

$$I_{\text{obs}}(hkl) \propto L_p A(hkl) F_T^2(hkl) \quad (2.16.)$$

and hence,  $|F_T(hkl)|^2_{\text{obs}} \propto I_{\text{obs}}(hkl) (L_p)^{-1} A^*_{hkl}$

where  $A^*(hkl) = 1/A(hkl)$ .

Structure factors are thus obtained experimentally on a relative scale, and their phase and absolute values are usually only obtained from calculated data in the process of crystal structure determination.

## 2.6. Crystal Structure Determination<sup>(15)</sup>

### 2.6.1. Fourier Synthesis

Since a crystal is periodic in three dimensions its electron density ( $\rho$ ) can be represented by a three dimensional Fourier series:-

$$\rho(x, y, z) = \frac{1}{V} \sum_h \sum_k \sum_l [F(hkl)] \exp\{-2\pi i(hx + ky + lz)\} \quad (2.17.)$$

where  $x, y, z$  are the fractional atomic coordinates

within the cell. Also  $f(hkl) = |F(hkl)| \exp \{i \alpha(hkl)\}$ .

As only  $|F(hkl)|$  can be measured experimentally, it is necessary to determine the phase angles,  $\alpha(hkl)$ , before the structure can be determined. To overcome this problem, the general method used in this work was to find the positions of the heavy atoms in the cell by a Patterson synthesis and then to assume the sign of  $F(hkl)_{obs}$  was the same as that of the calculated structure factor,  $F(hkl)$  calculated.

### 2.6.2. Patterson Function and the Heavy Atom Method

To overcome the phase problem, Patterson<sup>(16)</sup> defined a Fourier series using the experimentally obtained  $F^2(hkl)$  values and therefore not involving the phase of the structure factor:-

$$P(U,V,W) = \frac{1}{V} \sum_{h=-\alpha}^{\alpha} \sum_{k=-\alpha}^{\alpha} \sum_{l=-\alpha}^{\alpha} |F(hkl)|^2 \cos 2\pi(hU + kV + lW) \quad (2.18.)$$

This function represents the electron densities separated by U, V, W, and therefore has significant value at (U, V, W) when atoms are separated by U, V and W in the unit cell. The Patterson function represents all interatomic vectors reduced to a common origin. The magnitude of the Patterson peak is proportional to the product of the atomic numbers of the two atoms giving rise



to the peak, so that the vectors between the heaviest atoms produce the most intense peaks<sup>(17)</sup>. Thus if one atom has many more electrons than the others contained in the asymmetric unit of the crystal the "Heavy Atom" dominates the magnitude and phases of the structure factor.

If the space group is known, the general positions of the group allow the vectors to be calculated by vector subtraction and correlation with the peaks in the Patterson map. With the heavy atom positions known, the phase of each reflection can be approximated to that due to the heavy atoms alone, so that an electron density map is obtained from which more accurate heavy atom positions and the approximate positions of the lighter atoms can be found.

### 2.6.3. The Difference Fourier<sup>(18)</sup>

Calculations based on electron densities are subject to errors due to Fourier series termination errors. It is possible to eliminate these errors by subtracting the calculated electron densities from the observed, since only the observed reflections are usually included in the summations.

The difference function is given by:-

$$\Delta\rho(x, y, z) = \frac{1}{V} \sum_{h}^{\alpha} \sum_{k}^{\alpha} \sum_{l}^{\alpha} |F(hkl)_o - F(hkl)_c| \exp -2\pi i(hx + ky + lz)$$

(2.19.)

Hence in practice when the heavy atom positions are known a difference Fourier is used to locate the light atom positions. The final difference Fourier map is also used to confirm that there is no electron density in the cell which may be attributable to an atom.

#### 2.6.4. Least Square Refinement

The atomic positions  $x, y, z$  and the temperature factors  $B_j$  (or  $B_{ij}$  for anisotropic factors) are refined by a method of least squares<sup>(19)</sup> to obtain the best fit between  $F(hkl)_{obs}$  and  $F(hkl)_{calc}$ . The correctness of the structure is measured in terms of a residual,  $R$ , where

$$R = \sum_i \left( \frac{|F|_o - |F|_c}{|F|_o} \right)_i \quad (2.20.)$$

which tends to a minimum as a better fit between observed and calculated structure factors is achieved.

To carry out a least squares refinement it is necessary to weight the input data, to allow for variations in the observed data using a factor  $w_i$  such that:-

$$Rw = \left\{ \sum_i w_i \left( \frac{|F|_o - |F|_c}{|F|_o} \right)_i^2 \right\}^{\frac{1}{2}} \quad (2.21.)$$

For  $w_i = 1$  this reduces to  $Rw = R$ , other applied

weighting schemes are proportional to the inverse variance of the observations e.g.

$$w_i = (\sigma^2\{|F|_o\}_i + g\{|F|_o\}_i^2)^{-1} \quad (2.22.)$$

## 2.7. Computer Programs used in X-Ray Crystallography

### 2.7.1. SHELX - 76 (20)

SHELX - 76 is an integrated program for performing crystallographic calculations simply and efficiently. There is no limit to the number of reflections, and the calculations are valid for all space groups. Its facilities include (i) data reduction, including numerical absorption correction with crystal plots; (ii) rejection of systematic absences, least-squares determination of inter-batch scale factors, averaging equivalent reflection; (iii) full matrix, least-squares refinements; (iv) rigid group location on refinement; (v) various Fourier syntheses with peak search; (vi) structure factor lists.

### 2.7.2. POWDER AND POWREF (21)

These programs fit and refine respectively, data from powder camera diffractograms. They may be used separately or as a combined POWREF-POWDER run.

### 2.7.3.

### XRAY - 72<sup>(22)</sup>

XRAY - 72 is a manual report for the use of a library of crystallographic programs designed to perform the calculations needed to solve the structure of crystals by diffraction techniques.

### 2.7.4.

### CELLPLOT<sup>(23)</sup>

The program CELLPLOT produces, on a digital plotter, a normal or stereoscopic pair view of a cell of a crystal from any angle. Overlap of atoms across bands and across other atoms. Whether partially or completely, is considered, but no allowance is made for perspective. Ball-and-stick or space filling type models may be shown and any number and combination of views is possible for each structure. Usually atoms are shown by circles and bonds by straight lines.

## 2.8.

## Mössbauer Spectroscopy

### 2.8.1.

### General

Mössbauer spectroscopy is the study of resonant emission and reabsorption of nuclear  $\gamma$ -radiation between the ground state and, usually the first excited spin state of the nucleus. The transitions involved are of the order 5 -

150 KeV.

Since its discovery in 1958<sup>(24, 25)</sup> by MØssbauer, the effect has proved a valuable tool in physics. The first report of chemical applications of the effect came in 1960 when Kistner and Synyar<sup>(26)</sup> recognised the influence of varying electronic environments of a MØssbauer nucleus in different chemical compounds.

### 2.8.2.

### Fundamental Features

The population of an excited spin state of a nucleus and its decay to the ground state results in the emission of  $\gamma$ -radiation. Classically, the energy of the  $\gamma$ -ray would be degraded by recoil of the nucleus and could not then be resonantly reabsorbed by another identical nucleus. The MØssbauer effect is, however, a solid state effect and, since the lattice is quantised and can only take up recoil energy in discrete quanta, a significant proportion of the emission events must occur recoil free. A monochromatic  $\gamma$ -ray is then emitted which can be resonantly reabsorbed.

The fraction of emission events resulting in no transfer of energy to the lattice is known as the recoil-free fraction,  $f$ . It is possible to relate  $f$  to the vibrational properties of the crystal lattice by the equation:

$$f = \exp - (Ej^2 \langle x^2 \rangle / (\hbar c)^2) \quad (2.23.)$$

where  $\langle x^2 \rangle$  is the mean-square vibrational amplitude of the nucleus in the direction of the  $\gamma$ -ray and  $E_\gamma$  is the energy of the  $\gamma$ -ray.

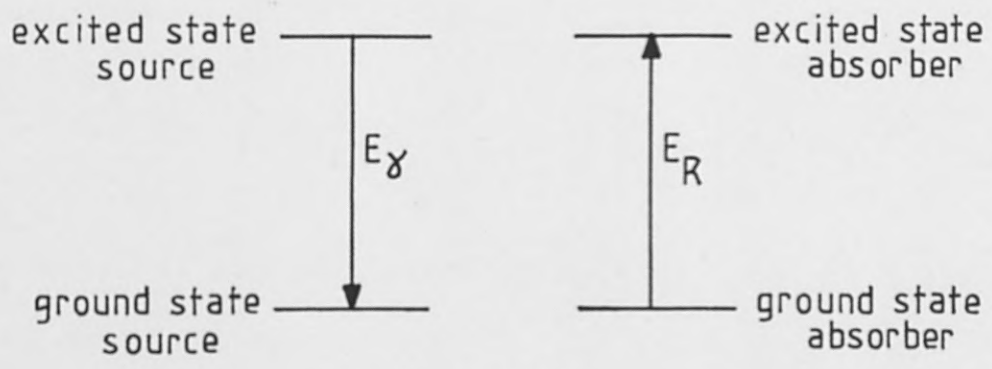
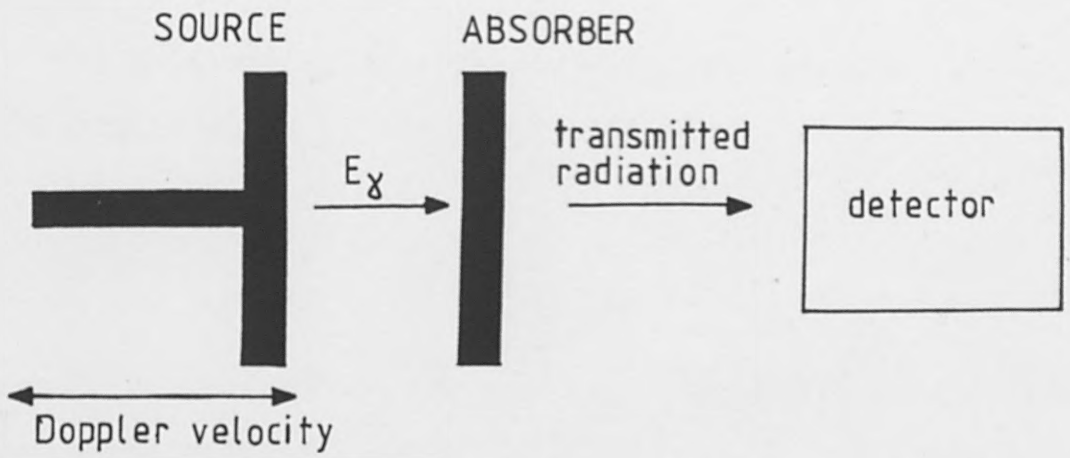
From the form of the exponent,  $f$  will only be large for a tightly bound atom with a small mean-square displacement, and for a small value of the  $\gamma$ -ray, energy.

The method of obtaining the Mössbauer absorption spectra is described with reference to Fig 2.11 which illustrates the energy levels involved and shows the type of spectrum obtained when both nuclei are in the same chemical environment. The spectrum is plotted by modulating the  $\gamma$ -energy ( $E_\gamma$ ) incident on the absorber, and recording the intensity of the transmitted radiation as a function of the incident energy. Maximum resonance will occur when  $E_\gamma = E_R$ , where  $E_R$  is the separation of the ground and excited states of the nucleus in the absorber. The energy modulation is achieved by introducing a Doppler motion (velocity  $V$ ) to the same relative absorber. The Doppler velocity ( $V$ ) produces an energy shift  $\Delta E$ , given by:-

$$-\Delta E = \frac{v}{c} E_\gamma \quad (c = \text{velocity of light})$$

(2.24.)

If the source and absorber are identical maximum resonance will occur at zero modulation of  $E_\gamma$ . The Mössbauer spectrum is usually plotted as the number of counts registered by the counter against the Doppler



Below: The spectrum obtained when source and absorber are in identical environments.

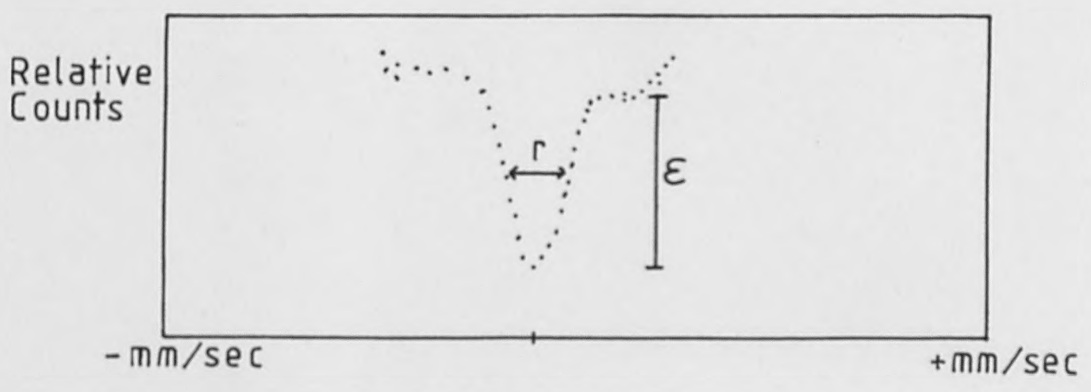


Fig. 2.11. Fundamental features of Mössbauer Spectroscopy.

velocity.

The Heisenberg Uncertainty Principle results in the small finite width of the spectral lines.

$$\Gamma \tau = 2h\pi \quad (2.25.)$$

where  $\Gamma$  is the width of the spectral line and  $\tau$  the mean life time of the excited states.

The observed spectral line approximates to a Lorentzian distribution, with the intensity,  $I(E)$ , at energy given by:-

$$I(E) = E_R / (1 + |2(E - E_R) / \Gamma_1|^2) \quad (2.26.)$$

where  $\Gamma_1$  is the line width at half maximum and  $E_R$  is the resonance energy.

The magnitude of the resonance effect is the difference in transmission at resonance maximum,  $I_0$ , and off resonance  $I_\infty$ . It is expressed as a percentage; the percentage resonance dip.

$$\epsilon_0 = \frac{100 (I_0 - I_\infty)}{I_\infty} \quad (2.27.)$$



### 2.8.3.

### Hyperfine Interactions

The main use of the Mössbauer effect in studies of chemical problems lies in the shifts and hyperfine splittings of the resonance line which occur as a result of interactions between the nucleus and its environment.

There are three interactions to be considered. These are:-

- 1) The changes in the electric monopole or Coulombic interaction between the electronic and nuclear charges, which is caused by a difference in the size of the nucleus in its ground and excited states. This is seen as a shift of the resonance line away from zero velocity and is known as the chemical shift.
- 2) The interaction of the charged, spinning and non-spherical nucleus with,
  - a) magnetic fields, or
  - b) electric field gradients

Both effects lead to a splitting of the resonance line of the spectrum. The centroid of the multiplet is, however, unshifted.

All three effects may occur together, but the magnetic and quadrupole interactions are directional and so have a complicated inter-relationship. These effects are now considered in more details.

2.8.4.

The Chemical Shift

When the source and absorber are in different environments a shift of the centre of the resonance line occurs. The chemical shift arises because of differing Fermi contacts of electrons with finite densities (e.g.  $|\psi_s(0)|^2$  for s electrons) at the nuclei of atoms in different chemical environments.

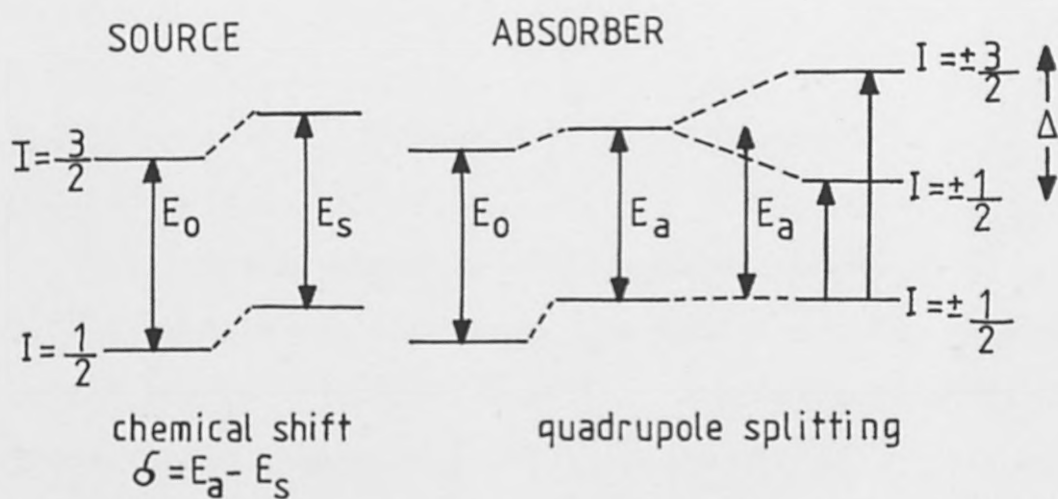
For a spherical nucleus with a uniform charge distribution, the change in energy separation of the ground and excited states due to electrostatic interaction is:-

$$\Delta E = \frac{1}{5\epsilon_0} Ze^2 R^2 |\psi_s(0)|^2 \Delta R/R \quad (2.28)$$

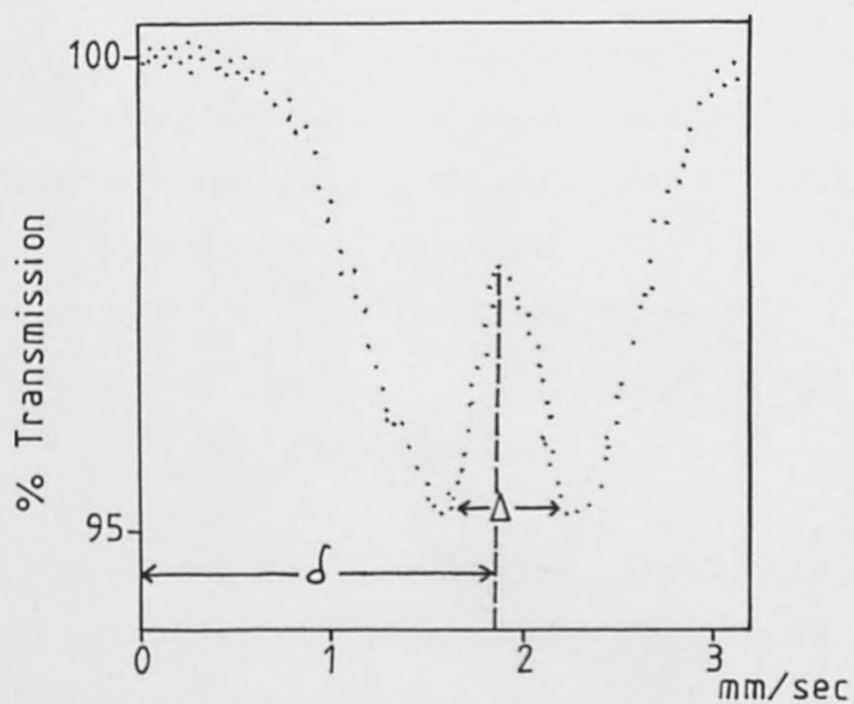
where R is the nuclear radius assuming that the nucleus is spherical and Ze is the nuclear charge.  $\Delta R$  is the difference between the nuclear radii in the ground state and  $|\psi_s(0)|^2$  is the total s-electron density at the nucleus. The value of  $\frac{\Delta R}{R}$  is characteristic of each transition, but is of the order of  $10^{-4}$  and can be of either sign. A positive sign means that the nucleus shrinks on de-excitation.

$\Delta E$  cannot be measured directly but only with respect to a reference material.

$$\sigma = E(\text{absorber}) - E(\text{source}) \quad (2.29.)$$



(a)



(b)

Fig. 2.12. (a) Origin of the chemical shift and quadrupole splitting: (b) Mössbauer spectrum of  $\alpha\text{-SnF}_2$  using a  $\text{BaSnO}_3$  source showing chemical shift and quadrupole splitting.

and

$$\delta = F(Z) \frac{\Delta R}{R} (|\psi_s(0)|^2 \text{ absorber} - |\psi_s(0)|^2 \text{ source}) \quad (2.30.)$$

This equation consists of two parts; the first  $F(Z) \frac{\Delta R}{R}$  contains only nuclear parameters, and the second  $|\psi_s(0)|^2 \text{ source} - |\psi_s(0)|^2 \text{ absorber}$ , an atomic parameter, represents the change in the electronic charge density at the nucleus.

Before information about changes in electron density can be gained the sign and magnitude of  $\Delta R/R$  must be known. Since the nuclear term,  $F(Z) \frac{\Delta R}{R}$ , is constant for a given transition, the chemical shift gives a measure of the change in s-electron density of the nucleus. For  $^{119}\text{Sn}/\Delta R/R$  is positive<sup>(27)</sup>, thus a positive chemical shift corresponds to an increase in s-electron density at the nucleus.

#### 2.8.5.

#### Quadrupole Splitting

The expression for the chemical shift assumes a spherical nucleus with a uniform charge distribution. However, in practice any nucleus with a spin quantum number not equal to  $I = 0$  or  $I = \frac{1}{2}$  has a non-spherical charge distribution and hence a nuclear quadrupole moment,  $eQ$ , which reflects the deviation from spherical symmetry. An oblate (flattened) nucleus has a negative moment and a

prolate (elongated) nucleus a positive moment. The quadrupole splitting arises from the interaction between possible orientations of the nuclear quadrupole moment with the electric field gradient, e. g. at the Mössbauer nucleus.  $^{119}\text{Sn}$  has transitions between the nuclear spin states  $I = \frac{1}{2}$  and  $I = \frac{3}{2}$ , therefore the spectral line is split into two (Fig 2.12(a)) with an energy difference of:-

$$\Delta = \frac{|e^2qQ|}{2} (1 - \eta^2/3)^{\frac{1}{2}} \quad (2.31.)$$

where  $\eta$  is an asymmetry parameter related to the electric field gradient. The centroid of the double corresponds to the chemical shift without a quadrupole interaction.

Mössbauer transitions in  $^{121}\text{Sb}$  are between nuclear spin states  $I = \pm \frac{5}{2}$  and  $I = \pm \frac{7}{2}$ , the  $I = \pm \frac{5}{2}$  being the ground state. The selection rules restrict the number of possible transitions to eight for  $\eta = 0$ . This situation is depicted in Fig 2.13 which shows the allowed transitions.

The extent of the quadrupole splitting is therefore a measure of the asymmetry of the s-electron density at the nucleus due to a non uniform electrical field gradient.

#### 2.8.6. Magnetic Hyperfine Splitting

In the presence of a magnetic field at the Mössbauer nucleus degeneracy of each nuclear spin state is lifted

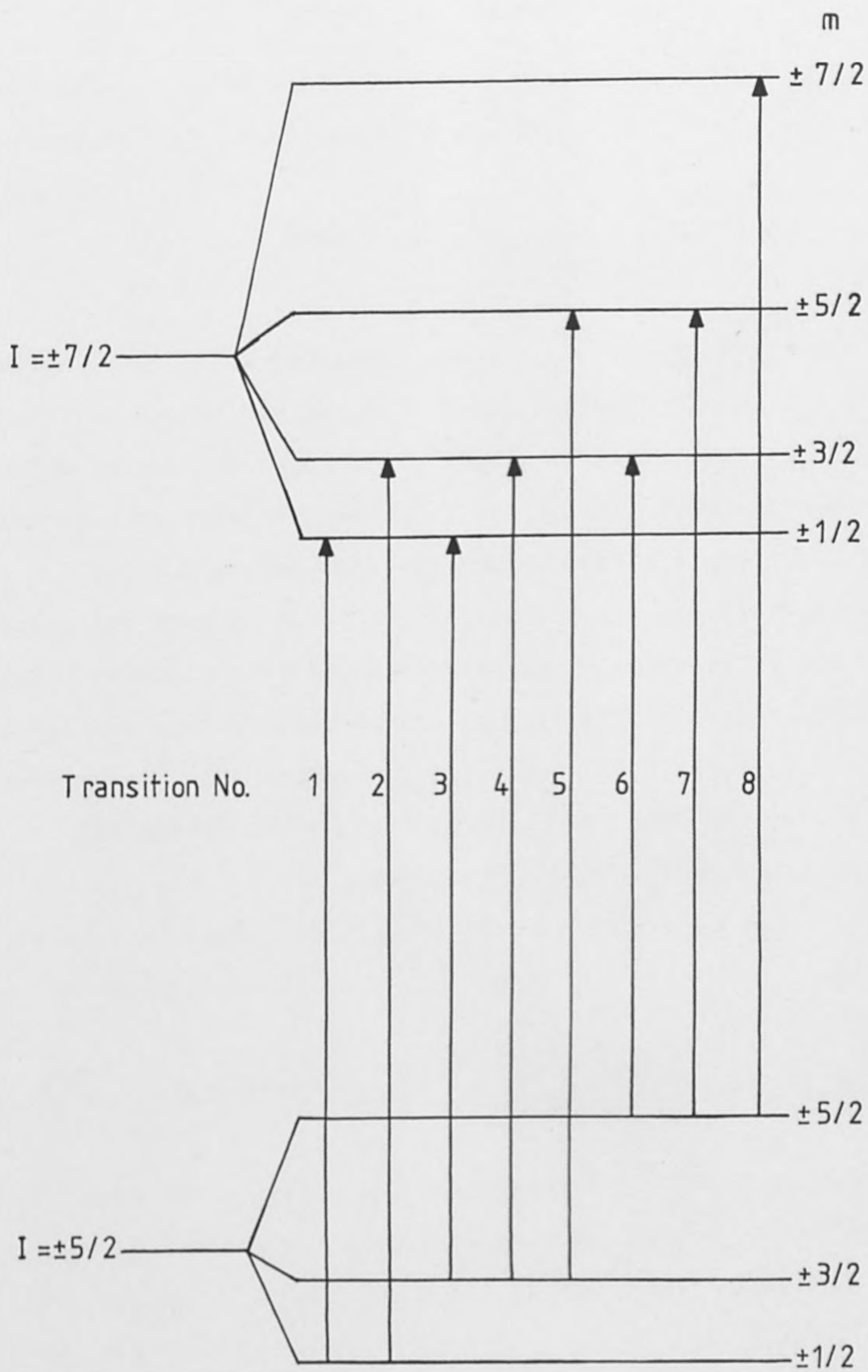


Fig. 2.13. Axial Symmetric Quadrupole Interaction in  $^{121}\text{Sb}$ .

and each is split into  $(2I + 1)$  sublevels such that the energy of each level,  $E_m$  is given by:-

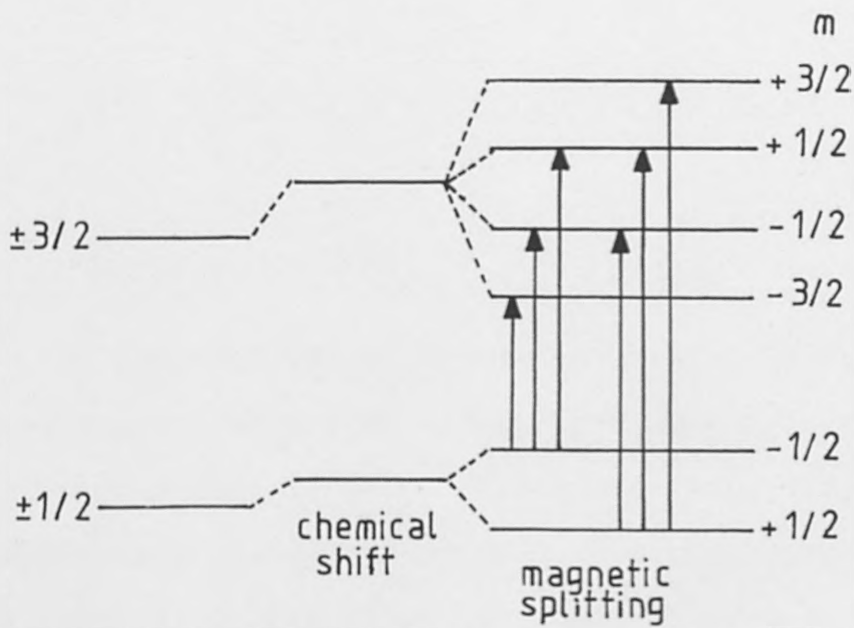
$$E_m = -g \mu_n H_{mI} \quad (2.32.)$$

where  $g$  is the magnetogyric ratio,  $\mu$  is the nuclear Bohr magnetron,  $H$  is the magnetic field strength, and  $M_I$  is the magnetic quantum number. In  $^{57}\text{Fe}$  an internal magnetic field causes a magnetic or Zeeman splitting (Fig 2.14) of the  $\pm 3/2$  and  $\pm 1/2$  states into six nuclear levels, and since the selection rule is  $M_I = 0 \pm 1$  there are six spectral lines. For a randomly orientated powder the intensities of the lines are proportional to the squares of the Clebsh-Gordon coefficients<sup>(28)</sup> and are in the ratio 3:2:1:1:2:3.

For Mössbauer transitions involving spin states  $I = \pm 5/2$  and  $I = \pm 7/2$  the ground state splits into six levels and the excited state into eight levels giving rise to eighteen possible transitions.

#### 2.8.7. Combined Magnetic and Quadrupole Interactions

Both the magnetic and quadrupole hyperfine interactions express a directional interaction of the nucleus with its environment. When the two are together their respective principle axis are not necessarily colinear and so the resultant behaviour can be much more complex.



(a)

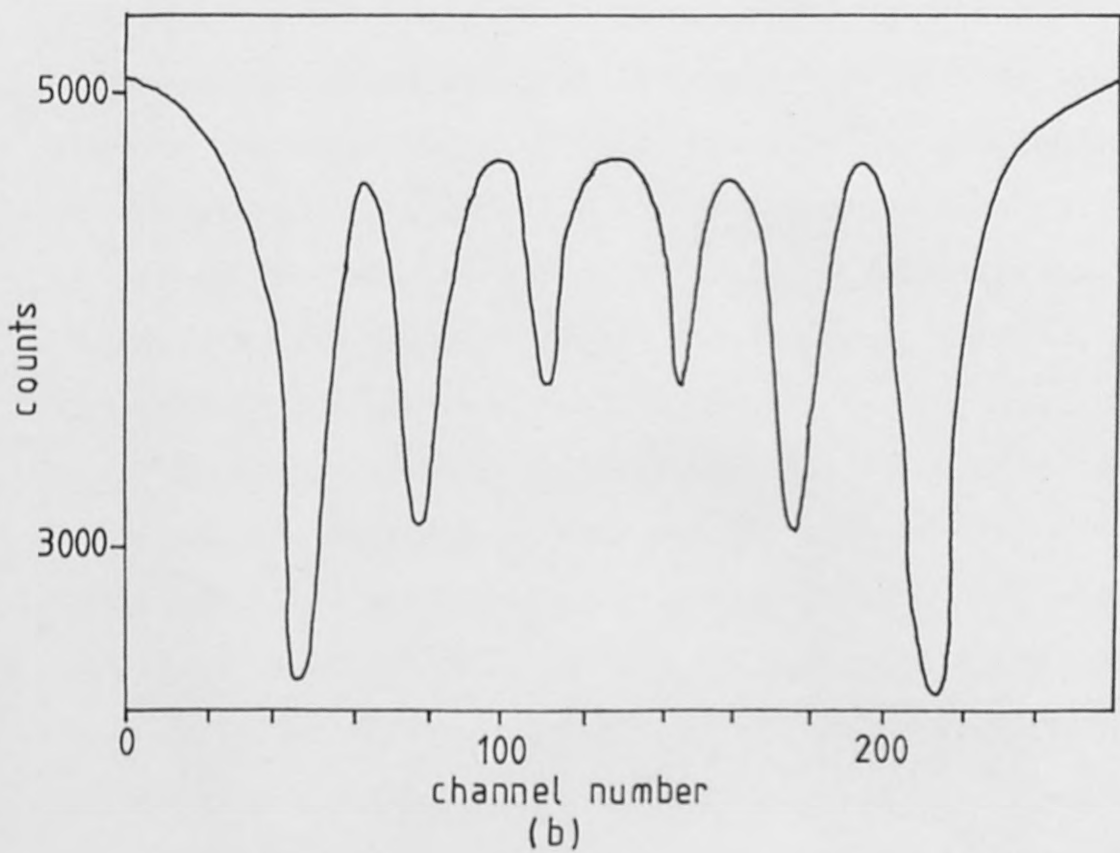


Fig. 2.14. (a) Origin of Mössbauer hyperfine splitting  
 (b) Mössbauer spectrum of natural iron



## The Mössbauer Spectra of Tin and Antimony

### 2.8.8.

### Tin

In terms of the number and diversity of investigation involving the Mössbauer effects, studies involving  $^{119}\text{Sn}$  come second only to  $^{57}\text{Fe}$ . Table 2.1 lists the Mössbauer parameters of a wide range of tin-containing materials. The chemical isomer shift is given relative to  $\alpha\text{-Sn}$ , a shift to higher energy being indicated by a positive sign. The chemical shifts fall into three distinct categories: the compounds with a positive shift being tin (II), those with a negative shift being Sn (IV), and alloys have shifts around zero. These observations imply that  $\Delta R/R$  is positive for tin compounds since tin (IV) has a  $4d^{10}s^0$  electronic configuration and tin (II) a  $4d^{10}5s^2$  configuration.

From the data in Table 2.1 it can be seen that an increase in the negative shifts for tin (IV) compounds is paralleled by the increase in the ionicity of the tin-ligand bond, a similar trend with increasing positive shift related to increasing ionicity is observed for most Sn (II) materials. The anomalous shift values for tin (II) fluoride and tin (II) oxide, which do not fit into this trend, have been explained<sup>(29)</sup> in terms of the loss of s-electron density caused by s-p mixing due to electrostatic crystal effects.

With few exceptions, a pyramidal bonding arrangement of ligands about tin is a recognised feature of compounds

Compound	mmsec <sup>-1</sup>	mmsec <sup>-1</sup>	Ref
SnF <sub>4</sub>	-2.57	1.66	32
SnCl <sub>4</sub>	-1.25	0	33
SnBr <sub>4</sub>	-0.95	0	33
SnI <sub>4</sub>	-0.45	0	34
Na <sub>2</sub> SnF <sub>6</sub>	-2.58	0	35
Rb <sub>2</sub> SnF <sub>6</sub>	-2.55	0	36
Rb <sub>2</sub> SnCl <sub>6</sub>	-1.67	0	35
Cs <sub>2</sub> SnCl <sub>6</sub>	-1.65	0	35
K <sub>2</sub> SnBr <sub>6</sub>	-1.35	0	35
Rb <sub>2</sub> SnI <sub>6</sub>	-0.75	0	35
SnF <sub>2</sub>	1.60	1.80	37
SnCl <sub>2</sub>	2.07	0	38
SnI <sub>2</sub>	1.85	0	38
SnBr <sub>2</sub>	1.93	0	38
NaSnF <sub>3</sub>	1.07	1.84	39
KSnF <sub>3</sub>	1.02	1.92	39
NaSn <sub>2</sub> F <sub>5</sub>	1.27	1.86	39
CsSnBr <sub>3</sub>		0	40
SnO	0.71	1.45	41
SnS	1.16	0.80	42
SnSe	1.30	cs0	43
SnTe	1.21	0	43
SnSO <sub>4</sub>	1.90	1.00	44
FeSn <sub>2</sub>	0.05	ca 0	45
CuSn	0.05		46

\* relative to -Sn

Table 2.1. Mössbauer Parameters of some tin compounds.

containing tin in the  $2^+$  oxidation state. Early theories regarding the origin of the electric field gradient could be either positive or negative. However, measurements on  $\text{SnF}_2$ ,  $\text{SnO}$ ,  $\text{SnS}$ ,  $\text{Sn}_3(\text{PO}_4)_2$ ,  $\text{SnC}_2\text{O}_4$ ,  $\text{NaSnF}_3$ ,  $\text{NaSn}_2\text{F}_5$ ,  $\text{SnSO}_4$ ,  $\text{Sn}(\text{HCO}_2)_2$ ,  $\text{Sn}(\text{CH}_3\text{CO}_2)_2$  and  $\text{K}_2\text{Sn}(\text{C}_2\text{O}_4)_2 \cdot \text{H}_2\text{O}$  applied magnetic fields<sup>(30, 31)</sup> have shown that  $e^2qQ$  is positive in every case. As  $Q$  is known to be negative, the sign of  $e^2qQ$  is consistent with an excess of electrons in the  $P_z$  orbital. Thus for many tin (II) compounds the lone pair has a significant  $P_z$  character which becomes the dominant contribution to the electric field gradient. Many tin (II) compounds, however, have no resolvable quadrupole splittings e. g.  $\text{CsSnBr}_3$  and  $\text{SnCl}_2$ , making it clear that the tin non-bonding lone-pair electrons are not always stereochemically active, nor do they always contain an excess of p-electron density.

#### 2.8.9.

#### Antimony

The parent isotope is  $^{121\text{m}}\text{Sn}$ , which has a half life of 80 years, and decays via the  $I = \pm 7/2$  spin state, to the  $I = \pm 5/2$  ground state of  $^{121}\text{Sb}$  (Fig 2.15). The 37.15 KeV resonance of  $^{121}\text{Sb}$  was first observed in antimony metal by Snyder and Beard<sup>(47)</sup>. This relatively high energy means that both the absorber and source must be maintained at low temperature in order to observe resonant absorption.

The Mössbauer transition is from the  $I = 7/2$  excited

state to the  $I = 5/2$  ground state, and although quadrupole splitting is seen in the  $^{121}\text{Sb}$  resonance in appropriate compounds, the line splitting is less than the experimental line width<sup>(48)</sup>. Large chemical shifts are found for antimony-containing materials with a range of about  $20\text{mm sec}^{-1}$ , and  $\Delta R/R$  is negative<sup>(49)</sup>. The two common oxidation states, Sb(III) and Sb(V), are distinct with Sb(V) absorbing at more positive velocities. A useful reference material is indium antimonide, materials with a chemical shift less than InSb can be considered to be formally Sb(III) materials and those having a larger shift formally Sb(V) materials. Some typical values are given on Table 2.2. The most negative chemical shifts are for the octahedral  $(\text{Sb}^{\text{III}}\text{Cl}_6)^{3-}$  anions. Here the lone-pair is said to have a high 5s character and to be stereochemically non active<sup>(50)</sup>. The Mössbauer parameters are sensitive to the nature of the cation, their being differences between the  $(\text{Rh}(\text{NH}_3)_6)^{3+}$  and  $(\text{Co}(\text{NH}_3)_6)^{3+}$  salts of  $(\text{SbCl}_6)^{3-}$  for example.

In compounds where there is quadrupole splitting, the complex pattern from the  $I_g = 5/2 \rightarrow I = 7/2$  transition allows, in principle, the determination of both  $eQV_{zz}$  and  $\eta$  but in many cases the resolution is such that only a single asymmetric envelope is seen and only an approximate value of the coupling constant can be obtained.

<u>Compound</u>	<u>mm/sec</u>	eQVzz	linewidth	
		<u>mm/sec</u>	<u>mm/sec</u>	
Co(NH <sub>3</sub> ) <sub>6</sub> SbCl <sub>6</sub>	-11.23	+6.80	3.70	
Co(NH <sub>3</sub> ) <sub>6</sub> SbBr <sub>6</sub>	-11.20	+4.45	2.72	
Cs <sub>3</sub> Sb <sub>2</sub> Cl <sub>9</sub>	-10.40	+6.75	3.00	
Cs <sub>3</sub> Sb <sub>2</sub> Br <sub>9</sub>	-9.80	+6.40	2.92	
Cs <sub>3</sub> Sb <sub>2</sub> I <sub>9</sub>	-9.20	+5.00	3.24	
Rb <sub>3</sub> Sb <sub>2</sub> Br <sub>9</sub>	-9.74	+6.00	2.92	
Rb <sub>3</sub> Sb <sub>2</sub> I <sub>9</sub>	-8.80	+8.66	2.40	
Rh(NH <sub>3</sub> ) <sub>6</sub> SbCl <sub>6</sub>	-19.3		2.80	
Co(NH <sub>3</sub> ) <sub>6</sub> SbCl <sub>6</sub>	-11.2		3.1	
K <sub>3</sub> SbCl <sub>6</sub>	-9.7		3.5	
Cs <sub>3</sub> SbCl <sub>6</sub>	-9.6		3.6	
(NH <sub>4</sub> ) <sub>3</sub> SbCl <sub>6</sub>	-8.7		4.3	
(NH <sub>4</sub> ) <sub>2</sub> SbCl <sub>5</sub>	-6.7		4.4	
pySbBr <sub>4</sub>	-7.25	+11.46	3.20	
pySbCl <sub>4</sub>	-7.98	+9.05	2.16	
Bu <sub>4</sub> <sup>n</sup> NSGI <sub>4</sub>	-6.88	-3.33	3.40	
SbF <sub>3</sub>	-6.2	+19.6		
SbCl <sub>3</sub>	-5.4	+12.2		
SbBr <sub>3</sub>	-5.6	+9.4		
SbI <sub>3</sub>	-7.5			
Cs <sub>2</sub> SbF <sub>5</sub>	-4.5	+14.8		
CsSbF <sub>4</sub>	-5.6	+18.6		
CsSb <sub>2</sub> F <sub>7</sub>	-5.9	+18.6		
	Site			
Rb <sub>2</sub> SbBr <sub>6</sub>	III	-10.5	+4.50	3.60

Table 2.2. Mössbauer parameters of some Antimony Compounds.

<u>Compound</u>	<u>Site</u>	<u>mm/sec</u>	<u>eQVzz</u> <u>mm/sec</u>	<u>linewidth</u> <u>mm/sec</u>
	V	+3.31	+2.80	3.40
(NH <sub>4</sub> ) <sub>2</sub> SbBr <sub>6</sub>	III	-10.6	0	2.80
	V	+3.19	3.20	3.00

\* relative to InSb

Table 2.2. (continued).

## References

1. R. J. Elliot, A. F. Gibson "An Introduction to Solid State Physics," MacMillan, London. 1974.
2. F. Seitz, Phys. Rev., 1974, 76, 1376.
3. N. F. Mott, Proc. Roy. Soc. (Lond.), 1939, A171, 27.
4. M. Shön, Ann. Physik., 1948, 3, 333:343.
5. N. Richl and M. Shön, Z. Physik., 1939, 114, 682.
6. R. P. Johnson, J. Opt. Soc. Am., 1939, 29, 283:387.
7. W. Kleinman, J. C. Philips, Phys. Rev. 1960, 118. 1164.
8. C. Kittel, "Introduction to Solid State Physics," 4<sup>th</sup> Ed., John Wiley, London, 1971.
9. E. H. Putley, "The Hall Effect and Related Phenomena," Butterworths, London, 1960.
10. D. Grieg, in "Progress in Solid State Chemistry," (H. Reiss, ed.), Vol. 1, Chap. 4, MacMillan, New York, 1964.
11. R. H. Bube, L. A. Barton, R.C.A. Rev., 1959, 20, 564.
12. L. E. Lyons, J. Chem. Soc., 1975, 5001.
13. M. J. Beurger, "Crystal Structure Analysis" John Wiley, New York, 1969.
14. "International tables for X-Ray Crystallography" Birmingham, Kynoch press, 1962.
15. G. H. Stout, L. H. Jenson, "X-Ray Structure Determination," MacMillan, London, 1968.
16. A. L. Patterson, Phys. Rev., 1934, 46, 372; Z. Krist., 1935, 10, 517.

17. H. Lipson, W. Cochran, "The Crystalline State", Bell, 1966. Vol. 3.
18. A. D. Booth, Proc. Roy. Soc., 1946, A188, 77; Ibid, 1948, A190, 482.
19. D. W. Cruickshank, "The Equations of Crystal Structure Refinement", 1964.
20. G. M. Sheldrick, "Program for Crystal Structure Determination," Univ. of Cambridge 1975.
21. D. Puxley, Ph.D. Thesis, London, 1972.
22. "The X-Ray System-Version of June 1972," Technical Report TR-192 of Computer Science Centre, Univ. of Maryland, USA.
23. D. C. Puxley, J. D. Donaldson, Acta Cryst., 1973, A29, 91.
24. R. L. Mössbauer, Z. Phys., 1958, 151, 124.
25. R. L. Mössbauer, Naturwiss., 1958, 45, 538.
26. O. C. Kristner, A. W. Sunyar, Phys. Rev. Letts., 1960, 4, 229.
27. W. H. Baur, Acta Cryst., 1956, 9, 515.
28. E. V. Condon, G. H. Shortley, "The Theory of Atomic Spectra," C. U. P., 1935.
29. T. C. Gibb, "Principles of Mössbauer Spectroscopy," Chapman and Hall, 1976.
30. T. C. Gibb, B. A. Goodman, N. N. Greenwood, Chem. Comm., 1970, 774.
31. J. D. Donaldson, G. J. Filmore, M. J. Tricker, J. Chem. Soc(A), 1971, 1109.



32. V. I. Goldanski, E. F. Marakov, R. A. Stukan, T. N. Sumarokova, V. A. Trukhtanov, V. V. Khrapov, Dolkady Akad. Nauk. S. S. S. R., 1964, 156, 400.
33. V. A. Bukarev, Zhur. eksp. teor. Fiz., 1963, 44, 249.
34. S. Bukshpan, R. H. Herber, J. Chem. Phys., 1967, 46, 3375.
35. V. S. Shpinel, V. A. Bryukhanov, V. Kothekar, B. Z. Iofa, Zhur. eksp. teor. Fiz., 1967, 53, 23.
36. V. F. Sukhovenkhov, B. E. Dzevitskii, Dolkady Akad. Nauk. S. S. S. R., 1967, 177, 611.
37. J. D. Donaldson, R. Oteng, B. J. Senior, Chem. Comm., 1965, 618.
38. J. D. Donaldson, B. J. Senior, J. Chem. Soc (A)., 1969, 2358.
39. J. D. Donaldson, B. J. Senior, J. Chem. Soc. (A)., 1966, 1798.
40. C. G. Davies, J. D. Donaldson, J. Chem. Soc. (A)., 1968, 946.
41. J. D. Donaldson, B. J. Senior, J. Inorg. Nucl. Chem., 1969, 31, 881.
42. J. D. Donaldson, B. J. Senior, J. Chem. Soc. (A)., 1966, 1796.
43. J. D. Donaldson, D. G. Nicholson, B. J. Senior, J. Chem. Soc. (A)., 1968, 2928.
44. G. Fabric, E. Germagnoli, M. Musci, G. C. Locati, Nuovo Cimento, 1965, B40, 178.
45. V. V. Chekin, V. G. Naumov, Zhur. eksp. teor. Fiz.,

1966, 50, 534.

(Soviet Physics - JETP, 1966, 23, 355).

46. L. H. Bowen, J. G. Stevens, G. G. Long, J. Chem. Phys., 1969, 51, 2010.
47. R. E. Snyder, G. B. Beard, Phys. Lett., 1965, 15, 264.
48. S. L. Ruby, G. H. Kalvius, R. E. Snyder, G. B. Beard, Phys. Rev., 1966, 148, 176.
49. S. L. Ruby, G. H. Kalvius, R. E. Snyder, G. B. Beard, Phys. Rev., 1967, 159, 239.
50. T. Birchall, B. Della Valle, E. Martineau, J. B. Milne, J. Chem. Soc. (A)., 1971, 1855.
51. M. J. Tricker, Ph. D. Thesis, London.

## Chapter Three

### Design and Construction

	<u>Page</u>
3.1. Introduction	95
3.2. Photoconductivity	95
3.2.1. Design and Construction of photoconductivity apparatus	96
3.2.2. Power Supply	97
3.2.3. Monochromator	99
3.2.4. Sample Holder	100
3.2.5. Light Sources	103
3.2.6. Detector	107
3.3. Four Probe Surface Resistivity	113
3.3.1. Design of four probe surface resistivity apparatus	116
3.4. Electrical Conductivity	117
3.4.1. High Temperature Apparatus	120
3.4.2. Low Temperature Apparatus	122

### 3.1.

### Introduction

The properties of semiconducting materials are often explained in terms of the band theory. Useful information about the band structure can be obtained from measurements such as photoconductivity, luminescence, the temperature dependence of electrical conductivity and optical reflectance. This chapter describes the design, construction, calibration and testing of apparatus to measure photoconductivity, and electrical conductivity because equipment necessary for the observation of these phenomena is not available commercially to the specifications required.

### 3.2.

### Photoconductivity

Photoconductivity is defined as the change in electrical conductivity of a material under the action of absorbed radiation. The photocurrent can be expressed as the ratio of the applied voltage,  $V$ , to the electrical resistance,  $R$ , of the sample. In accordance with Ohm's Law:-

$$\frac{I}{e} = \frac{V}{eR} = \frac{VA}{epL} = \frac{VA n \mu}{L} \quad (3.1)$$

Since  $\rho = \frac{1}{ne\mu}$ , and  $L$  is the distance between two electrodes of area  $A$ .

This simple relationship formed the basis on which the photoconductivity apparatus was designed and constructed. A photoconductive response will result in a change in the resistance, which, can be monitored as a function of the current, provided the voltage is kept constant.

### 3.2.1. Design and Construction

In the initial design stage several factors had to be considered, and these are listed below:-

- 1) The intensity of the light. A light source with suitable spectral range and intensity is needed to produce a detectable change in the resistance of the sample on illumination.
- 2) A monochromator is required which will cover the wavelength region of interest (300 - 1000nm).
- 3) The likely change in resistance of the samples on illumination.
- 4) The nature of the sample; this needs to be such that the light illuminates the sample to give the largest percentage change in resistance.
- 5) A method of detecting a relatively small resistance change i.e. of the order  $10^{-6}$  ohms.

Consideration of these factors led to the construction of the equipment illustrated in the block diagram(Fig 3.1.). The component parts shown in the block diagram are now discussed in more detail.

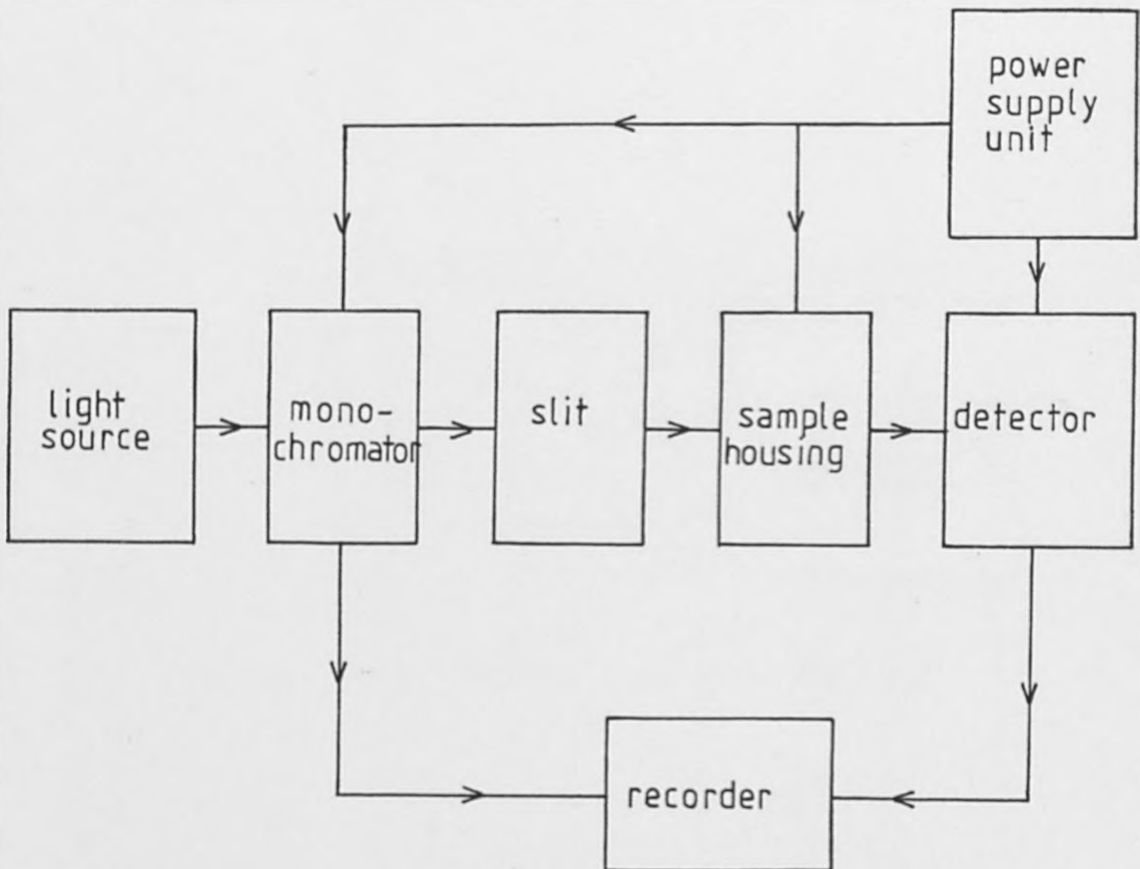


Fig.3.1. Block diagram of photoconductivity apparatus.

3.2.2. Power Supply (Fig 3.2)

The purpose of the power supply is to provide the voltage necessary to operate the amplifier circuit and to supply a stable voltage to the sample for resistance measurements. The current requirement of the circuit was a few hundred milliamps, therefore the readily available regulators, 78L type for positive volts, and 79L type for negative volts, were used. These regulators met the specifications and have the advantage of a fold back characteristic, which prevents device failure by shutting down in the event of short circuit or overload.

The power supply was run off the mains to avoid battery problems. The 240V mains supply was stepped down

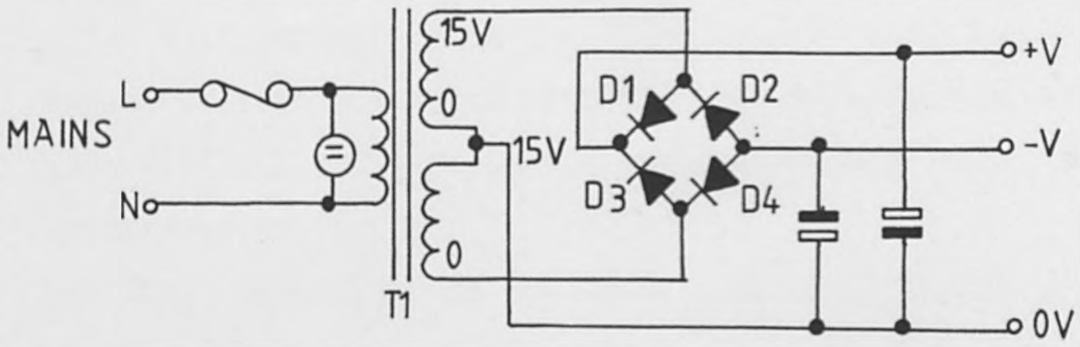


Fig. 3.2. (a) Unregulated Power Supply.

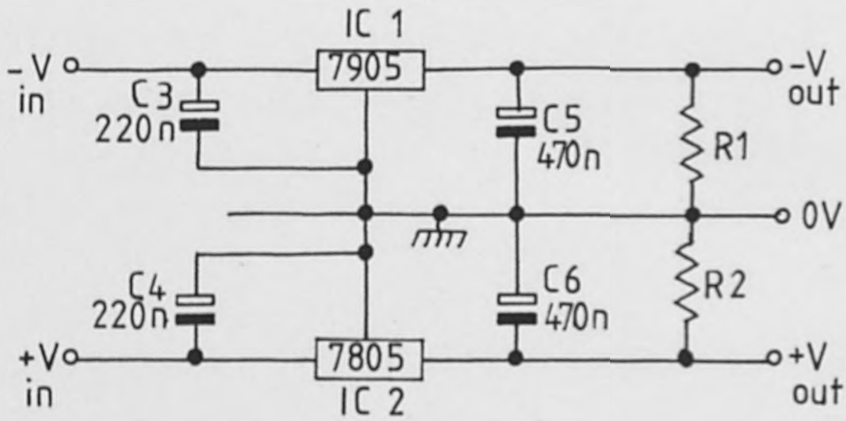


Fig. 3.2. (b) Voltage Regulator Power Supply.

by a centre tapped transformer (Fig 3.2(a)T1) to give  $\sim 30V$ . The AC voltage from the secondary coil of the transformer was connected via a diode bridge (Fig 3.2(a)D1-4) to provide  $\pm 21V$  with respect to earth. This part of the circuit was housed in a separate box with the smoothing capacitors (Fig 3.2(a)C1 & C2) to reduce mains frequency noise interference.

The second part of the power supply was housed within the main amplifier unit. This comprised of two similar circuits; one 78L05 regulator (Fig 3.2(b)IC1) and one 79L05 regulator (Fig 3.2(b)IC2) which were connected as shown (Fig 3.2(b)) with capacitors C3 and C4 across the input and earth respectively, to provide 50 Hz ripple attenuation and C<sub>5</sub> and C<sub>6</sub> across the output and earth respectively, to further reduce ripple and any noise generated within the circuit. The two regulators were bolted via mica washers to the case which acted as a heat sink. To maintain the stability of the regulator integrated circuits a load must be applied at all times, this is provided by resistors R<sub>1</sub> and R<sub>2</sub>.

### 3.2.3.

### Monochromator

Monochromatic light may be produced in a number of ways, three of which were considered in this work. Filters, which are probably the simplest type of monochromator, would be unsuitable for use in the scanning mode required. Diffraction grating or prism type monochromator would, however, be



suitable although the latter was chosen for use.

The prism type monochromator, lamp housing and slit assembly used were obtained from a Unicam SP 500 U. V./visible spectrometer.

#### 3.2.4. Sample Holder

During the course of testing and calibration three different sample holders were used.

The first sample holder (Fig 3.3) used had sprung copper contacts but because of problems encountered in loading the sample and ensuring good electrical contacts this design was discarded.

A second sample housing was constructed from a 50Ω elbow b.n.c. type socket, with a brass screw thread attached with epoxy resin and solder. The sample was held in an insulated sleeve by a brass nut and metal support ring to provide one electrical contact. The other contact was made via a brass plate inserted in the connector and insulated from the brass screw thread (Fig 3.4). Silver loaded paint was applied to the circumference of the pelleted sample to ensure a good electrical contact. Although this sample holder was much simpler to use it reduced the area of the sample exposed to the light. For this sample holder, as with the first one, the sample is prepared in the form of a compacted 13mm disc of about 1.5 - 2.00mm thickness. This is not the ideal form for the

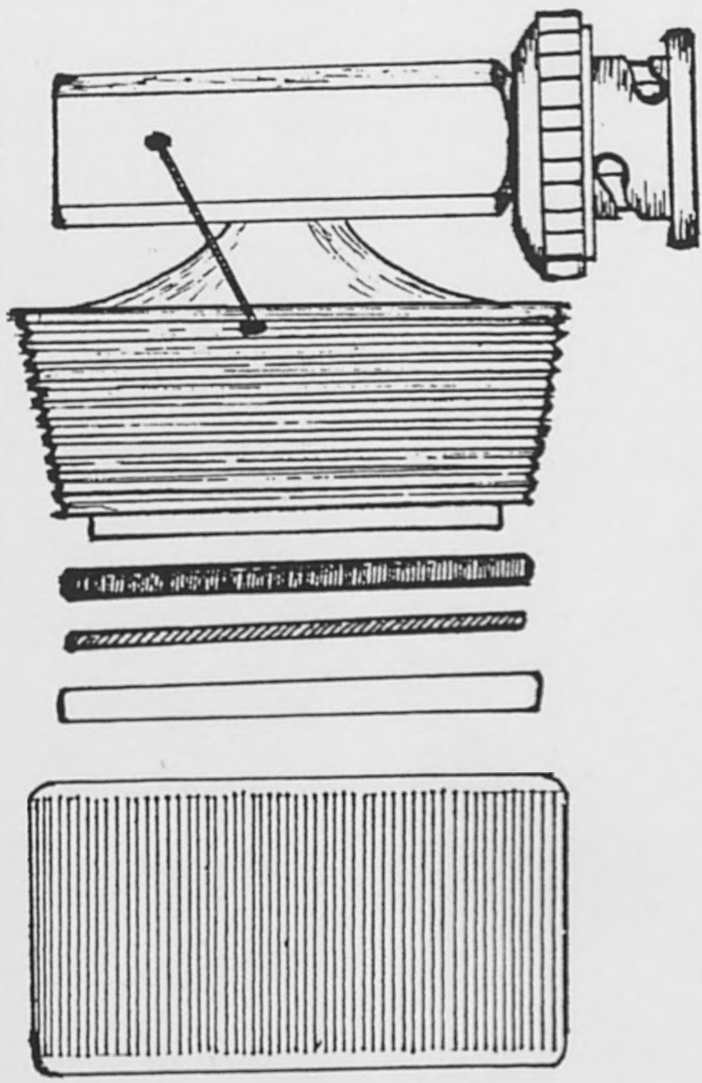


Fig. 3.3. Exploded diagram of a sample holder used in photoconductivity measurements .

Fig 3.3. Disc sample holder for  
photoconductivity measurements

Fig 3.5. Thick film sample holder  
for photoconductivity measurements



sample because only the surface is affected by illumination, and the penetration of photons is small in comparison with the thickness of the sample. In an attempt to achieve a larger change in resistance a third sample holder was devised which used thick film samples. This holder consisted of a piece of epoxy glass laminate circuit board with an etched copper pattern to provide the electrodes as shown in (Fig 3.5). The connection to a 50  $\Omega$  to b.n.c. socket was made by a short length of co-axial cable.

#### 3.2.5.

#### Light Sources

A tunable laser would have provided the best light source as it would have been of high intensity and produced monochromatic light over a wide spectral range. However, this was not available. For this reason other light sources had to be considered.

The lamps from the Unicam SP500 spectrometer were standard deuterium and tungsten lamps, which covered the wavelength range 200nm to 1000nm. These lamps were unsuitable for this application because of their relatively low light intensity.

Xenon and flash tubes, although high intensity light sources were considered unsuitable due to their limited spectral range. A number of quartz-halogen and filament type bulbs were investigated for possible use. A slide projector 150W tungsten-halogen bulb was found to produce a reasonable

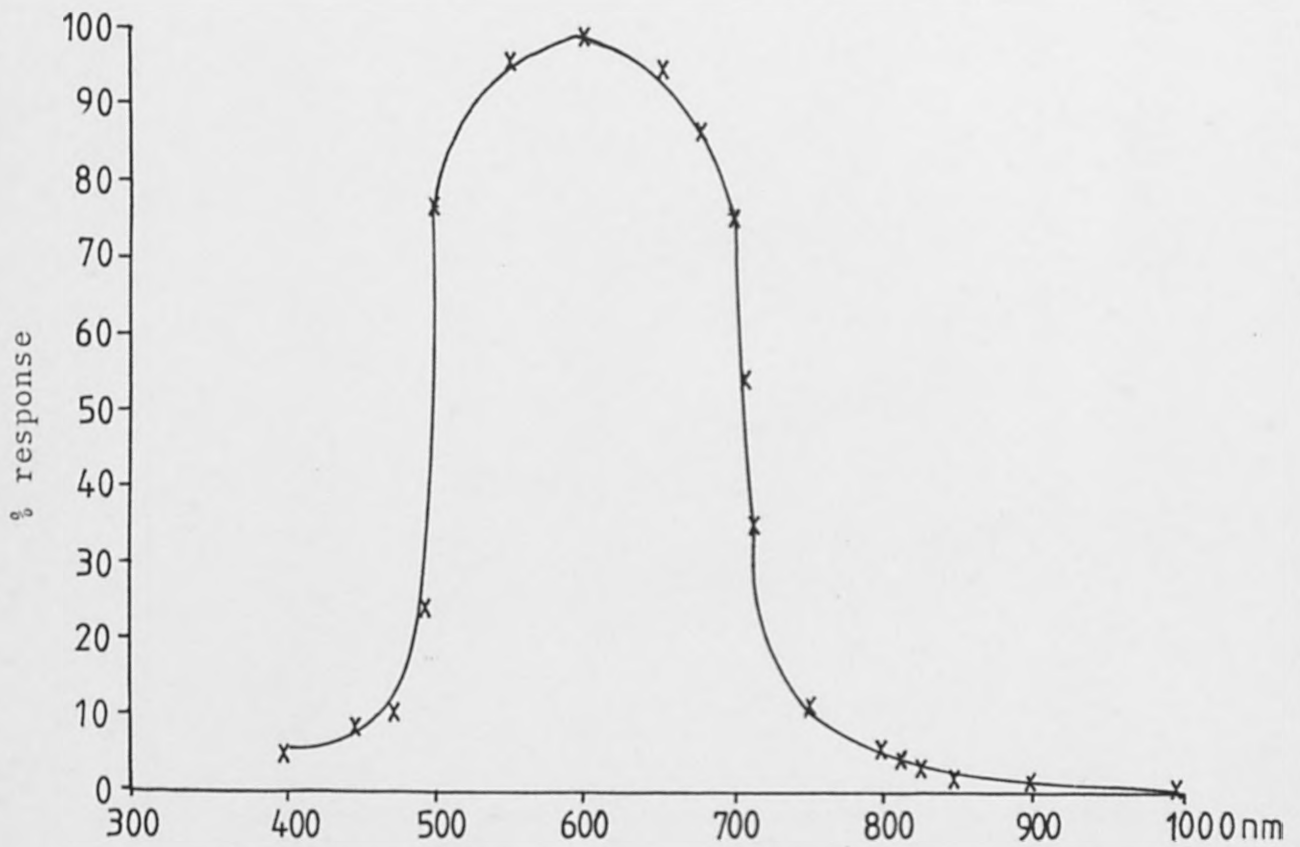


Fig. 3.6. Spectral output of a 150W tungsten-halogen bulb (0.04 mm slit)

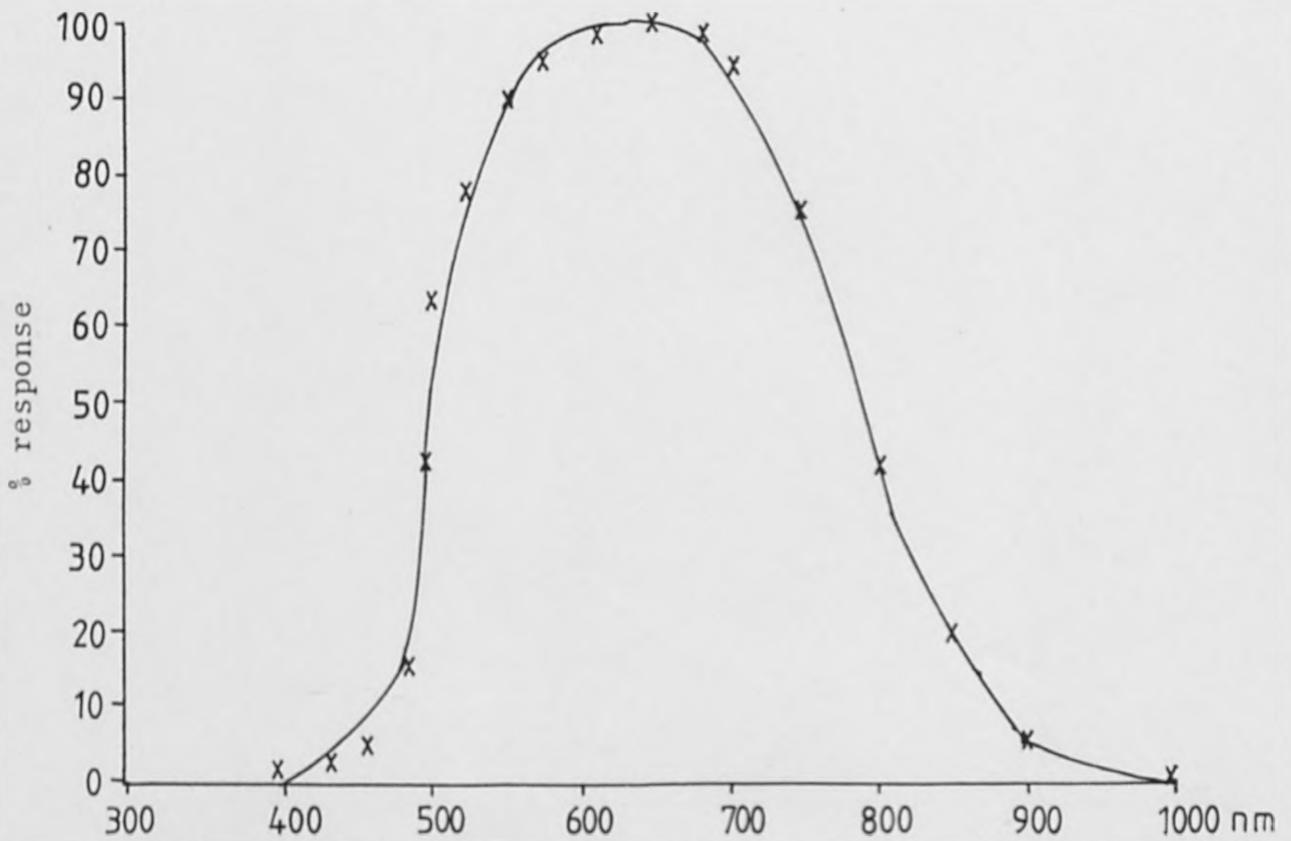
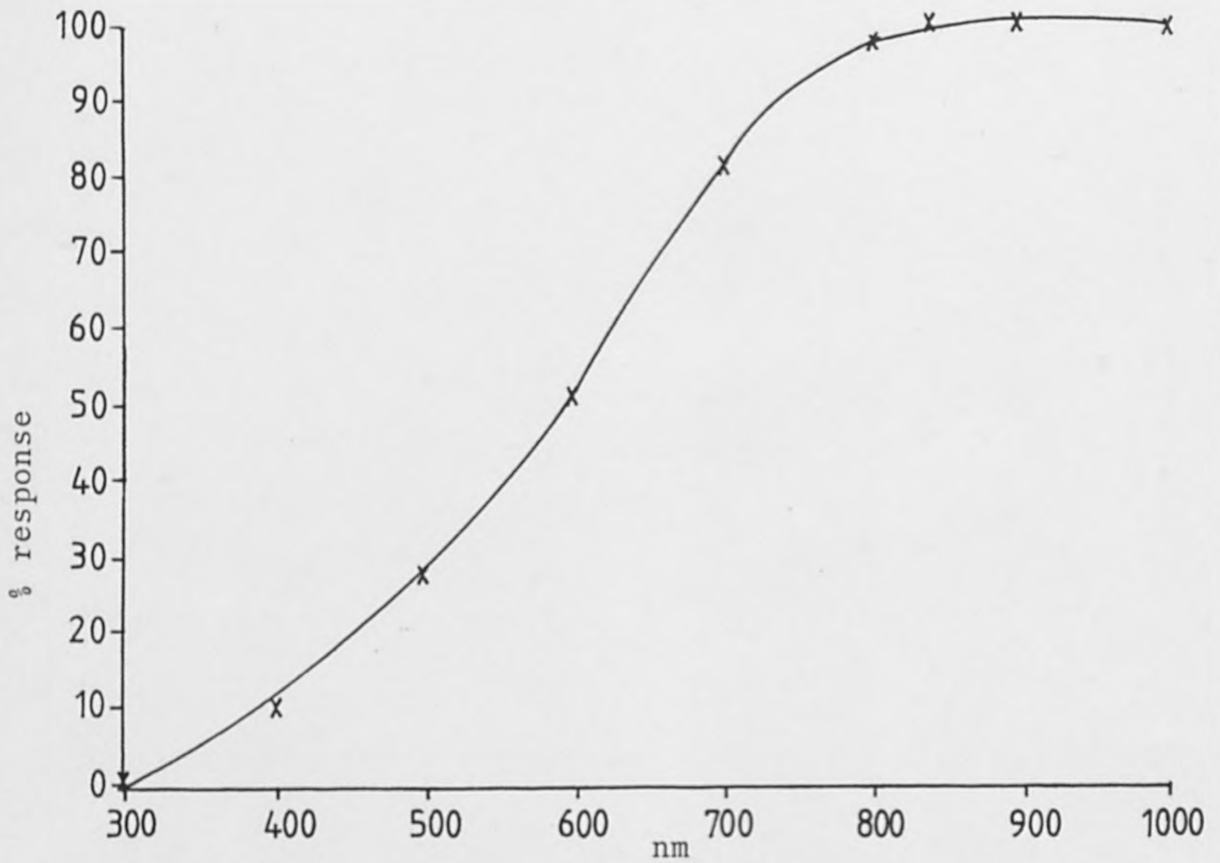


Fig. 3.7. Spectral output of a 150W photoflood bulb (0.15mm slit)



STD Curve Tungsten Lamp

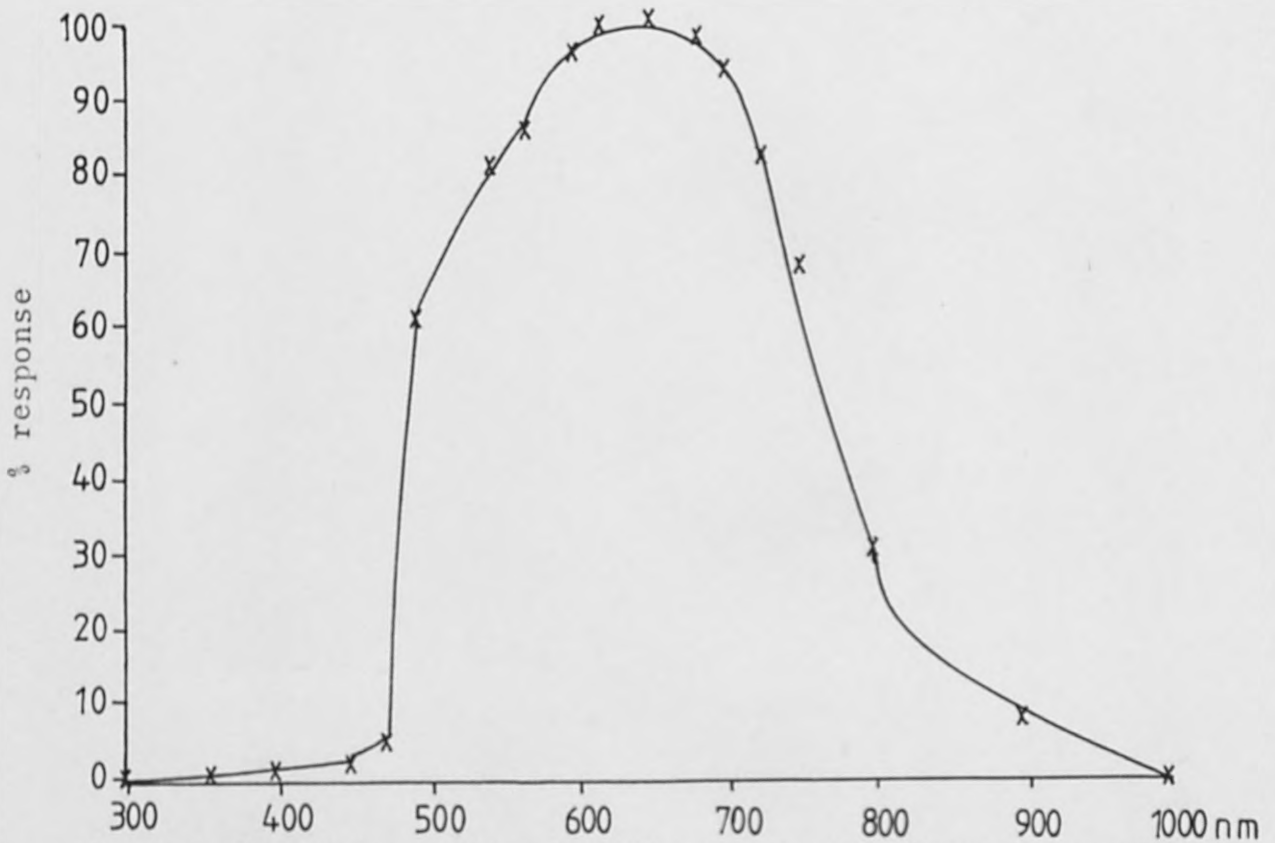


Fig.3.8. Spectral output of a 100W filament bulb (0.02mm slit)

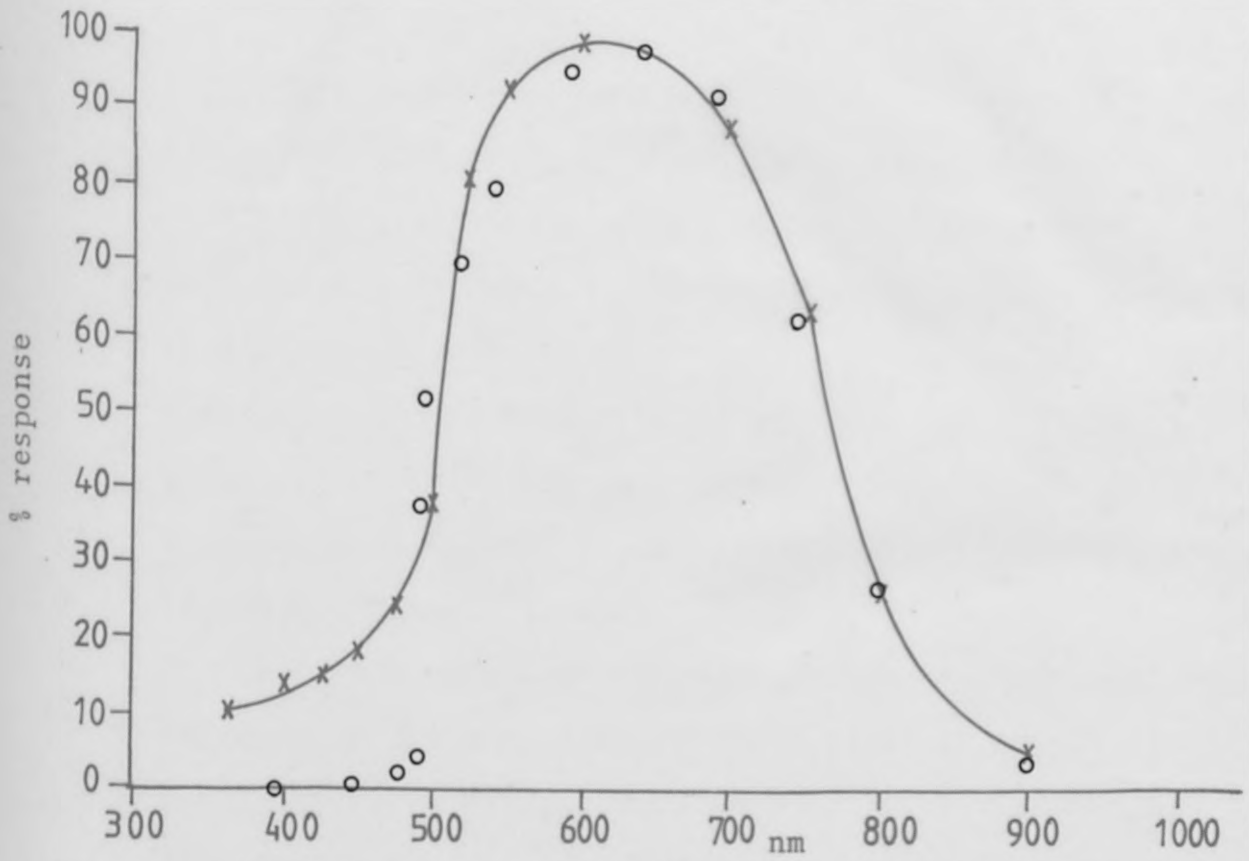


Fig. 3.9. CdS light dependant resistor ORP12.

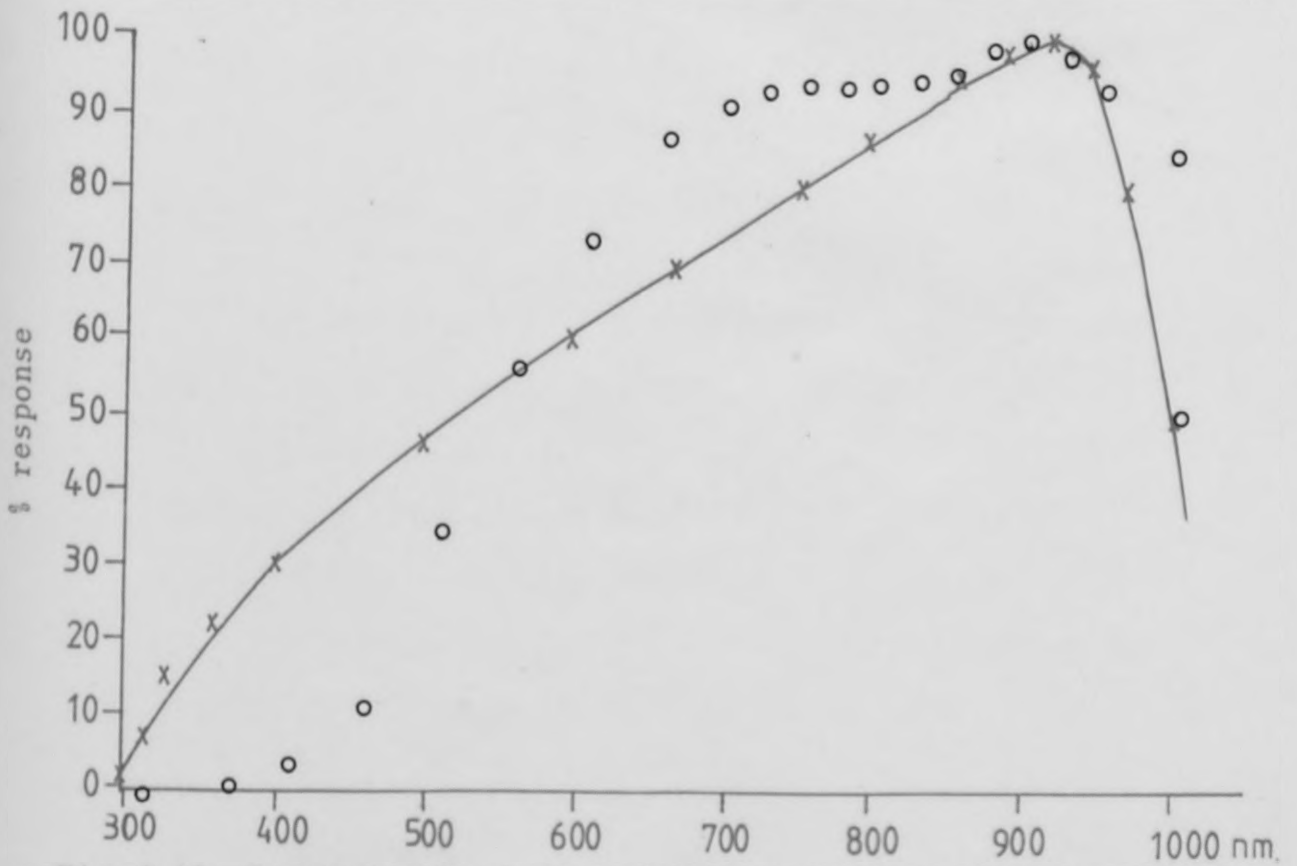


Fig. 3.10. Spectral output of a silicon photo diode (type RS 308067)



intensity, but had a restricted spectral output (Fig 3.6). A domestic 100W filament bulb proved unsuitable because of low light intensity. Although a 150W photoflood photographic filament type bulb appeared to have adequate light intensity the spectral response was limited (Fig 3.7). Finally, a 100W filament bulb, as used on a Vickers microscope was tested, this provided a suitable compromise between light intensity and spectral range (Fig 3.8) and is the lamp currently in use.

A method of comparison between the various lamps was required in order to confirm their spectral output and light intensity. Two devices were used, firstly a CdS-light dependent resistor, type ORP12, was selected as it has a spectral response similar to that expected from the samples (Fig 3.9). Secondly, a Silicon photo diode, type RS 308067, was used as this has a spectral response that allowed light emission to be monitored over a wider range (Fig 3.10).

#### 3.2.6.                      Detector (Fig 3.11)

The detector circuit consists of four basic parts, viz:

- 1) a bridge detector circuit
- 2) a measuring circuit
- 3) an amplifier circuit
- 4) a voltage bias circuit

The bridge part of the circuit is a standard four resistor Wheatstone bridge (Fig 3.12), consisting of two

fixed resistors  $R_1$  and  $R_2$ , one variable resistor  $R_s$  and an unknown resistor (the sample)  $R_x$ .  $R_1$  and  $R_2$  are of equal resistance and of the same order as  $R_x$ , whilst the value of  $R_s$  selected was of comparable magnitude to that expected from the sample  $R_x$ .

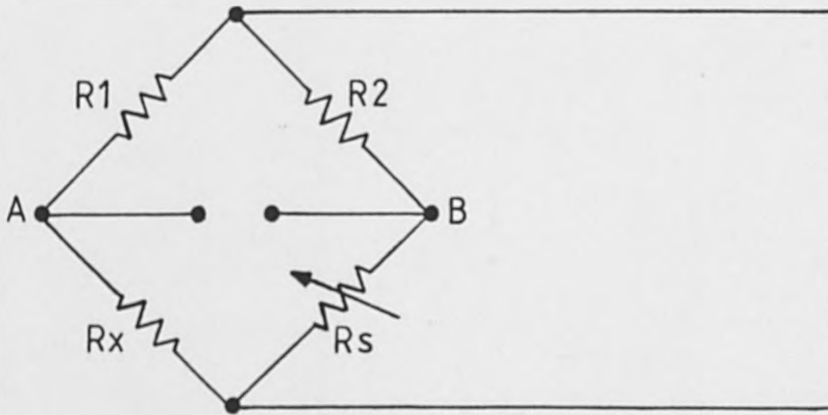


Fig. 3.12. Standard four resistor Wheatstone bridge circuit.

It can be seen that at balance

$$\frac{R_v}{R_s} = \frac{R_1}{R_2} \quad \text{and hence} \quad R_x = R_s \left\{ \frac{R_1}{R_2} \right\} \quad (3.2.)$$

Thus if  $R_1 = R_2$  then  $R_x = R_s$  and the bridge is in balance.

If the bridge is balanced at dark current, any change in resistance of the sample ( $R_x$ ) on illumination will unbalance the bridge. In this condition a potential difference develops across A and B. This difference is fed to two buffer amplifiers (ICIA, ICIB) contained in one integrated

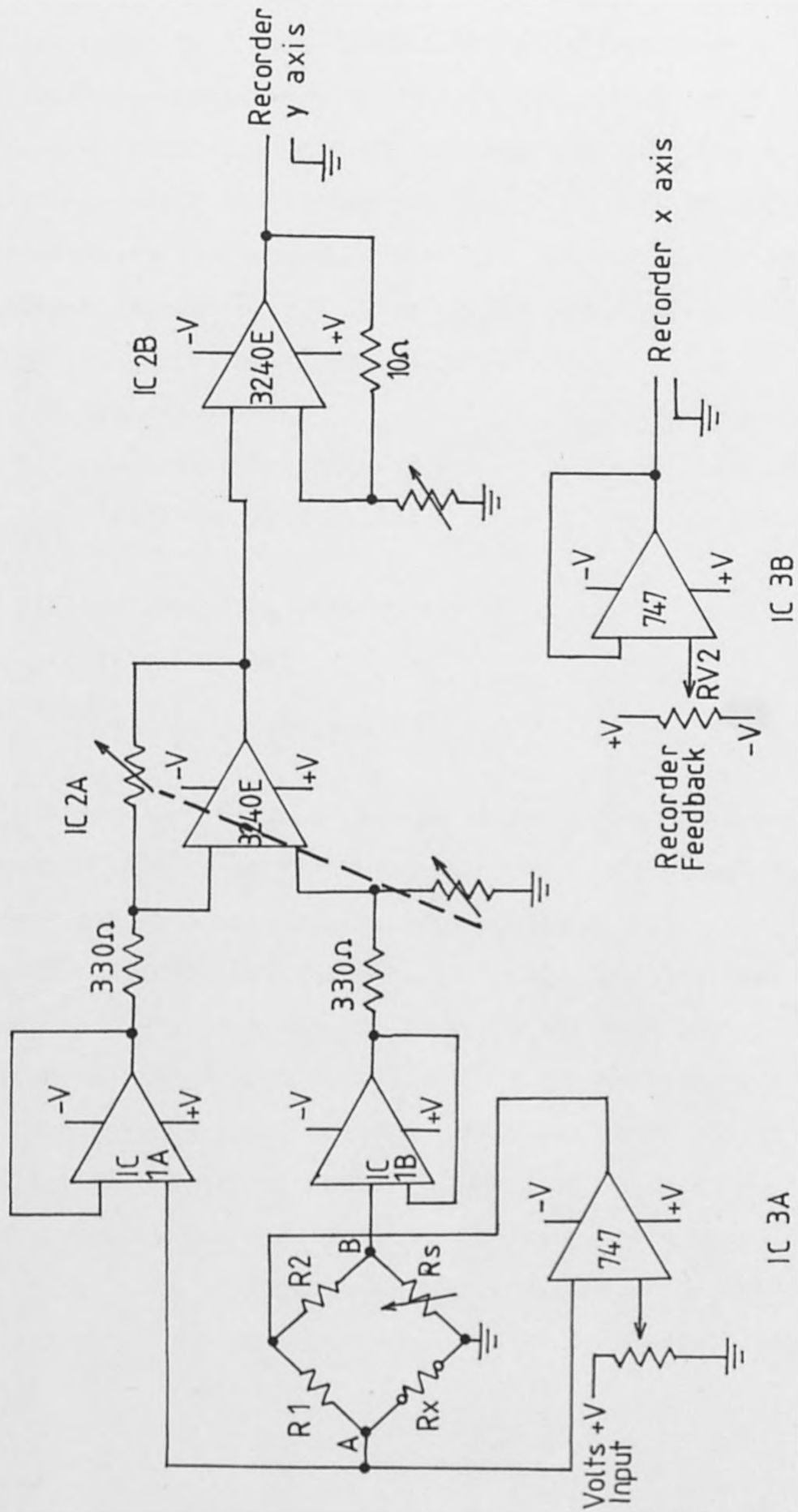


Fig. 3.11. Detector Circuit

circuit which is a dual 3240E-1 MOSFET OPERATIONAL AMPLIFIER, connected for unity gain and a high input impedance of greater than  $10^{12}\Omega$ . Omission of these buffer amplifiers would render the difference between  $R_s$  and  $R_x$  insignificant in comparison with the relatively low input impedance (approximately  $100\Omega$ ) of the differential amplifier (IC 2A) to which the signal is then fed.

By ohm's law:

Resistors in series  $R = r_1 + r_2 + r_3 \dots\dots\dots$  etc.

Resistors in parallel  $\frac{1}{R} = \frac{1}{r_1} + \frac{1}{r_2} + \frac{1}{r_3} \dots\dots\dots$  etc.

If the amplifier impedance =  $r_1$

and  $r_2 = R_x + R_s$

than  $\frac{1}{R} = \frac{1}{r_1} + \frac{1}{(R_s + R_x)}$  (3.3.)

From equation(3.3.) it can be shown that a low input impedance will cause the change in sample resistance to become insignificant and therefore undetectable.

The differential amplifier (IC 2A) amplifies the potential difference between points A and B on the Wheatstone bridge by a factor of 10. As the signal is still relatively small a second stage amplifier (IC 2B) with variable gain was used to amplify the signal to a level suitable for detection on the y axis of a recorder.

Bias voltage is supplied to the sample by an operational amplifier (IC 3A) connected as a voltage follower. Voltage

is supplied to the input of this amplifier via a potential divider. The purpose of this amplifier is to provide a voltage to the Wheatstone bridge such that, the voltage at point A is equal to the voltage from the potential divider on the input. This ensures that the voltage across the sample is that selected by the operator.

Feedback from the calibrated wavelength dial of the monochromator was provided by variable resistor ( $RV_2$ ) to the input of IC 3B which was wired as a simple voltage follower to provide d.c. voltage to the x-axis of a recorder. This allowed a direct plot of resistance change against wavelength.

Two alternative detector systems were investigated prior to the final design. Firstly, a simple resistance measurement using the circuit illustrated in Fig 3.13. The circuit was designed to measure the voltage drop across an accurately known resistor ( $R_s$ ) in series with the unknown resistor  $R_x$ . By application of Ohm's Law the value of  $R_x$  could be determined as shown above. On testing, the sensitivity of this circuit was found inadequate.

The other method of detection investigated was a bridge network, as described previously, fitted with a chopper assembly which chopped the light beam giving fixed periods of light and no light. A chopper amplifier was run in conjunction with this to provide a differential output of the voltage (Fig 3.14). The advantages of this design are: compensation for base line drift due to charging effects with

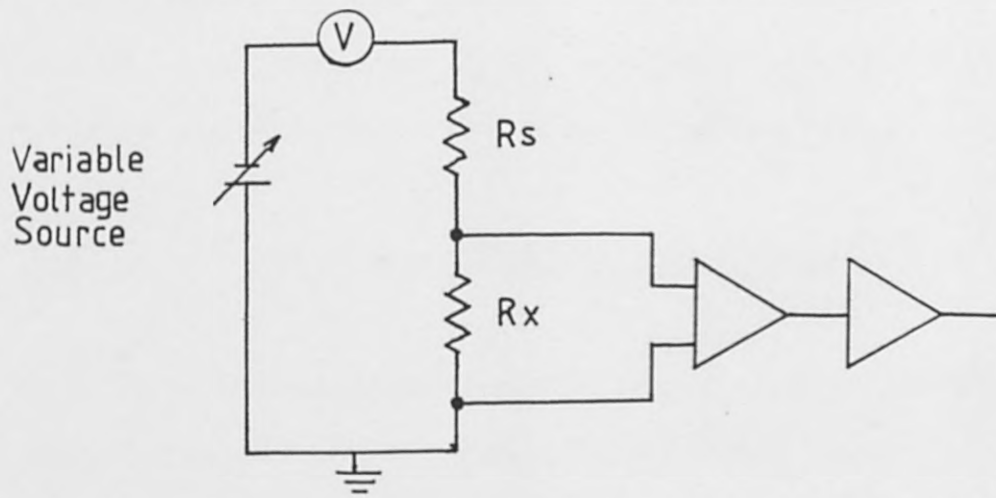


Fig. 3.13. Simple Resistance Circuit

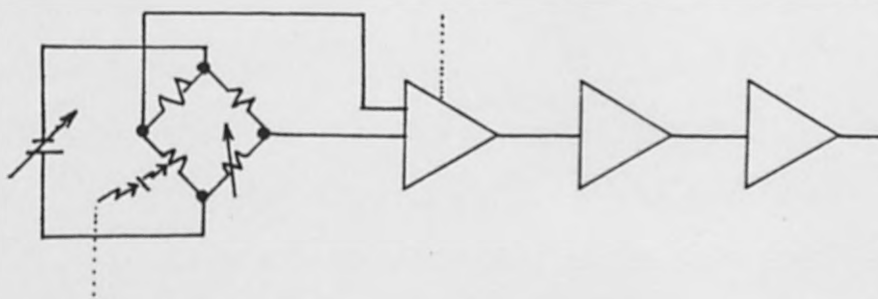


Fig. 3.14. Chopper Circuit

the sample and reduced noise resulting from the inherent time constant of the system. The major problem encountered was the slow response of the samples which necessitated a chopper speed outside the range of this design.

### 3.3. Four Probe Surface Resistivity

Many conventional methods for measuring resistivity are unsatisfactory for semiconductors, since metal - semiconductor contacts produce contact potentials. The method described here overcomes this difficulty and permits the rapid measurement of resistivity or conductivity by simple application of four points to a specimen, and, within limits the results are independent of the size or shape of the specimen. Where as conventional conductivity measurements, using two electrodes, measures the electrical conduction of the bulk material, this method provides a means of measuring the electrical conductivity along the surface of the compacted material.

The basic model for these measurements is that of Valdes<sup>(1)</sup>, indicated in Fig 3.15. Four probes are placed on a flat surface of the material to be measured, current is passed through the outer two electrodes and the floating potential is measured across the inner pair.

If the flat surface on which probes rest is adequately large then the material may be considered to be a semi-infinite volume. The resistivity is computed as:

$$\rho = \frac{V}{I} \frac{2\pi}{\left( \frac{1}{s_1} + \frac{1}{s_3} - \frac{1}{s_1 + s_2} - \frac{1}{s_2 + s_3} \right)} \quad (3.4.)$$

where

$V$  = floating potential difference between the inner probes (volts)

$I$  = current through outer pair of probes (amps)

$s_1, s_2, s_3$  = point spacings, in cm

$\rho$  = resistivity in ohm - cm

when  $s_1 = s_2 = s_3 = s$  this equation simplifies to:-

$$\rho = \frac{V}{I} 2\pi s$$

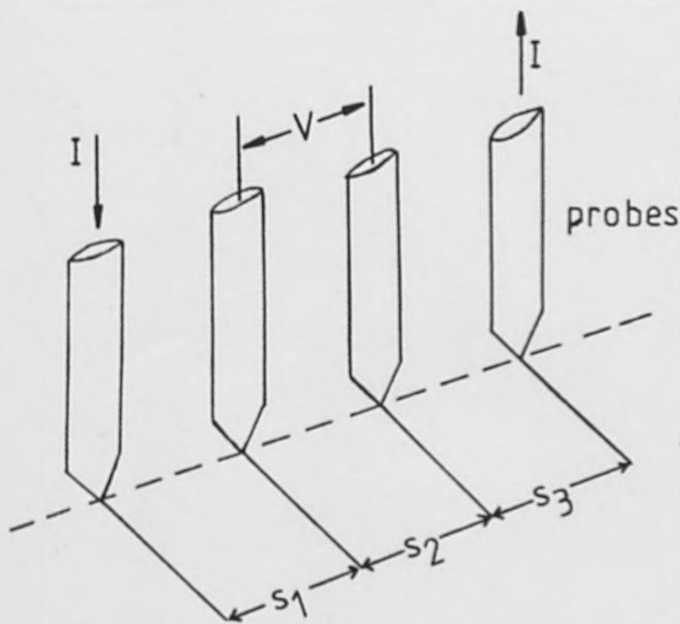


Fig 3.15 Model for four probe resistivity measurements.




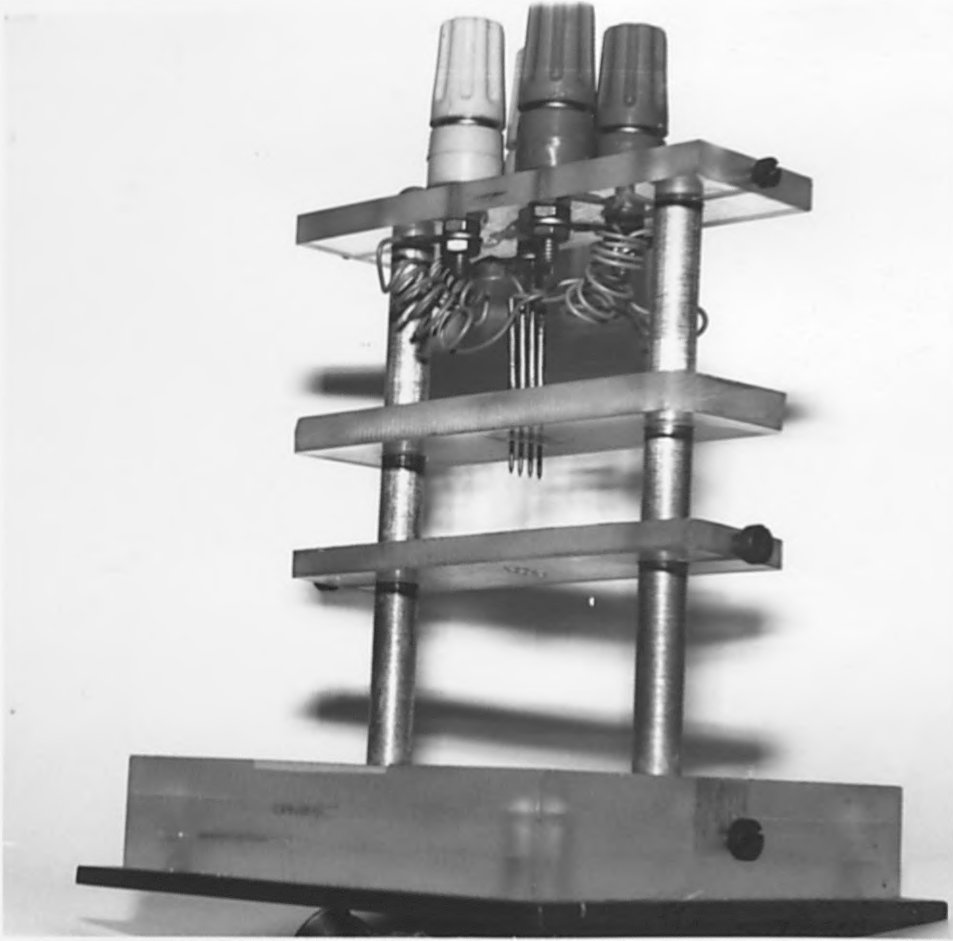


Fig 3.16. Four probe surface resistivity apparatus



### 3.3.1.

### Design

The sample holder / four probe assembly was the only part of the circuit which had to be designed and constructed.

In order to make the required resistivity measurements the four probes had to be placed on a flat surface of the sample. To fulfill this requirement the samples were compacted into a disc 13mm in diameter. The disc was placed in a hollow in a piece of perspex which was supported on rods at either end (Fig 3.16). A second piece of perspex with the probes mounted in it was supported above the first such that the probes could be lowered onto the sample and held in position. Soldered wire connections were made from the probes to standard 4mm sockets mounted in a third piece of perspex fixed at the top of the rods.

The selection of suitable probes was the only problem encountered in the construction and subsequent testing of the equipment. The first probes used were stainless steel dressmaking pins fixed to the perspex sheet with epoxy resin cement. These probes were unsuccessful as the pressure required to produce good contacts invariably cracked the compacted sample. This failure led to the use of flat ended stainless steel pins. However, it proved difficult to make reliable solder connection and contact with all four probes simultaneously so this method was quickly abandoned. Finally, spring loaded gold plated test probes were investigated. Although having sharp, point contacts

like the pins, the spring loading reduced the pressure required for good contact and overcame the problem encountered with the pins and reliable solder connections could be made to the test probes.

The effect of the current flowing through the outer probes on the measured resistivity was investigated by one set of reading taken on a 6.3 ohm - cm sample. A 37% reduction in resistivity observed at 100ma is attributed primarily to heating of the sample, since its temperature was at least 30°C above ambient with this high current.<sup>(1)</sup> To avoid this type of problem all resistivity measurements were carried out with 0.1 - 1.0ma through the probes. Three Ever Ready 22.5v batteries were connected in series to provide the required current. The current flowing through the outer probes was measured on a Keighthly Model 616 Digital Electrometer, and the potential drop across the two inner probes were measured on an Avo voltmeter.

#### 3.4. Electrical Conductivity

The variation of the electrical conductivity with temperature depends on both the excitation of electrons to the condition band, as given by the equation

$$n_e = \text{constant} \times T^{3/2} \exp \left( -(E_g - E_F)/kT \right) \quad (3.5.)$$

where  $E_g$  is the energy gap and  $E_F$  is the Fermi level of a

given semiconductor, and on the variation of the mobilities with temperature. The mobilities, at all but the lowest temperatures, are largely determined by lattice scattering of the charge carriers and decrease with increasing temperature. In simple terms the mobilities are expected to vary with temperature as

$$\mu = \text{constant} \times T^{-3/2} \quad (3.6)$$

thus the conductivity of an intrinsic semiconductor is

$$\sigma_I = \sigma_{OI} \exp(-E_g/2kT) \quad (3.7)$$

For extrinsic semiconductors the excitation of carriers from the impurity levels, of energy  $E_i$ , must also be allowed for, hence:

$$\sigma_E = \sigma_{OE} \exp(-E_i/kT) \quad (3.8)$$

where  $\sigma_{OE}$  is a constant and  $\sigma_E$  is the 'extrinsic' contribution to the conductivity of the material due to the presence of impurities.

In general the conductivity of a semiconductor is made up of two terms which, because of the different magnitudes of  $E_g$  and  $E_i$ , predominate in different temperature regions. At low temperatures the extrinsic term is most important

while the intrinsic term dominates at high temperatures. The total conductivity is

$$\sigma_{\text{tot}} = \sigma_{\text{oI}} \exp(-E_g/2kT) + \sigma_{\text{oE}} \exp(-E_i/kT) \quad (3.9)$$

The form of the equation provides a method for measuring both  $E_g$  and  $E_i$  for one or other term can be neglected depending on the temperature. Thus, if the electrical conductivity is measured as a function of temperature and if  $\ln\sigma$  is plotted against  $1/T$  a graph of the form shown in Fig 3.17 is obtained. The graph consists of two straight line regions the slopes of which yield  $E_i$  and  $E_g$  for the low and high temperature regions respectively. The intercepts of the two regions give the constants  $\sigma_{\text{oI}}$  and  $\sigma_{\text{oE}}$ .

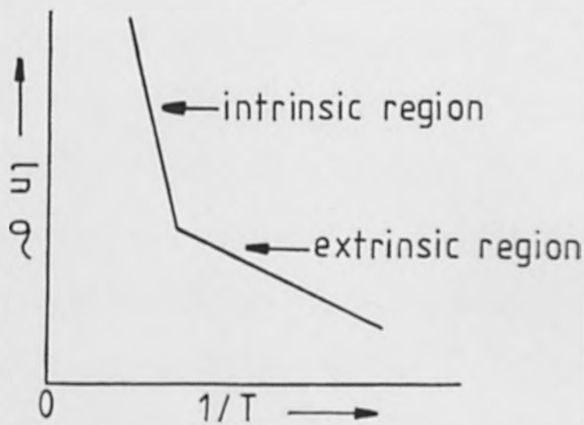


Fig 3.17 Variation of conductivity with temperature for an ideal extrinsic semiconductor.

Two pieces of equipment were designed to measure the electrical conductivity as a function of temperature. The

first covered the temperature range ambient to 300°C, and the second liquid nitrogen temperature to 100°C.

#### 3.4.1. "High" Temperature Apparatus

The apparatus was designed to measure the change in electrical conductivity from ambient to 300°C, and as such the only major consideration was the uniform heating of the sample.

The sample was finely ground and about 2g was placed in a 13mm stainless steel die and was put under vacuum and an external pressure of 5 tonnes was applied to the disc for 5 minutes. The disc was painted on either side with silver loaded paint, to ensure good electrical contact, and placed between two electrodes. The two identical electrodes were constructed of Cu tube (10mm o.d. and 5mm bore) with a copper disc (13mm diameter x ~ 1mm thick) silver soldered to one end. This disc was polished flat and gold plated to improve electrical contact. The electrodes were supported using "Quickfit" stirrer glands and ground glass joints in a pyrex glass furnace assembly (Fig 3.18).

The furnace consisted of a glass tube around which approximately 30 turns of 10Ω per meter Nichrome wire was wound non-inductively. A copper - constantan thermocouple was incorporated within the windings which were covered with alumina cement to prevent heat loss. The furnace windings and the thermocouple were connected to a Eurotherm temperature controller.

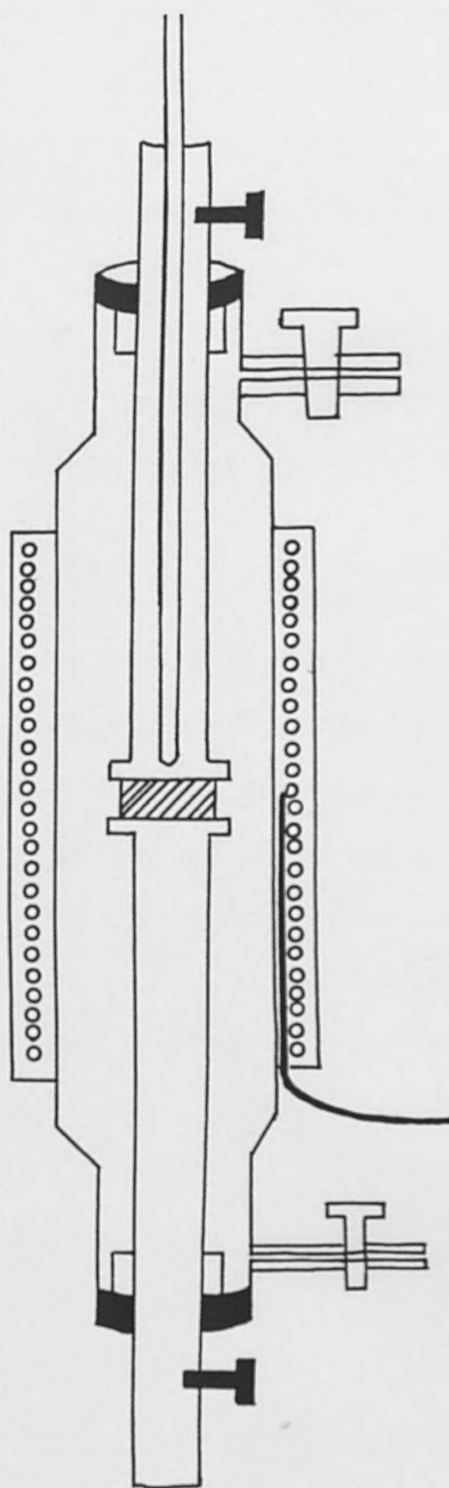


Fig. 3.18. "High" Temperature Variable Conductivity Apparatus.



A second alumina sheathed copper-constantan thermocouple was inserted in one of the electrodes to monitor the temperature of the sample itself. The output from this thermocouple was recorded on a Linseis two pen flat bed chart recorder.

The resistance of the sample was measured, via the copper electrodes, by a Keightley Model 616 Digital Electrometer and recorded on the second pen of the chart recorder.

It was found that if a sample was heated above a critical temperature characteristic for each sample, the temperature at which a phase change occurred was shifted (Fig 3.19) on subsequent runs. Consequently, each disc of a sample could only be heated above this limit once, fresh discs being used to verify results.

The temperature and resistance data from the chart recorder was fed into a computer programme, written by Dr. S. J. E. Clark, which gave a graphical output of the data, in the form of a plot  $\ln \sigma$  vs.  $1/T$ . From the graph it was possible to determine  $E_g$ ,  $E_i$  and the temperatures at which any phase changes occurred.

#### 3.4.2. "Low" Temperature Apparatus

The design of this equipment was necessarily more complex than the "high" temperature apparatus due to the low temperatures required. In order to reach and maintain

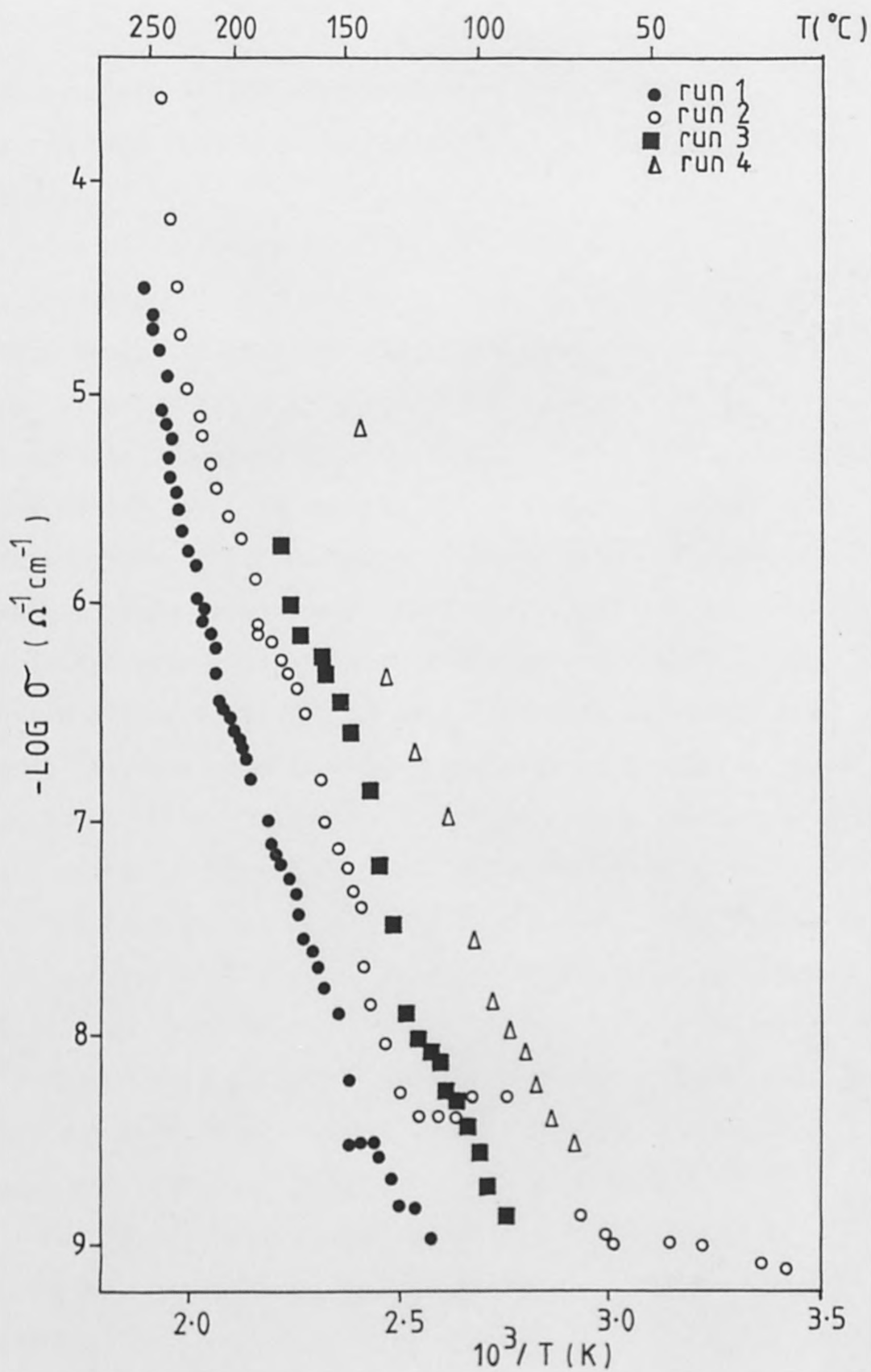


Fig. 3.19. Variable Temperature Conductivity of  $\text{Cs}_2\text{NaSbCl}_6$ , showing the shift that occurs on rerunning the same sample.

a temperature of 70K efficient heat transfer to the sample was required from both the liquid nitrogen chamber and the furnace.

The basic design is illustrated in Fig 3.20. The pelleted sample, prepared as previously described, was placed between two copper electrodes situated in an alumina tube. A metal sheathed copper-constantan thermocouple was embedded in the alumina tube. A furnace was non-inductively wound around the tube and sealed with alumina cement. The bottom copper electrode was drilled to house an alumina sheathed copper-constantan thermocouple which monitored the sample temperature. The electrode-furnace assembly was located at the bottom of an evacuated chamber within the liquid nitrogen chamber, which was made of stainless steel type 321 to provide good heat transfer. The whole assembly being mounted on a flange to provide stability.

The furnace was controlled by a temperature programmer, which incorporated facilities for heating, cooling and cycling the temperature at rates varying from  $1^{\circ}\text{K}/\text{minute}$  to  $10^{\circ}\text{K}/\text{minute}$  with a digital display for the temperature. The upper and lower temperatures being preset by a series of decade switches.

The signals from the electrodes and sample thermocouple were recorded as described for the high temperature apparatus.

When the apparatus was tested it was found that several modifications were required for optimum operating conditions

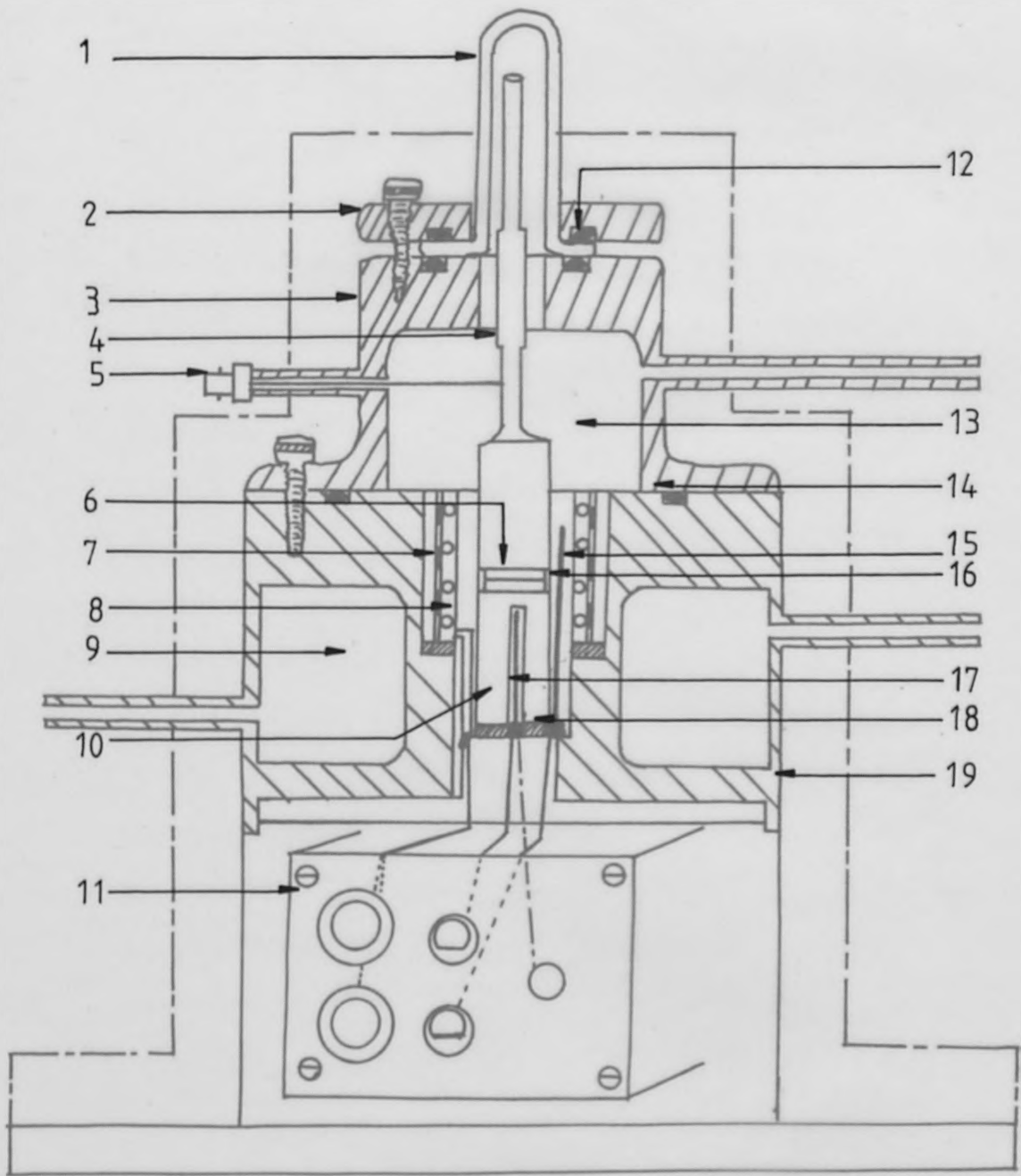


Fig. 3.20. Diagram of 'low temperature' variable conductivity apparatus.

Key for Fig. 3.20.

1. Sight Glass
2. Clamp
3. Cover
4. Upper Copper Electrode
5. B.N.C. connection to upper electrode
6. Sample
7. Mica Sheet
8. Nichrome ribbon
9. Liquid Nitrogen chamber
10. Lower Copper Electrode
11. Control Panel
12. 'O' ring
13. Vacuum chamber
14. 'O' ring
15. Copper-constantan thermocouple
16. Ceramic Furnace tube
17. Alumina sheathed copper-constantan thermocouple
18. Gasket
19. Housing

to be achieved. The vacuum necessary in the inner chamber was difficult to maintain due to the lack of suitable vacuum fed-throughs for the thermocouple, furnace and electrode wires. The flange at the base, although providing stability to the assembly, could not be adequately insulated because of its shape and acted as a heat sink. These factors coupled with the absence of an outer vacuum jacket resulted in icing up of the apparatus and failure to attain the desired minimum temperature. The lowest temperature reached on testing was 95K.

The electrical connection to the upper electrode was made by a B.N.C. socket and stainless steel tube, to the casing. At low temperatures the socket iced up, so that any resistance measurements obtained were totally arbitrary.

The removal of the lower flange, the addition of suitable vacuum fed-throughs and an outer vacuum jacket are being currently considered.

## References

1. L. B. Valdes, Proc. I. R. E., (1954), 42, 420.

## Chapter Four

	<u>Page</u>
4.1. Experimental	131
4.1.1. Emission Spectra	131
4.1.2. Absorption Spectra	133
4.1.3. Electrical Conductivity Measurements	133
4.1.4. Differential Thermal Analysis	138
4.2. Simple Iodide Systems	141
4.2.1. Optical Properties	142
4.2.2. Electrical Properties	142
4.3. Caesium Lead Trihalides	145
4.3.1. Preparation	146
4.3.2. Optical Properties	146
4.3.3. Electrical Conductivity	149
4.3.4. Photoconductivity Measurements	149
4.4. A Comparative Study of $A_2^I A^I B^{III} X_6$ Compounds	154
4.4.1. Preparation and Analysis	155
4.4.2. X-Ray Analysis	157
4.4.3. Thermal Analysis	162
4.4.4. Optical Properties	165
4.4.5. Electrical Conductivity	168
4.4.6. Variable Temperature Measurements	172
4.4.7. Replacement of Antimony (III) by Indium (III) in $Cs_2NaSbX_6$ (X = Cl, Br)	176



	<u>Page</u>
4.5. Miscellaneous Systems	177
4.5.1. Cadmium Iodides	177
4.5.2. 'High Temperature' Electrical Conductivity Study of the $\text{CsSnCl}_{3-x}\text{Br}_x$ System	181
4.6. Crystal Structure Determination of $\text{Cs}_2\text{NaBiBr}_6$	186
4.6.1. Determination of Space Group and Cell Dimensions	187
4.6.2. Discussion of the Crystal Structure	188
Appendix	192

## Introduction

In this chapter a brief outline is given of the experimental techniques used throughout this study. This is followed by the description of series of investigations on simple iodides and of a comparative study of the effect of the halogen on the semiconducting properties.

### 4.1. Experimental

#### 4.1.1. Emission Spectra

The apparatus used to record photoluminescence spectra is illustrated in Fig. 4.1. The beam from a tunable argon laser passes through a filter (A), to remove plasma lines, and is focussed through a silica window in the cryostat onto the powdered sample which is pressed into a notch on the cold finger of the cryostat. From the sample the light is collected through a second window at right angles to the first and focussed by lens B onto the first monochromator slit. Before it reaches the slit it passes through a filter (D) selected so as to cut out the original laser line. Typical monochromator slit widths used were 0.05 - 0.25mm. The intensity of the monochromated light is measured by the photomultiplier tube using a Brookdeal 5C1 Photon Counter and displayed on the digital counter prior to output on the chart recorder. The laser can be tuned to emit light at

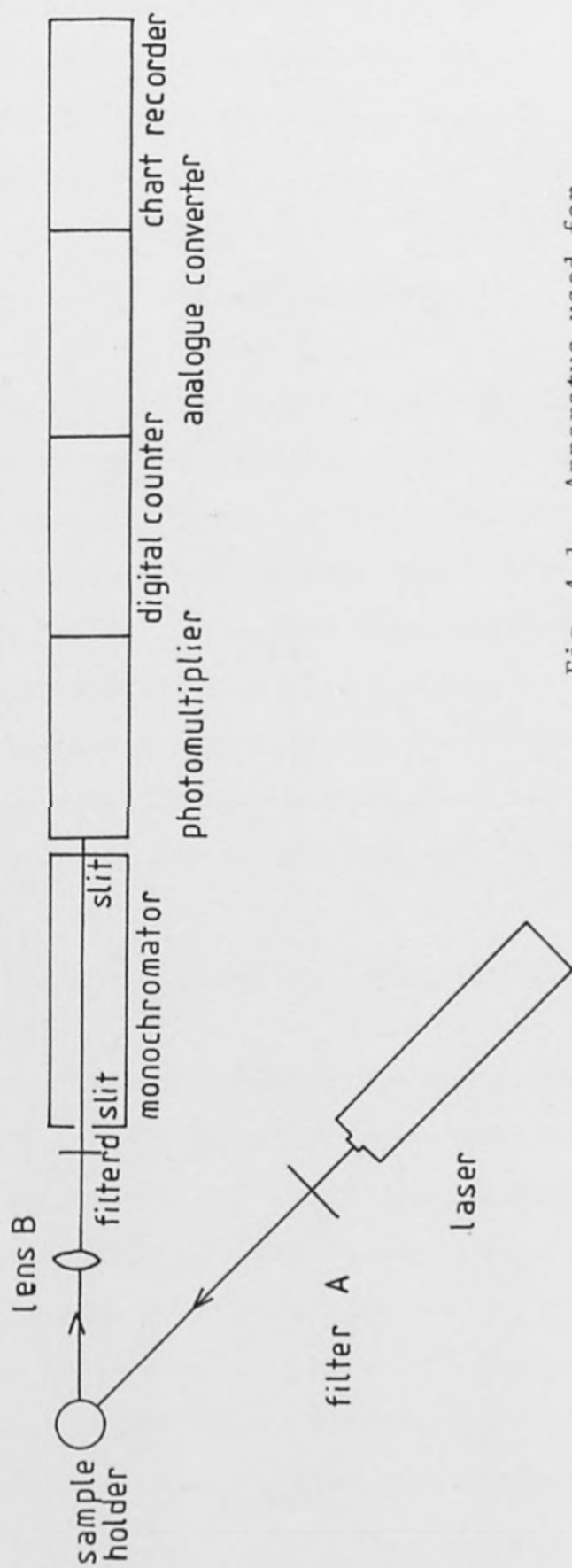


Fig. 4.1. Apparatus used for photoluminescence Spectroscopy

wavelengths between 457nm and 514nm with varying efficiency. The photomultiplier tube used for this work was a RCA C31034 GaAs photomultiplier tube, which has a linear response of up to 840nm.

#### 4.1.2.                    Absorption Spectra

The absorption spectra of powdered samples were determined at ambient temperature using a Perkin-Elmer-Hitachi Model EPS 3T visible spectrophotometer. (The finely powdered sample was supported between two glass slides which were placed in the beam of a tungsten lamp.) The range of wavelengths scanned was 340 - 700m $\mu$ .

Preliminary experiments were performed to determine whether the position of the absorption edge was affected by grain size or the amount of sample.

#### 4.1.3.                    Electrical Conductivity Measurements

Due to the difficulty in growing suitable single crystals, conductivity measurements were performed on powdered polycrystalline discs using a two probe technique. Approximately 0.5g of fresh finely ground, dry sample was placed in a 13mm stainless steel die and a pressure of 5 tonnes was applied for approximately 5 minutes. A good quality disc of about 2mm thickness resulted. To ensure good electrical contact silver paint was applied to both

sides of the disc, care being taken that there was no contact between the two layers of silver paint.

Electrical conductivity measurements were carried out immediately after preparation to minimise atmospheric contamination.

During the course of this work three devices were used to measure the electrical conductivity, namely a Vibron electrometer, a model B221 Wayne-Kerr bridge and a Keightley Model 616 digital multimeter.

a) Vibron electrometer circuit. The circuit diagram used in the conductivity measurements is shown in Fig 4.2.

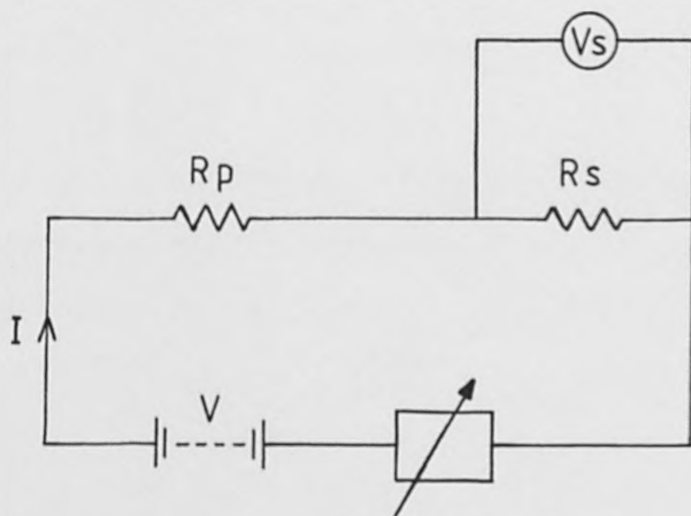


Fig. 4.2. Circuit for electrical conductivity measurements using a Vibron electrometer.

The pellet was connected in series with a set of standard resistors ( $R_s$ ) and a d.c. voltage ( $V$ ), supplied by a bank of dry cells, which could be varied by means of course and fine potentiometric controls. The voltage across the circuit was measured using an Avometer and the voltage drop across the standard resistors was measured using a Vibron Electrometer. To eliminate stray capacitance effects the complete circuit was contained in an earthed metal box. Applying Ohm's Law to the circuit, where  $I$  is the total current, and  $R_p$  is the resistance of the pellet, then:-

$$I = \frac{V}{R_s + R_p} = \frac{V_s}{R_s} \quad (4.1.)$$

therefore, 
$$R_p - R_s \frac{V}{V_s} - 1 \quad (4.2.)$$

A graph of  $V/R$  vs.  $V$  applied was plotted, and from the gradient, the resistance of the sample was calculated. Hence using the formula:-

$$\sigma = \frac{L}{AR_p} \quad (4.3.)$$

where  $L$  = thickness of the disc (cm)

$A$  = the area of contact between the pellet and the electrode, each electrode being 1cm in diameter.  
the conductivity was obtained.

b) Wayne-Kerr bridge (Model B221). This consists of two bridges, a resistive and capacitive bridge connected in parallel to balance out both resistive and capacitive effects induced in the sample. In addition, this technique unlike the other two, uses an a.c. voltage supply of 1000 Hz which overcomes certain difficulties in d.c. measurements. Among these are polarisation effects in ionic conductors and electrolytes, barriers at internal surfaces and contact resistances such as occur in powders, films and certain micellar structures such as selenium.

The a.c. bridge circuit is shown in Fig 4.3. Assuming that the sample is represented by a parallel combination of capacitance and resistance, the values of  $R_s$  and  $C_s$  obtained at balance then describe the unknown directly.

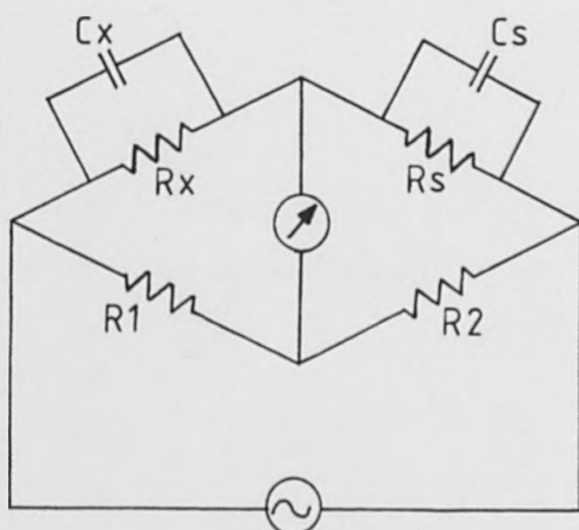


Fig. 4.3. Basic bridge circuit for obtaining equivalent parallel-connected capacitance and resistance.

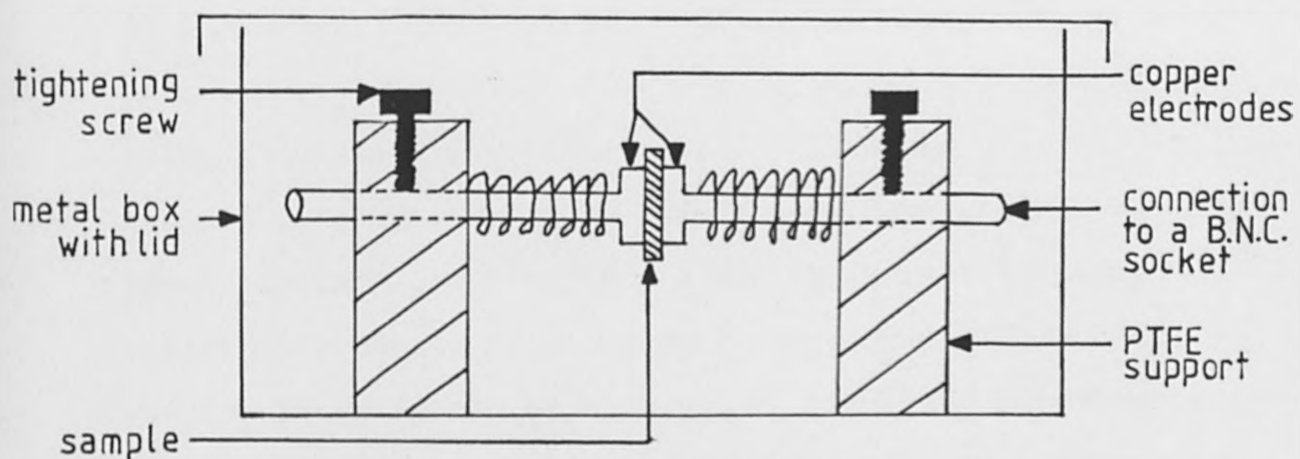


Fig. 4.4. The Sample holder for electrical conductivity measurements in cross section



The readings obtained are in reciprocal resistance (Mho), within the limits  $1 \times 10^{-2}$  to  $1 \times 10^{-5} \Omega$ , from which the conductivity can be calculated as above.

c) Keightley digital electrometer. Some of the electrical conductivity measurements were carried out on a Keightley Model 616 digital electrometer. This is essentially a digital multimeter optimized for measurements from high source impedance. For this application the meter was used in the Normal ohm measurement mode. In this mode the model 616 measures resistance over a wide range,  $1 \Omega$  to  $10^{14} \Omega$  using a constant current method. This means that the digital readout is proportional to the voltage developed across the input terminals, where  $V = I \times R$  (the current  $I$ , being selected in decade steps using a range switch). For the samples investigated in this study, which had resistances in the range  $10^4$  to  $10^{12} \Omega$ , the applied voltage was typically about 1V, as above this voltage dielectric breakdown occurred.

A direct reading of sample resistance was obtained by this method, from which the conductivity was calculated as previously.

In all these measurements the pelleted sample was held between spring loaded copper electrodes of 1cm diameter Fig 4.4. which were housed in an earthed metal box.

#### 4.1.4. Differential Thermal Analysis (DTA)

This is a technique which involves the heating and cooling of a test material and an inert reference sample

under identical conditions and recording any temperature differences that arises between them. The differential temperature is then plotted against either the temperature at some fixed point within the apparatus or time.

Any physical or chemical change which occurs within the test sample which involves the evolution of heat will cause its temperature to rise temporarily above that of the reference sample, giving rise to an exothermic peak on the DTA plot. Conversely a process which is accompanied by the absorption of heat will cause the temperature of the sample to lag behind that of the reference material leading to an endothermic peak. (Fig. 4.5.)

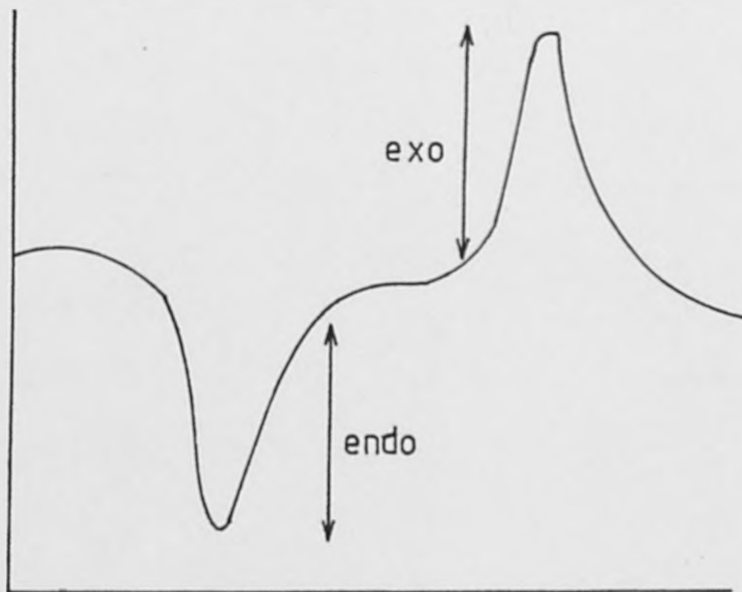


Fig. 4.5. Hypothetical DTA trace showing an endo and exothermic peak.

Transitions in which no heat is evolved or absorbed by the sample e.g. certain solid-state phase changes can also be studied by DTA. Since, even if no physical or chemical processes are occurring a small and steady differential temperature normally develops between test and reference material. This is due primarily to differences in the heat capacity and thermal conductivities of the two materials. The difference in the heat capacity of the sample before and after the transition has occurred will be reflected in a new steady differential temperature being established between the test and reference sample.

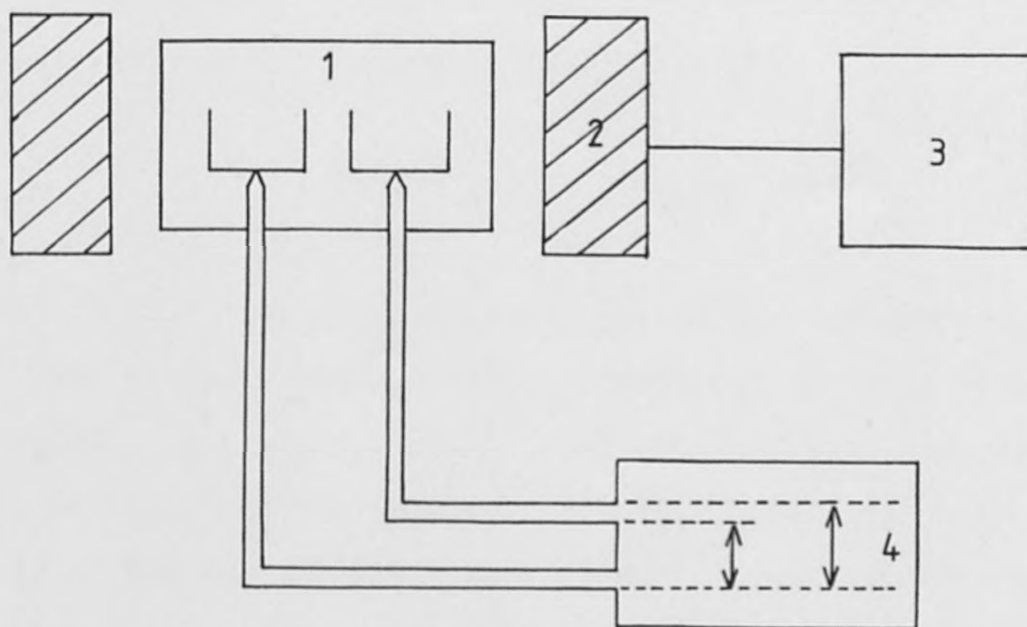


Fig. 4.6. Diagram of DTA Apparatus.

## Experimental

DTA studies in this work carried out using a Stanton Redcroft STA 780 simultaneous thermal analyser. Fig 4.6. shows a simplified diagram of the DTA apparatus.

- 1) Sample holder-measuring system. Samples are contained in crucibles which make contact with thermocouple junctions.
- 2) Furnace-heat source having a large temperature zone.
- 3) Temperature programmer - supplies energy to the furnace in such a manner to ensure a reproducible rate of change of temperature.
- 4) Recording system - For STA 780 this is a 4-pen chart recorder which records temperature, DTA, Thermogravimetry (TG - weight of sample (vs), temperature) and DTG (differential thermogravimetry).

### 4.2.

#### Simple Iodide Systems.

In this work the solid state properties of complex iodides of types such as  $\text{CsMI}_3$ ,  $\text{CsMI}_4$ ,  $\text{Cs}_2\text{NaMI}_6$  have been studied. It is well known<sup>(1)</sup> that many of these compounds are coloured and possess semiconducting properties but many of the main group iodides from which these complexes are prepared are themselves highly coloured, and little is known about their optical and electronic properties. For example,  $\text{SnI}_2$  is orange, yet it does not possess a colour centre<sup>(2)</sup>.

In order to understand the nature of the complex iodide systems a preliminary study was carried out on main group iodides of the types  $MI_1$ ,  $MI_2$ ,  $MI_3$  and  $MI_4$ . Recrystallised commercial samples were used where possible, while the less stable materials were prepared by standard methods<sup>(3)</sup>.

#### 4.2.1.                      Optical Properties

The absorption spectra were recorded for each of the samples listed in table 4.1. These spectra show changes in the optical band gap of the bulk material (transitions from the valence band to the conduction band). Various internal transitions were observed the relative intensities of which are governed by selection rules, but the fundamental absorption edge always dominates the spectra.

#### 4.2.2.                      Electrical Properties

The bulk electrical conductivities of the samples were recorded as described in Section 4.1.3. The effects of (a) contact material and (b) a.c. and d.c. measurements (using a Wayne-Kerr bridge and Keightley electrometer) on the measured electrical conductivities were also investigated (Table 4.2.).

It was not possible to make a.c. measurements on all samples as some of the resistances were outside the range

Sample	Colour	Half Edge (nm)	Energy Gap (eV + 0.03)
GeI <sub>2</sub>	Yellow	511	2.43
SnI <sub>2</sub>	Orange	560	2.21
PbI <sub>2</sub>	Yellow	531	2.34
GeI <sub>4</sub>	Orange	527	2.35
SnI <sub>4</sub>	Orange	525	2.36
AsI <sub>3</sub>	Red	553	2.24
SbI <sub>3</sub>	Red/Orange	573	2.16
BiI <sub>3</sub>	Black	690	1.79
TeI <sub>4</sub>	Grey/Black	674	1.84
TlI	Yellow	474	2.62
HgI <sub>2</sub>	Red	589	2.10

Table 4.1. Optical Data for various iodides.

Sample	Gold Leaf		Silver Loaded Paint		Tin Foil	
	AC	DC	AC	DC	AC	DC
Ge I <sub>2</sub>		4.89 x 10 <sup>-8</sup>		3.86 x 10 <sup>-8</sup>		7.92 x 10 <sup>-8</sup>
Sn I <sub>2</sub>			1.97 x 10 <sup>-7</sup>	1.94 x 10 <sup>-7</sup>		
Pb I <sub>2</sub>	4.61 x 10 <sup>-9</sup>	9.36 x 10 <sup>-10</sup>	4.16 x 10 <sup>-9</sup>	4.3 x 10 <sup>-10</sup>	7.18 x 10 <sup>-9</sup>	2.64 x 10 <sup>-9</sup>
Sn I <sub>4</sub>	8.63 x 10 <sup>-11</sup>	1.51 x 10 <sup>-10</sup>	1.04 x 10 <sup>-10</sup>	1.18 x 10 <sup>-10</sup>	1.2 x 10 <sup>-10</sup>	1.66 x 10 <sup>-9</sup>
Ge I <sub>4</sub>		1.38 x 10 <sup>-8</sup>		3.10 x 10 <sup>-8</sup>		1.28 x 10 <sup>-8</sup>
As I <sub>3</sub>		2.34 x 10 <sup>-8</sup>		5.25 x 10 <sup>-8</sup>		1.19 x 10 <sup>-8</sup>
Sb I <sub>3</sub>	7.13 x 10 <sup>-8</sup>	7.48 x 10 <sup>-11</sup>	9.95 x 10 <sup>-10</sup>	1.51 x 10 <sup>-9</sup>	1.65 x 10 <sup>-9</sup>	9.82 x 10 <sup>-11</sup>
Bi I <sub>3</sub>	8.91 x 10 <sup>-8</sup>	8.66 x 10 <sup>-8</sup>	7.48 x 10 <sup>-8</sup>	4.3 x 10 <sup>-8</sup>	3.63 x 10 <sup>-8</sup>	2.24 x 10 <sup>-11</sup>
Te I <sub>4</sub>		4 x 10 <sup>-5</sup>	5.88 x 10 <sup>-4</sup>	5.13 x 10 <sup>-4</sup>	4.86 x 10 <sup>-4</sup>	1.45 x 10 <sup>-4</sup>
TlI		3.89 x 10 <sup>-9</sup>		3.89 x 10 <sup>-9</sup>		3.51 x 10 <sup>-9</sup>
HgI <sub>2</sub>		7.2 x 10 <sup>-8</sup>		8.77 x 10 <sup>-7</sup>		7.92 x 10 <sup>-6</sup>

Table 4.2. Electrical Conductivity Data for Various Samples, Showing Effects of Contacts and a.c. and d.c. Measurements. ( $\Omega^{-1} \text{cm}^{-1}$ , at room temperature.)

of the Wayne-Kerr bridge. The data for those samples on which both a.c. and d.c. measurements were possible do not show any general trends. However, the absolute values of the conductivities measured by both methods are not necessarily the same. The effect of changing the contact material does, however, show some trends. Tin foil contacts produce the highest electrical conductivities in the Group IV metal 2+ iodides. While gold leaf proved to be the best contact for the Group V metal 3+ iodides.

#### 4.3. Caesium Lead Trihalides

The series of compounds of the general formula  $\text{CsPbX}_3$  ( $X = \text{F, Cl, Br, I}$ ) was first described by Wells<sup>(4)</sup> in a general survey of alkali-halide-lead systems.  $\text{CsPbF}_3$  has cubic perovskite structure at room temperature<sup>(5)</sup> whereas the chloride and bromide have this structure in their high temperature forms, above  $47^\circ\text{C}$  and  $133^\circ\text{C}$  respectively.<sup>(6)</sup> The low temperature forms of  $\text{CsPbCl}_3$  and  $\text{CsPbBr}_3$  are lone pair distorted and consequently have lower symmetry structures. The iodide forms a monoclinically distorted perovskite-like structure above  $308^\circ\text{C}$ <sup>(7)</sup>. Apart from the fluoride all  $\text{CsPbX}_3$  compounds are coloured at room temperature, the chloride being pale yellow, the bromide orange and the iodide yellow-green. Above the transition temperatures the colours change to yellow, red-orange and black respectively. The distortion of the structures of



the low temperature forms away from the cubic perovskite structure increases from the fluoride to the iodide, i.e. with increasing halide size. This suggest halide covalency is important at room temperature and that this prevents crystal field or direct population of solid state band effects.

In this section the variation in electrical properties and electronic spectra of  $\text{CsPbX}_3$  materials (X = Cl, Br or I) prepared from molten and aqueous systems are reported.

#### 4.3.1.                      Preparation

Although complicated by the low solubility of  $\text{PbX}_2$ , preparations of lead phases from aqueous solution are well known<sup>(6)</sup>. However the compounds formed are usually contaminated<sup>(8)</sup>. The materials discussed in this section were prepared from molten and aqueous systems containing the appropriate stoichiometric ratios of the starting materials. The  $\text{PbX}_2$  moiety was recrystallised from water prior to the preparation to enhance purity. The phases were identified and checked for purity by comparison of their x-ray powder diffraction data with those obtained by Møller<sup>(6,8)</sup>.

#### 4.3.2.                      Optical Properties

It has long been known that inorganic lead compounds luminesce<sup>(9,10,11)</sup>. Several bands have been reported in

the emission spectra of  $\text{PbX}_2$  ( $X = \text{Cl}, \text{Br}$  or  $\text{F}$ ) and attributed to transitions between the localised levels of the  $\text{Pb}^{2+}$  ion, although in the literature there is considerable variation in the reported energies of the emission bands. More recently, the luminescence of  $\text{CsPbCl}_3$  single crystals have been studied<sup>(12)</sup> and the observed transitions attributed to the same mechanism as that observed in  $\text{PbCl}_2$  crystals<sup>(11)</sup> i.e. the  $6s^2 - 6s^1p^1$  transition of the lead ion.

The photoluminescence and reflectance spectra of the caesium trihaloplumbates were obtained as described earlier. (Table 4.3.) No emission was observed for the chloride but the bromide and iodide displayed very sharp, very intense bands. At 80K  $\text{CsPbBr}_3$  samples prepared from the melt have a main emission line at 2.32 eV (half width 0.03eV) often with a shoulder, while samples prepared from solution show a single broad line at 2.33eV. Similar results were obtained for  $\text{CsPbI}_3$  at 80K, the main emission line of the fused sample being at 1.73eV, and at 1.75eV for the sample prepared from solution. The  $\text{CsPbCl}_3$  emission band lies outside the range of the apparatus used and could not be observed in this work, but the emission maximum reported by Belikovich et al<sup>(12)</sup> is included in Table 4.3. and used in subsequent discussion.

		Emission Maximum (eV $\pm$ 0.03)	Absorption Edge (eV $\pm$ 0.03)
CsPbCl <sub>3</sub>	(melt)	2.96 <sup>(12)</sup>	2.93
CsPbCl <sub>3</sub>	(aq)	----	2.95
CsPbBr <sub>3</sub>	(melt)	2.32	2.29
CsPbBr <sub>3</sub>	(aq)	2.33	2.27
CsPbI <sub>3</sub>	(melt)	1.73	2.76
CsPbI <sub>3</sub>	(aq)	1.75	2.72

Table 4.3. Electronic spectra of caesium trihaloplumbates.

The shape of the emission bands are similar to those assigned to  $6s^2 - 6s^1p^1$  atomic lead transitions<sup>(13)</sup>. However the caesium trihaloplumbates have absorption edges, rather than bands, which is more characteristic of direct band to band transitions. It should be noted that in contrast to the chloride and bromide, the emission and absorption features of the iodide occur at very different energies.

#### 4.3.3.

#### Electrical Conductivity

A study was made into the effects of the contact material on electrical conductivity measurements of the fused samples. In this investigation resistivity measurements were made on a Wayne-Kerr bridge, as this is more accurate than the Vibron Electrometer circuit. The a.c. current at 1000Hz used in the Wayne-Kerr bridge helps to reduce capacitive effects and ionic conduction in the sample is minimised.

Due to the difficulties in growing suitable single crystals electrical conductivity measurements were carried out on pelleted, polycrystalline samples, using the two probe technique described previously<sup>(14)</sup>. The results of this study are listed in Table 4.4. For  $\text{CsPbCl}_3$ , tin foil contacts proved to be the most effective, whilst gold leaf was the best contact material for the bromide and iodide. The results obtained with, gold leaf, silver loaded paint, tin foil and indium metal contacts were all within a half order of magnitude, whilst the conductivities obtained with aluminium foil, solder and no contact were usually lower by at least a factor of ten.

#### 4.3.4.

#### Photoconductivity Measurements

The band gap measurements of the previous sections suggest that the optical and electrical properties of the

Contact	Conductivity ( $\Omega^{-1} \text{ cm}^{-1}$ )		
	CsPbCl <sub>3</sub>	CsPbBr <sub>3</sub>	CsPbI <sub>3</sub>
Gold Leaf	$3.00 \times 10^{-9}$	$2.63 \times 10^{-8}$	$1.68 \times 10^{-8}$
Silver loaded paint	$3.2 \times 10^{-9}$	$8.25 \times 10^{-9}$	$5.08 \times 10^{-9}$
Tin foil	$1.83 \times 10^{-9}$	$3.77 \times 10^{-9}$	$9.99 \times 10^{-9}$
Indium metal	$2.95 \times 10^{-9}$	$6.57 \times 10^{-9}$	$1.03 \times 10^{-9}$
Aluminium foil	$5.68 \times 10^{-10}$	$2.56 \times 10^{-9}$	$1.19 \times 10^{-10}$
Solder*	_____	_____	$4.24 \times 10^{-13}$
no contact	$7.54 \times 10^{-11}$	$3.13 \times 10^{-10}$	$7.8 \times 10^{-10}$

Table 4.4. Conductivity Data for Fused Caesium Trihaloplumbates.

\*Difficulty in making solder adhere to the surface of the discs.

caesium trihaloplumbates arise from the same process. If this is the case they should exhibit photoconductivity when illuminated by radiation of energy equal to or greater than the width of the forbidden band.

Møller<sup>(15)</sup> has reported that the perovskite phases of the caesium trihaloplumbates are photoconducting with maximum sensitivity for CsPbCl<sub>3</sub> in the violet, CsPbBr<sub>3</sub> in the blue-green and CsPbI<sub>3</sub> in the red i.e. in the regions of their absorption edges.

The samples were all tested for photoconductivity using the apparatus described in Chapter 3.2. The method of sample preparation which proved most successful for the caesium trihaloplumbates was to use a pelleted sample in conjunction with the B.N.C. sample holder<sup>(16)</sup>. Old and new samples of CsPbCl<sub>3</sub> were prepared and tested for photoconductivity (Fig 4.7). The maxima and half-edges shifted to lower energies (Table 4.5) with ageing. The energy gap, as determined by photoconductivity, is the same gap as that associated with the optical properties. Therefore the optical absorption edge must arise from a direct band to band transition.

The effect of varying the monochromator slit width was investigated using CsPbBr<sub>3</sub>, which also gave a positive photoconductive response. It was found that the magnitude of the response decreased as the slit width was narrowed (Fig 4.7'). The fact that CsPbBr<sub>3</sub> exhibits photoconductivity is evidence for a direct transition mechanism. Although of

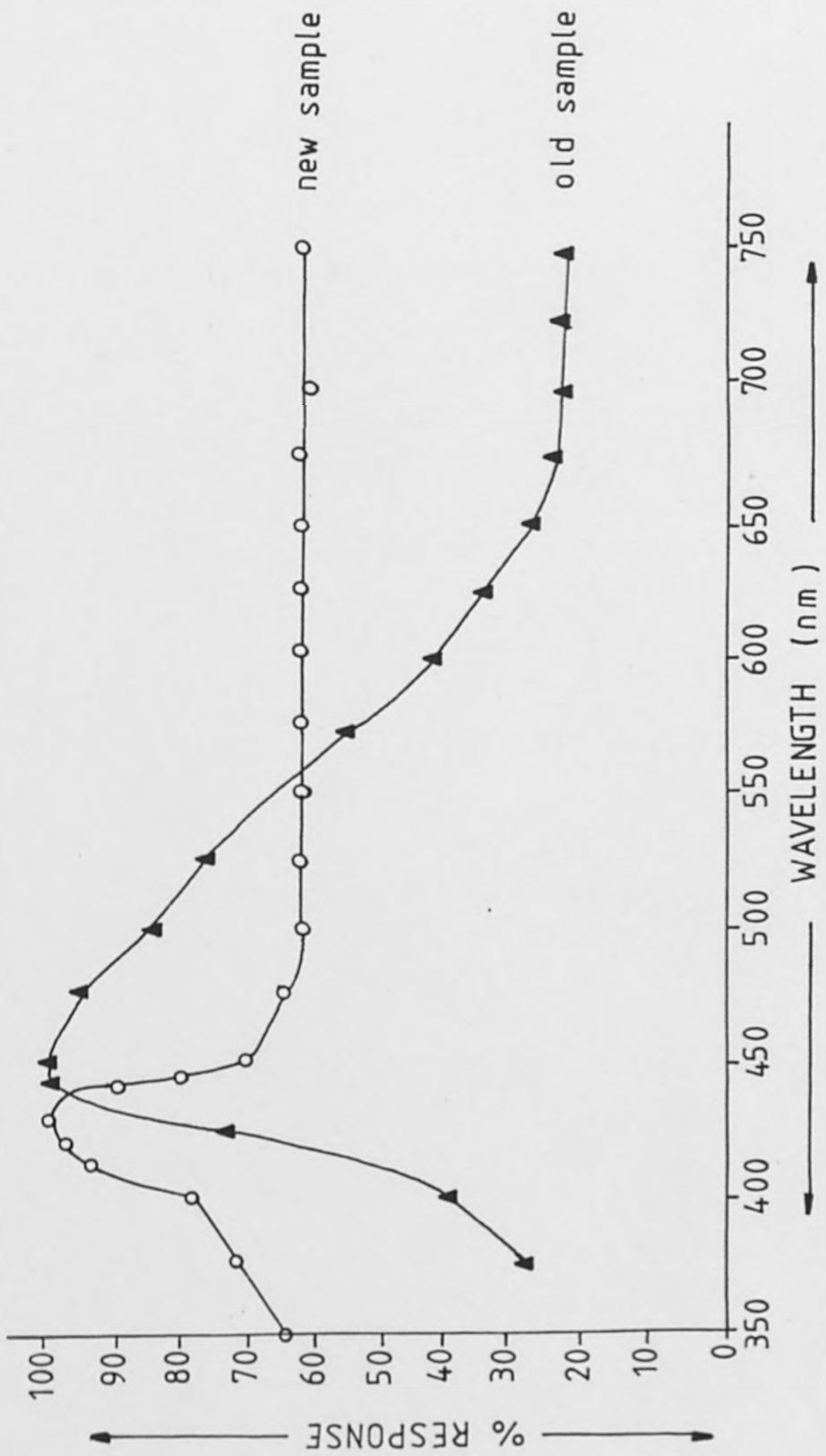


Fig. 4.7. Photoconductivity spectra of CsPbCl<sub>3</sub>

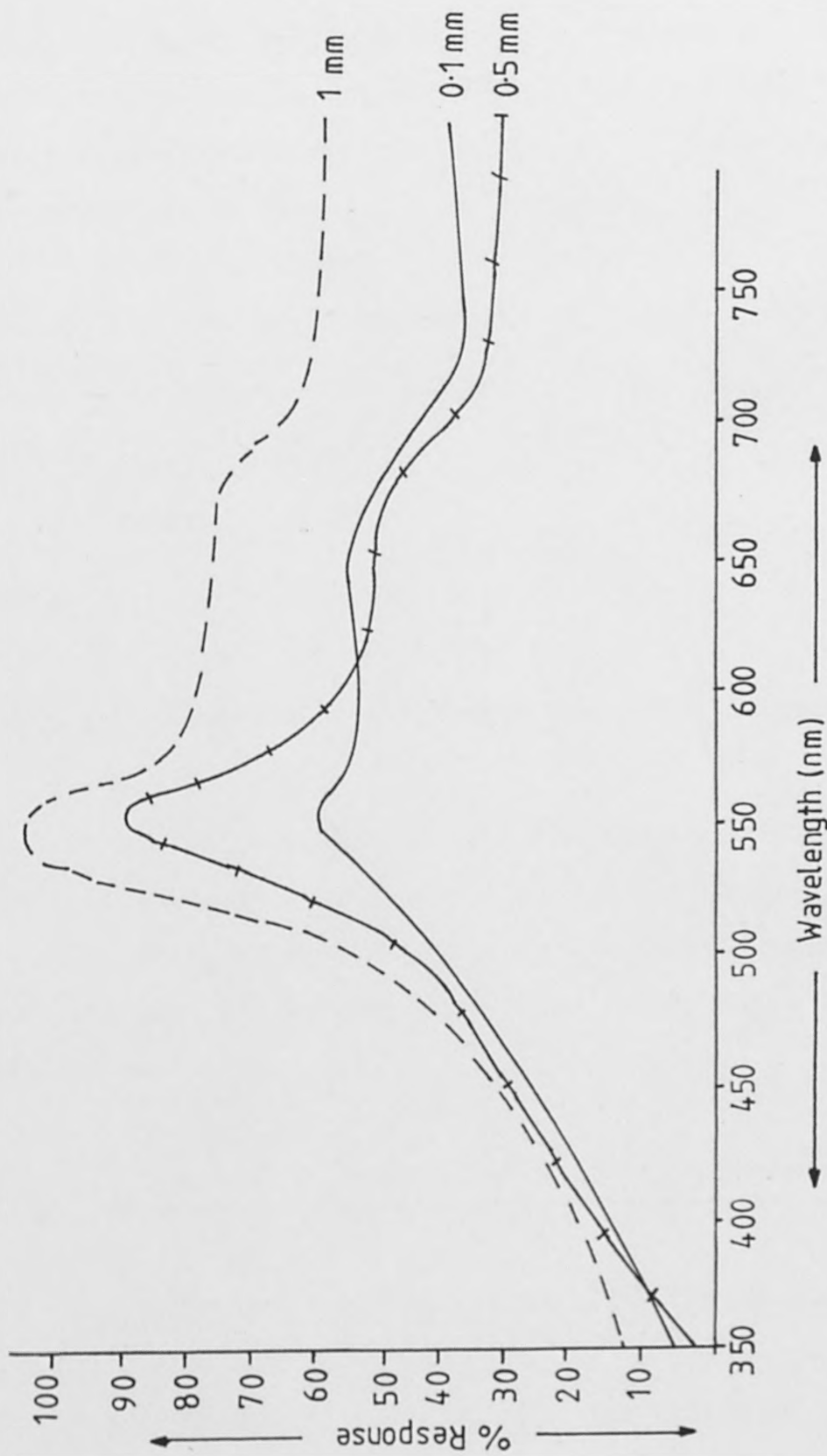


Fig. 4.7. Photoconductivity spectra of  $\text{CsPbBr}_3$ , using various monochromator slit widths.



lower energy (2.12eV) the band gap determined by photoconductivity is close enough to that (2.29eV) associated with the optical properties to assume that both properties arise from the same transition.

Sample	Maximum Response (eV $\pm$ .5)	Half Edge (eV $\pm$ .5)	Absorption Edge (eV $\pm$ 0.03)
CsPbCl <sub>3</sub> (new)	2.88	2.79	2.93
(old)	2.79	2.25	—
CsPbBr <sub>3</sub>	2.12	2.10	2.29

Table 4.5. Photoconductivity data for CsPbX<sub>3</sub> phases.

It was not possible to obtain a result for CsPbI<sub>3</sub> due to the energy output of the lamp below 600nm.

The positive results obtained for CsPbCl<sub>3</sub> and CsPbBr<sub>3</sub> indicate that the optical properties arise from a direct band-to-band transition.

#### 4.4. A Comparative Study of A<sup>1</sup><sub>2</sub>A<sup>1</sup>B<sup>III</sup>X<sub>6</sub> Compounds

The compounds investigated in this part of the work are halides of the type A<sub>2</sub>A<sup>1</sup>B<sup>III</sup>X<sub>6</sub> (A<sup>1</sup> = alkali metal; B<sup>III</sup> = As, Sb, Bi; X = Cl, Br, I). The chlorides and bromides are well characterised and in general have structures related to that of perovskite (BaTiO<sub>3</sub>). They

also tend to be coloured compounds and to have semiconductor properties. The iodides are less well known and have been little investigated. In this section a comparative study of  $A_2^1A^1B^{III}X_6$  compounds is made, with emphasis being placed on the effect of the halide on the observed properties.

#### 4.4.1. Preparation and Analysis

The simplest technique for preparing  $Cs_2NaMCl_6$  is to evaporate to dryness a hot aqueous  $MCl$  solution of the appropriate cations. This procedure has been found successful for the heavy lanthanides and for several other trivalent metals, including antimony<sup>(17)</sup> but the X-ray powder diffraction data of compounds prepared by this method show lines due to  $CsCl$ ,  $NaCl$  and other unidentified phases, which renders the technique unsuitable for the preparation of reproducibly pure phases. Consequently, the complexes were prepared by the method of Robinson<sup>(18)</sup>, this method involves maintaining the ratios of  $0.02M CsX (RbX):0.01MNaX:0.01M MX_3$ , in the appropriate  $2M$  mineral acid ( $HX$ ). By redissolving the precipitate obtained from this reaction in the mother liquor, and cooling the resulting solution slowly it was possible to obtain crystals of the chloride and bromide complexes. The iodide precipitates, however, could not be redissolved in the mother liquor, or in a variety of organic and inorganic solvents so remained as powders.

The colours of the complexes showed a marked alteration

Compound	% Halide	% Arsenic	% Antimony	% Bismuth	% Sodium	Colour
$Cs_2NaAsCl_6$	37.0 (36.90)	13.0 (12.99)			(3.99)	white platelets
$Cs_2NaSbCl_6$	33.90 (34.12)		19.5 (19.54)		1.25 (3.69)	white platelets
$Cs_2NaBiCl_6$	28.8 (29.93)			29.7 (29.41)	3.09 (3.22)	white platelets
$Rb_2NaAsCl_6$	44.7 (44.17)	15.48 (15.54)			4.53(4.77)	white cubes
$Rb_2NaSbCl_6$	39.9 (40.25)		13.7 (13.68)		3.75 (4.35)	white needles
$Rb_2NaBiCl_6$	33.9 (34.55)			33.3(33.95)	3.62 (3.73)	white platelets
.....						
$Cs_2NaAsBr_6$	56.50 (56.86)	8.9 (8.88)			1.50 (2.72)	ochre platelets
$Cs_2NaSbBr_6$	52.0 (53.87)		23.0 (23.04)		2.16 (2.58)	green-yellow platelets
$Cs_2NaBiBr_6$	48.6 (49.06)			21.4 (21.39)	2.00 (2.35)	yellow platelets
$Rb_2NaAsBr_6$	63.50 (64.07)	10.0 (10.01)			2.98 (3.06)	yellow platelets
$Rb_2NaSbBr_6$	59.8 (60.29)		15.3 (15.31)		1.50 (2.89)	yellow platelets
$Rb_2NaBiBr_6$	54.3 (54.33)			23.6 (23.68)	2.75 (2.61)	yellow platelets
.....						
$Cs_2NaAsI_6$	67.7. (67.65)	6.54 (6.66)			1.93 (2.04)	red powder
$Cs_2NaSbI_6$	64.9 (64.97)		9.55 (10.38)		1.81 (1.96)	orange powder
$Cs_2NaBiI_6$	60.4 (60.47)			16.61 (16.59)	1.91 (1.83)	crimson powder
$Rb_2NaAsI_6$	74.0 (73.81)	7.33 (7.28)			2.17 (2.23)	red powder
$Rb_2NaSbI_6$	70.6 (70.69)		11.32 (11.30)		0.80 (2.13)	red platelets
$Rb_2NaBiI_6$	65.5 (65.39)			17.99 (17.95)	2.15 (1.97)	red platelets

Table 4.6. Analytical Data for  $M_2 Na M^I M^{III} X_6$  Compound.

over the series Cl→Br→I. The chlorides were all white, the bromides yellow and the iodides red. This observation may be attributed to the increasing size of the halide ( $\text{Cl}^- = 1.81\text{\AA}$ ,  $\text{Br}^- = 1.96\text{\AA}$ ,  $\text{I}^- = 2.20\text{\AA}$ ) facilitating the transition of electrons between metal and or halide bands due to increased overlap.

The complexes were analysed as follows:- halide by potentiometric titration with 0.01M  $\text{AgNO}_3$ : antimony and arsenic by titration against 0.01N  $\text{KBrO}_3$  using methyl red indicator: bismuth by titration against 0.05M EDTA using xylenol orange indicator: and sodium by atomic absorption spectroscopy. The correlation between the experimental and theoretical percentages (Table 4.6) of the constituents shows that,  $\text{Cs}_2\text{NaMX}_6$  and not the related  $\text{Cs}_2\text{NaM}_2\text{X}_9$  has been formed and that the products are not hydrated.

#### 4.4.2.

#### X-ray Analysis

It has been suggested that in halide complexes of the type  $\text{Cs}_2\text{NaMCl}_6$  ( $\text{M} = \text{Sb}$  or  $\text{Bi}$ ) the p-block element is in a regular octahedral site.<sup>(18)</sup> The octahedral symmetry of  $\text{BiCl}_6^{3-}$  and  $\text{SbCl}_6^{3-}$  has been attributed to two mechanisms viz: (1) donation of  $ns^2$  electrons into a conduction band (2) shielding of the s-electrons by f- and d- electrons in the inner shell.

X-ray powder diffractograms were run for each sample.  $\text{Cs}_2\text{NaBiCl}_6$ ,  $\text{Cs}_2\text{NaSbCl}_6$ ,  $\text{Cs}_2\text{NaBiBr}_6$ ,  $\text{Cs}_2\text{NaSbBr}_6$  and  $\text{Cs}_2\text{NaAsBr}_6$

<u>hkl</u>	<u>Cs<sub>2</sub>NaBiCl<sub>6</sub></u>		<u>Cs<sub>2</sub>NaSbCl<sub>6</sub></u>	
	<u>d(Å)</u>	<u>I/I<sup>0</sup></u>	<u>d(Å)</u>	<u>I/I<sup>0</sup></u>
111	6.194	3		
200	5.373	8	5.357	5
220	3.794	100	3.770	100
221	3.583	3		
310	3.402	2		
311	3.243	5		
222	3.100	5	3.090	33
400	2.687	39	2.675	51
410	2.611	3		
331	2.468	19	2.452	13
422	2.196	46	2.184	36
511	2.072	13	2.058	9
440	1.903	37	1.892	34
531	1.819	5	1.804	3
620	1.703	10	1.692	11
622			1.612	6
444	1.554	7	1.550	7

Peaks not assigned Miller Indices

6.559	3	6.511	7
5.887	6	5.829	4
5.609	8	5.574	4
4.809	3	4.771	2
4.647	3	4.623	4
4.231	3		
4.133	3		
3.961	4		
3.192	2		
3.176	2		
2.536	3		
2.310	7	2.260	15
1.752	4	1.743	3
1.674	4		

$$a_0 = 10.74 \text{ \AA}$$

$$a_0 = 10.66 \text{ \AA}$$

Fig. 4.7. X-Ray Data for Cs<sub>2</sub>NaMX<sub>6</sub>. (M= Bi, Sb, As)

hkl	$\text{Cs}_2\text{NaBiBr}_6$		$\text{Cs}_2\text{NaSbBr}_6$		$\text{Cs}_2\text{NaAsBr}_6$	
	d(Å)	I/I <sup>o</sup>	d(Å)	I/I <sup>o</sup>	d(Å)	I/I <sup>o</sup>
100	_____		_____		9.46	7
110	_____		_____		6.66	4
111	_____		_____		5.44	6
200	5.681	25*	5.736	6	4.71	4
210	_____		_____		3.84	33
220	4.022	65*	4.013	28	_____	
221	_____		_____		3.13	100
222	3.291	80	3.267	100	2.711	97
330	_____		_____		2.23	18
331	2.615	2	_____		_____	
332	_____		_____		2.006	3
400	2.832	100*	2.823	54	_____	
420	2.532	8	2.529	2	_____	
422	2.324	45	2.304	16	_____	
521	2.076	2	_____		_____	
440	2.006	58	1.994	38	_____	
522	1.975	10	_____		_____	
600	1.899	2	_____		_____	
622	1.714	9	1.697	13	_____	
444	1.645	19	1.625	20	_____	
700	1.629	7	_____		_____	
711	1.600	8	1.575	4	_____	
642	1.510	3	1.502	4	_____	
731	1.484	3	_____		_____	

Peaks not assigned Miller Indices

10.05	15	9.07	4
6.94	7	7.03	3
4.96	25	4.96	7
3.71	3	_____	
3.46	2	_____	
3.26	31	_____	
3.11	11	3.11	4
2.97	17	2.96	2
2.38	7	2.38	1
2.30	15	_____	
2.05	4	2.09	1
1.88	3	_____	
1.77	8	_____	
1.70	4	_____	
1.59	1	_____	

$$a_o = 11.36 \text{ \AA}$$

$$a_o = 11.25 \text{ \AA}$$

$$a_o = 9.40 \text{ \AA}$$

Fig. 4.7. (Contd).

$\text{Rb}_2\text{NaBiCl}_6$ ,  $\text{Rb}_2\text{NaSbCl}_6$ ,  $\text{Rb}_2\text{NaBiBr}_6$  and  $\text{Rb}_2\text{NaSbBr}_6$  all have similar structures, however they are not cubic and consequently none of the d-spacings will be assigned Miller indices.

$\text{Rb}_2\text{NaBiCl}_6$		$\text{Rb}_2\text{NaSbCl}_6$		$\text{Rb}_2\text{NaBiBr}_6$		$\text{Rb}_2\text{NaSbBr}_6$	
d(Å)	I/I <sup>0</sup>	d(Å)	I/I <sup>0</sup>	d(Å)	I/I <sup>0</sup>	d(Å)	I/I <sup>0</sup>
6.916	1	8.547	2	7.226	12	8.980	5
6.657	1	6.349	28	6.998	14	6.708	15
6.394	10	6.026	14	6.682	36		
6.067	7	5.681	11	6.371	70	6.371	16
5.754	1	5.574	7	5.966	19	5.946	26
5.373	2	5.141	3	5.609	30	5.505	36
4.251	3	4.271	7	5.341	9		
4.105	10	4.231	9	4.720	9	4.928	7
3.987	2	4.022	2	4.281	51	4.077	33
3.786	11	3.901	60	3.952	39	3.943	25
3.619	3	3.731	100	3.786	20	3.74	25
3.548	4	3.569	34	3.747	10	3.56	26
3.434	3	3.279	3	3.963	9	3.664	8
3.327	1	3.226	5	3.619	20	3.267	41
3.255	1	3.105	20	3.493	19	3.303	19
3.221	1	3.108	2	3.395	14	3.074	19
3.176	1	2.969	4	3.327	17	2.974	49
2.989	4	2.806	20	3.243	11	2.832	100
2.969	1	2.699	78	3.090	50	2.763	27
2.854	6	2.578	28	2.989	100	2.707	51
2.832	2	2.522	4	2.950	39	2.641	19
2.715	2	2.442	15	2.823	41	2.543	85
2.667	8	2.284	4	2.806	81	2.295	19
2.600	2	2.186	34	2.743	20	2.271	22
2.543	100	2.154	37	2.667	71	2.222	79
2.508	2	2.047	11	2.629	26	2.159	8
2.488	2	2.015	12	2.585	14	2.118	16
2.442	1	1.953	6	2.582	11	2.036	16
2.393	1	1.922	2	2.502	14	2.000	7
2.356	1	1.890	19	2.452	9	1.965	22
2.293	3	1.859	15	2.411	24	1.936	11
2.254	3	1.824	5	2.362	44	1.916	11
2.207	3	1.788	5	2.301	14	1.899	11
2.156	2	1.731	6	2.268	29		
2.125	9	1.687	6	2.217	49		
2.045	1	1.595	10	2.144	14		
2.023	3			2.118	14		
2.004	1			2.081	9		
1.937	2			2.045	20		

Fig. 4.8. X-Ray Data  $\text{Rb}_2\text{NaMX}_6$ .

<u>Rb<sub>2</sub>NaBiCl<sub>6</sub></u>		<u>Rb<sub>2</sub>NaSbCl<sub>6</sub></u>		<u>Rb<sub>2</sub>NaBiBr<sub>6</sub></u>		<u>Rb<sub>2</sub>NaSbBr<sub>6</sub></u>	
<u>d(Å)</u>	<u>I/I<sup>0</sup></u>	<u>d(Å)</u>	<u>I/I<sup>0</sup></u>	<u>d(Å)</u>	<u>I/I<sup>0</sup></u>	<u>d(Å)</u>	<u>I/I<sup>0</sup></u>
1.918	3			2.023	11		
1.892	5			1.973	26		
1.856	1			1.953	14		
1.812	1			1.933	46		
1.762	1			1.909	14		
				1.892	11		
				1.838	50		

Fig. 4.8. (Contd).



were found to be isostructural. The x-ray data for these compounds was indexed on an Fm3m space group (Table 4.7) using the computer programmes POWDER and POWREF. The materials were found to contain lines which could not be identified, however they were not due to the starting materials or  $\text{Cs}_2\text{NaM}_2\text{X}_9$ . It is possible to form a whole series of similar compounds which vary slightly in the proportion of halogen, it may be that such compounds are the cause of the unaccounted lines.

$\text{Rb}_2\text{NaBiCl}_6$ ,  $\text{Rb}_2\text{NaSbCl}_6$ ,  $\text{Rb}_2\text{NaBiBr}_6$  and  $\text{Rb}_2\text{NaSbBr}_6$  are isostructural, but do not have the same structure as their caesium analogues i.e. they are not cubic. (Table 4.8) The smaller size of the rubidium ion,  $1.47\text{\AA}$  compared with  $1.67\text{\AA}$  for caesium, might be expected to result in distortions from cubic symmetry.

The caesium/iodide complexes are neither hexagonal nor cubic but are isostructural. The rubidium phases crystallise with a different lattice to that of the caesium derivatives.

The x-ray powder diffraction data show that as the size of the halide ion increases the lattice expands and the amount of distortion is increased.

#### 4.4.3.

#### Thermal Analysis

No phase changes were observed for any of the phases within the temperature range  $-50^\circ\text{C}$  to  $+400^\circ\text{C}$ .

To investigate the decomposition of  $\text{Cs}_2\text{NaSbI}_6$  a

thermogravimetric study was performed using the Stanton Redcroft STA 780 simultaneous thermal analyser. Approximately 1g of sample was heated to constant weight at 400°C. The sample chamber was flushed with a fast flow of nitrogen so that any vapourised decomposition products could be collected. X-ray powder diffractograms, reflectance spectra and electrical conductivity measurements were carried out on the residue and decomposition product(s).

The only product lost on heating had the appearance of  $\text{SbI}_3$  (red-hexagonal platelets) and was identified as such by its x-ray powder data.

The residue, which was red, did not give a purple solution on addition of carbon tetrachloride. This indicated there was no free or loosely associated iodine. Since the x-ray data (Table 4.9) show no trace of  $\text{SbI}_3$ , and this was the only decomposition product, the residue must contain  $\text{CsI}$ ,  $\text{NaI}$  and possibly some iodine. The red colour of the residue could not be explained if only  $\text{CsI}$  and  $\text{NaI}$  were present. Hydrochloric acid and one drop of carbon tetrachloride were added to the residue. The acid dissolved the  $\text{CsI}$  and  $\text{NaI}$  present, thus liberating iodine which gave a purple colouring with carbon tetrachloride.

The x-ray data, reflectance spectra and electrical conductivity of the decomposition product are not consistent with it being a heterogenous phase, and it must therefore be concluded that the decomposition leads to a new distinct phase.

Residue	$SbI_3$		$Cs_2NaSbI_6$	
---------	---------	--	---------------	--

X-ray Data.

	d	I/I <sup>0</sup>	d	I/I <sup>0</sup>	d	I/I <sup>0</sup>
	7.255	5	8.934	4	6.86	40
	5.946	11.6	6.916	40.4	4.25	27
	4.220	10.7	5.810	2	4.19	7
(NaI)	3.739	2	5.309	2	3.63	35
	3.648	3	4.796	2	3.58	76
	3.440	99	3.900	2.5	3.46	78
(CsI,NaI)	3.226	66	3.786	2	3.427	100
	2.988	100	3.466	100	3.27	15
	2.862	2.5	3.302	17	3.218	99
	2.763	2.5	2.557	13	2.981	94
	2.671	7	2.429	6	2.767	11
	2.374	8	2.327	26	2.743	69
(CsI,NaI)	2.281	10	2.161	2.4	2.718	26
	2.196	2	1.977	10	2.683	17
	2.108	45	1.828	6	2.423	6
	2.019	2.5	1.807	5	2.309	13
	1.890	2	1.743	55.4	2.293	11
(CsI,NaI)	1.863	19	1.583	5	2.123	26
	1.796	21	1.561	3	2.090	57
	1.746	2	1.460	4	1.959	29
	1.719	11			1.955	7
(CsI,NaI)	1.614	6			1.814	7
	1.575	3			1.795	7
	1.542	2			1.789	17
	1.526	3			1.755	18
	1.491	6			1.710	12
(CsI,NaI)	1.444	7			1.663	10

<u>Reflectance Spectra</u>	band gap/eV $\pm$ 0.03
1.97	2.13
	2.18

<u>Electrical Conductivity</u>	$\sigma / \Omega^{-1} \text{ cm}^{-1}$
$1.05 \times 10^{-10}$	$1.51 \times 10^{-9}$
	$1.24 \times 10^{-3}$

Table 4.9. X-ray diffraction reflectance spectra and electrical conductivity data for  $Cs_2NaSbI_6$  thermogravimetric study.

The absorption spectra of the samples were determined by a reflection method (Fig 4.8), using a Perkin-Elmer Model 157 U.V./visible spectrometer. The samples were supported, by vaseline on the underside of a glass slide positioned over an aluminised mirror assembly. This allowed the incident beam to be collected and reflected into the photocell. A beam attenuator was used to reduce the intensity of the second reference beam. The range of wavelengths scanned was 200-750 nm. Preliminary experiments were performed to determine whether the position of the absorption edge was affected by the attenuation of the reference beam, the grain size or the amount of sample.

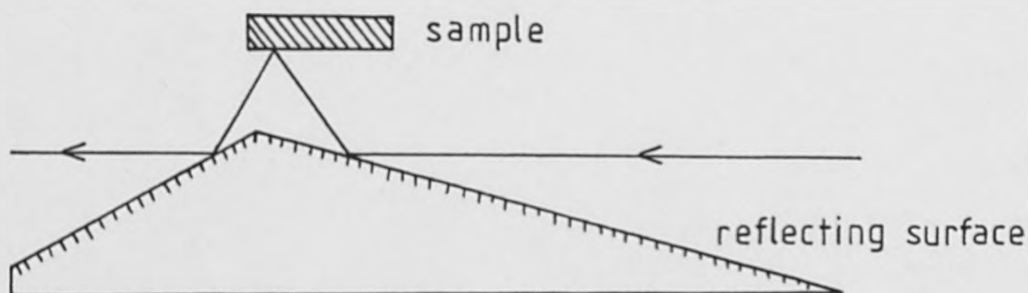


Fig. 4.8. Geometry of the Reflectance Mirror Assembly.

None of the chlorides gave an absorption edge either in the visible or U.V. region of the spectrum.

A single sharp absorption edge, in the fundamental

Compound	Optical Energy Gap (RT) eV $\pm$ 0.03	Band Maxima 80K eV $\pm$ 0.01	Band Edge 80K eV $\pm$ 0.01
$\text{Cs}_2\text{NaBiCl}_6$	—	1.68	1.70
$\text{Cs}_2\text{NaAsBr}_6$	2.41	—	—
$\text{Cs}_2\text{NaSbBr}_6$	2.44	—	—
$\text{Cs}_2\text{NaBiBr}_6$	2.52	1.58	1.74
$\text{Rb}_2\text{NaAsBr}_6$	2.46	—	—
$\text{Rb}_2\text{NaSbBr}_6$	2.52	—	—
$\text{Rb}_2\text{NaBiBr}_6$	2.61	1.89	2.00
$\text{Cs}_2\text{NaAsI}_6$	1.96	—	—
$\text{Cs}_2\text{NaSbI}_6$	2.18	—	—
$\text{Cs}_2\text{NaBiI}_6$	2.07	—	—
$\text{Rb}_2\text{NaAsI}_6$	1.82	—	—
$\text{Rb}_2\text{NaSbI}_6$	1.93	1.93	2.04
$\text{Rb}_2\text{NaBiI}_6$	2.09	—	—

Table 4.10. Absorption and Emission Data for  $\text{M}_2\text{NaM}^{\text{III}}\text{X}_6$ .

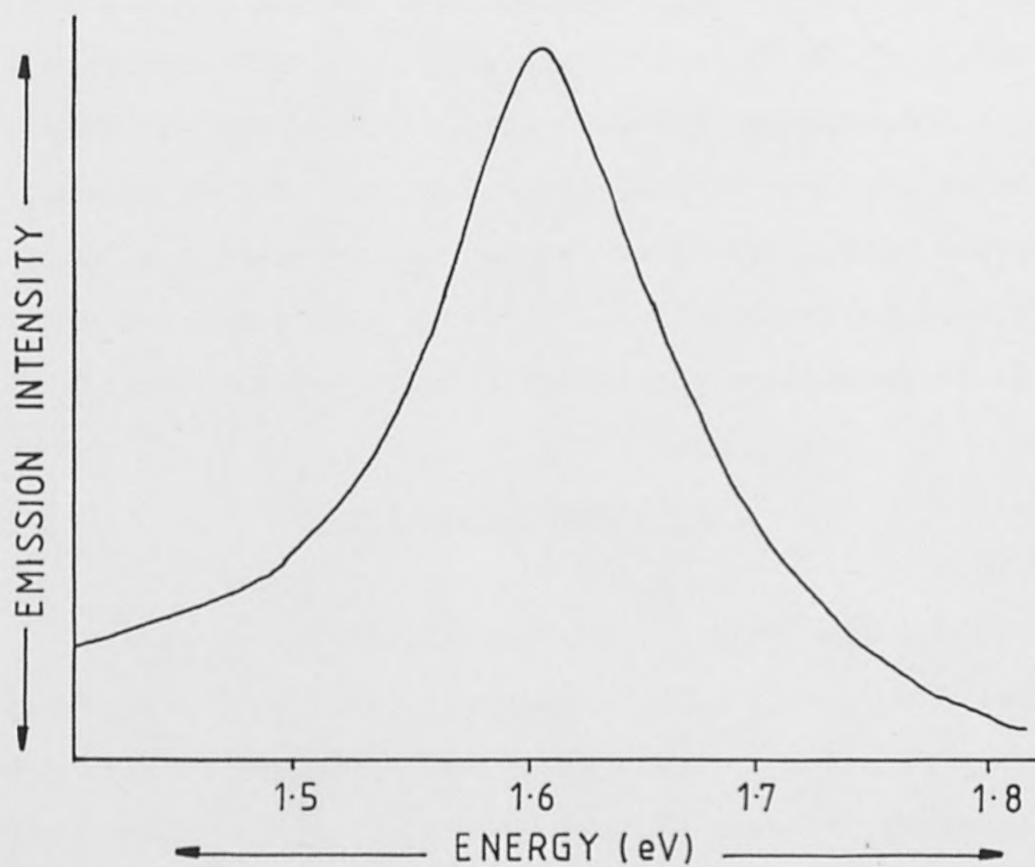


Fig. 4.9. Photoluminescence Spectra of  $\text{Cs}_2\text{NaBiBr}_6$

absorption region, was observed for the iodides and bromides (Table 4.10). For the bromides the optical band gap increased in energy as the size of the p-block element increased. The same observation was made for the iodides, with the exception of  $\text{Cs}_2\text{NaSbI}_6$ . However, the replacement of bromide by iodide results in a marked decrease in the width of the optical band gap.

All the samples were examined for luminescence at room temperature and 80K. With the exceptions of  $\text{Rb}_2\text{NaBiBr}_6$ ,  $\text{Cs}_2\text{NaBiCl}_6$  and  $\text{Rb}_2\text{NaSbI}_6$  which showed luminescence at 80K, the results were negative. The spectra obtained at 80K showed a pronounced low energy "tail" and a high energy "emission edge" (Fig 4.9). A shoulder observed at 1.911eV in all spectra was an artifact of the monochromator slit.

#### 4.4.5. Electrical Conductivity

Electrical conductivity measurements were performed on polycrystalline pelleted samples using a two probe technique.<sup>(14)</sup> The results are listed in Table 4.11.. It can be seen that the conductivities increase down the arsenic, antimony and bismuth series from chloride to iodide. The replacement of caesium by rubidium increases the conductivity by a factor of ten in the bromides and chlorides but has little effect in the iodide complexes.

As described in Section 4.4.1. the colours of the compounds move toward the red end of the spectrum as chloride is

Compound	$\sigma (\Omega^{-1} \text{ cm}^{-1})$	t
$\text{Cs}_2\text{NaAsCl}_6$	$1.85 \times 10^{-8}$	0.95
$\text{Cs}_2\text{NaSbCl}_6$	$1.55 \times 10^{-8}$	0.92
$\text{Cs}_2\text{NaBiCl}_6$	$2.88 \times 10^{-8}$	0.89
$\text{Rb}_2\text{NaAsCl}_6$	$1.7 \times 10^{-6}$	0.89
$\text{Rb}_2\text{NaSbCl}_6$	$2.8 \times 10^{-6}$	0.86
$\text{Rb}_2\text{NaBiCl}_6$	$1.4 \times 10^{-7}$	0.83
$\text{Cs}_2\text{NaAsBr}_6$	$3.05 \times 10^{-6}$	0.94
$\text{Cs}_2\text{NaSbBr}_6$	$1.44 \times 10^{-7}$	0.91
$\text{Cs}_2\text{NaBiBr}_6$	$2.7 \times 10^{-6}$	0.88
$\text{Rb}_2\text{NaAsBr}_6$	$1.7 \times 10^{-6}$	0.89
$\text{Rb}_2\text{NaSbBr}_6$	$1.62 \times 10^{-5}$	0.87
$\text{Rb}_2\text{NaBiBr}_6$	$1.49 \times 10^{-5}$	0.84
$\text{Cs}_2\text{NaAsI}_6$	$5.62 \times 10^{-6}$	0.92
$\text{Cs}_2\text{NaSbI}_6$	$1.24 \times 10^{-3}$	0.89
$\text{Cs}_2\text{NaBiI}_6$	$1.07 \times 10^{-4}$	0.86
$\text{Rb}_2\text{NaSbI}_6$	$1.48 \times 10^{-4}$	0.85
$\text{Rb}_2\text{NaBiI}_6$	$1.32 \times 10^{-4}$	0.82

Fig. 4.11. Electrical Conductivity Data and tolerance factors (t) for  $\text{A}_2\text{A}^{\text{I}}\text{B}^{\text{III}}\text{I}_6$ .



replaced by bromide and then by iodide, and a similar trend is observed in the distortion of the structures from the cubic perovskite of the chlorides.

For ions to pack in a cubic perovskite lattice, the following relationship between the ionic radii of the 12-coordinate ion (A), the b-coordinate ion (B), and the halogen (X) must be approximately true:-

$$R_A + R_X \approx \sqrt{2} (R_B + R_X)$$

If the ions are assumed to be hard spheres the cubic perovskite lattice is only stable if the tolerance factor,  $t$ , lies in the range 0.8 to 1.05 where  $t$  is defined by:-

$$t = \sqrt{2} (R_A + R_X) / R_B^{(+)} + R_B^{(3+)} + 2R_X$$

$t$  is therefore a measure of the stability of the perovskite lattice, the lower the value of  $t$  the greater the tendency towards distortion from the cubic perovskite. When  $t$  is greater than 1.05 hexagonal structures are formed. Fig 4.10 shows the relationship between  $t$  and the room temperature electrical conductivity. It can be seen from this, that while all the tolerance factors lie within the range allowed for the perovskite structure none actually possess an undistorted structure at room temperature.

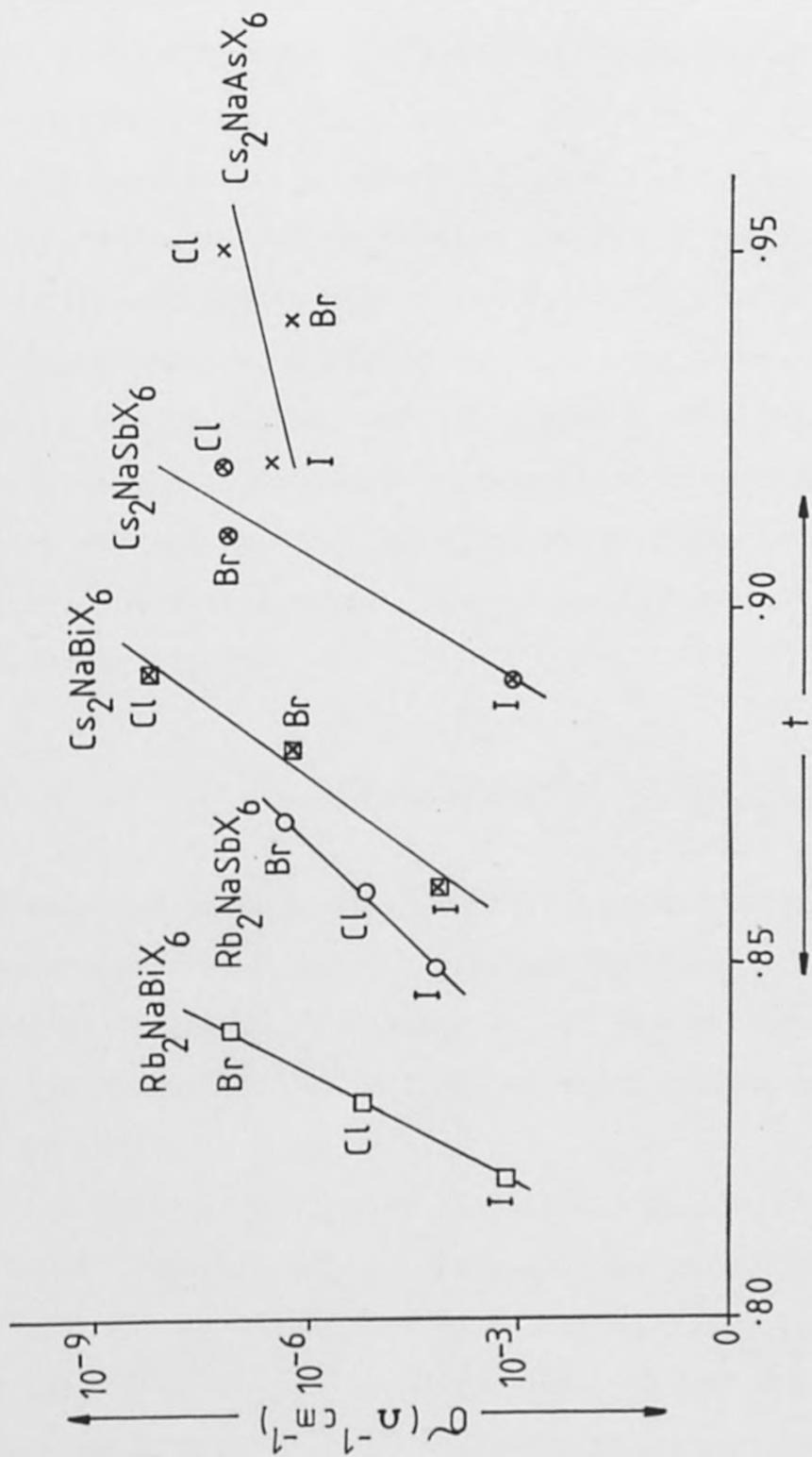


Fig. 4.10. Conductivity and tolerance factor of  $M^I Na M^{III} X_6$  compounds

From the trends of the series it can be seen that the conductivities of the rubidium complexes do not follow the expected pattern which implies that a different mechanism may be responsible for their colour and electrical conductivity.

Photoconductivity measurements were made but none of the compounds, except  $\text{Cs}_2\text{NaSbI}_6$ , exhibited any response. The photoconductivity maxima for  $\text{Cs}_2\text{NaSbI}_6$  was at  $2.15 \pm 0.05\text{eV}$ , i.e. in the region of its absorption edge, however, the response was very broad and ill defined. The existence of a photoconductive response is conclusive evidence that the optical and electrical properties arise from the same process, and that a direct band-to-band transition is involved in  $\text{Cs}_2\text{NaSbI}_6$ .

#### 4.4.6. Variable Temperature Measurements

Variable temperature electrical conductivity measurements were carried out using the 'high temperature' apparatus discussed in Chapter 3. It was not possible to investigate any of the iodides, as heating them results in loss of iodine.

The data are presented graphically as plots of  $-\log\sigma$  vs  $1000/T$  (Figs 4.11-12). Phase changes were observed that were not detectable by differential thermal analysis (D.T.A.). The changes in conductivity at the phase changes is only small e.g.  $0.25 \Omega^{-1} \text{cm}^{-1}$  for  $\text{Cs}_2\text{NaBiBr}_6$ , which

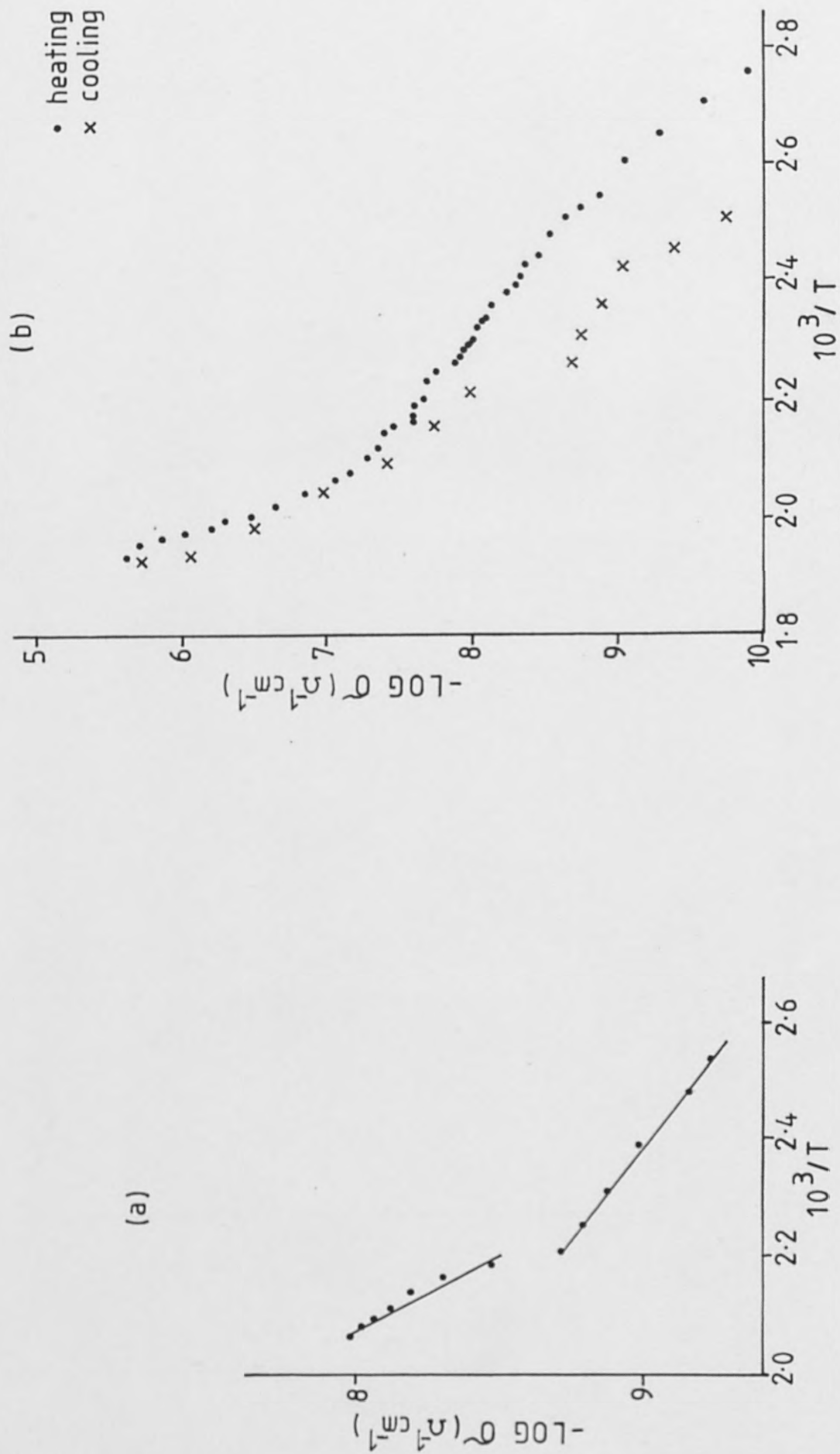
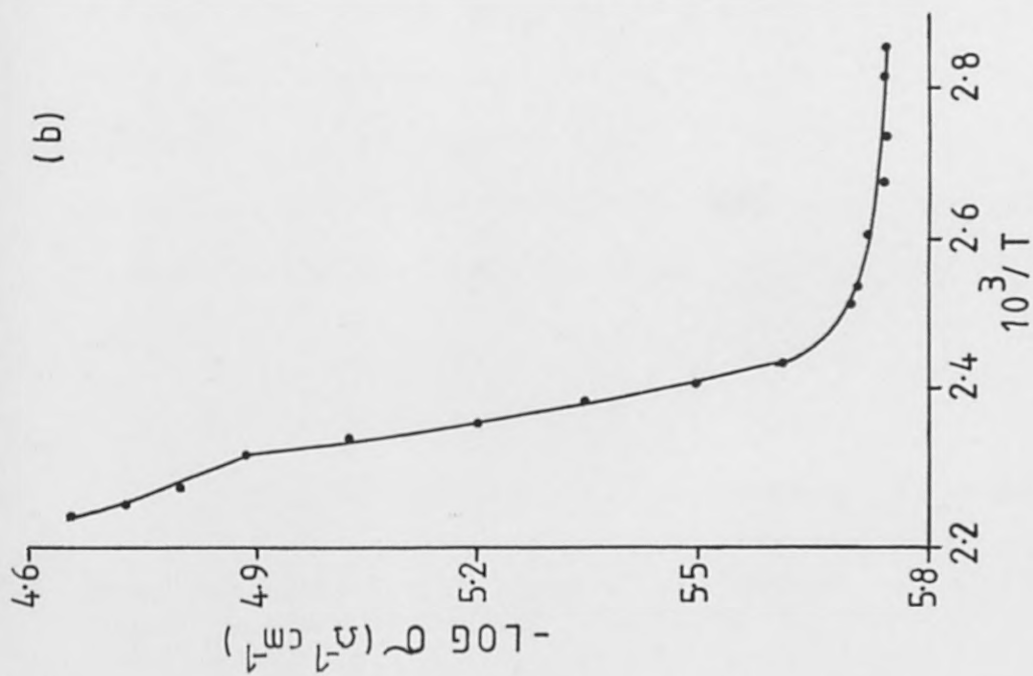


Fig. 4.11. Variable Temperature Curves for (a)  $\text{Cs}_2\text{NaBiBr}_6$  (b)  $\text{Cs}_2\text{NaSbCl}_6$



(b)

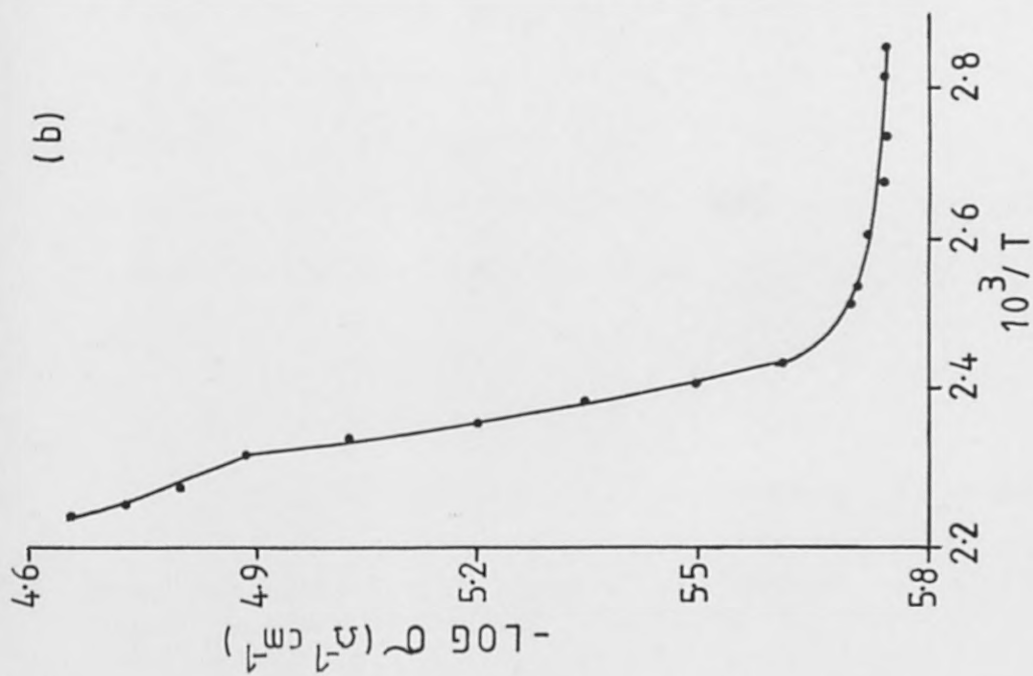


Fig. 4.12. Variable Temperature Conductivity plots for (a)  $\text{Cs}_2\text{NaSbBr}_6$  and (b)  $\text{Rb}_2\text{NaSbBr}_6$

could account for the failure to detect a change in the D.T.A.. The energy gaps above and below the phase changes were calculated and are listed in Table 4.12. If,  $\text{Cs}_2\text{NaSbBr}_6$  is an impurity semiconductor the 'curling over' effect at  $\sim 115^\circ\text{C}$  may be interpreted as an 'exhaustion region' where the impurity level is saturated.

	$\text{Cs}_2\text{NaSbCl}_6$	$\text{Cs}_2\text{NaSbBr}_6$	$\text{Rb}_2\text{NaSbBr}_6$	$\text{Cs}_2\text{NaBiBr}_6$
band gap below phase change (eV $\pm$ 0.03)	$2.71 \times 10^{-1}$	$2.28 \times 10^{-1}$	$3.47 \times 10^{-1}$	$1.28 \times 10^{-1}$
phase change temperature ( $^\circ\text{C}$ )	171	121	128	182
band gap above phase change (eV $\pm$ 0.03)	$6.4 \times 10^{-1}$	---	---	$2.4 \times 10^{-1}$

Table 4.12. Data from 'high temperature' electrical conductivity experiments.

4.4.7. Replacement of Antimony (III) by Indium (III) in  
 $Cs_2NaSbX_6$  (x = Cl or Br)

A preliminary study was carried out to investigate the effects of replacing antimony (III) by indium (III) in  $Cs_2NaSbX_6$  (X = Cl or Br). Indium (III) was selected for this study as it is of similar size to antimony (III) (0.81 and 0.76 Å respectively) but it does not have a lone pair of electrons.

The results of the absorption spectra and bulk electrical conductivity measurements are listed in Table 4.13. It is not possible to draw any conclusions from the data, except to say that the introduction of In(III) into the  $Cs_2NaSbX_6$  lattice increases the energy of the optical energy gap.

Sample	Energy Gap (eV $\pm$ 0.03)	Electrical Conductivity ( $\Omega^{-1} \text{ cm}^{-1}$ )
$Cs_2NaSbCl_6$		$1.55 \times 10^{-8}$
$Cs_2NaSb_{.8}In_{.2}Cl_6$	2.80	$3.56 \times 10^{-8}$
$Cs_2NaInCl_6$	2.995	$8.17 \times 10^{-11}$
$Cs_2NaSbBr_6$	2.44	$1.44 \times 10^{-7}$
$Cs_2NaSb_{.8}In_{.2}Br_6$	2.55	$1.83 \times 10^{-10}$
$Cs_2NaInBr_6$	2.82	$5.84 \times 10^{-7}$

Table 4.13. Optical and Electrical Conductivity data for In(III) doped  $Cs_2NaSbX_6$  (X = Cl or Br)

#### 4.5.

#### Miscellaneous Systems

This section outlines preliminary investigations, of systems, the results of which were not concerned with the general argument i.e. whether the iodine electrons themselves or the non-bonding lone-pair of electrons associated with the main group element are responsible for the semiconducting properties.

##### 4.5.1.

##### Cadmium Iodides

A brief study was made of cadmium containing iodides as cadmium was used as a non-lone-pair element in mixed metal iodide systems (see Chapter 5).

The effect of varying the ratio of CsI:CdI on electrical conductivity was investigated. The data (Table 4.14) show that as the ratio increases from 1:1 to 1:4 the conductivity increases, however the values are at least  $10^4$  times lower than  $\text{CdI}_2$  itself.

The replacement of 15% of the iodine by chlorine in  $\text{CsCdI}_3$  reduces the conductivity by a factor of ten, although the energy of the optical band gap is reduced by 0.51 eV.

None of the phases studied have a high thermal conductivity (Table 4.14).

The effect of contact material on the electrical conductivity measurements was investigated for  $\text{CsCdI}_3$



(Table 4.15). Gold foil- silver paint and indium metal contacts all proved to be suitable contact materials.

"High temperature" electrical conductivity measurements on  $\text{CsCdI}_3$  showed no phase change up to  $120^\circ\text{C}$  (Fig 4.13) in agreement with D.T.A. measurements. The band gap calculated from these measurements is  $0.513\text{eV}$ .

Contact Material	Conductivity of $\text{CsCdI}_3$ ( $\Omega^{-1} \text{cm}^{-1}$ )
Gold leaf	$7.34 \times 10^{-10}$
Silver paint	$7.14 \times 10^{-10}$
Indium metal	$6.32 \times 10^{-10}$
Tin foil	$2.34 \times 10^{-10}$
Aluminium foil	$3.86 \times 10^{-11}$
no contact	$9.47 \times 10^{-11}$

Table 4.15. Electrical conductivity data of  $\text{CsCdI}_3$  using a variety of contacts.

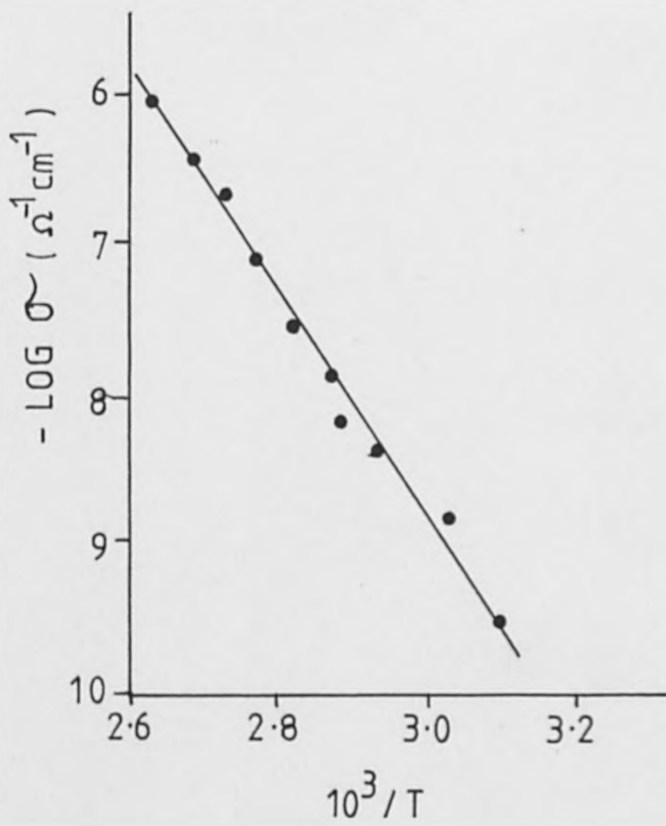


Fig. 4. 13. Variable temperature conductivity plot for  $\text{CsCdI}_3$ .

Sample	Conductivity ( $\Omega^{-1} \text{ cm}^{-1}$ )	Thermal Conductivity ( $\text{W cm}^{-1} \text{ T}^{-1}$ )	Optical Band Gap (eV + 0.03)
$\text{CdI}_2$	$1.93 \times 10^{-4}$	—————	—————
$\text{CsCdI}_3$	$9.36 \times 10^{-9}$	0.096	3.31
$\text{Cs}_2\text{CdI}_4$	$6.12 \times 10^{-9}$	—————	—————
$\text{Cs}_3\text{CdI}_5$	$2.5 \times 10^{-8}$	0.0574	
$\text{Cs}_4\text{CdI}_6$	$2.88 \times 10^{-8}$	0.0914	
$\text{CsCdI}_{2.85}\text{Cl}_{.15}$	$1.43 \times 10^{-9}$	—————	2.80

Table 4.14. Electrical and thermal conductivity data for  $\text{CsI}:\text{CdI}_3$  phases.

4.5.2. 'High Temperature' Electrical conductivity study  
the CsSnCl<sub>3-x</sub>Br<sub>x</sub> System

'High temperature' electrical conductivity measurements were performed on CsSnCl<sub>3-x</sub>Br<sub>x</sub> phases where x = 0, 1 and 1.5. The data are presented graphically as -logδ vs 1000/T (Figs. 4.14-4.16), the computer programme listed in appendix 1 being used to calculate the data. The phases all show phase changes in the heating graphs, the discontinuities are not, however, reflected in the cooling lines. This may be indicative of metastable changes. The band gaps above and below the phase changes were calculated using the following equation:-

$$-\log\delta = \frac{2.303 E_g}{2K} \left( \frac{1}{T} \right) \quad (4.4.)$$

and all relevant data are listed in Table 4.16.

The data show that as the percentage bromine is increased so the first phase change temperature decreases with a concurrent decrease in the calculated band gap of this phase. The second phase change temperatures do not follow the same pattern but, there is a decrease in band gap with an increase in bromine content.

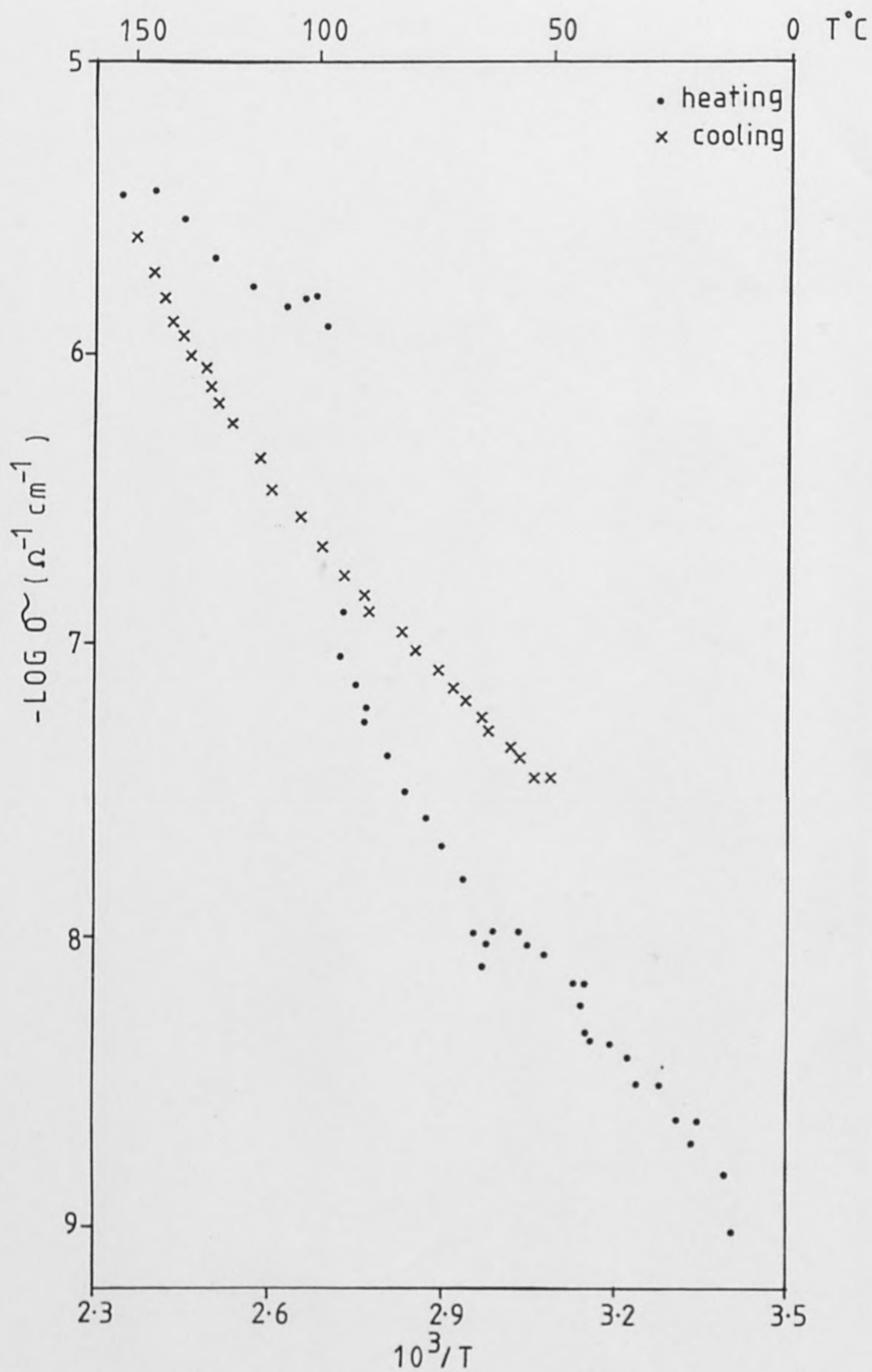


Fig. 4.14. Variable Temperature Conductivity plot for  $\text{CsSnCl}_3$

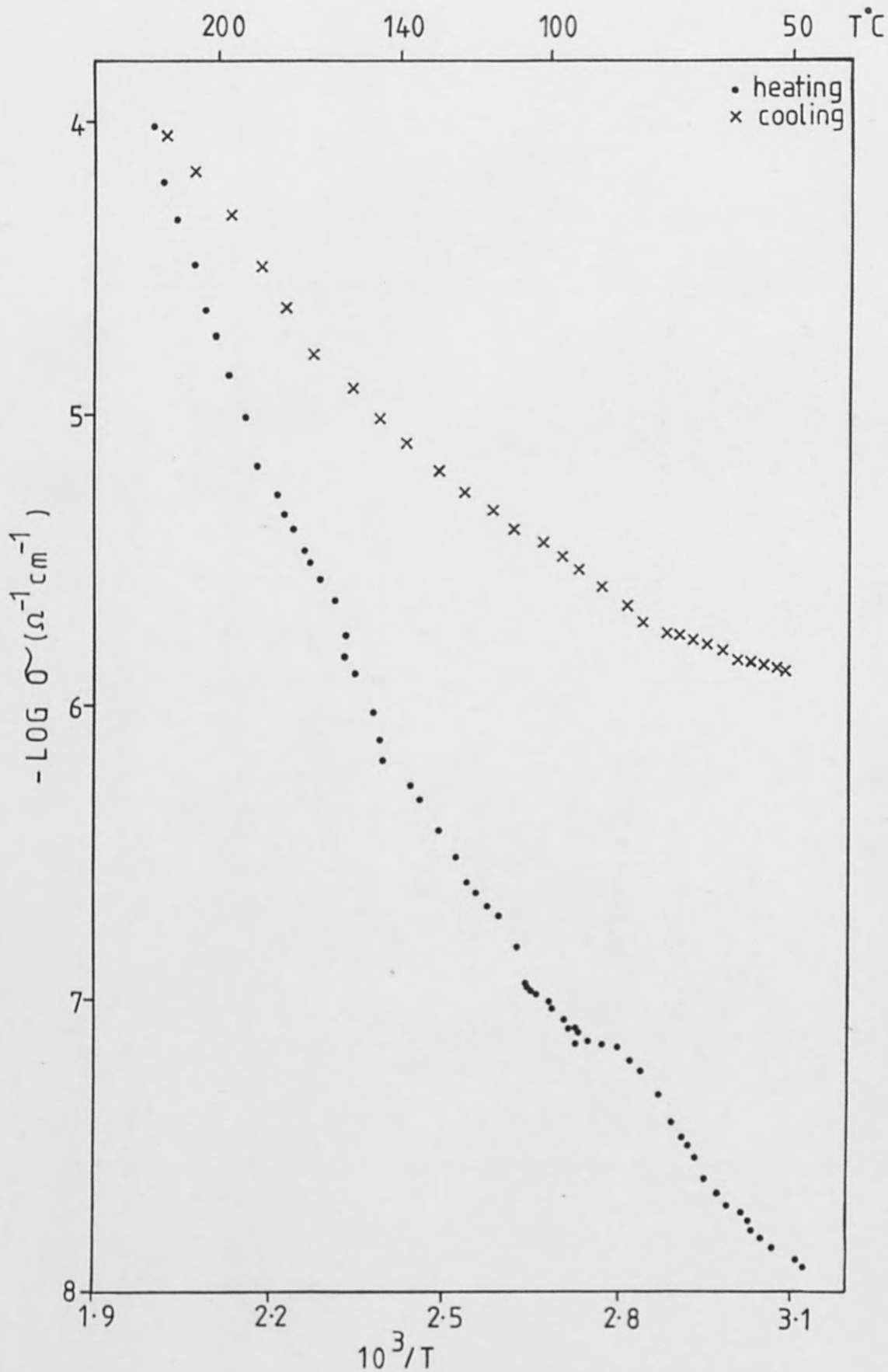


Fig. 4.15. Variable Temperature Conductivity plot for  $\text{CsSnCl}_2\text{Br}$ .

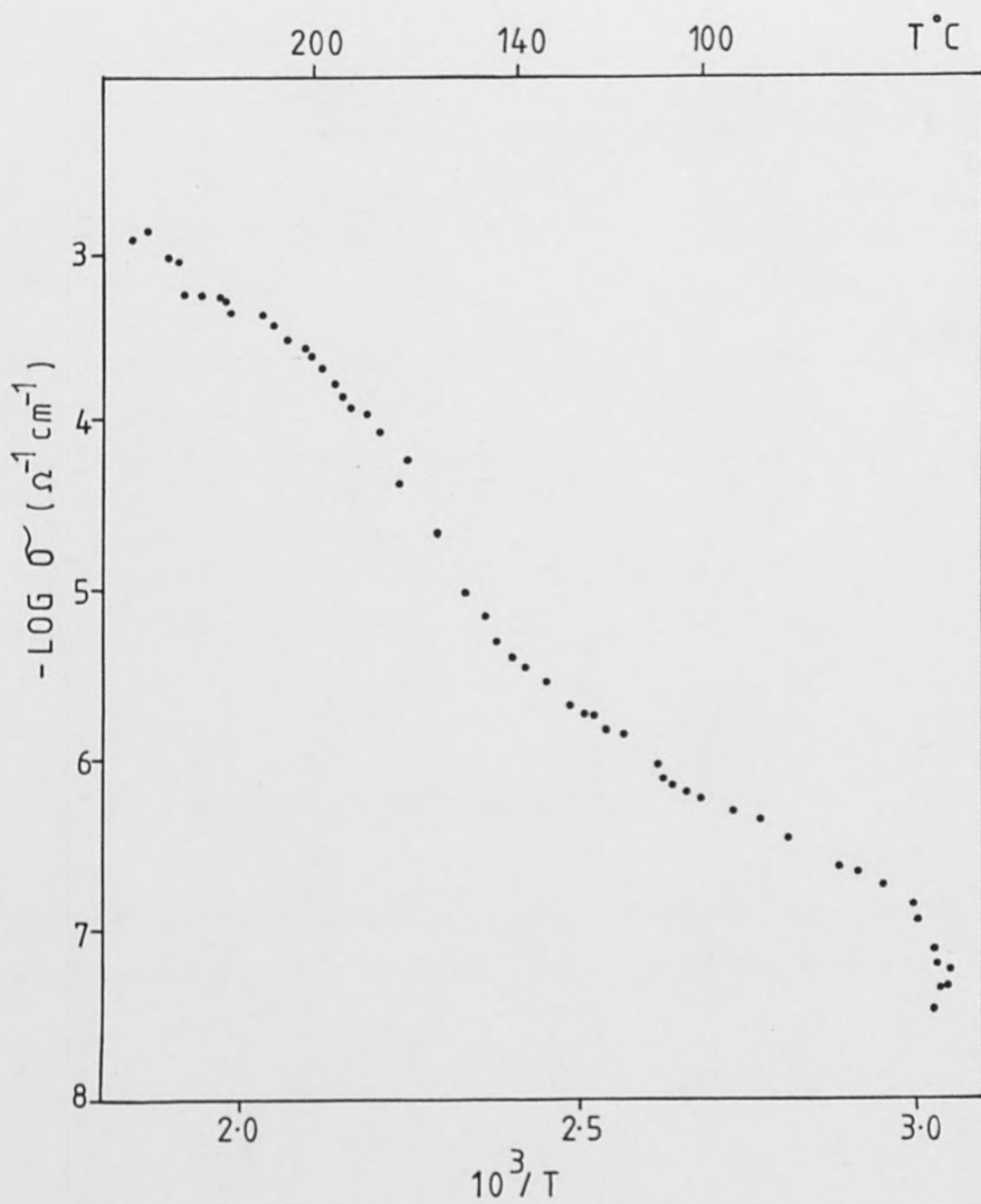


Fig. 4.16. Variable Temperature Conductivity plot of  $\text{CsSnCl}_{1.5}\text{Br}_{1.5}$

	<u>CsSnCl<sub>3</sub></u>	<u>CsSnCl<sub>2</sub>Br</u>	<u>CsSnCl<sub>1.5</sub>Br<sub>1.5</sub></u>
(a) phase change temperature (°C)	90-97.3	84.1-94.6	86-89.3
(b) phase change temperature (°C)	-----	147.2	167
band gap (a) (eV ± 0.05)	0.193	0.183	0.154
band gap (b) (eV ± 0.05)	-----	0.372	0.342

Table 4.16. Data for CsSnCl<sub>3-x</sub>Br<sub>x</sub> system obtained from 'high temperature' electrical conductivity measurements.



#### 4.6. Crystal Structure Determination of $\text{Cs}_2\text{NaBiBr}_6$ .

##### Introduction

The Group V metal trihalides on reaction with alkali halides form crystals with the formula  $\text{A}_3\text{B}_2\text{X}_9$  and  $\text{A}_2\text{A}^1\text{BX}_6$ . The structures of  $\text{Cs}_3\text{As}_2\text{Cl}_9$ <sup>(19)</sup>,  $\text{Cs}_3\text{Sb}_2\text{Cl}_9$ <sup>(20)</sup> and  $\text{Cs}_3\text{Bi}_2\text{Cl}_9$ <sup>(20)</sup> and the corresponding bromides<sup>(21)</sup> and iodides are known. The iodides have structures related to  $\text{Cs}_3\text{Cr}_2\text{Cl}_9$  which is hexagonal with space group  $\text{P6}_3/\text{mmc}$ . In this structure the  $\text{Cs}^+$  ions have twelve  $\text{I}^-$  nearest neighbours and the  $\text{As}^{3+}$ ,  $\text{Sb}^{3+}$  or  $\text{Bi}^{3+}$  ions are in distorted octahedral sites occupying two-thirds of the available octahedral voids in the close packed structure.

The  $\text{Cs}_2\text{NaMCl}_6$  compounds ( $\text{M} = \text{Sb}, \text{Bi}$ ) have cubic structures of  $\text{Fm}\bar{3}\text{m}$  space group with  $a = 10.7780$  (20)Å and  $a = 10.8386$ (10)Å respectively. The structures of the corresponding bromides and iodides have not been determined.

As the iodide analogues are less stable and difficult to prepare in crystalline form, the structure of  $\text{Cs}_2\text{NaBiBr}_6$  was investigated.

The crystals used in the structure determination were prepared by the method of Robinson<sup>(18)</sup> as discussed in section 4.4.1.

#### 4.6.1. Determination of Space Group and Cell Dimensions

A crystal of about 0.35cm was sent to Queen Mary's College, London, for the collection of intensity data. The intensities of 1053 reflections were measured on an Enraf-Nonius CAD 4 diffractometer for up to a maximum of  $35^{\circ}$  by the  $\omega - 2\theta$  scan technique using graphite-monochromatized Mo -  $K\alpha$  radiation.

The data was corrected for Lorentz, polarization and absorption effects before being used in the Shelex-<sup>76</sup> programme (Section 2.7.1) for the structure determination.

The cell dimensions obtained from the diffractometer measurements were:-

Cell dimensions ( $\text{\AA}$ )	$a = 7.8946 \pm .001$
	$b = 7.8977 \pm .001$
	$c = 9.7083 \pm .001$
	$\alpha = 89.99 (\pm .01)$
	$\beta = 89.98 (\pm .01)$
	$\gamma = 120.00 (\pm .01)$

The other crystal data are as follows:-

Cell Volume (V)	542.2 $\text{\AA}^3$
Molecular weight (M)	890.005
Density measured	4.19 $\text{gcm}^{-3}$
Density calculated ( $z = 1.5$ )	4.09 $\text{gcm}^{-3}$
Systematic absences	none

The density of the crystals was obtained by displacement of bromoform and the unit cell content was calculated from the formula.

$$Z = \frac{D_M V}{1.66 M} \quad (4.5.)$$

The crystal data and systematic absences are consistent with a centrosymmetric hexagonal or trigonal space group,  $P\bar{3}m1$  and  $P\bar{3}$  being likely possibilities.

#### 4.6.2. Discussion of the Crystal Structure

The density data showed that the cell content is 1.5 which means that positions have to be assigned to  $Cs_3(NaSb)_3Br_9$ . This composition is very similar to  $Cs_3MBr_9$  for which structures are known<sup>(21)</sup>. Initially, therefore, the data for  $Cs_2NaSbBr_6$  were assigned to the  $P\bar{3}m1$  space group to discover if it is isostructural with  $Cs_3BiBr_9$ . Table 4.17 lists the values of  $F_{obs}$ ,  $F_{calc}$  and  $|F_{obs} - F_{calc}|$  for a typical range of reflections assuming that  $Cs_2NaSbBr_6$  is indeed isostructural. The residual calculated from these figures is high ( $R = .83$ ) and therefore it can be concluded that they are not isostructural despite similar compositions and cell dimensions.

The atoms present in the unit cell are Cs (3) Na (1.5) Sb (1.5) Br (9) therefore one would expect the sum of the Br - Br vectors to give the largest peak in the Patterson

H K L	Fobs	Fcalc	Fobs-Fcalc
0 1 0	49	67	17
0 3 0	358	139	219
-1 2 0	409	161	248
0 2 0	49	51	1
-1 3 0	49	33	16
-2 4 0	510	355	155
-1 4 0	104	48	56
0 4 0	49	40	9
0 5 0	49	10	39
0 6 0	560	211	349
0 7 0	49	31	18
0 8 0	50	6	44
-4 4 1	49	221	171
-2 2 2	49	398	348
0 2 1	99	279	179
0 3 1	49	23	26
0 0 6	560	285	275
0 2 4	99	336	236
0 3 4	49	12	37
-4 4 4	49	274	224
0 4 2	99	302	202
0 0 3	358	269	89
-4 6 2	50	247	196

$$R = \frac{\sum |F_{obs} - F_{calc}|}{\sum F_{obs}} \quad (4.6.)$$

$$R = .83$$

Table 4.17 Calculation of the residual assuming  $Cs_2NaSbBr_6$  is isostructural with  $Cs_3Bi_2Br_9$ .

synthesis. A Patterson synthesis was carried out for  $P\bar{3}m1$ . The highest peak in the Patterson was the origin 0, 0, 0 with weaker peaks at:

0	$\frac{1}{2}$	0
.17	.33	.333
0	0	$\frac{1}{2}$
.16	.327	.831
0	$\frac{1}{2}$	$\frac{1}{2}$

Three bromines were put into the special position 0,  $\frac{1}{2}$ , 0, and the remaining six into the general position .17, .33, .333. A further Fourier synthesis located the antimony and sodium atoms at .3237, .1619, .1705. These positions were fixed and the structure refined using 7 cycles of full-matrix least squares refinement which converged to a residual of 0.36 with all the interlayer scale factors held at 1.0.

The Br - Sb bond distances of 2.70Å are larger than the sum of the atoms ionic radii (1.95 + 0.76Å) showing that the bonding is largely electrostatic .

The addition of the 3 caesium atoms into any further positions suggested by the Fourier synthesis resulted in an increase in the residual and rejection of the established bromine and antimony positions. If the sodium and antimony fractions are put into the same positions individually the residual again increases.

The failure to reduce the residual below 0.36 may be

attributed to disorder within the cation sublattices. As with other known structures of this type it is likely that the antimony is octahedrally surrounded by bromines. It would be possible for the sodium ions to occupy vacancies either within the antimony sublattice or the caesium sublattice. It did not prove possible to satisfactorily place  $\text{Na}^+$  ions, as a separate entity into either sublattice. Only by treating  $\text{Na}^+$  ions as antimony atoms could they be positioned in the sublattice. The disorder in the structure of  $\text{Cs}_2\text{NaBiBr}_6$  can therefore be directly attributed to the sodium ions.

```

2 REM***** THERMAL *****
3 REM*****
10 PRINT " "
11 DIMS(100):DIMT(100):DIMA(100):DIML(100)
12 DIMFB(100):DIMTC(100):DIMID(100)
13 DIMFF(100):DIMSL(100):DIMSH$(100):DIMST$(100):DIMSR$(100)
14 INPUT "PRINTER OUTPUT Y";YB$
15 IF YB$="Y" THEN JK=10000:GOTO 10
16 JK=18
17 POKE 59468!,14
18 PRINT " "
20 INPUT "RESISTANCE KOHMS":R
30 INPUT "APPLIED VOLTAGE MV";V
40 INPUT "SAMPLE THICKNESS CMS";TA
50 INPUT "CONTACT AREA CM^2";A
90 PRINT "ENTER 0,0 TO STOP"
100 INPUT "VOLTAGE AND TEMPERATURE";VA,T
104 J=J+1:IF J=JK GOTO 300
105 IF VA=0 GOTO 300
110 TB(N)=T+273
120 S(N)=TA/((R*((V/VA)-1))*A)
125 TF(N)=1000/TB(N)
126 SL(N)=LOG(S(N))/LOG(10)
130 N=N+1
200 GOTO 100
300 REM *****OUTPUT*****
305 PRINT " ":POKE 59468!,12
310 PRINT " T S LOGS 1000/T"
315 PRINT"
-----"
320 FOR B= 0 TO (N-1)
330 TC(B)=(INT((TB(B))*100)/100)
335 TD(B)=(INT((TF(B))*100)/100)
340 SL(B)=(INT((SL(B))*100)/100)
345 SH$(B)=STR$(S(B))
346 ST$(B)=LEFT$(SH$(B),5):SR$(B)=RIGHT$(SH$(B),4)
366 PRINT TAB(1);TC(B);TAB(8);ST$(B)SR$(B);TAB(20);SL(B);TAB(30);TD(B)
400 NEXT
500 POKE 59468!,12
510 STOP
515 PRINT " "
520 GOTO 100

```

APPENDIX 1 C.B.M 3040 COMPUTER PROGRAM FOR TREATMENT OF VARIABLE TEMPERATURE CONDUCTIVITY DATA.

## References

1. R. A. Howie, W. Moser, I. C. Trevena, Acta Cryst., (1972), B28, 2965.
2. C. K. Møller, Kgel. Dan. Vid. Selsk. Mat. Fys. Med., (1954), 32, 1.
3. Vogel's Textbook of Quantitative Inorganic Analysis, 4<sup>th</sup> Ed., Longman.
4. H. L. Well, Z. Anorg. Chem., (1893) 3, 195.
5. O. Schmitz-Dumont, G. Bergerhoff, Z. Anorg. Allgem. Chem., (1956) 283, 314.
6. C. K. Møller, Mat. Fys. Medd. Dan. Vid. Selsk., (1959) 32 No. 2.
7. J. D. Donaldson, J. S. Silver, S. D. Ross, S. Hadjimindis, J.C.S. Dalton Trans., (1975) 1500.
8. C. K. Møller, Mat. Fys. Medd. Dan. Vid. Selsk., (1959) 32, No. 1.
9. Y. Sost, L. Langrøvet, Comptes Rend., (1967) B264, 1603.
10. C. Bettinali, G. Ferrarresso, Z. Phys. Chem., (1969), 67, 1.
11. A. J. H. Eijekenkamp, J. Luminescence, (1977) 15, 217.
12. B. A. Belikovich, I. P. Pashchuk, N. S. Pidzyrailo, Opt. Spectrosc., (1977) 42, 62.
13. K. Heidrich, H. Künzel, J. Trensck, Solid State Commun., (1978) 25, 887.
14. See Section 4.1.3.
15. C. K. Møller, Nature, (1958), 182, 1436.
16. See Section 3.2.4.
17. Morss, Siegal, Inorg. Chem., (1970) 9, 1771.
18. Robinson, Acta Cryst., (1972) B28, 653.



19. J. L. Hoard, L. Goldstein, J. Chem. Phys. (1935) 3, 117.
20. K. Kihara, T. Sudo, Acta Cryst., 1974, B30, 1088.
21. F. Lazamini, Acta. Cryst., 1977, B33, 2961.

## Chapter Five

	<u>Page</u>
5.1. The CsPbI <sub>3</sub> : CsCdI <sub>3</sub> System	197
5.1.2. Preparation and Analysis	198
5.1.3 X-Ray Powder Data	202
5.1.4. Optical Properties of CsPb <sub>1-x</sub> Cd <sub>x</sub> I <sub>3</sub> System	208
5.1.5. Photoconductivity	212
5.1.6. Room Temperature Electrical Conductivity Measurements	213
5.2. The CsSnBr <sub>3</sub> : CsCdBr <sub>3</sub> System	215
5.2.1. Sample Preparation	216
5.2.2. Analysis	216
5.2.3. Optical Properties	218
5.2.4. Electrical Conductivity Measurements	222
5.2.5. Photoconductivity	225
5.3. The CsSnI <sub>3</sub> : CsPbI <sub>3</sub> System	227
5.3.1. Preparation	227
5.3.2. Analysis	228
5.3.3. X-Ray Studies	228
5.3.4. Absorption Spectra	229
5.3.5. Room Temperature Electrical Conductivity Measurements	230
5.4. The CsPb <sub>.5</sub> Cd <sub>.5</sub> I <sub>3-x</sub> X <sub>x</sub> (X = Cl or Br) System	234
5.4.1. Preparation and Analysis	234
5.4.2. Optical Properties	235
5.4.3. Electrical Conductivity	237

	<u>Page</u>
5.5. The $\text{Cs}_2\text{NaSbI}_6$ : $\text{Cs}_2\text{NaBiI}_6$ System	238
5.5.1. Sample Preparation and Analysis	239
5.5.2. X-Ray Data	242
5.5.3. Optical Properties	252
5.5.4. Electrical Properties	255
5.5.5. Photoconductivity	255

## Introduction

High optical colouration and electrical conductivity is a general feature of many compounds that contain close-packed iodide lattices. These properties are said to arise from population of solid state bands by the iodide electrons themselves<sup>(1)</sup>. For compounds such as  $\text{CsSnI}_3$  and  $\text{CsPbI}_3$ , therefore, it is possible to obtain colouration and conductivity by two mechanisms viz: donation of electrons to the conduction band by the iodide ions or donation from the non-bonding electron pair of the group (IV) ion. To investigate these effects a series of mixed metal systems, of the type  $\text{CsA}_x\text{B}_{1-x}\text{I}_3$  and  $\text{Cs}_2\text{NaA}_x\text{B}_{1-x}\text{I}_6$ , have been prepared and investigated. The results are presented in this chapter and discussed in Chapter 6.

### 5.1. The $\text{CsPbI}_3$ : $\text{CsCdI}_3$ System

The solid state properties of  $\text{CsPbX}_3$  ( $X = \text{Cl}, \text{Br}, \text{I}$ ) materials are well known<sup>(2)</sup>, and have been interpreted in terms of donation of lead  $ns^2$  electrons to the conduction band.

In  $\text{PbI}_2$  and in many complex iodides  $\text{Pb(II)}$  is octahedrally coordinated, however there is apparently appreciable distortion of the  $\text{PbI}_6^{4-}$  octahedra in  $\text{CsPbI}_3$  in which there are three different Pb - I distances viz: 3.01, 3.25 and 3.42Å. It has been found<sup>(3)</sup> that the

compounds of  $\text{Pb}^{2+}$  are often isostructural with cadmium salts, for instance,  $\text{Cs}_4\text{PbX}_6$  ( $X = \text{Cl}, \text{Br}, \text{I}$ ) has the  $\text{K}_4\text{CdCl}_6$  structure with discrete  $\text{PbX}_6^{4-}$  ions while the  $\text{CsPbX}_3$  compounds ( $X = \text{F}, \text{Cl}, \text{Br}$ ) and the high temperature form of  $\text{CsPbI}_3$  have perovskite-type lattices. The yellow low temperature form of  $\text{CsPbI}_3$  has the  $\text{NH}_4\text{CdCl}_3$  structure.

The  $\text{Cd}^{2+}$  ion has no ligand field stabilization arising from d- orbital population effects and its stereochemistry is determined solely by considerations of size, electrostatic forces and covalent bonding forces. The  $\text{Cd}^{2+}$  ion is slightly smaller than the  $\text{Pb}^{2+}$  ion ( $0.97\text{\AA}$  and  $1.21\text{\AA}$  respectively) and has no lone pair of electrons to donate to the band system. The introduction of cadmium (II) into  $\text{CsPbI}_3$  should therefore provide evidence for the type of donation mechanism operative.

In this section the electrical and optical properties of  $\text{CsPb}_x\text{Cd}_{1-x}\text{I}_3$  ( $x = 0 - 1$ ) are investigated.

### 5.1.2. Preparation

The lead and mixed lead-cadmium phases described in this chapter were prepared from molten systems containing the appropriate stoichiometric ratios of the starting materials. Aqueous solution preparations of lead phases are well known<sup>(6)</sup> but are complicated by the low solubility of lead iodide, and the products obtained are usually contaminated with other phases<sup>(6,7)</sup>.  $\text{CsCdI}_3$  was prepared

with equal purity from both molten and aqueous systems.

### Analysis

The lead and cadmium in all of the phases were determined by atomic absorption spectrometry using a Perkin Elmer Model 370 atomic absorption spectrophotometer.

Potentiometric determination of iodine gave inconsistent results, and therefore an alternative method had to be used. 0.5g of sample was dissolved in a known volume of 2M nitric acid and the iodine extracted into chloroform. Preliminary tests, using various volumes of chloroform, showed that a two stage extraction process was the most efficient, total extraction being possible with 2 x 100ml volumes. The extracted iodine was then titrated against 0.1 sodium thiosulphate solution in the usual manner. The results thus obtained were consistent (Table 5.1) within experimental error. The analytical data are given in Table 5.1.  $\text{CsCdI}_3$  and  $\text{CdPbI}_3$  were analysed by electron microprobe and the results were as follows:-

1) $\text{CsPbI}_3:\text{CsCdI}_3$ mixture	2) $\text{CsPbI}_3:\text{CsCdI}_3$ fused
Cd      12    atomic %	Cd      10.8   atomic %
I       44.7   atomic %	I       49.0   atomic %
Cs      24    atomic %	Cs      29.8   atomic %
Pb      18.8   atomic %	Pb      9.9    atomic %

3)	$\text{CsPbI}_3$			4)	$\text{CsCdI}_3$		
	I	40.8	atomic %		I	50.2	atomic %
	Cs	23.2	atomic %		Cs	25.2	atomic %
	Pb	35.9	atomic %		Cd	24.5	atomic %

As can be seen from the results this method is only qualitative, viz: in  $\text{CsCdI}_3$ (4) the ratio of atoms should be 1Cs:1Cd:3I, the Cs:Cd ratio is indeed 1:1 however the iodine content is only 1:1:2. similarly for  $\text{CsPbI}_3$ . One reason for this discrepancy could be that iodine has an  $\alpha$  line overlapping a K line which would tend to enhance the intensities of some peaks whilst reducing others.

Compound	% Pb	% Cd	% I
CsCdI <sub>3</sub>		18.0 (17.96)	60.7 (60.8)
CsCd <sub>.99</sub> Pb <sub>.01</sub> I <sub>3</sub>	0.33 (0.330)	17.8 (17.75)	60.7 (60.7)
CsCd <sub>.98</sub> Pb <sub>.02</sub> I <sub>3</sub>	0.66 (0.66)	17.6 (17.54)	60.5 (60.60)
CsCd <sub>.95</sub> Pb <sub>.05</sub> I <sub>3</sub>	1.1 (1.64)	16.9 (16.93)	60.9 (60.25)
CsCd <sub>.93</sub> Pb <sub>.07</sub> I <sub>3</sub>	2.3 (2.29)	16.7 (16.52)	59.8 (59.73)
CsCd <sub>.90</sub> Pb <sub>.1</sub> I <sub>3</sub>	3.4 (3.26)	16.8 (15.92)	61.0 (59.91)
CsCd <sub>.88</sub> Pb <sub>.12</sub> I <sub>3</sub>	4.1 (3.90)	15.5 (15.52)	59.9 (59.75)
CsCd <sub>.80</sub> Pb <sub>.2</sub> I <sub>3</sub>	6.4 (6.42)	14.1 (13.94)	59.1 (59.02)
CsCd <sub>.7</sub> Pb <sub>.3</sub> I <sub>3</sub>	11.0 (9.50)	11.9 (12.02)	58.7 (58.17)
CsCd <sub>.6</sub> Pb <sub>.4</sub> I <sub>3</sub>	13.1 (12.48)	9.5 (10.16)	57.2 (57.34)
CsCd <sub>.5</sub> Pb <sub>.5</sub> I <sub>3</sub>	18.4 (15.38)	7.6 (8.35)	56.5. (56.53)
CsCd <sub>.4</sub> Pb <sub>.6</sub> I <sub>3</sub>	17.9 (18.20)	6.1 (6.58)	55.9 (55.7 )
CsCd <sub>.3</sub> Pb <sub>.7</sub> I <sub>3</sub>	23.7 (20.95)	4.7 (4.87)	55.4 (54.98)
CsCd <sub>.2</sub> Pb <sub>.6</sub> I <sub>3</sub>	23.7 (23.62)	3.1 (3.20)	54.3 (54.24)
CsCd <sub>.1</sub> Pb <sub>.9</sub> I <sub>3</sub>	26.2 (26.2)	1.4 (1.58)	53.4 (53.52)
CsPbI <sub>3</sub>	28.7 (28.74)		52.8 (52.82)

Table 5.1. Analytical Data For CsPbI<sub>3</sub>:CsCdI<sub>3</sub> System (Theoretical results are given in brackets).



Each sample in the series was examined using x-ray powder diffractometry and the data showed no peaks attributable to the starting materials. The results show that the phases have the  $\text{CsCdI}_3$  structure for  $x \geq 0.2$ , and the  $\text{CsPbI}_3$  structure for  $x < 0.2$ . As might be expected the lattice parameters increase as  $\text{Cd}^{2+}$  is replaced by the larger  $\text{Pb}^{2+}$  ion, (0.97Å and 1.20Å respectively). The powder data are listed in Table 5.2.

#### Differential Thermal Analysis (DTA)

DTA is a widely used technique for the determination of phase transitions in multi-component systems and in the construction of phase diagrams and offers many advantages over classical methods.

Thermal analyses were performed using a Stanton Redcroft STA 780 simultaneous thermal analyser (Section 4). Initially each phase was heated to 900°C to determine the decomposition temperature. All the phases were found to decompose under 500°C, so subsequent cycled runs were carried out between 50° - 500°C. From the onset temperatures of exo- and endo-thermic peaks it was possible to construct a partial phase diagram. Fig. 5.1 (a) shows the solidus/liquidus line, which shows an abrupt discontinuity at  $x = 0.3$ , corresponding to the structural change observed

CsCdI <sub>3</sub>	99% Cd	98% Cd	95% Cd	93% Cd	90% Cd	88% Cd
d(Å)	d(Å)	d(Å)	d(Å)	d(Å)		
12.1	12.9*	12.9*	12.85*	12.9*	13.05*	12.8*
13.6		13.55	13.6			13.5
17.2		17.1		17.25	17.15	17.1
21.1	21.1	21.15	21.2	21.25	20.9	21.1
					21.7	
					22.6	
23.65	23.8	23.8	23.5	23.55		23.7
24.3	24.35	24.4	24.4	24.45	24.3	24.35
					25.3	
25.9	25.9	25.9	25.9	25.95	25.6	25.9
26.55	26.6	26.55	26.6	26.6	26.4	26.5
27.35	27.4	27.4		27.45	27.1	27.3
28.7	28.6				28.6	
32.4	32.4	32.5	32.5	32.5	31.3	32.4
					32.6	
					33.3	
					37.7	
39.05	39.0	39.1	39.1	39.1	39.1	39.0
40.6			40.50		40.5	
41.0	41.0	41.0	41.0	41.1	41.1	40.9
41.9	41.85				42.2	
	42.5*	42.5*	42.4*	42.4*		42.4*
43					*44.4	
46.6	46.6	46.6	46.55	46.6	46.4	46.5
47.7			47.40		47.1	47.6
				48.7*		
49.2	49.2		49.	49.15		
50	50.1	50.15	50.05			50
51.1	51.2	51.15	51.1			51.1
	53.3*	53.3*	53.2*	53.4*	53.2*	weak
55	54.9	54.9	55	55		
60.5						

Table 5.2. X RAY DATA FOR CsCdI<sub>3</sub>, CsPbI<sub>3</sub> and CsCd<sub>x</sub>Pb<sub>1-x</sub>I<sub>3</sub>.

80% Cd	70% Cd	60% Cd	50% Cd	40% Cd	30% Cd	20% Cd
			12.1			
*12.75			*12.80	*13.0		
13.50	13.55	13.50	13.60			
17.05		17.10	17.10	17.20		
21.05	21.1	21.1	21.10	21.05	21.05	
22.7	22.8		22.7	22.65	22.60	
23.7						
24.2	24.35	24.3	24.35	24.30	24.30	
25.00		25.3	25.4	25.30	25.30	
25.75	25.75	25.75	25.8	25.70	25.60	
26.50	26.50	26.5	26.50	26.50	26.50	
27.2	27.30	27.3	27.30	27.30	27.1	
28.5	28.60	28.6	28.6		28.5	
*30.4	*30.5			*30.5	*30.5	
31.2	31.3	31.35	31.4	31.3	31.3	
32.3	32.4	32.4	32.4	32.35	32.5	
33.3		33.3	33.35	33.3	33.2	
					*36.65	
37.5	37.7	37.7	37.7	37.6	37.7	
38.9	39.0	39.0	39.00	38.9	39.00	
					*39.4	
40.45	weak	40.6	40.5	40.5	40.55	
40.9	40.9	41.1	41.05	41.1	41.1	
*41.4						
41.8						
*42.2	*42.3	*42.3	*42.3	*42.25	*42.20	
42.9		43.00	43.0	43.0	43.00	
*43.2	*43.30	*43.3	*43.25			
		*44.5	*44.3	*44.3	*44.3	
46.5	46.5	46.6	46.5	46.45	46.45	
		47.55	47.70			
49.05						
49.90	50.10	50.00	50.00	50.00		
51.0	51.05	50.90				
*53.2			*53.3	*53.30	*53.2	
54.75	54.8					

Table 5.2. (continued)

10% Cd      CsPbI<sub>3</sub>      CsPbI<sub>3</sub> (contd)      CsPbI<sub>3</sub>:POWDER using A = 4.795,  
 B = 10.457, C = 17.76<sup>o</sup>Å cubic.

			Line	h	k	l	
	18.30	60.45	43.3	0	1	4	
13.05	21.30	60.70	48.0	1	0	3	
	21.65	61.80	59.3	0	3	3	
	23.55	62.70	71.4	1	0	6	
20.9	24.00	62.90	75.6	1	3	4	
	28.50	63.15		or	2	0	1
22.6	29.75	63.35	78.9	0	2	7	
	30.65		81.2		2	0	3
24.3	34.10			or	1	4	2
25.3	35.70			or	0	0	8
25.6	37.15		85.5	2	2	2	
26.4	37.80		88.3	0	3	7	
27.1	39.10		96.4	1	3	7	
28.6	39.45		96.7	1	2	8	
30.1			97.2	2	3	3	
31.3	40.6			or	0	3	8
32.6	42.75			or	1	5	2
	43.45		97.4	0	3	8	
37.7	44.15		104.6	0	1	10	
	46.15		105.8	2	4	2	
	47.90		106.1	2	3	5	
41.1	48.20		108.8	1	5	5	
	48.35		112.4	1	6	0	
42.2	48.60		116.6	0	3	10	
	48.70			or	2	4	5
	49.10		117.00	1	6	3	
44.4	49.90		118.1	0	6	5	
46.4			126.3	0	7	2	
	50.35		126.7	0	4	10	
	52.3			1	2	11	
	52.4						
	52.90						
	53.05						
53.3	54.4						
	55.05						
	55.5						
	56.2						
	56.9						
	57.1						
	58.3						
	58.5						
	59.05						
	59.2						
	59.85						
	60.00						

Table 5.2. (continued).

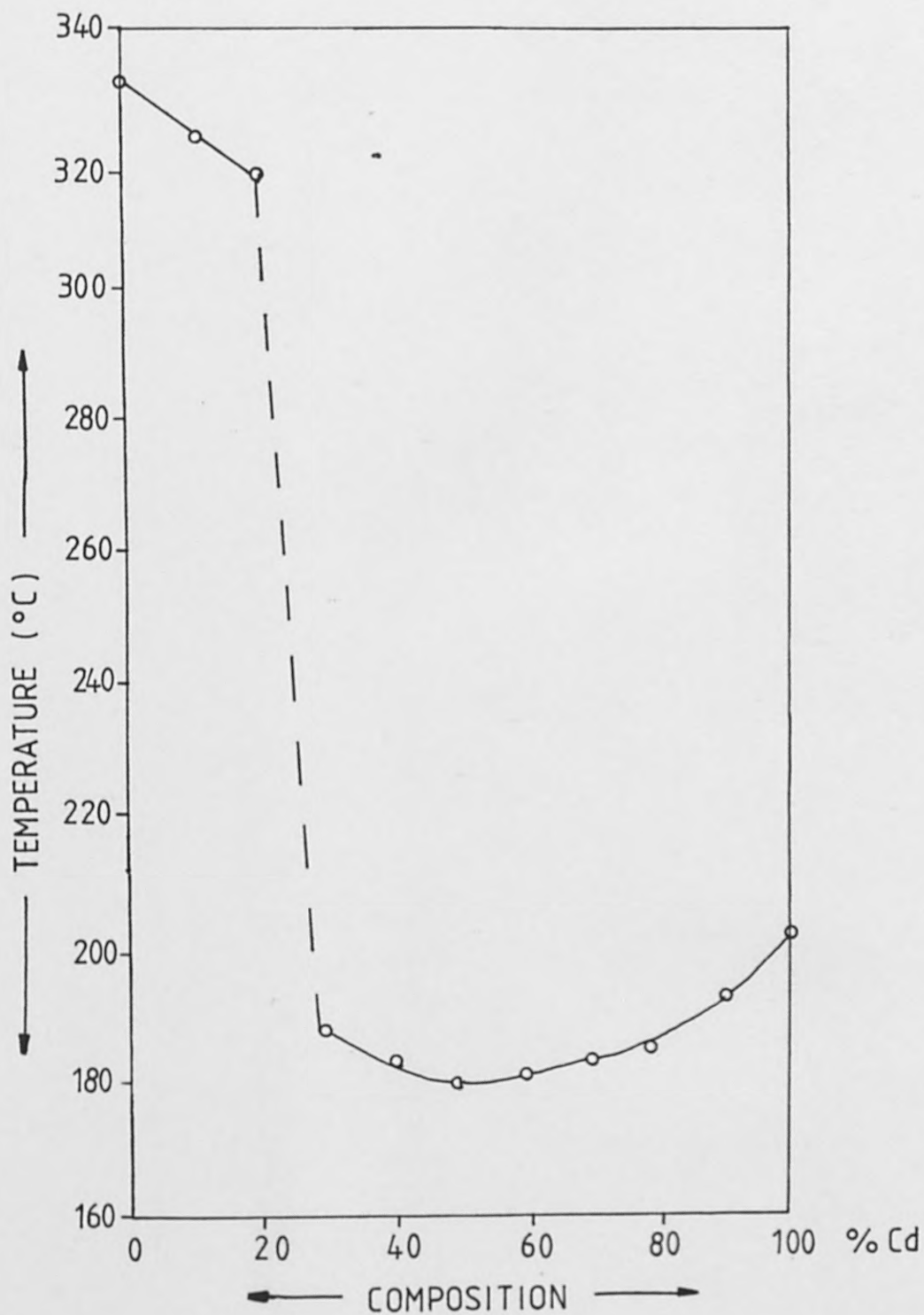


Fig. 5.1(a). Partial Phase Diagram of  $\text{CsPbI}_3:\text{CsCdI}_3$  system, showing the solidus/liquidus line.

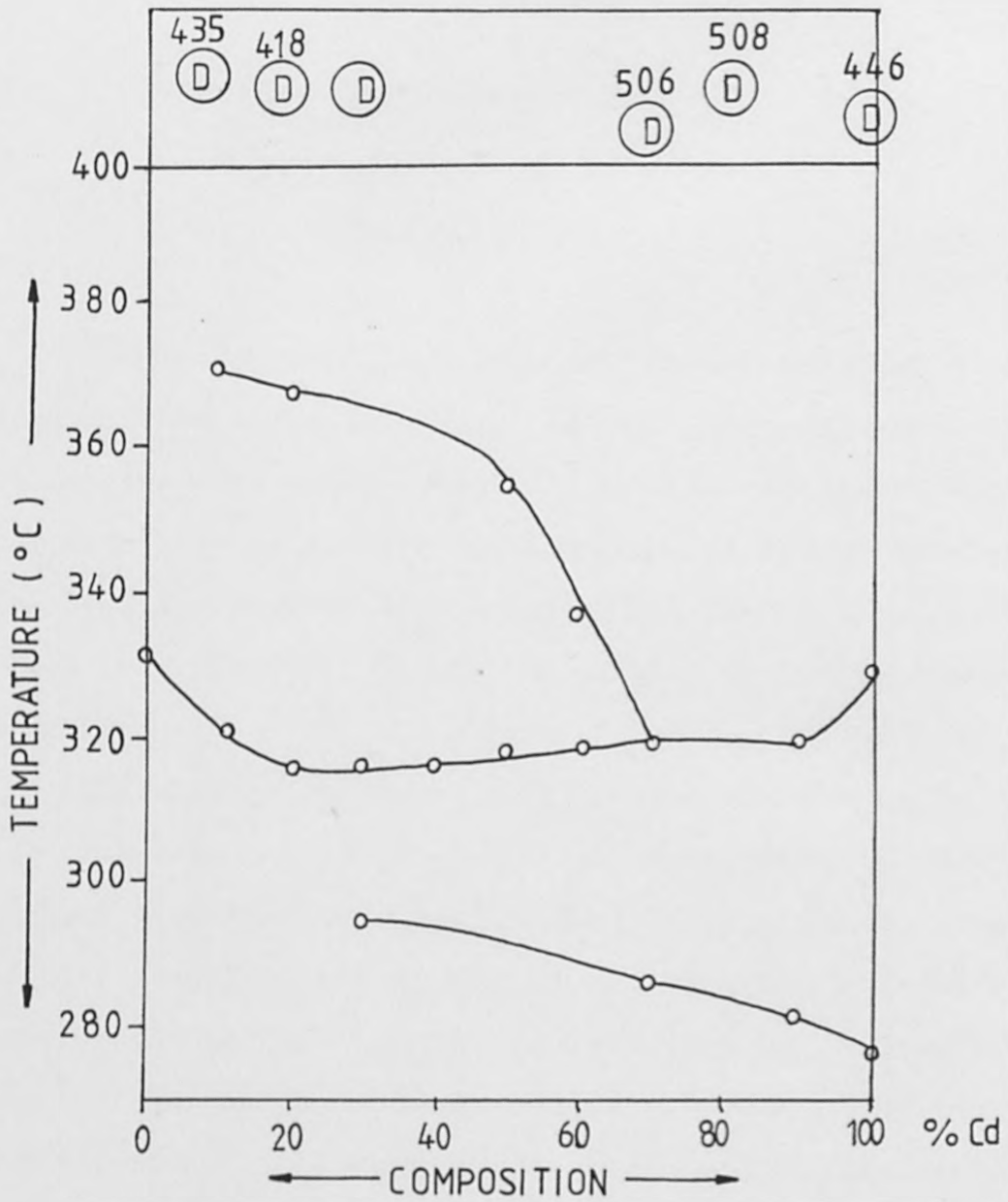


Fig. 5.1(b). Partial Phase diagram of CsPbI<sub>3</sub>:CsCdI<sub>3</sub> system, showing reactions within the liquidus phase.

in the x-ray data. From 315 - 375°C reactions occurred within the liquidus phase (Fig 5.1 (b)) which were not identified. The phases decomposed in the temperature range 400 - 550°C.

#### 5.1.4. Optical Properties of $\text{CsPb}_{1-x}\text{Cd}_x\text{I}_3$ System

##### Absorption Spectra

The absorption spectra of the samples were recorded as described in Section 4.1. In each case a single sharp absorption edge was observed and this is consistent with the formation of a series of homogenous mixtures in which the lead and cadmium are randomly distributed throughout the M (II) sites of the lattice to give an "average metal" effect.

The absorption edges shift towards lower energies as the composition moves away from the pure phases to give a minimum of 2.46eV at  $x = 0.90$  (Table 5.3, Fig 5.2). The initial red shift may be readily interpreted in terms of a progressive reduction in the optical band gap as lead ions are replaced by the smaller cadmium (II) ions, 1.20 and 0.97Å respectively, with a concurrent lattice contraction. This contraction will increase the self-overlap between the iodine d-states and any overlap of the non-bonding lead  $6s^2$  orbitals with the halide orbitals and thus give rise to lower energy transitions.

	Optical Energy $E_{\text{abs}} /$ (eV) $\pm$ 0.03	Energy Gap $E_{\text{lum}} /$ (eV) $\pm$ 0.05	Bulk Conductivity $\sigma / \Omega^{-1} \text{ cm}^{-1}$	Surface Conductivity $\sigma / \Omega^{-1} \text{ cm}^{-1}$
CsPbI <sub>3</sub>	2.76	1.734	5.07 x 10 <sup>-4</sup>	2.25 x 10 <sup>-7</sup>
CsPb <sub>.9</sub> Cd <sub>.1</sub> I <sub>3</sub>	2.737	1.733	2.31 x 10 <sup>-10</sup>	—————
CsPb <sub>.3</sub> Cd <sub>.2</sub> I <sub>3</sub>	2.72	1.735	2.14 x 10 <sup>-10</sup>	5.64 x 10 <sup>-8</sup>
CsPb <sub>.7</sub> Cd <sub>.3</sub> I <sub>3</sub>	2.68	1.744	1.19 x 10 <sup>-9</sup>	—————
CsPb <sub>.6</sub> Cd <sub>.4</sub> I <sub>3</sub>	2.68	1.754	5.58 x 10 <sup>-10</sup>	1.18 x 10 <sup>-7</sup>
CsPb <sub>.5</sub> Cd <sub>.5</sub> I <sub>3</sub>	2.68	1.751	3.69 x 10 <sup>-9</sup>	1.25 x 10 <sup>-7</sup>
CsPb <sub>.4</sub> Cd <sub>.6</sub> I <sub>3</sub>	2.65	1.68	3.06 x 10 <sup>-9</sup>	2.27 x 10 <sup>-7</sup>
CsPb <sub>.3</sub> Cd <sub>.3</sub> I <sub>3</sub>	2.55	1.687	1.5 x 10 <sup>-9</sup>	1.52 x 10 <sup>-7</sup>
CsPb <sub>.2</sub> Cd <sub>.8</sub> I <sub>3</sub>	2.475	1.754	6.51 x 10 <sup>-9</sup>	3.24 x 10 <sup>-7</sup>
CsPb <sub>.12</sub> Cd <sub>.88</sub> I <sub>3</sub>	2.45	1.744	1.21 x 10 <sup>-9</sup>	9.09 x 10 <sup>-8</sup>
CsPb <sub>.1</sub> Cd <sub>.9</sub> I <sub>3</sub>	2.446	1.746	1.05 x 10 <sup>-9</sup>	—————
CsPb <sub>.07</sub> Cd <sub>.93</sub> I <sub>3</sub>	2.47	1.645	5.67 x 10 <sup>-10</sup>	5.01 x 10 <sup>-8</sup>
CsPb <sub>.05</sub> Cd <sub>.95</sub> I <sub>3</sub>	2.49	1.68	3.15 x 10 <sup>-10</sup>	1.07 x 10 <sup>-7</sup>
CsPb <sub>.02</sub> Cd <sub>.98</sub> I <sub>3</sub>	2.88	1.681	4.07 x 10 <sup>-10</sup>	3.98 x 10 <sup>-7</sup>
CsPb <sub>.01</sub> Cd <sub>.99</sub> I <sub>3</sub>	2.95	1.744	1.16 x 10 <sup>-10</sup>	1.08 x 10 <sup>-7</sup>
CsCdI <sub>3</sub>	3.31	1.681	9.36 x 10 <sup>-9</sup>	7.96 x 10 <sup>-7</sup>

Table 5.3. Data for the CsPbI<sub>3</sub> : CsCdI<sub>3</sub> System.



## Photoluminescence Spectra

Samples of each of the compositions in the  $\text{CsPb}_{1-x}\text{Cd}_x\text{I}_3$  system were examined for luminescence at room temperature and at 80K. No emission was observed at room temperature for any of the phases, but they all showed a blue/green luminescence at 80K. The spectra obtained at 80K showed a pronounced low energy "tail" and a high energy "emission edge". A shoulder at 648nm observed in many spectra was found to be an artifact of the monochromator system.

The energies of the maxima of the principal emission bands show a similar trend to the absorption edges with a shift in the emission maxima occurring at  $x = 0.93$ , but this time gradually decreasing in energy to  $\text{CsCdI}_3$  (Fig 5.2, Table 5.4). When  $x = 0$  to 0.5 a single sharp emission is observed at 1.73eV with a half width of approximately 0.05eV. In the cadmium rich phases this band is present only as a shoulder. This single sharp emission is attributable to the  $6s^1p^1 \rightarrow 6s^2, 1s_0 - 3p_1$ , transition of the  $\text{Pb}^{2+}$  ion, previously observed in  $\text{CsPbCl}_3$  and  $\text{CsPbBr}_3$ <sup>(8)</sup>. This transition, as would be expected, is virtually unaffected by changes in composition until  $x = 0.93$  when the emission due to pure  $\text{CsCdI}_3$  is observed.

Sample	Band Maxima 80K (eV)	Other Peaks (eV)
CsPbI <sub>3</sub>	1.734	
CsRb <sub>.9</sub> Cd <sub>.1</sub> I <sub>3</sub>	1.733	
CsPb <sub>.8</sub> Cd <sub>.2</sub> I <sub>3</sub>	1.735	
CsPb <sub>.7</sub> Cd <sub>.3</sub> I <sub>3</sub>	1.744	
CsPb <sub>.6</sub> Cd <sub>.4</sub> I <sub>3</sub>	1.754	
CsPb <sub>.5</sub> Cd <sub>.5</sub> I <sub>3</sub>	1.751	
CsPb <sub>.4</sub> Cd <sub>.6</sub> I <sub>3</sub>	1.754	1.68
CsPb <sub>.3</sub> Cd <sub>.7</sub> I <sub>3</sub>	1.687	1.73
CsPb <sub>.2</sub> Cd <sub>.8</sub> I <sub>3</sub>	1.754	1.97
CsPb <sub>.4</sub> Cd <sub>.88</sub> I <sub>3</sub>	1.744	
CsPb <sub>.1</sub> Cd <sub>.9</sub> I <sub>3</sub>	1.746	1.94
CsPb <sub>.07</sub> Cd <sub>.93</sub> I <sub>3</sub>	1.645	
CsPb <sub>.05</sub> Cd <sub>.95</sub> I <sub>3</sub>	1.680	
CsPb <sub>.02</sub> Cd <sub>.08</sub> I <sub>3</sub>	1.680	2.17
CsPb <sub>.01</sub> Cd <sub>.99</sub> I <sub>3</sub>	1.744	
CsCdI <sub>3</sub>	1.681	

Table 5.4. Emission Spectra of CsPb<sub>1-x</sub>Cd<sub>x</sub>I<sub>3</sub>.

The photoconductive properties of each phase in the,  $\text{CsPb}_x\text{Cd}_{1-x}\text{I}_3$ , series was investigated. Two methods of sample preparation were used, viz: (1) a pelleted sample for use in the 'B.N.C.' sample holder (described in Section 3.2.4.) (2) a mull of the sample was made with acetone and painted evenly over the circuit board sample holder (Section 3.2.4.)

The samples were illuminated with light in the frequency range 380-1000nm using the apparatus previously described (Section 3.2.). Illumination of the samples caused no observable deviation from the dark conductivity.

The failure to detect photoconductivity does not mean that the materials are not photoconductors but that any photoconductive response they may show is either outside the range of the light frequency or too weak for detection. In support of this observation, Møller<sup>(2)</sup> in his work on  $\text{CsPbX}_3$  (X = Cl, Br, I) reported that all the caesium trihaloplumbates show a photoconductive response in the region of their absorption edges. Thus,  $\text{CsPbI}_3$  would be expected to show a response in the red, at about 342nm. The absorption edges of all the phases in this series lie within the range 410-342nm. Although the lower limit of the lamp is 380nm, the energy output from the lamp drops off rapidly below 600nm, giving only 3% of the maximum energy at 400nm. Consequently, any photoconductive response that might exist is either outside the range of the lamp or there is insufficient energy to

produce a detectable signal. Another factor which may well effect a photoconductive response in the cadmium rich phases is temperature. Cadmium iodide single crystals show two photoconductive bands at 210nm and 384nm, attributed to excitation of carriers to localized levels<sup>(27)</sup>, but only when the temperature is > 335K or 120-200K.

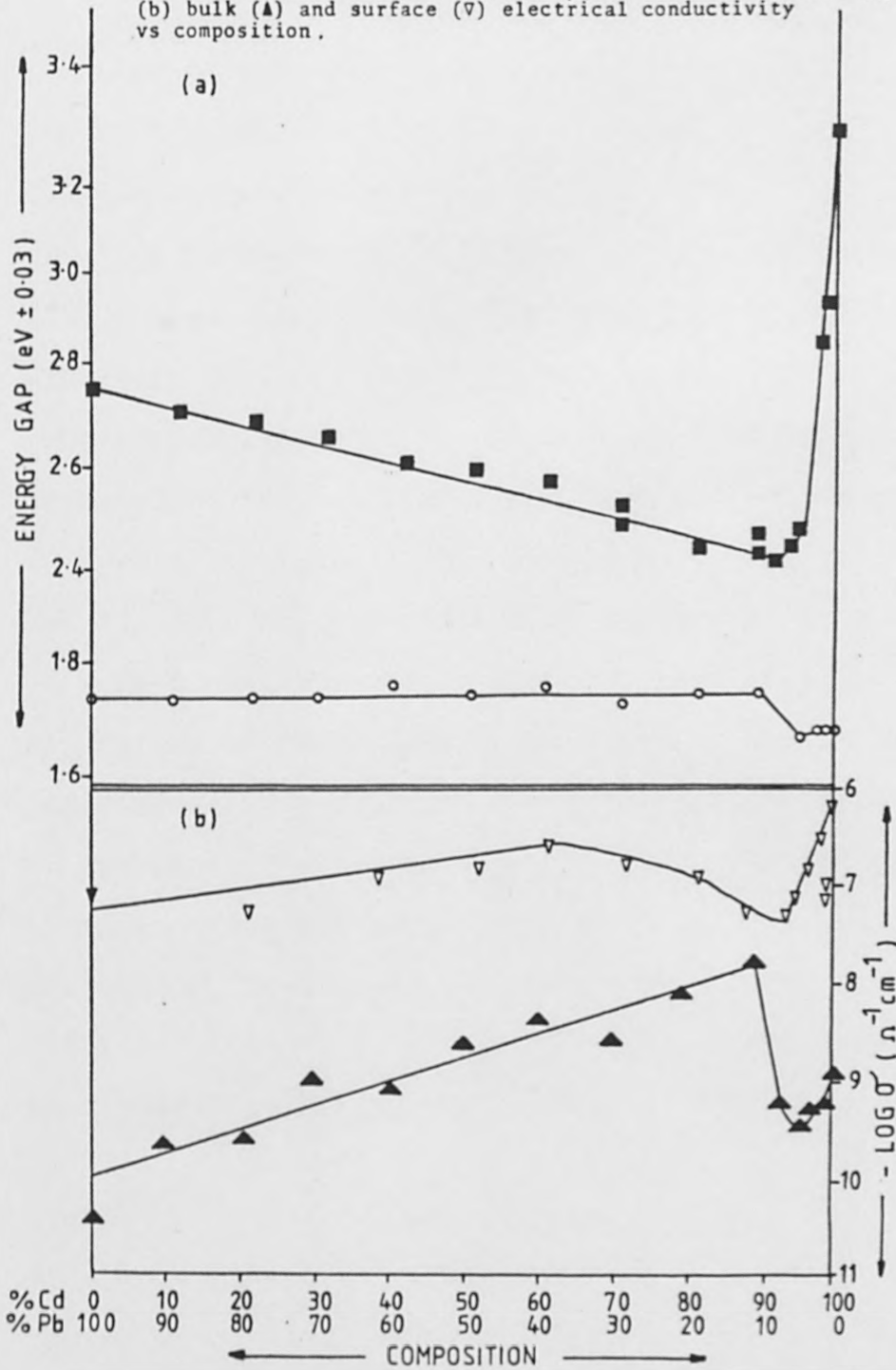
It is not possible to conclude from this negative result that the optical band gap is not the band gap associated with the conductivity of  $\text{CsPb}_x\text{Cd}_{1-x}\text{I}_3$ .

#### 5.1.6. Room Temperature Electrical Conductivity Measurements

Room temperature bulk and surface electrical conductivity measurements were made on pellets of the dry, powdered samples, using the apparatus described in Sections 4.1.3 & 3.3 respectively. The results are shown in Fig 5.2 and Table 5.3 After each measurement the circuit polarity was reversed to ensure that conduction was not ionic or that the sample had become polarised. Discs showing either of these effects were discarded and the measurements repeated on a fresh disc.

The bulk conductivity for this series of samples lies in the region  $10^{-7} - 10^{-10} \Omega^{-1} \text{cm}^{-1}$ , while surface conduction ranges from  $10^{-6} - 10^{-7} \Omega^{-1} \text{cm}^{-1}$ . Although varying in magnitude the two sets of data show the same trend across the series and mirror the optical band gap (Fig 5.2). As the band gap decreases in energy from  $x = 0$  to 0.9 the conductivity increases, and as it increases in energy from

Fig. 5.2. CsPbI<sub>3</sub>:CsCdI<sub>3</sub> system (a) showing energy gap as determined from absorption spectra (■) and emission spectra (○) (b) bulk (▲) and surface (▽) electrical conductivity vs composition.



$x = 0.9$  to  $1.0$  the conductivity falls.

If the semiconducting properties arise from the donation of lead 6s-electron density to a conduction band level, formed by the overlap of iodide d-states, then, as cadmium replaced lead, the lattice contraction would be paralleled by an increase in electrical conductivity until the lead concentration became too dilute to donate sufficient electrons into the band system. At the same time a progressive reduction in the optical band gap would be observed as long as sufficient lead were present to produce an observable transition. Reference to Fig 5.2. shows that the trends consistent with this hypothesis were observed.

On the other hand if these properties arise from the population of conduction band levels by iodide electrons the semiconducting properties would be expected to be unaffected by the lead:cadmium ratio per se while only changes in the lattice parameters would lead to changes in the semiconducting properties. Since only small variations in the x-ray data over most of the composition range have been observed, this hypothesis is less likely.

## 5.2.                    The CsSnBr<sub>3</sub> : CsCdBr<sub>3</sub> System

To investigate the theory that the non-bonding electron pair is responsible for the semiconducting properties the related system CsSn<sub>1-x</sub>Cd<sub>x</sub>Br<sub>3</sub> was investigated. The semiconducting properties of CsSnBr<sub>3</sub> have been described <sup>(9)</sup>,

and those of the mixed system  $\text{CsSn}_{1-x}\text{Pb}_x\text{Br}_3$  investigated.<sup>(10)</sup> Since the ionic radii of  $\text{Cd}^{2+}$  and  $\text{Sn}^{2+}$  are very similar (0.97 and 0.93Å respectively) the addition of cadmium to  $\text{CsSnBr}_3$  would be expected to give information on the effects of the non-lone-pair ion in the lone-pair system.

#### 5.2.1. Sample Preparation

Samples were prepared from melts containing the appropriate molar ratios of the caesium, cadmium and tin (II) bromides by heating the mixture under an atmosphere of nitrogen. The colours of the products ranged from the black  $\text{CsSnBr}_3$  to brick-red  $\text{CsSn}_{.05}\text{Cd}_{.95}\text{Br}_3$  and white  $\text{CsCdBr}_3$ . The samples were stored in vacuo OVER SODIUM HYDROXIDE PELLETS.

#### 5.2.2. Analysis

Bromine was determined potentiometrically using  $\text{AgNO}_3$ ;  $\text{Sn}^{2+}$  by the Donaldson and Moser method<sup>(11)</sup> and  $\text{Cd}^{2+}$  by EDTA titration<sup>(12)</sup>. For the  $\text{Cd}^{2+}$  determination approximately 0.5g of sample was dissolved in dilute HCl and made up to 250 ml with water. A 25 ml aliquot was taken and adjusted to pH5 with hexamine, the solution was then titrated against ca. 0.05 M EDTA using xylenol orange indicator. The results are given in Table 5.5.

X-ray diffractograms were recorded for selected phases throughout the series. These show that the phases have the

Sample	% Cd	% Sn	% Br
$\text{CsSnBr}_3$		24.22 (24.16)	48.8 (48.79)
$\text{CsSn}_{.9}\text{Cd}_{.1}\text{Br}_3$	2.29 (2.29)	21.79 (21.77)	48.8 (48.83)
$\text{CsSn}_{.8}\text{Cd}_{.2}\text{Br}_3$	4.57 (4.59)	19.27 (19.38)	48.9 (48.91)
$\text{CsSn}_{.7}\text{Cd}_{.3}\text{Br}_3$	6.87 (6.89)	16.89 (16.98)	49.0 (48.98)
$\text{CsSn}_{.6}\text{Cd}_{.4}\text{Br}_3$	9.16 (9.20)	14.61 (14.57)	49.0 (49.04)
$\text{CsSn}_{.5}\text{Cd}_{.5}\text{Br}_3$	11.51 (11.51)	12.09 (12.16)	49.1 (49.10)
$\text{CsSn}_{.4}\text{Cd}_{.6}\text{Br}_3$	13.47 (13.83)	9.91 (9.74)	49.1 (49.16)
$\text{CsSn}_{.3}\text{Cd}_{.7}\text{Br}_3$	16.04 (16.16)	7.21 (7.31)	49.2 (49.23)
$\text{CsSn}_{.2}\text{Cd}_{.8}\text{Br}_3$	18.38 (18.49)	5.23 (4.88)	49.3 (49.29)
$\text{CsSn}_{.1}\text{Cd}_{.9}\text{Br}_3$	20.55 (20.83)	2.47 (2.44)	49.3 (49.36)
$\text{CsSn}_{.05}\text{Cd}_{.95}\text{Br}_3$	22.15 (22.00)	1.18 (1.22)	49.4 (49.39)
$\text{CsCdBr}_3$	23.60 (23.20)		49.4 (49.42)

Table 5.5. Analytical Results For  $\text{CsSn}_{1-x}\text{Cd}_x\text{Br}_3$  (Theoretical values are given in brackets).



CsSnBr<sub>3</sub> structure for  $x \leq 0.1$  and the CsCdBr<sub>3</sub> structure for other compositions, the lattice parameters remaining constant throughout.

### 5.2.3. Optical Properties

The absorption spectra were recorded as described in Section 4.1. . For each phase a single sharp absorption edge was observed, which shift to higher energies as the Sn:Cd ratio approached unity (Fig 5.3 & Table 5.6). A progressive red shift is observed from  $x = 0.4$  to 0.95 then a rapid increase in energy to  $3.22 \pm 0.03\text{eV}$  for CsCdBr<sub>3</sub>.

The initial increase in energy for phases containing less than 40% cadmium may result from more efficient overlap of the tin  $5s^2$  orbital with the bromine 4d orbital at low cadmium concentration.

The absorption spectra were repeated on the same samples after a period of nine months. The absorption edges were still sharp and the shift to higher energies as the Sn:Cd ratio approached unity, followed by a red shift then a rapid increase in energy to the pure CsCdBr<sub>3</sub> was again observed (Fig 5.3 & Table 5.6). However, the energy of the forbidden gap was found to have decreased. This may be due to absorbed water or the formation of impurity levels with aging.

The emission spectra of all phases were recorded at room temperature and 80K. None of the phases showed emission at room temperature but all luminesced at 80K. The cadmium

containing phases showed a single broad emission band at  $1.90 \pm 0.03\text{eV}$  and the pure  $\text{CsSnBr}_3$  had an intense red emission with a maximum at  $1.72 \pm 0.03\text{eV}$ , as previously observed<sup>(9)</sup>. The similarity of the position of the absorption edge of  $\text{CsSnBr}_3$  itself, and the cadmium containing phases, to the onset of the emission band (Table 5.6, Fig 5.3) indicates that the optical properties in the visible region are to be associated with direct band-to-band transitions. The band widths,  $0.08 - 0.11\text{eV}$  at 80K for  $\text{CsSnBr}_3$ , are consistent with this. If the optical properties are due to internal transitions the energy levels of the tin must be highly modified by the presence of the caesium, cadmium and bromine atoms with the lattices of  $\text{CsSn}_x\text{Cd}_{1-x}\text{Br}_3$  and related materials. Therefore, the observed transition must be a direct band-to-band transition (i.e. without phonon assistance) between two bands at the same position in K space. The width of the emission band implies a purely Heissenberg lifetime of the order  $10^{-14}$  seconds at 80K, a very small value, which suggests other factors may be involved in broadening the emission line. The broadening of the emission line is generally said to occur when the  $s^2$  ion occupies a large hole in the host lattice or when the site symmetry of the  $s^2$  ion is lower than cubic. However, the exact cause of line broadening is as yet unclear.

The possibility of impurity spectra may be discarded for two reasons; (1) the emission spectra of  $\text{CsSn}_x\text{Cd}_{1-x}\text{Br}_3$

	Energy Gap from Reflectance Spectra		Energy Gap from Luminescence	Bulk Conductivity $\sigma$	Surface Conductivity
	Fresh Samples $eV \pm 0.03$	Aged Samples $eV \pm 0.03$			
	$E_{lum}/eV \pm 0.03$	$\sigma/\Omega^{-1} \text{ cm}^{-1}$	$\sigma/\Omega^{-1} \text{ cm}^{-1}$		
CsSnBr <sub>3</sub>	1.80	1.70	1.72	$8.78 \times 10^{-4}$	$2.31 \times 10^{-1}$
CsSn <sub>.9</sub> Cd <sub>.1</sub> Br <sub>3</sub>	1.94	1.765	1.90	$5.02 \times 10^{-7}$	$1.03 \times 10^{-3}$
CsSn <sub>.8</sub> Cs <sub>.2</sub> Br <sub>.3</sub>	2.00	1.79	1.88	$3.05 \times 10^{-7}$	$5.49 \times 10^{-6}$
CsSn <sub>.7</sub> Cd <sub>.3</sub> Br <sub>3</sub>	2.06	1.82	1.89	$1.72 \times 10^{-7}$	
CsSn <sub>.6</sub> Cd <sub>.4</sub> Br <sub>3</sub>	2.19	1.85	1.91	$1.66 \times 10^{-7}$	$6.59 \times 10^{-6}$
CsSn <sub>.5</sub> Cd <sub>.5</sub> Br <sub>3</sub>	2.12	1.86	1.91	$7.96 \times 10^{-8}$	$3.68 \times 10^{-6}$
CsSn <sub>.4</sub> Cd <sub>.6</sub> Br <sub>3</sub>	2.095	1.84	1.91	$5.51 \times 10^{-8}$	$6.24 \times 10^{-6}$
CsSn <sub>.3</sub> Cd <sub>.7</sub> Br <sub>3</sub>	2.05	1.82	1.88	$5.04 \times 10^{-8}$	$7.42 \times 10^{-8}$
CsSn <sub>.2</sub> Cd <sub>.8</sub> Br <sub>3</sub>	1.97	1.78	1.90	$2.04 \times 10^{-8}$	$2.14 \times 10^{-6}$
CsSn <sub>.1</sub> Cd <sub>.9</sub> Br <sub>3</sub>	1.94	1.77	1.86	$8.21 \times 10^{-8}$	$1.23 \times 10^{-7}$
CsSn <sub>.05</sub> Cd <sub>.95</sub> Br <sub>3</sub>	1.93	1.76		$1.02 \times 10^{-8}$	
CsSn <sub>.02</sub> Cd <sub>.98</sub> Br <sub>3</sub>	2.34	1.95	1.83	$1.11 \times 10^{-8}$	$1.66 \times 10^{-8}$

Table 5.6. Data for CsSnBr<sub>3</sub>:CsCdBr<sub>3</sub> System.

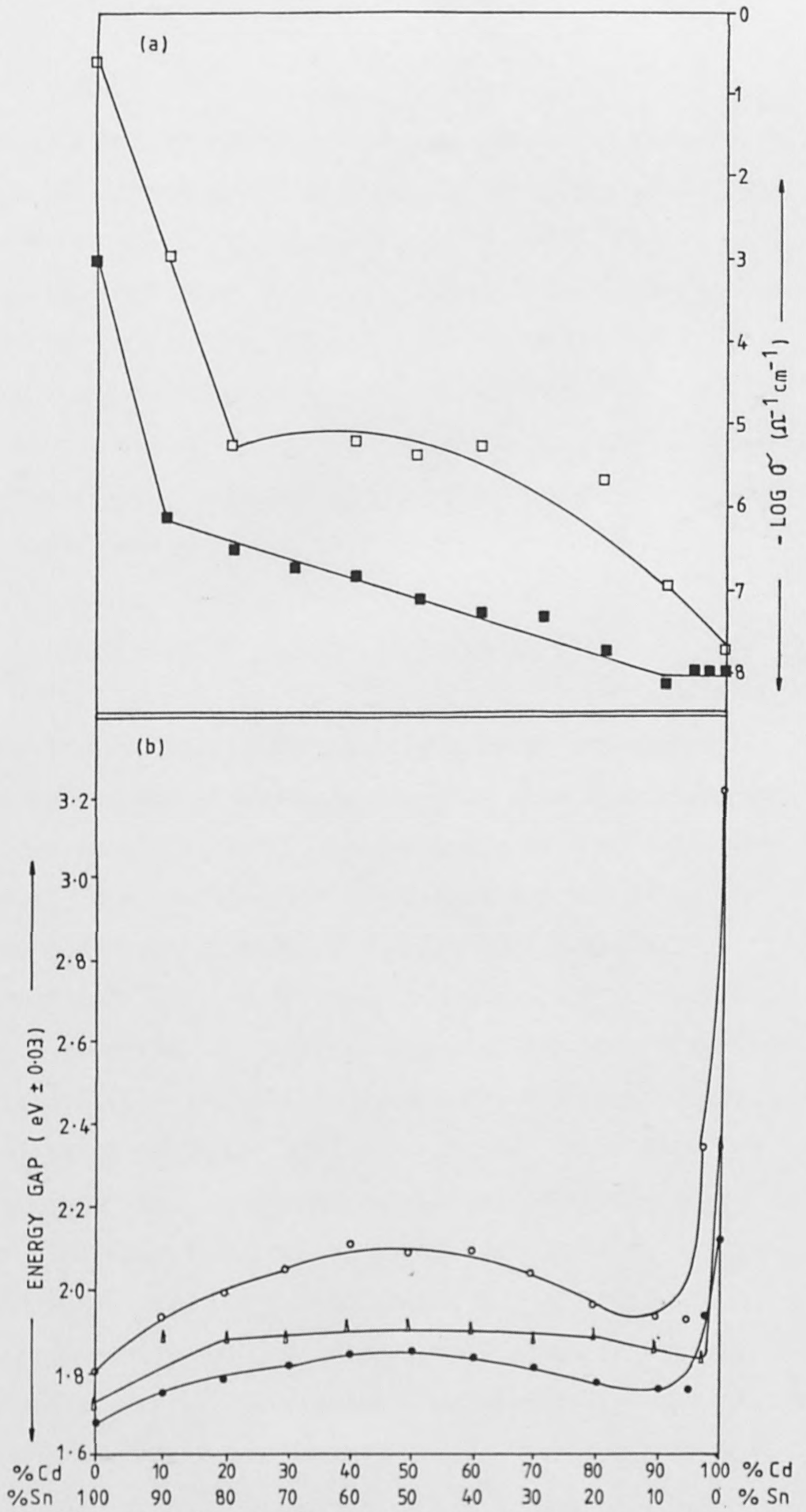


Fig.5.3. CsSnBr<sub>3</sub>:CsCdBr<sub>3</sub> system (a) surface ( $\square$ ) and bulk ( $\blacksquare$ ) electrical conductivities (b) energy gaps determined from absorption spectra, new ( $\circ$ ) aged ( $\bullet$ ) samples, and emission spectra ( $\blacktriangle$ ) vs. composition.

appears at the same energy for each individual set of samples; (2) emission spectra are most often due to impurities in a host lattice<sup>(13)</sup> but the absorption spectrum of a material is a bulk property and is unaffected by small levels of impurities. Since the absorption and emission spectra of  $\text{CsSn}_x\text{Cd}_{1-x}\text{Br}_3$  are in reasonably good agreement the emission spectra should arise from the same bulk property effect as the absorption spectra i.e. a direct band-to-band transition.

#### 5.2.4. Electrical Conductivity Measurements

The room temperature bulk conductivity measurements carried out on the phases  $\text{CsSn}_x\text{Cd}_{1-x}\text{Br}_3$  show a decrease in electrical conductivity ( $\sigma$ ) as the proportion of cadmium increases. The conductivity falls from a value of  $10^{-3}$   $\text{ohm}^{-1} \text{cm}^{-1}$  for the pure cubic  $\text{CsSnBr}_3$  to a value of  $10^{-8}$   $\text{ohm}^{-1} \text{cm}^{-1}$  for  $\text{CsCdBr}_3$  (Fig 5.3, Table 5.6). With reference to Fig 5.3 it may be seen that the bulk electrical conductivities for the whole series can be divided into three distinct regions. When  $x < 0.1$  the phases have the  $\text{CsSnBr}_3$  band structure and corresponding conductivities. However, as cadmium is introduced into the  $\text{CsSnBr}_3$  lattice, the band gap widens (Fig 5.3) and for  $0.1 < x < 0.95$  the conductivity falls exponentially, which tends to suggest that these phases have a similar band structure. The effect of the tin  $5s^2$  electrons becomes negligible when  $x \geq 0.95$

and the conductivity rises slightly to  $10^{-8} \Omega^{-1} \text{ cm}^{-1}$  for pure  $\text{CsCdBr}_3$ . The changes in the optical band gap are not reflected in the bulk electrical conductivity measurements and this indicates that the two processes arise from different transitions. The observed decrease in conductivity with reduced  $\text{Sn}^{2+}$  indicates that the tin  $5s^2$  electrons are responsible for electrical conduction in the bulk samples.

Surface conductivity measurements were also recorded, for each phase in the series nine months after preparation, using the four probe apparatus previously described. This technique measures the conductivity along the surface of the compacted sample rather than the bulk conductivity obtained by conventional methods, and described above.

The values of the conductivity obtained in this way again show three distinct regions (Table 5.6.). However, the limits of each region are shifted in comparison with the bulk conductivity measurements (Fig 5.3.).

A rapid decrease of  $10^{-4} \text{ ohm}^{-1} \text{ cm}^{-1}$  is observed from  $\text{CsSnBr}_3$  to  $x = .2$ . It is possible to calculate the difference in energy gap between these two phases since:-

$$\sigma = Ne (\mu_e + \mu_h) e^{-E_g/2kT} \quad (5.1.)$$

where

$$N = 2 \left( \frac{2\pi m^* kT}{h^2} \right)^{3/2} \quad (5.2.)$$

As  $m^*$  depends only on the shape of the band it can be assumed that  $m_1^* = m_2^* = m^*$ .

Therefore

$$\log \frac{\sigma_1}{\sigma_2} = \log \left( \frac{\mu e_1 - \mu h_1}{\mu e_2 - \mu h_2} \right) - \left( \frac{E_{g1} - E_{g2}}{2kT} \right)^{2.303} \quad (5.3.)$$

The difference in energy of the forbidden gap between  $\text{CsSnBr}_3$  and  $\text{CsSn}_{.8}\text{Cd}_{.2}\text{Br}_3$  is found to be significant, which explains the rapid decrease in electrical conductivity observed in this region. The conductivity falls gradually from  $x = 0.2$  to  $0.8$ . There is no significant change in the band gap over this region which indicates that the decrease in electrical conductivity is due to the reduced tin (II) content. In the third region, when  $x > 0.8$ , the contribution of the tin (II)  $5s^2$  electrons to the electrical conductivity is negligible as the probability of two tin nearest neighbours is less than 1%, and the conductivity falls by  $10^{-2} \text{ ohm}^{-1} \text{ cm}^{-1}$ .

The  $^{119}\text{Sn}$  Mössbauer data for three phases in the  $\text{CsSn}_x\text{Cd}_{1-x}\text{Br}_3$  system (Table 5.7) show an increase in chemical shift with increased cadmium content. The higher chemical shift and narrower linewidth of  $\text{CsSn}_{.3}\text{Cd}_{.7}\text{Br}_3$  is consistent with an increase in the electrostatic character of the longer tin-halide bonds. This means that as the proportion of cadmium is increased, the tin (II) becomes more ionic and the  $5s^2$  electrons are more localised and

less labile. This would result in a decrease in electrical conductivity with increased cadmium content. The Mössbauer data therefore provide confirmation of the electrical conductivity data.

Sample	$\sigma$ (mm/sec)	$\Gamma$ (mm/s)	$\Delta$ (mm/s)
$\text{CsSn}_{.7}\text{Cd}_{.3}\text{Br}_3$	4.05 ( $\pm$ 0.02)	1.12 ( $\pm$ 0.07)	0
$\text{CsSn}_{.5}\text{Cd}_{.5}\text{Br}_3$	3.99 ( $\pm$ 0.03)	1.74 ( $\pm$ 0.1 )	0
$\text{CsSn}_{.3}\text{Cd}_{.7}\text{Br}_3$	4.22 ( $\pm$ 0.07)	1.0 ( $\pm$ 0.2)	0

Table 5.7. Mössbauer Data for  $\text{CsSn}_x\text{Cd}_{1-x}\text{Br}_3$  Phases.

### 5.2.5.                      Photoconductivity

The band gap measurements in the previous sections suggest that the optical and electrical properties of the  $\text{CsSn}_x\text{Cd}_{1-x}\text{Br}_3$  series arise from different processes. If the conductivity and optical properties did arise from the same process  $\text{CsSn}_x\text{Cd}_{1-x}\text{Br}_3$  phases should exhibit photoconductivity when illuminated with radiation of energy greater or equal to the energy of the forbidden band.

The two processes of luminescence and photoconductivity impose conflicting requirements. Good luminescent materials require a long free carrier lifetime, i.e. slow recombination,



although the rate of recombination can be changed by the presence of impurities or defects, also if luminescence involves localised centres (e.g. impurities) no photoconductivity will be observed at that wavelength. The  $\text{CsSn}_x\text{Cd}_{1-x}\text{Br}_3$  materials would be expected to be poor photoconductors for either of three reasons: (1) they are strongly luminescent materials with a short excited state lifetime (2) if they have a narrow band gap the conductivity i.e. free carrier density, is already high and illumination would cause only a small deviation from dark conductivity (3)  $\text{CsSnBr}_3$  is known not to photoconduct<sup>(9)</sup>.

Photoconductivity measurements were carried out on compacted powder and "thin film" samples for each phase in the series using the apparatus previously described. None of the phases showed photoconductivity within the range 380 - 1000nm. The negative result does not mean that the materials are not photoconductors, only that any photoconductivity is too weak to detect. However, the absence of photoconductivity does indicate that the optical band gap is not the band gap associated with conductivity.

The data collected for this systems indicates that the semiconducting properties arise from the non-bonding  $ns^2$  electrons of Sn (II).

### 5.3.

### The CsSnI<sub>3</sub> : CsPbI<sub>3</sub> System

In previous work on the cesium group (IV) iodides CsSnI<sub>3</sub> and CsPbI<sub>3</sub> have been shown to be isomorphous<sup>(2)</sup>. CsSnI<sub>3</sub> has a yellow, low temperature, orthorhombic form and a black, tetragonal, high temperature modification<sup>(6,14)</sup>. The lead complex also exists in two modifications, a yellow orthorhombic form which transforms to a black distorted perovskite structure at high temperatures.<sup>(15)</sup> Black, cubic phases of the type CsSnBr<sub>3-x</sub>I<sub>x</sub> (x = 0 - 0.24) have been obtained from cooled melts and the <sup>119</sup>Sn Mössbauer data for these phases suggest that the Sn(II) occupies an O<sub>h</sub> symmetry site<sup>(16)</sup>. As CsSnI<sub>3</sub> is rapidly oxidised to Cs<sub>2</sub>SnI<sub>6</sub>, only limited data was collected for this system and the CsSnI<sub>3</sub>:CsCdI<sub>3</sub> system was not investigated.

#### 5.3.1.

#### Preparation

All the samples were prepared by fusion of the appropriate molar ratios of the starting materials, in an inert atmosphere. The colours of the products ranged from yellow CsSnI<sub>3</sub> to yellow/green CsPbI<sub>3</sub>. CsSnI<sub>3</sub> underwent a colour change from yellow to black on storage for 2-3 days, due to oxidation and disproportionation to Cs<sub>2</sub>SnI<sub>6</sub>. When the black CsSnI<sub>3</sub> was melted in an atmosphere of nitrogen it failed to regain its original yellow colour and, remained black. The mixed metal phases showed the colour change, but

to a lesser degree for  $x = 1$  to 3.

### 5.3.2.

### Analysis

Tin was determined by the Donaldson and Moser method<sup>(11)</sup>; lead by titration against EDTA using xylenol orange indicator after the sample solution had been adjusted to pH6 with a hexamine buffer; and bromine potentiometrically with  $\text{AgNO}_3$ .

### 5.3.3.

### X-Ray Studies

X-ray diffractograms were obtained for each sample in the series.  $\text{CsSnI}_3$  and  $\text{CsPbI}_3$  showed very similar patterns as would be expected from their isomorphous relationship. The mixed metal phases gave patterns to suggest that they have similar structures to the parent compounds.

Yellow  $\text{CsSnI}_3$  has a perovskite-like lattice with orthorhombic symmetry, in which  $\text{Sn}^{2+}$  is at the centre of a octahedron of iodine atoms. The octahedra, linked by caesium ions, form double chains along the c-axis. The lattice parameters might be expected to increase as tin (II) is replaced by the larger lead (II) ion, 0.93 and 1.20Å respectively. However, the results obtained show that the cell size remains constant as  $\text{Pb}^{2+}$  is introduced. The reported length of the c axis is 4.765(2)Å, nearly twice the ionic radius of  $\text{I}^-$ ,  $r = 2.20\text{Å}$ . It therefore seems likely that iodine determines the cell size in a close packed array with metal ions occupying spaces.

The spectra obtained for each sample, as described previously, showed absorption edges indicative of an interband transition. The effect of varying the ratio of Sn:Pb in the mixed phases is reflected by the position of the absorption edge (Fig 5.4 & Table 5.8). The x-ray data showed no apparent change in cell dimensions and this is supported by the optical band gap, which narrows progressively from the parent compounds,  $\text{CsSnI}_3$  and  $\text{CsPbI}_3$  respectively, to a minimum of  $2.42\text{eV} \pm 0.05$  between  $0.1 <x> 0.7$ . This differs from the  $\text{CsSn}_x\text{Pb}_{1-x}\text{Br}_3$  system<sup>(17)</sup>, in which the optical band gap narrows regularly as replacement of lead (II) by tin (II) contracts the lattice and reduces the average interatomic distances, allowing increasing overlap between the tin-5s and bromine 4d-orbitals and hence increasing the conductivity.

All the absorption spectra are smooth curves with well defined absorption edges indicating a series of homogenous mixtures in which the lead and tin atoms are randomly distributed throughout the  $\text{M}^{\text{II}}$  sites of the lattice to give an 'average metal' effect.

The  $^{119}\text{Sn}$  Mössbauer data for the  $\text{CsSn}_x\text{Pb}_{1-x}\text{I}_3$  system (Table 5.9) show a linear increase in chemical shift with increasing lead content. The higher chemical shifts are consistent with an increase in the electrostatic character of the longer tin-halide bonds and the narrow linewidths provide confirmation of the undistorted octahedral

environment of the tin (II). Even in the  $\text{CsSn}_{.3}\text{Pb}_{.7}\text{I}_3$  phase the chemical shift is relatively low and the narrow linewidth provides evidence for the loss of s-electron density to the solid state band.

Sample	$\delta$ (mm/s) $\pm 0.02$	$\Delta$ (mm/s)	$\Gamma$ (mm/s) $\pm 0.03$
$\text{CsSnI}_3$	1.92	0	0.81
$\text{CsSn}_{.6}\text{Pb}_{.4}\text{I}_3$	1.96	0	0.68
$\text{CsSn}_{.3}\text{Pb}_{.7}\text{I}_3$	2.17	0	0.55

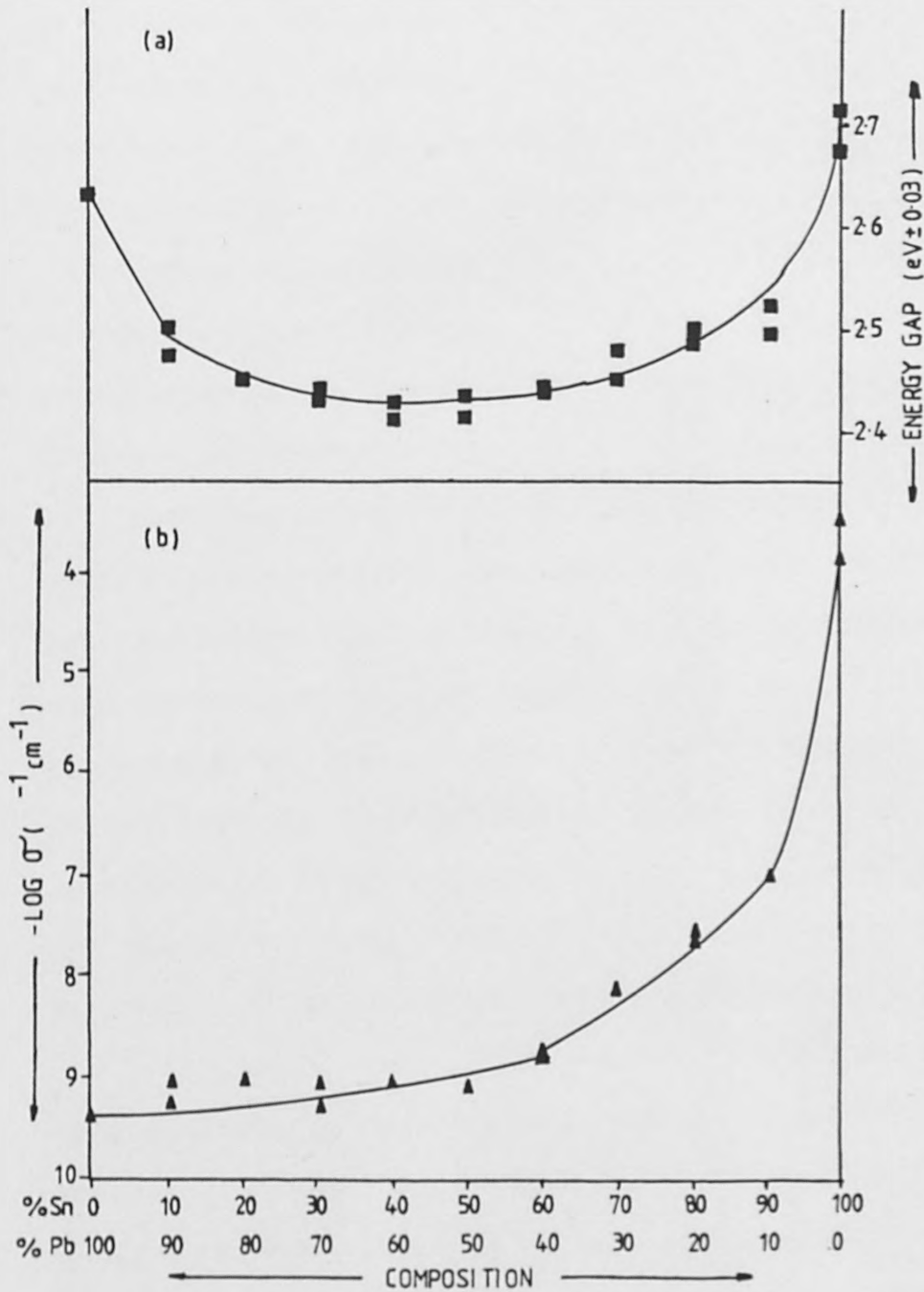
Table 5.9. Mössbauer Data for  $\text{CsSn}_x\text{Pb}_{1-x}\text{I}_3$  Phases

### 5.3.5. Room Temperature Electrical Conductivity Measurements

Room temperature bulk electrical conductivity measurements were made on pellets of the dry, powdered samples, using the apparatus described previously (Section 4.1.3). For each sample the resistance was measured over a range of applied voltages, typically 0.2 - 1.0V, and the conductivity determined graphically. (Table 5.8)

The conductivities for this series of compounds can be divided into three distinct regions (Fig 5.4). The

Fig.5.4. (a) Plot of absorption edge (eV) vs composition  
 (b) Plot of electrical conductivity vs composition for  
 the CsSnI<sub>3</sub>:CsPbI<sub>3</sub> system.



conductivity of the parent lead compound,  $\text{CsPbI}_3$ , increases by  $10 \Omega^{-1} \text{ cm}^{-1}$  as 20% of the lead (II) is replaced by tin (II). Concurrent with this increase in conductivity is a decrease of 0.19eV in the energy of the optical band gap. When less than 20% of the lead has been replaced by tin, the  $\text{Pb}^{2+}$  is in an octahedral environment, and it is the band structure of  $\text{CsPbI}_3$  which dominates. The tin (II) ions would occupy vacancies in the  $\text{CsPbI}_3$  lattice, however, they may form an impurity level in the  $\text{CsPbI}_3$  band structure, which would explain the decrease in optical band gap and the increase in conductivity.

Both the conductivity and optical band gap remain approximately constant for  $0.2 \leq x \leq 0.6$ . At tin (II) concentrations greater than  $x = 0.6$  the conductivity rises progressively to that of  $\text{CsSnI}_3$ , in spite of, the accompanying increase in the width of the optical band gap. In the high tin (II) containing phases, the tin (II) occupies an octahedral site, as shown by the  $^{119}\text{Sn}$  Mössbauer data, optimising overlap of tin ns-orbitals and empty iodine nd-orbitals, and hence increasing the conductivity.

The changes in conductivity are reflected in the optical band gap measurements from  $x = 0$  to 0.6, which suggests that the two processes arise from the same transition in these phases. This is not true, however, of the phases containing more than 60% tin (II), where the optical band gap is not reflected in the conductivity measurements. The observed decrease in electrical conductivity with decreasing tin (II) content, although the fall is not

Sample	Conductivity ( $\Omega^{-1} \text{ cm}^{-1}$ )	Absorption Edge (eV $\pm$ 0.03)
CsSnI <sub>3</sub>	$2.32 \times 10^{-4}$	2.72
CsSn <sub>.9</sub> Pb <sub>.1</sub> I <sub>3</sub>	$6.94 \times 10^{-8}$	2.53
CsSn <sub>.8</sub> Pb <sub>.2</sub> I <sub>3</sub>	$2.05 \times 10^{-8}$	2.50
CsSn <sub>.7</sub> Pb <sub>.3</sub> I <sub>3</sub>	$6.16 \times 10^{-9}$	2.48
CsSn <sub>.6</sub> Pb <sub>.4</sub> I <sub>3</sub>	$1.32 \times 10^{-9}$	2.43
CsSn <sub>.5</sub> Pb <sub>.5</sub> I <sub>3</sub>	$6.53 \times 10^{-10}$	2.44
CsSn <sub>.4</sub> Pb <sub>.6</sub> I <sub>3</sub>	$6.81 \times 10^{-10}$	2.41
CsSn <sub>.3</sub> Pb <sub>.7</sub> I <sub>3</sub>	$7.19 \times 10^{-10}$	2.43
CsSn <sub>.2</sub> Pb <sub>.8</sub> I <sub>3</sub>	$7.72 \times 10^{-10}$	2.45
CsSn <sub>.1</sub> Pb <sub>.9</sub> I <sub>3</sub>	$4.45 \times 10^{-10}$	2.52
CsPbI <sub>3</sub>	$3.8 \times 10^{-10}$	2.64

Table 5.8. Conductivity and Absorption Data for CsSn<sub>x</sub>Pb<sub>1-x</sub>I<sub>3</sub> Phases.



exponential, it indicates that tin 5 s<sup>2</sup>-electrons play a vital role in the mechanism of conduction.

The data collected for this system indicates that a cationic mechanism is responsible for the observed properties.

#### 5.4. The CsPb<sub>.5</sub>Cd<sub>.5</sub>I<sub>3-x</sub>X<sub>x</sub> (X = Cl or Br) System

The semiconducting properties of the CsPb<sub>x</sub>Cd<sub>1-x</sub>I<sub>3</sub> system (Section 5.1.) were best explained by the donation of lead ns<sup>2</sup> electrons and not iodine electrons to the conduction band.

To investigate this further the related system CsPb<sub>.5</sub>Cd<sub>.5</sub>I<sub>3-x</sub>X<sub>x</sub> (x = Cl or Br) was studied.

##### 5.4.1. Preparation and Analysis

The phases discussed in this section were prepared by fusion of the appropriate molar ratios of caesium, cadmium and lead halides. All the samples prepared (x = 0 to 3) were yellow, with the exception of CsPb<sub>.5</sub>Cd<sub>.5</sub>Cl<sub>3</sub> which was white. The samples were stored in vacuo over sodium hydroxide pellets.

Cadmium, lead and iodine were analysed as described in Section 5.1.2. Chlorine and bromine were determined potentiometrically using silver nitrate.

The x-ray powder diffractograms showed no lines

attributable to any of the starting materials,  $\text{CsPbX}_3$  or  $\text{CsCdX}_3$ , which shows that new phases were formed. The data showed that the cell dimensions increase with increasing iodine content in both the chlorine and bromine systems, and that none of the systems have a cubic structure. If  $\text{CsPb}_{.5}\text{Cd}_{.5}\text{I}_{3-x}\text{X}_x$  has an elpasolite structure the radius of the hole in the centre of an undistorted close packed octahedron of  $\text{I}^-$  ions,  $\text{Br}^-$  ions and  $\text{Cl}^-$  ions would be 0.93, 0.81 and 0.75Å respectively. From the relative sizes of  $\text{Pb}^{2+}$  and  $\text{Cd}^{2+}$  ions, 1.20 and 0.97Å respectively, it is evident that  $\text{Pb}^{2+}$  will determine the structure and the replacement of iodine by the other halides will have little effect. Therefore the halide sub-lattice is not close packed.

#### 5.4.2. Optical Properties

Absorption spectra were recorded for each sample using the apparatus described in Section 4.1. Each sample gave a spectrum with a single sharp absorption edge and no domain structure.

$\text{CsPb}_{.5}\text{Cd}_{.5}\text{Cl}_3$  is the only white phase in the series, which means that any optical transitions occur with energies greater than 3.54eV. As the larger iodide ions (2.20Å) were replaced by the smaller chloride ions (1.81Å) the absorption edges shifted to higher energy (Fig 5.5(a)). The increase in the energy of the optical band gap with

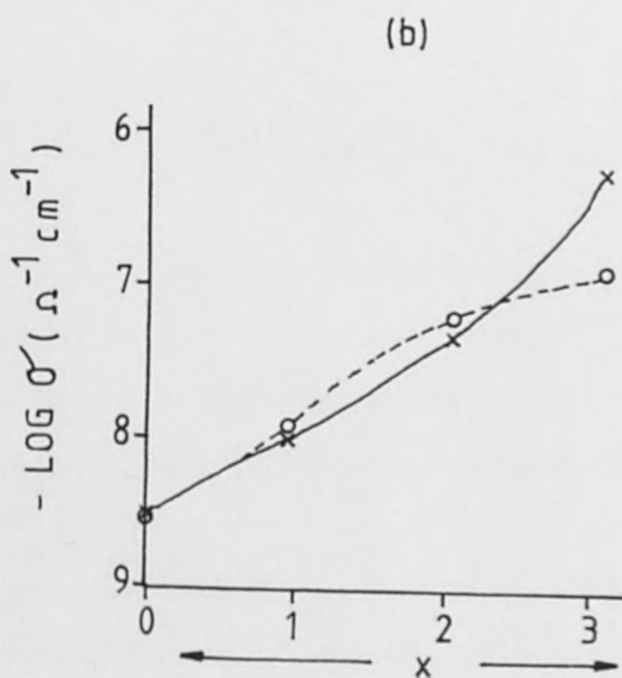
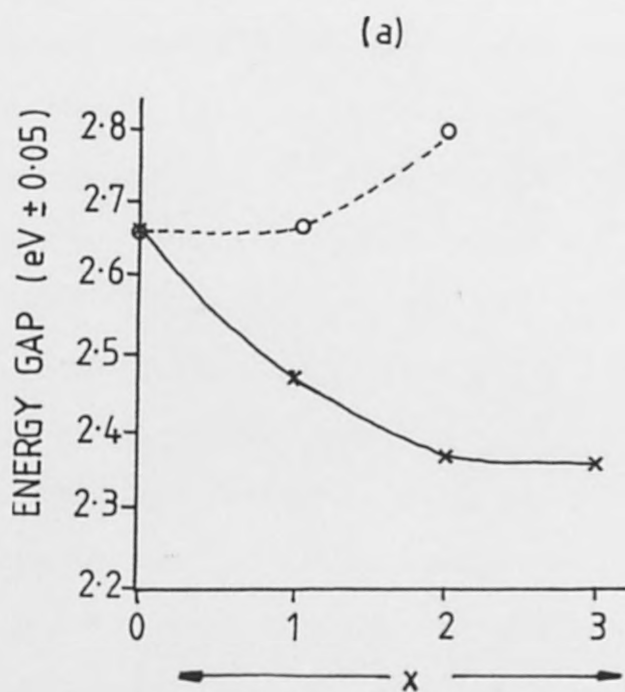


Fig. 5.5. (a) Plot of energy gaps and (b) electrical conductivity vs composition for the  $\text{CsPb}_{.5}\text{Cd}_{.5}\text{I}_{3-x}\text{X}_x$  (where  $\text{X} = \text{Cl}(\text{o})$  or  $\text{Br}(\text{x})$ )

increasing chloride ion content can be explained in terms of reduced overlap of metal and halide orbitals. The x-ray data showed that the cell decreased in size as iodine was replaced by the other halides and that the halide sub-lattice is not close packed. Thus, when iodine is totally replaced by chlorine, the less diffuse nature and different geometrical orientation of the chlorine p- orbitals will reduce metal-halide overlap.

Conversely, as iodine is replaced by bromine, the optical band gap decreases in energy (Fig 5.5(a)). It is possible that although the orbital overlap is reduced by the presence of the smaller ion, the increase in overlap due to the orbital reorientation and lattice contraction more than compensates.

#### 5.4.3. Electrical Conductivity

The bulk electrical conductivity measurements were determined using the Wayne-Kerr bridge<sup>(18)</sup>. The substitution of iodide ions by both chloride and bromide ions resulted in a progressive increase in the conductivities. (Fig 5.5(b))

In the bromine containing phases the conductivity mirrors the optical band gap, in that, as the energy of the optical band gap decreases so the conductivity rises. Whereas, in the chlorine containing phases, the conductivity increases despite the increasing energy of the optical band

gap.

It would appear that these materials adopt the  $\text{CsPb}_{.5}\text{Cd}_{.5}\text{I}_3$  band structure when iodide ions are present. The electrical properties being determined by the amount of iodine present. The phases in which up to  $2/3$  of the iodine has been replaced have essentially the same electrical conductivities, regardless of the second halide. This shows that the Pb-halide overlap determines the conductivity. The increase in electrical conductivity on replacement of iodine is strong evidence against any contribution of iodine electrons to the conduction mechanism.

In general for halide systems of this type it has been shown that the relative magnitudes of the electrical conductivities are  $\text{Cl} < \text{Br} < \text{I}$ <sup>(19)</sup>. Therefore, the  $\text{CsPb}_{.5}\text{Cd}_{.5}\text{I}_{3-x}\text{X}_3$  system is an exception. This suggests that the transition of lead  $5s^2$  electrons to the empty halide d-orbitals determines the absorption edge and conductivity. In the pure chlorine phase an indirect transition would result, whereas a direct transition would be possible in the phases containing bromine and iodine. Such a hypothesis would explain the experimental data.

#### 5.5.            The $\text{Cs}_2\text{NaSbI}_6$ : $\text{Cs}_2\text{NaBiI}_6$ System

A number of Group V metal trihalides, on reaction with alkali halides, form crystals with the formula  $\text{A}_3\text{B}_2\text{X}_9$  and  $\text{A}_2^1\text{A}^{11}\text{B}_2\text{X}_6$ .  $\text{Cs}_3\text{Sb}_2\text{I}_9$  and  $\text{Cs}_3\text{Bi}_2\text{I}_9$  are known to have

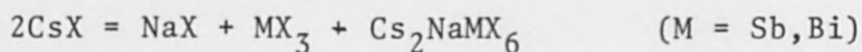
structures closely related to the  $\text{Cs}_3\text{Cr}_2\text{Cl}_9$  structure<sup>(20)</sup>, which is hexagonal with space group  $P6_3/mmc$ . In this structure the  $\text{Cs}^+$  ions have twelve chloride nearest neighbours and the  $\text{Sb}^{3+}$  and  $\text{Bi}^{3+}$  ions are in distorted octahedral sites occupying two-thirds of the available octahedral spaces in the chloride close-packed lattice. Laughlin has prepared phases in which  $\text{Sb(III)}$  and  $\text{Bi(III)}$  are mixed and he showed that the structure of  $\text{Cs}_3\text{SbBiCl}_9$  was very similar to  $\beta$ - $\text{Cs}_3\text{Sb}_2\text{Cl}_9$  and that  $\text{Cs}_3\text{SbBiBr}_9$  had the same structure as  $\alpha$ - $\text{Cs}_3\text{Sb}_2\text{Br}_9$ <sup>(21)</sup>. The optical reflectance, resistivity and  $^{121}\text{Sb}$  Mössbauer data for  $\text{Cs}_3\text{Sb}_{2-x}\text{Bi}_x\text{X}_9$  have been reported<sup>(22)</sup>.

The properties of  $\text{Cs}_2\text{NaMX}_6$  where  $M = \text{Sb, As or Bi}$  have been discussed in Section 4.4. The purpose of this section was to prepare and investigate the properties of phases in which  $\text{Sb(III)}$  and  $\text{Bi(III)}$  were mixed in the  $\text{Cs}_2\text{NaMI}_6$  system.

#### 5.5.1. Sample Preparation and Analysis

The simplest technique for preparing the  $\text{Cs}_2\text{NaMCl}_6$  analogues of the corresponding iodides compounds is to evaporate to dryness a hot  $\text{HCl}$  solution of the appropriate cations. However, the x-ray data for compounds prepared in this way show lines due to  $\text{NaCl}$ ,  $\text{CsCl}$  and other unidentified phases, consequently rendering this technique unsuitable for the production of reproducing pure compounds. Therefore the

compounds were prepared by the method according to Robinson<sup>(23)</sup>



5.1962 g (0.02M) of CsI were dissolved in the minimum volume of freshly distilled HI, then added to a solution of 1.4989 g (0.01M) NaI in water. To this solution was added a 2M HI solution of 0.01M  $\text{MI}_3$ . The product,  $\text{Cs}_2\text{NaMI}_6$ , precipitated out immediately. Unlike the corresponding chlorides and bromides it was not possible to recrystallise the iodides from the mother liquor, and attempts to recrystallise from a variety of organic solvents proved unsuccessful. Therefore the precipitates were filtered and dried in vacuo over sodium hydroxide. The mixed antimony, bismuth phases were prepared in the same way, using the appropriate molar ratios of the starting materials. The colour of the products ranged from orange  $\text{Cs}_2\text{NaSbI}_6$  through to red  $\text{Cs}_2\text{NaBiI}_6$ .

That the desired iodide complex had indeed been formed was shown by analysis. (Table 5.10). Antimony was determined by titration with  $\text{KBrO}_3$  using methyl red indicator and bismuth by titration with E.D.T.A. using xylenol orange indicator. Sodium was determined by flame photometry and iodine potentiometrically with  $\text{AgNO}_3$ .

Compound	Colour	% Bi	% Sb	% Na	% I
$\text{Cs}_2\text{NaSbI}_6$	orange	—	9.55 (10.38)	1.81 (1.96)	64.9 (64.97)
$\text{Cs}_2\text{NaSb}_{.9}\text{Bi}_{.1}\text{I}_6$	red/orange	1.76 (1.78)	9.25 (9.28)	1.72 (1.95)	64.5 (64.49)
$\text{Cs}_2\text{NaSb}_{.8}\text{Bi}_{.2}\text{I}_6$	brick red	3.43 (3.51)	7.98 (8.19)	1.68 (1.93)	64.8 (64.02)
$\text{Cs}_2\text{NaSb}_{.7}\text{Bi}_{.3}\text{I}_6$	brick red	5.17 (5.23)	7.07 (7.11)	1.99 (1.92)	63.5 (63.55)
$\text{Cs}_2\text{NaSb}_{.6}\text{Bi}_{.4}\text{I}_6$	brick red	7.05 (6.93)	5.13 (6.05)	1.92 (1.90)	63.1 (63.10)
$\text{Cs}_2\text{NaSb}_{.5}\text{Bi}_{.5}\text{I}_6$	brick red	8.81 (8.60)	4.82 (5.01)	1.83 (1.89)	62.5 (62.64)
$\text{Cs}_2\text{NaSb}_{.4}\text{Bi}_{.6}\text{I}_6$	brick red	10.02 (10.24)	3.40 (3.97)	1.85 (1.83)	61.8 (62.19)
$\text{Cs}_2\text{NaSb}_{.3}\text{Bi}_{.7}\text{I}_6$	brick red	11.42 (11.86)	3.04 (2.96)	1.84 (1.86)	61.8 (61.75)
$\text{Cs}_2\text{NaSb}_{.2}\text{Bi}_{.8}\text{I}_6$	brick red	12.10 (13.15)	1.63 (1.96)	2.02 (1.85)	61.5 (61.32)
$\text{Cs}_2\text{NaSb}_{.1}\text{Bi}_{.9}\text{I}_6$	brick red	14.94 (15.04)	0.714 (0.97)	1.92 (1.84)	60.9 (60.89)
$\text{Cs}_2\text{NaBiI}_6$	crimson	16.61 (16.59)	—	1.91 (1.83)	60.4 (60.47)

Table 5.10. Analytical Data for  $\text{Cs}_2\text{NaSb}_x\text{Bi}_{1-x}\text{I}_6$  Series. (Figures in brackets are the calculated percentages).



X-ray powder diffraction analysis has shown that  $\text{Cs}_2\text{NaBiCl}_6$  and  $\text{Cs}_2\text{NaSbCl}_6$  are isostructural<sup>(23)</sup>. The x-ray data were indexed on the basis of an fcc lattice with the most probable space group being  $\text{Fm}\bar{3}\text{m}$ .  $\text{Sb}^{\text{III}}$  and  $\text{Bi}^{\text{III}}$  occupy octahedral sites in these compounds<sup>(23)</sup>. It has been suggested that the octahedral symmetry of the  $\text{BiCl}_6^{3-}$  and  $\text{SbCl}_6^{3-}$  moieties can be attributed either to the donation of  $ns^2$ - electron density to a conduction band<sup>(24)</sup> or to the considerable shielding of the outer s-electrons by the f- and d- electrons in the inner shells<sup>(2)</sup>.

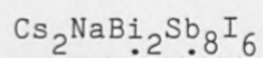
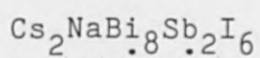
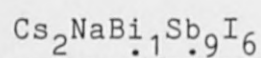
The x-ray powder data obtained for the  $\text{Cs}_2\text{NaSb}_x\text{Bi}_{1-x}\text{I}_6$  series (Table 5.11) show that the phases are neither cubic nor hexagonal. For  $\text{Cs}_2\text{NaSb}_x\text{Bi}_{1-x}\text{I}_6$  to have the elpasolite structure the radius of the hole in the centre of an undistorted close packed octahedron of  $\text{I}^-$  ions would be  $\sim 0.93\text{\AA}$ . From the relative sizes of the  $\text{Na}^+$ ,  $\text{Bi}^{3+}$  and  $\text{Sb}^{3+}$  ions (0.97, 0.96 and 0.76 $\text{\AA}$  respectively), it is evident that the replacement of  $\text{Bi}^{3+}$  by  $\text{Sb}^{3+}$  would have little effect on the structure at low antimony concentrations. The position of the Na ions would have a greater effect on the structure. Since, the crystal class is neither hexagonal nor cubic, the  $\text{M}^{\text{III}}$  ion will occupy a site of less than  $\text{O}_h$  symmetry and will probably be distorted toward  $\text{C}_{3v}$  symmetry with three long and three short Sb-I interactions.

<u>Cs<sub>2</sub>NaBiI<sub>6</sub></u>		<u>Cs<sub>2</sub>NaSbI<sub>6</sub></u>	
<u>d(Å)</u>	<u>I/I<sup>0</sup></u>	<u>d(Å)</u>	<u>I/I<sup>0</sup></u>
7.400	10.6	6.682	19.5
6.970	40.4	4.250	8.8
5.340	12.8	4.191	10.7
4.332	6.4	3.633	11.7
4.250	26.6	3.576	15.1
3.934	7.5	3.460	65.8
3.685	34.6	3.427	100.0
3.612	6.4	3.270	9.3
3.458	76.0	3.218	99.5
3.507	78.2	2.981	86.3
3.466	100.0	2.767	5.9
3.314	15.4	2.743	46.8
3.261	98.9	2.718	11.2
3.198	6.9	2.683	6.3
2.810	10.6	2.423	4.0
2.776	69.2	2.309	16.6
2.747	26.1	2.293	4.9
2.723	17.0	2.123	22.0
2.442	6.4	2.119	13.7
2.344	12.8	2.092	60.5
2.321	10.6	2.087	36.1
2.249	4.3	1.959	26.0
2.222	5.3	1.955	16.6

Table 5.11.

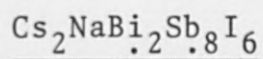
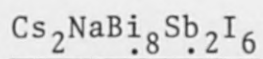
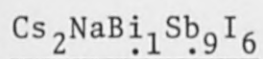
<u>Cs<sub>2</sub>NaBiI<sub>6</sub></u>		<u>Cs<sub>2</sub>NaSbI<sub>6</sub></u>	
<u>d(Å)</u>	<u>I/I<sup>0</sup></u>	<u>d(Å)</u>	<u>I/I<sup>0</sup></u>
2.151	25.5	1.814	9.8
2.113	56.4	1.795	30.7
2.045	4.3	1.791	20.5
2.019	5.5	1.786	15.6
2.010	5.5	1.755	13.6
1.985	28.9	1.748	11.7
1.965	7.4	1.712	11.7
1.903	5.3	1.708	6.4
1.870	6.4	1.663	7.3
1.858	7.0		
1.814	17.0		
1.771	18.1		
1.731	11.7		
1.681	9.6		

Table 5.11. (continued).



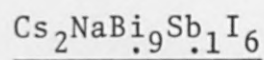
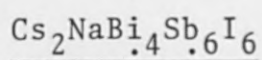
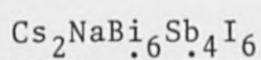
<u>d(Å)</u>	<u>I/I<sup>0</sup></u>	<u>d(Å)</u>	<u>I/I<sup>0</sup></u>	<u>d(Å)</u>	<u>I/I<sup>0</sup></u>
7.314	8.6	7.284	10.0	7.314	8.6
6.916	19.5	6.862	28.0	6.916	19.3
		5.277	6.0		
		4.281	7.0		
4.210	11.2	4.210	16.0	4.201	12.7
3.900	3.4	3.900	5.0		
3.648	15.5	3.655	24.0	3.648	13.2
3.576	17.2	3.590	9.0	3.576	13.2
3.507	60.3	3.520	66.0	3.507	57.9
3.440	99.1	3.440	90.0	3.440	97.9
3.278	12.1	3.290	12.0	3.284	10.2
3.220	100.0	3.232	100.0	3.232	100.0
2.988	94.0	2.998	90.0	2.988	79.2
2.747	43.6	2.763	58.0	2.780	8.1
2.722	12.9	2.730	19.0	2.747	46.7
2.691	6.9	2.698	11.0	2.722	14.2
2.433	5.6	2.442	4.0	2.691	8.1
2.309	13.8	2.430	6.0	2.423	5.1
		2.327	16.0	2.315	14.2
		2.309	8.0	2.298	7.1
		2.206	4.0	2.127	20.3
2.127	20.3	2.141	20.0		
2.096	58.6	2.103	57.0	2.096	58.4

Table 5.11. (continued).



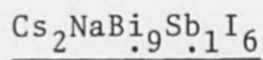
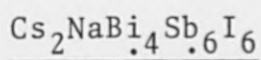
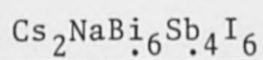
<u>d(Å)</u>	<u>I/I<sup>0</sup></u>	<u>d(Å)</u>	<u>I/I<sup>0</sup></u>	<u>d(Å)</u>	<u>I/I<sup>0</sup></u>
1.963	24.0	1.975	26.0	1.965	24.4
1.881	4.3	1.888	4.0		
1.817	9.5	1.824	8.0	1.817	8.6
1.797	35.9	1.807	19.0	1.797	23.8
		1.794	11.0	1.789	12.2
1.752	12.1	1.763	16.0	1.759	10.2
1.716	9.9	1.722	11.0	1.752	12.2
1.684	7.7	1.673	10.0	1.716	10.2
1.551	6.5	1.500	3.0	1.667	6.6
1.492	4.3				

Table 5.11. (continued).



<u>d(Å)</u>	<u>I/I<sup>0</sup></u>	<u>d(Å)</u>	<u>I/I<sup>0</sup></u>	<u>d(Å)</u>	<u>I/I<sup>0</sup></u>
7.314	9.4	7.314	9.6	7.314	13.1
6.916	23.6	6.889	25.5	6.916	39.2
5.324	12.6			5.324	7.8
4.271	5.9	4.271	4.3		
4.201	15.7	4.201	11.7	4.220	23.5
3.900	4.7	3.900	5.3	3.917	6.5
3.648	12.2	3.648	14.9	3.678	28.7
3.590	10.2	3.576	11.3		
3.520	74.0	3.507	57.4	3.548	54.9
3.440	92.9	3.434	100.0	3.460	96.7
3.284	12.6	3.278	10.6	3.302	18.3
3.209	98.4	3.226	97.9	3.249	100.0
3.176	3.9	3.154	5.3		
2.993	100.0	2.988	83.5	3.008	94.0
2.755	59.1			2.772	65.4
2.730	15.0	2.722	13.8	2.739	24.8
2.698	9.4	2.691	7.4	2.706	13.1
2.423	6.3	2.423	5.3	2.436	9.8
2.318	15.0	2.315	13.8	2.335	17.0
2.304	7.9	2.298	6.4	2.315	12.4
2.134	23.6	2.129	19.1	2.243	4.6
2.101	59.8	2.096	55.3	2.212	5.9
1.969	32.2	1.965	21.3	2.146	23.5

Table 5.11 (continued).



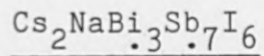
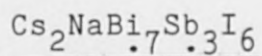
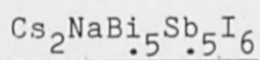
$d(\text{\AA})$	$I/I^0$	$d(\text{\AA})$	$I/I^0$	$d(\text{\AA})$	$I/I^0$
1.821	7.9	1.817	8.5	2.108	71.9
1.759	14.2	1.752	13.8	1.831	6.5
1.719	11.0	1.716	10.6	1.811	18.3
1.670	9.1	1.667	6.4	1.794	11.7
1.554	3.9			1.725	10.4
1.572	3.9			1.768	18.3
1.497	5.5			1.676	9.0

Table 5.11 (continued).

<u>Cs<sub>2</sub>NaBi<sub>.5</sub>Sb<sub>.5</sub>I<sub>6</sub></u>		<u>Cs<sub>2</sub>NaBi<sub>.7</sub>Sb<sub>.3</sub>I<sub>6</sub></u>		<u>Cs<sub>2</sub>NaBi<sub>.3</sub>Sb<sub>.7</sub>I<sub>6</sub></u>	
<u>d(Å)</u>	<u>I/I<sup>o</sup></u>	<u>d(Å)</u>	<u>I/I<sup>o</sup></u>	<u>d(Å)</u>	<u>I/I<sup>o</sup></u>
7.314	13.8	7.284	11.0	7.255	7.7
6.916	33.0	6.916	24.4	6.862	22.0
4.271	5.4				
4.210	16.9	4.210	13.4	4.191	10.6
3.917	7.0			3.892	4.8
3.655	20.5	3.648	18.2	3.633	16.4
3.590	11.6	3.583	12.2	3.576	13.5
3.520	54.0	3.513	54.9	3.500	59.9
3.440	94.0	3.440	99.0	3.427	97.5
3.290	12.0	3.284	14.6	3.278	9.7
3.232	100.0	3.232	100.0	3.220	100.0
3.175	6.7			3.148	3.9
2.998	88.4	2.993	86.6	2.998	88.8
2.755	55.0	2.755	53.6	2.747	50.2
2.730	20.5	2.728	17.0	2.722	13.5
2.698	9.8	2.698	9.7	2.683	7.0
2.442	4.5	2.417	6.0	2.423	5.8
2.423	6.3	2.318	14.6		
2.321	14.3			2.315	14.5
2.306	7.6				
2.206	4.5			2.201	3.8
2.137	20.0	2.132	19.5	2.127	22.2

Table 5.11. (continued).





<u>d(Å)</u>	<u>I/I°</u>	<u>d(Å)</u>	<u>I/I°</u>	<u>d(Å)</u>	<u>I/I°</u>
2.100	64.0	2.099	57.3	2.094	61.8
1.971	25.0	1.969	32.0	1.961	24.0
1.892	3.0				
1.824	6.3			1.814	9.2
1.804	19.6	1.821	7.3	1.797	24.0
1.794	10.7	1.801	21.3	1.751	15.0
1.762	15.2	1.759	14.6	1.713	10.6
1.719	9.8	1.717	9.8	1.666	7.7
1.670	8.9	1.670	7.9		
1.575	3.6				
1.551	4.5			1.550	3.0
1.497	4.5			1.492	4.3

Table 5.11. (Continued).



By analogy with the  $\text{Cs M}^{\text{III}}\text{X}_3$  systems little donation of lone-pair s-electrons density to a band system would be expected.

As  $\text{Sb}^{3+}$  is replaced by  $\text{Bi}^{3+}$ , however, the lone pair is more tightly bound to the larger and more ionic  $\text{Bi}^{3+}$  ion. The tendency would be for the  $\text{Bi}^{3+}$  ion to occupy a site closer to the centre of the iodine octahedra, and the greater size of the  $\text{Bi}^{3+}$  ion would also serve to expand the lattice.

Inspection of the x-ray diffraction patterns showed a slight increase in cell size between  $\text{Cs}_2\text{NaSbI}_6$  and  $\text{Cs}_2\text{NaSb}_{.9}\text{Bi}_{.1}\text{I}_6$ , then a second larger increase at  $\text{Cs}_2\text{NaSb}_{.5}\text{Bi}_{.5}\text{I}_6$ . From  $\text{Cs}_2\text{NaSb}_{.3}\text{Bi}_{.7}\text{I}_6$  the cell size appears to increase progressively to its maximum at  $\text{Cs}_2\text{NaBiI}_6$ . The discontinuity at  $x = 0.5$  approximates to the minimum absorption edge and the lowest electrical conductivity (Fig 5.6).

To gain further information of the geometry of  $\text{Sb}^{3+}$  ions in these materials Sb Mössbauer were carried out at Birmingham University. However, it proved impossible to obtain a Mössbauer spectra for all the phases. The failure

to collect data is attributed to the high concentration of iodine in the samples absorbing the  $\gamma$ -rays.

### 5.5.3.                      Optical Properties

No emission spectra were observed for any of the  $\text{Cs}_2\text{NaSb}_x\text{Bi}_{1-x}\text{I}_6$  phases either at room temperature or 80K.

The absorption spectra of freshly prepared samples are given in Table 5.12. The absorption edges became sharper as the percentage bismuth was increased (Fig. 5.6). Structure was observed at shorter wavelengths to the absorption edge and this is attributed to interband transitions. The magnitudes of these energy bands follows the same pattern throughout the  $\text{Cs}_2\text{NaSb}_x\text{Bi}_{1-x}\text{I}_6$  series as the absorption edge.

The absorption spectra were repeated on the same samples nine months after preparation (Table 5.12). It was found that the edges still followed the same trend but were shifted to lower energies, typically by approximately 0.04eV. No structure was observed in any of the repeated spectra. The shift in energies of the aged samples may be due to partial decomposition, although single sharp absorption edges were obtained which suggests a homogenous phase.

Compound	Absorption Edge (eV $\pm$ 0.03)		Interband Transition (eV $\pm$ 0.03) Fresh Sample	
	Fresh Sample	Aged Sample		
$\text{Cs}_2\text{NaSbI}_6$	2.18	2.14		
$\text{Cs}_2\text{NaSb}_{.9}\text{Bi}_{.1}\text{I}_6$	2.03	2.00	3.01,	2.45
$\text{Cs}_2\text{NaSb}_{.8}\text{Bi}_{.2}\text{I}_6$	2.01	1.96	3.02,	2.45
$\text{Cs}_2\text{NaSb}_{.7}\text{Bi}_{.3}\text{I}_6$	1.99	1.95	3.01,	2.45
$\text{Cs}_2\text{NaSb}_{.6}\text{Bi}_{.4}\text{I}_6$	1.97	1.93	—,	2.43
$\text{Cs}_2\text{NaSb}_{.5}\text{Bi}_{.5}\text{I}_6$	1.94	1.91	2.99,	2.41
$\text{Cs}_2\text{NaSb}_{.4}\text{Bi}_{.6}\text{I}_6$	1.93	1.88	—,	2.43
$\text{Cs}_2\text{NaSb}_{.3}\text{Bi}_{.7}\text{I}_6$	1.95	1.88	3.02,	2.45
$\text{Cs}_2\text{NaSb}_{.2}\text{Bi}_{.8}\text{I}_6$	1.96	1.91	3.02,	2.46
$\text{Cs}_2\text{NaSb}_{.1}\text{Bi}_{.9}\text{I}_6$	1.98	1.96	3.04,	2.56
$\text{Cs}_2\text{NaBiI}_6$	2.07	2.01	3.02,	2.56

Table 5.12. Absorption Spectra Data for  $\text{Cs}_2\text{NaSb}_x\text{Bi}_{1-x}\text{I}_6$  Series.

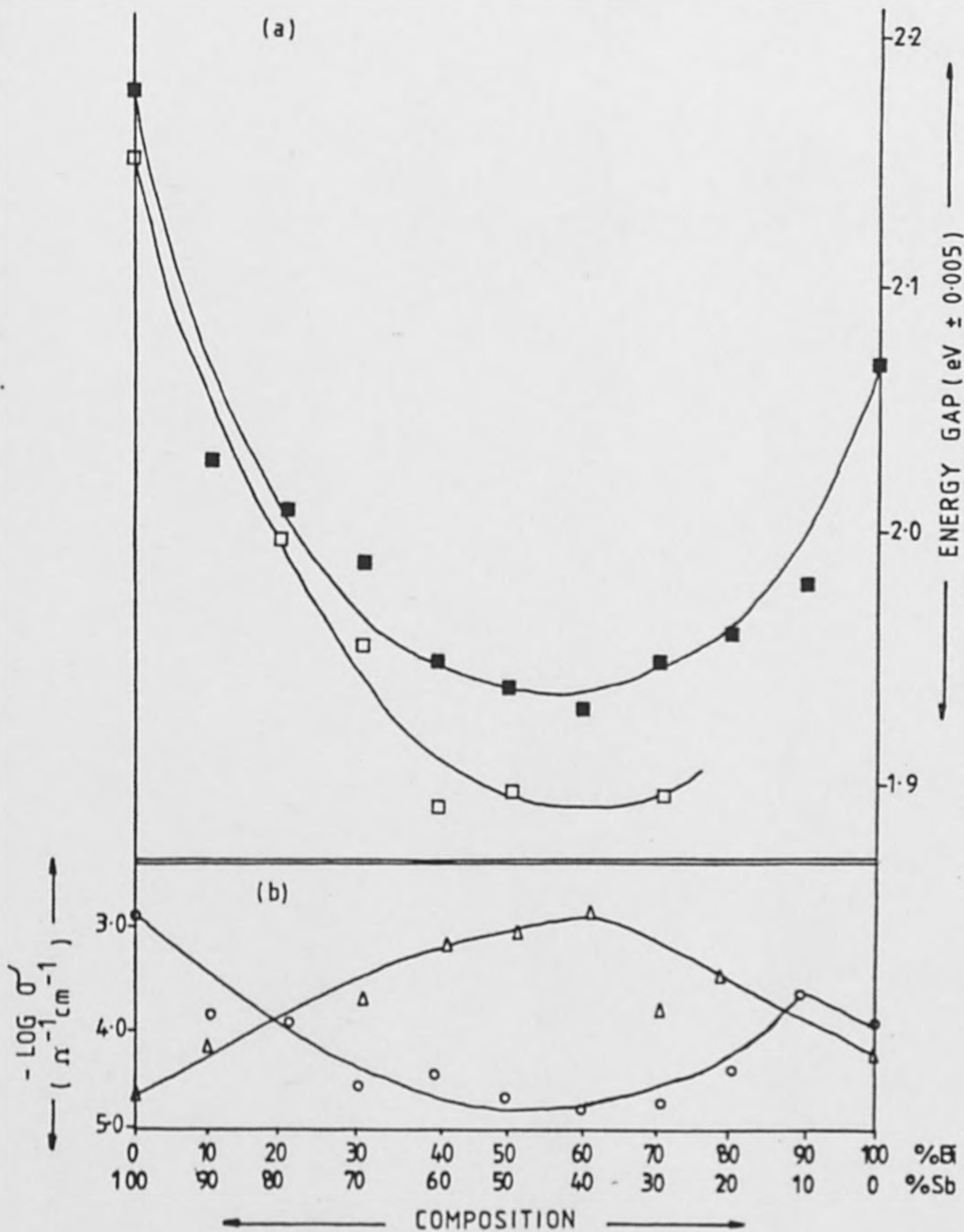


Fig. 5.6. Plot of (a) energy gaps determined from absorption (■) and photoconductivity (□) spectra and (b) bulk (○) and surface (Δ) electrical conductivity vs composition for the  $\text{Cs}_2\text{NaSb}_x\text{Bi}_{1-x}\text{I}_6$  system.

#### 5.5.4.

#### Electrical Properties

The surface electrical conductivities of the  $\text{Cs}_2\text{NaSb}_x\text{Bi}_{1-x}\text{I}_6$  phases were determined using the four probe apparatus described in Section 3.3. As Sb (III) was replaced by Bi (III) the surface conduction increased (Fig 5.6) reaching a maximum when 60% of the antimony had been replaced. Further addition of Bi (III) resulted in a decrease in conduction. These results mirror the optical band gap, in that, as the energy of the band gap decreases the conductivity increases, and as the gap widens the conductivity falls. It would therefore seem likely that the same transition is responsible for both of these properties. Such a relationship was not, however, observed for the bulk conductivities of the materials.

The bulk electrical conductivities of the  $\text{Cs}_2\text{NaSb}_x\text{Bi}_{1-x}\text{I}_6$  series were measured using the Vibron Electrometer and compacted discs of material<sup>(25)</sup>. As Sb (III) was replaced by Bi (III) the conductivity decreased reaching a minimum at 60% replacement. A progressive increase in conduction was observed on further substitution of antimony by bismuth.

#### 5.5.5.

#### Photoconductivity

If the electrical and optical properties of the  $\text{Cs}_2\text{NaSb}_{1-x}\text{Bi}_x\text{I}_6$  series arise from the same process, a

photoconductive response should be observed when the phases are illuminated with radiation of energy greater or equal to the energy of the forbidden band.

The photoconductive properties of materials in the  $\text{Cs}_2\text{NaSb}_{1-x}\text{Bi}_x\text{I}_6$  series were investigated using the apparatus described previously (Section 3.2) and two methods of sample preparation<sup>(26)</sup>.

Illumination of compacted discs of powdered material produced no detectable change in the conductivity within the wavelength range 380 - 950nm. However, when a mull of the sample with acetone was painted evenly over the circuit board sample holder a signal was detected. The large surface to volume ratio of the discs may account for the failure to detect a signal as only the surface would be affected by the radiation. Any alteration in the resistance is measured between both faces of the disc, which means that a signal has to cross the bulk of unaffected sample before detection. This problem is overcome with the circuit board sample holder as only a thin layer of sample is used.

The photoconductivity data for the phases studied is given in Table 5.13. As the shape of the spectra obtained for different phases varied (Fig 5.7) the maximum was used to determine the band gap rather than the edge. The shapes of the spectra may indicate changes in the band structure above or within the conduction band itself. Within the limits of experimental error, other than for the phases where  $x = 0.3$  and  $0.4$ , the maximum photoconductive response occurs

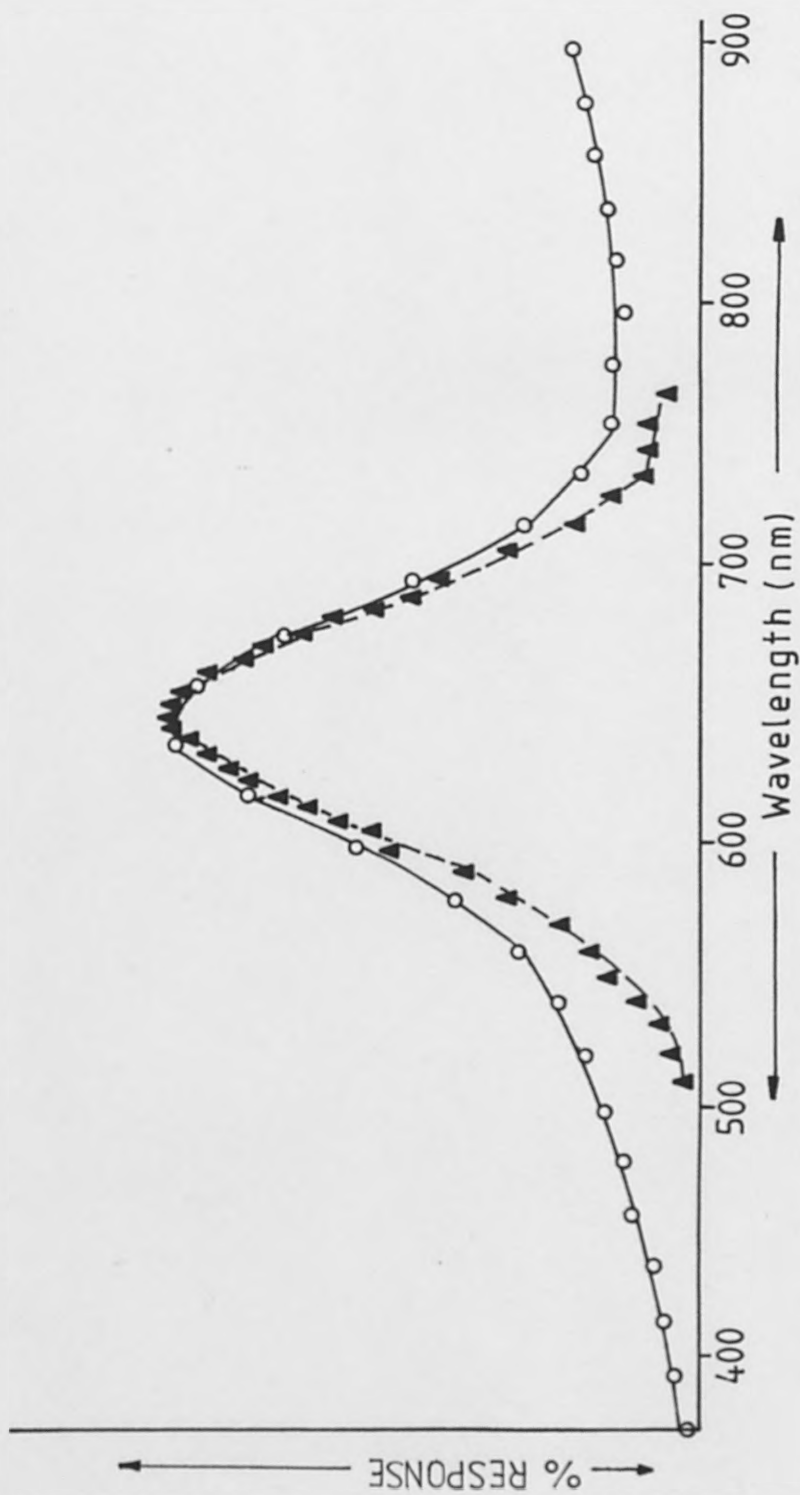


Fig. 5.7. Photoconductivity spectrum of  $\text{Cs}_2\text{NaSb}_{.5}\text{Bi}_{.5}\text{I}_6$  (using circuit board sample holder and a 0.8mm monochromator slit)



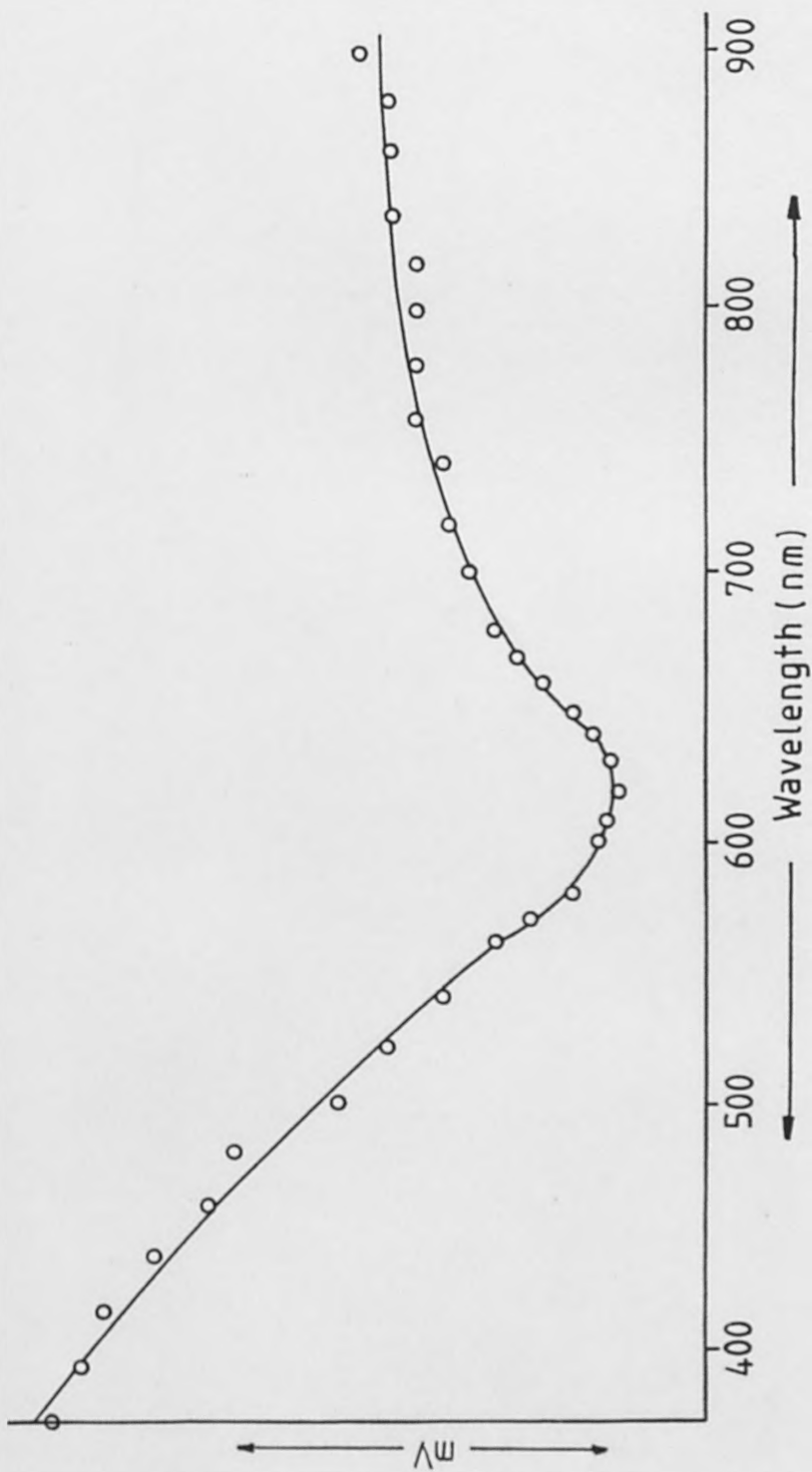


Fig. 5.7. Photoconductivity spectrum of Cs<sub>2</sub>NaSb<sub>0.8</sub>Bi<sub>0.2</sub>I<sub>6</sub> (using circuit board sample holder and a monochromator slit of 2.00mm)

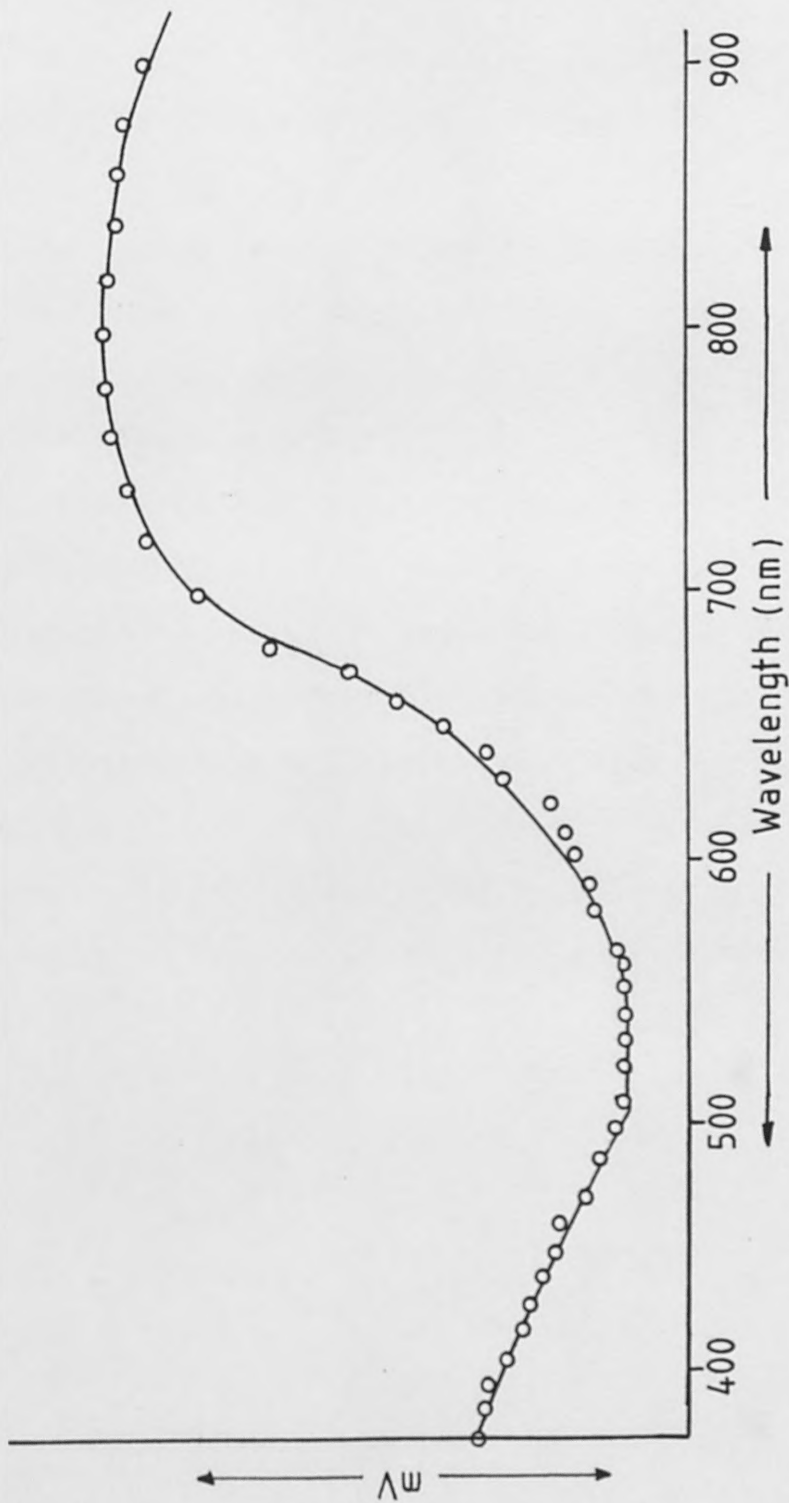


Fig. 5.7. Photoconductivity spectrum of  $\text{Cs}_2\text{NaSb}_{.6}\text{Bi}_{.4}\text{I}_6$  (using circuit board sample holder and a monochromator slit of 2.0mm)

at the same energy as the absorption edge. Since photoconductivity provides the most accurate measure of band gap, it can be concluded without fear of contradiction that the optical absorption edges arise from a direct band-to-band transition.

All the phases in the series are isostructural and the shape of the bands is determined solely by symmetry considerations. The photoconductivity data shows that the bands have the same shape regardless of their respective energies. Therefore, to the first approximation, it can be assumed that the shape of the valence band edge does not vary throughout the series. Since an accurate value of the band gap is known the number and sign of the carriers involved in conduction and their mobilities can be determined.

As  $m^*$  depends only on the shape of the bands, which as we have shown are constant throughout the series, the relationship  $m_1^* = m_2^* = m^*$  must be true.

$$n_1 = p_1 = 2 \left( \frac{k_B T}{2\pi\hbar^2} \right)^{3/2} (m^*)^{3/4} e^{-E_g/2k_B T} \quad (5.4.)$$

at 300K

$$N = n_1 + p_1 = 4 \left( \frac{300k_B}{2\pi\hbar^2} \right)^{3/2} (m^*)^{3/4} e^{-E_g/600k_B} \quad (5.5.)$$

The total number of carriers,  $N$ , for each phase in the series was determined using equation(5.5), and the values are listed in Table 5.13. Since, the electrical conductivity is the sum of the electron and hole contributions:

$$\sigma = (n\mu_h + p\mu_e) \quad (5.6.)$$

where  $n$  and  $p$  are the concentrations of electrons and holes.  
and

$$n + p = N \quad (5.7.)$$

$$\sigma = N\mu_T \quad (5.8.)$$

Using the values of  $N$  calculated above it was possible to determine the mobilities using Equation(5.8), these are given in Table 5.13.

In germanium the intrinsic electron concentration,  $n$ , at 300K is  $6 \times 10^{19} \text{ m}^{-3}$  (28). Since the number of holes and electrons are equal in intrinsic conduction the total number of carriers,  $N$ , for germanium is  $1.2 \times 10^{19} \text{ m}^{-3}$ , which has a conductivity of  $2.3 \times 10^{-2} \Omega^{-1} \text{ cm}^{-1}$ . However, the lowest impurity concentrations attained at present for germanium are of the order of  $10^{10} \text{ cm}^{-3}$ . The carrier concentration in the  $\text{Cs}_2\text{NaSb}_x\text{Bi}_{1-x}\text{I}_6$  series is much lower than that of germanium as would be expected from the lower

Sample	Photoconductivity		Absorption Edge (eV ± 0.03)	Number of Carriers n (m <sup>-3</sup> )	Rates of Mobilities μx <sup>0</sup> /μx <sup>1</sup>
	Max. Response (eV ± 0.05)	Half edge (eV ± 0.05)			
Cs <sub>2</sub> NaSbI <sub>6</sub>	2.15	—	2.18	2.51 x 10 <sup>+7</sup>	3.09 x 10 <sup>-6</sup>
Cs <sub>2</sub> NaSb <sub>9</sub> Bi <sub>1</sub> I <sub>6</sub>	no response		2.03	4.56 x 10 <sup>+8</sup>	1.86 x 10 <sup>4</sup>
Cs <sub>2</sub> NaSb <sub>8</sub> Bi <sub>2</sub> I <sub>6</sub>	2.00	1.85	2.01	6.72 x 10 <sup>+8</sup>	1.42 x 10 <sup>4</sup>
Cs <sub>2</sub> NaSb <sub>7</sub> Bi <sub>3</sub> I <sub>6</sub>	1.65	1.96	1.99	9.89 x 10 <sup>+8</sup>	1.99 x 10 <sup>3</sup>
Cs <sub>2</sub> NaSb <sub>6</sub> Bi <sub>4</sub> I <sub>6</sub>	2.33	1.89	1.97	1.46 x 10 <sup>-9</sup>	1.61 x 10 <sup>3</sup>
Cs <sub>2</sub> NaSb <sub>5</sub> Bi <sub>5</sub> I <sub>6</sub>	1.91	1.75	1.94	2.6 x 10 <sup>9</sup>	5.82 x 10 <sup>2</sup>
Cs <sub>2</sub> NaSb <sub>4</sub> Bi <sub>6</sub> I <sub>6</sub>	no response		1.93	3.16 x 10 <sup>9</sup>	2.83 x 10 <sup>2</sup>
Cs <sub>2</sub> NaSb <sub>3</sub> Bi <sub>7</sub> I <sub>6</sub>	1.89	1.76	1.95	2.14 x 10 <sup>9</sup>	5.75 x 10 <sup>2</sup>
Cs <sub>2</sub> NaSb <sub>2</sub> Bi <sub>8</sub> I <sub>2</sub>	no response		1.96	1.77 x 10 <sup>9</sup>	1.41 x 10 <sup>3</sup>
Cs <sub>2</sub> NaSb <sub>1</sub> Bi <sub>9</sub> I <sub>6</sub>	no response		1.98	1.20 x 10 <sup>9</sup>	1.30 x 10 <sup>4</sup>
Cs <sub>2</sub> NaBiI <sub>6</sub>	no response		2.07	2.10 x 10 <sup>8</sup>	3.63 x 10 <sup>4</sup>

Table 5.1.3.

conductivities. The calculated mobilities (Table 5.13) are all very high. For a mobility  $\mu$  (assuming  $\mu_e = \mu_h$ ) of  $4000 \text{ cm}^2/\text{V s}$ , to give a conductivity of  $1.24 \times 10^{-3} \Omega^{-1} \text{cm}^{-1}$ , a carrier concentration of ca.  $2 \times 10^{12}$  would be needed. Therefore to give the observed conductivity a large concentration of impurity carriers must be present.

As antimony (III) is replaced by bismuth (III) the number of carriers increases towards a maximum at  $x = 0.6$ . Concurrent with this increase is a decrease in the calculated mobilities which reach a minimum at the same molar ratio. Antimony (III) is a better donor of electrons than bismuth (III) due to its more covalent character, this is illustrated by the ionization potentials.

	<u>Ionization Potentials (eV)</u>				
	1 <sup>st</sup>	2 <sup>nd</sup>	3 <sup>rd</sup>	4 <sup>th</sup>	5 <sup>th</sup>
Sb	8.641	16.53	25.3	44.2	56.0
Bi	7.289	16.69	25.56	45.3	56.0

The mobilities would, therefore, be expected to decrease as antimony is replaced by bismuth. The mobilities of  $\text{Cs}_2\text{NaSbI}_6$  and  $\text{Cs}_2\text{NaBiI}_6$ ,  $3.09 \times 10^8$  and  $3.63 \times 10^6 \text{ cm}^2/\text{V s}$  further support this observation. A plot of total number of carriers,  $N (\text{m}^{-3})$ , vs electrical conductivity  $\sigma (\Omega^{-1} \text{cm}^{-1})$  produce a straight line (Fig 5.8) which indicates that the changes in conduction are due to mobility effects.

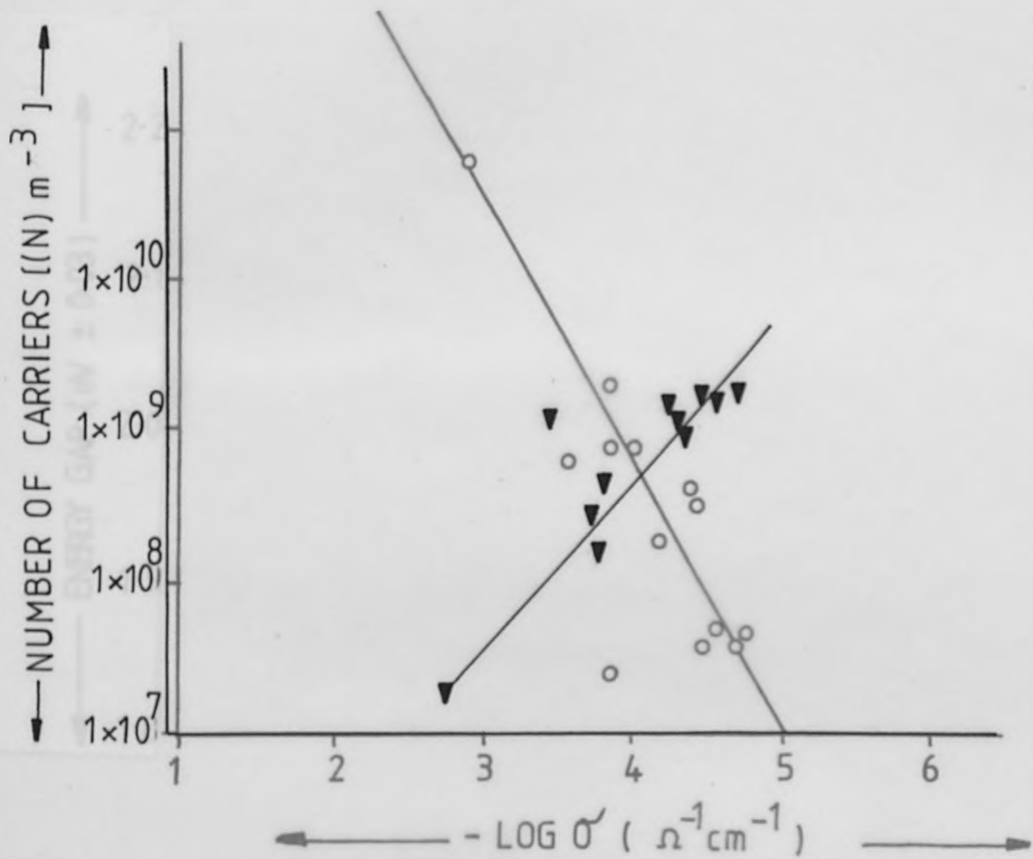


Fig. 5.8.  $eV$  vs  $-\log\delta$ , and  $N(m^{-3})$  vs  $-\log\delta$

From the foregoing arguments it can be concluded that the phases are direct band gap semiconductors, in which the number and mobility of carriers has a direct effect on the changes in conductivity. Impurities, such as hydroxyl ions, iodine vacancies or even the sodium ions, make a significant contribution to the conductivity.



### References

1. Personnel communication J. D. Donaldson.
2. C. K. Møller, Nature, 1958, 182, 1436.
3. Wells, Structural Inorganic Chemistry.
4. H. Brasseur, L. Pauling, J.A.C.S., 1938, 60, 2886.
5. C. H. MacLillavry, Rec. Trav. Chim., 1939, 58, 193.
6. C. K. Møller, Mat. Fys. Medd. Dan. Vid. Selsk., 1959, 32, No. 2.
7. C. K. Møller, Mat. Fys. Medd. Dan. Vid. Selsk., 1960, 32, No. 3.
8. B. A. Belikovich, J. P. Pashchuk, N. S. Polzyrailo, Opt. Spectrosc., 1977, 42, 62.
9. S. J. Clark, C. D. Flint, J. D. Donaldson, J. Phys. Chem. Solids, 1981, 42, 133.
10. S. J. Clark, C. D. Flint, J. D. Donaldson, unpublished work.
11. Vogel's Textbook of Quantitative Inorganic Analysis, 4<sup>th</sup> Ed., Longman 1978.
13. A. J. Thompson, "Electronic Structures and Magnetism of Inorganic Compounds" (P. Day, ed.) Vol. 4, London; Chemical Society; 1976.
14. P. Mauersberger, F. Huber, Acta. Cryst., 1980, B,36, 683.
15. J. D. Donaldson, J. Silver, S. Hadjimildis, S. D. Ross, J.C.S. Dalton Trans., 1975, 1500.
16. J. D. Donaldson, J. Silver, J. C. S. Dalton Trans., 1973, 666.

17. S. J. Clark, Ph. D. Thesis, London, 1979.
18. See Chapter 4 Section 1.3 (b).
19. C. K. Møller, Kgel. Dan. Vid. Selsk. Mat. Fys. Med., (1954), 32, 1.
20. B. Chebot, E. Parthe, Acta Cryst., 1978, B34, 645.
21. D. R. Laughlin, Ph. D. Thesis, Univ. of London, 1974.
22. M. J. K. Thomas, Ph. D. Thesis, Univ. of London, 1980.
23. Robinson, Acta Cryst., 1972, B28, 653.
24. Martinea, Milne, J. Chem. Soc. (A), 1970, 2971.
25. See Chapter 4 Section 1.3(a).
26. See Chapter 3, Section 3.2.4.
27. O. B. Kushner, Fiz. Elecktron, 1978, 17, 64.
28. C. Kittel, Introduction to Solid State Physics, 5<sup>th</sup> Ed., John-Wiley, 1976.

## Chapter Six

### Discussion

	<u>Page</u>
6.1. Introduction	269
6.2. General Comments	273
6.3. Optical Properties	274
6.4. Electrical Properties	280
6.5. Conclusion	286

Introduction

It is the purpose of this chapter to discuss the experimental data for simple iodides, single metal phases and mixed metal phases presented in the preceding chapters.

The iodide compounds investigated contain at least one main group element in its lower oxidation state. A general feature of p-block elements with an  $ns^2$  outer electronic configuration is that the environment of the element is distorted in most of its compounds.  $^{119}\text{Sn}$  Mössbauer parameters of tin (II) derivatives, of the type  $\text{MSnX}_3$ , show that electronegative ligands such as fluorine give rise to more distorted tin environments and less electronegative ligands such as iodine to more regular environments.<sup>(1)</sup> The electronic implication is that the lone pair in the  $\text{MSnX}_3$  fluorides is highly directional and therefore stereochemically active and contains high tin 5p character but that the lone pair in the iodides contains high tin 5s character and therefore has less directional effect. The binding energies of the tin 5s and 5p and halogen np orbitals are shown in Fig 6.1. It can be seen that, in order to obtain a good energy match with the appropriate halogen group orbital, the tin  $a_1$  bonding orbital should contain high 5s character when bound to fluorine but high  $5p_z$  character when bound to iodine. The non-bonding

orbital (because of orthogonality requirements) thus contains high tin 5p<sub>z</sub> in SnF<sub>3</sub><sup>-</sup> and low tin 5p<sub>z</sub> in SnI<sub>3</sub><sup>-</sup>. This would lead to highly directional lone-pairs containing high p-character and hence distorted tin (II) environments for SnX<sub>3</sub><sup>-</sup> ions containing electronegative ligands. While, in contrast, for SnX<sub>3</sub><sup>-</sup> ions containing less electronegative ligands the lone-pair would contain high tin 5s character and would therefore be much less stereochemically active. One of the strengths of such an orbital matching model is the ease with which it can be extended to describe the bonding and properties of the tin (II) compounds with high symmetry structures. Fig 6.2. which shows the binding energies of As(III), Sb(III) and Bi(III) ns and np orbitals and halogen ns and np orbitals, illustrates how orbital matching arguments can be extended to Group V elements.

The increase in ns character of the non-bonding pair in going from fluorides to iodides is paralleled by a decrease in distortion. As the distortion decreases it becomes possible to remove the distorting effects of the non-bonding electron pair by solid-state effects as well as by direct alteration in the p-character of the electrons in the orbital. The removal of distortion by solid-state effects can be explained in terms of direct population of empty delocalised bands by the non-bonding electrons.

There are, in general, two classes of compounds of main group elements in their lower oxidation states which do not have a distorted main group element environment: viz

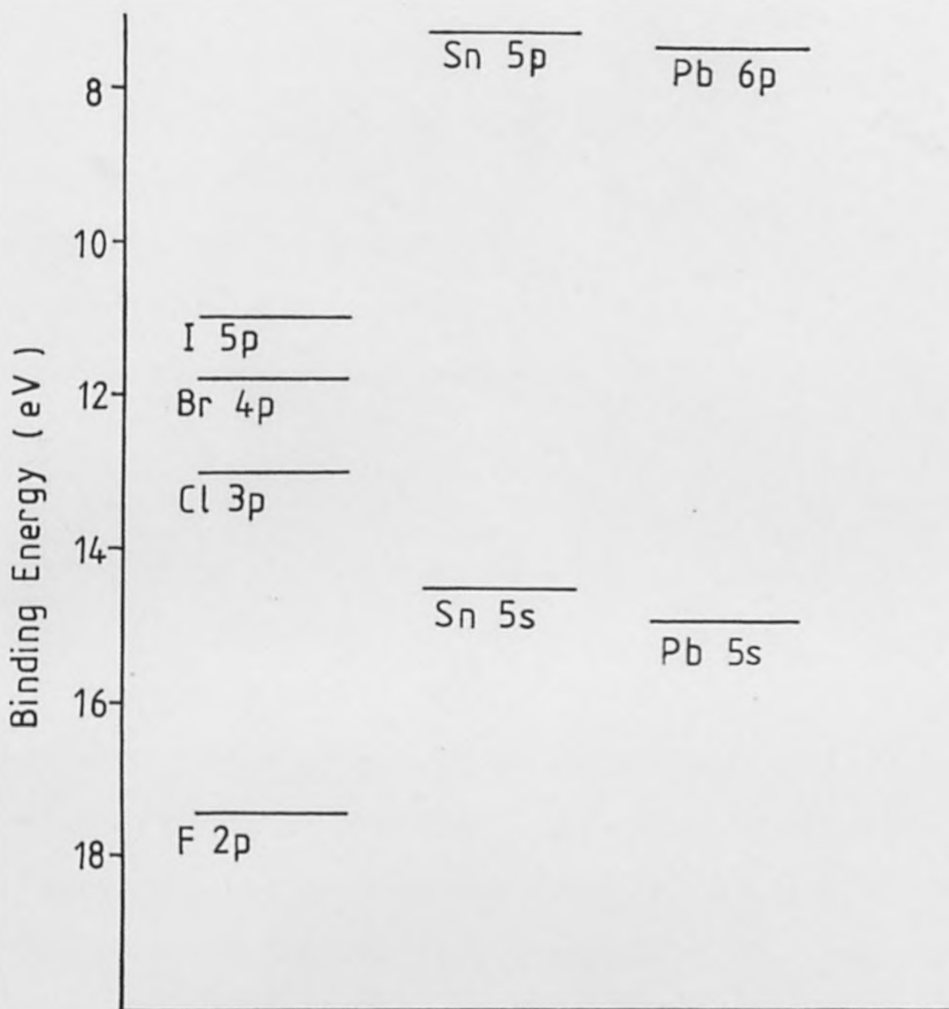


Fig. 6.1. Relative binding energies of halogen np orbitals and Group IV ns and np orbitals.

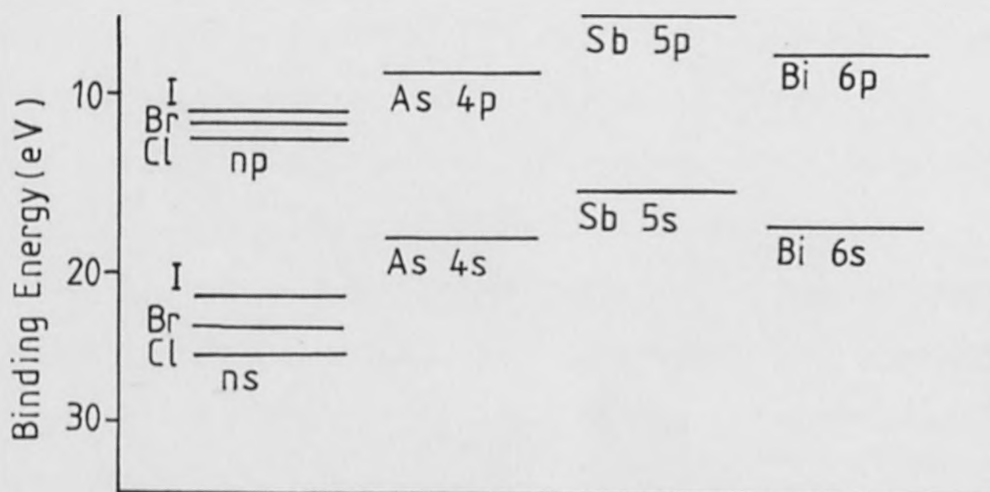


Fig. 6.2. Relative binding energies of halogen and Group V ns and np orbitals.

(1) electrostatically bonded compounds containing  $6s^2$  ions, e.g.  $TlCl$  and  $PbSO_4$  (2) compounds like  $CsSnBr_3$  in which the distorting effects of the lone pair are removed by the direct population of empty solid state bands by the  $ns^2$  electrons. Many compounds of the first class are however, susceptible to forces that can cause distortion.  $TlCl$  for example has a high dielectric constant.<sup>(2)</sup>

In many other compounds containing  $ns^2$  ions there is also evidence for the direct population of solid state bands, of the type found in  $CsSnBr_3$ , by the  $ns^2$  electrons. For  $CsSnBr_3$  the symmetry, orbital energies and unit cell size at room temperature, appear to be ideal for the formation of empty delocalised solid state bands from the empty valence shell bromine orbitals and for the population of these bands by the tin (II) non-bonding electron pair. For other compounds, such as  $CsSnCl_3$  and  $CsPbBr_3$ , the conditions for direct population are only met in high temperature modifications. It does, however, appear that in all compounds of the main group elements containing an approximately close packed array of halide anions, solid state bands can be formed by the mutual overlap of the empty orbitals of these anions or the overlap of empty orbitals of both the anions and cations, if appropriate. Once the empty solid state bands are formed the conditions are available for the elimination or reduction of the distorting effects of the lone pair non-bonding orbitals provided their energies are compatible with those of the acceptor bands.

For iodine, complexes of this type, as opposed to other halide, it has been suggested that the colour and semiconducting properties arise from the population of solid state bands by the iodine electrons themselves and not from population by the lone-pair of the main group element<sup>(3)</sup>. The objective of the present work was to investigate this hypothesis.

6.2. General Comments

All the iodides studied in this work were coloured. The colouration can be explained in terms of donation of electrons from the valence band to a conduction band.

An important, general observation was that all the iodides studied lost iodine with aging and on heating to  $\sim 115^{\circ}\text{C}$ . Such a loss of iodine will result in the formation of iodine vacancies and / or impurity levels within the forbidden band gap. It is possible, therefore that optical band gap measurements yield information on the energy separation between the valence band and an impurity level rather than between the valence band and the conduction band. Additional experimental evidence is required to show the existence of a direct band gap. Likewise, the presence of impurity levels would increase the electrical conductivity since:-

$$\sigma_{\text{total}} = \sigma_{e^{-}} + \sigma_{h^{+}} + \sigma_{\text{ionic}^{+}} + \sigma_{\text{ionic}^{-}} + \underbrace{\sigma_{\text{donor}} + \sigma_{\text{acceptor}}}_{\text{impurity contribution}}$$



Whereas it is possible to detect an ionic contribution when actually taking d.c. electrical conductivity measurements, an impurity contribution can only be identified by additional data e.g. as found for the  $\text{Cs}_2\text{NaSb}_x\text{Bi}_{1-x}\text{I}_6$  system using photoconductivity data. Due to the vital role impurity levels, if present, have on the semiconducting properties, all measurements, unless otherwise stated, were performed on freshly prepared samples to minimise the effects of the loss of iodine.

The X-ray powder diffraction data show that none of the iodides have a cubic structure. In an ideal case, e.g.  $\text{CsSnBr}_3$  the predicted distortion is removed by the donation of the tin (II) lone-pair of electrons to a conduction band formed by overlap of bromine  $4t_2$  orbitals. For the iodides the deviation from cubic geometry may be so large that donation of lone-pair electron density to a conduction band can never completely remove the distortion.

To summarise, the iodide materials to be discussed are coloured, non-cubic phases in which the existence of impurity levels can not be excluded.

### 6.3.                      Optical Properties

The room temperature absorption and reflectance data for all the phases studied gave absorption edges as opposed to bands. Absorption edges arise from band-to-band transitions while absorption bands are attributed to

intraionic transitions e.g. between the  $6s^2$  and  $6s^1p^1$  states of the  $Pb^{2+}$  ion. A comparative study on the effect of the method of preparation viz: from the melt or aqueous solution, on the semiconducting properties of the caesium trihaloplumbates was performed. All the samples gave absorption edges rather than an absorption band. The energies of which were unaffected by the mode of preparation. The 80K emission spectra for  $CsPbBr_3$  (melt) gave a main emission line at 2.32eV often with a shoulder while samples prepared from solution gave a single broader line at 2.33eV. Similar results were obtained for the iodides, 1.73eV (melt) and 1.75eV (aqueous). The reported emission band of  $CsPbCl_3$  is 2.96eV which lies outside the excitation range of the apparatus. The sharp intense emission bands of  $CsPbCl_3$  and  $CsPbBr_3$  have been attributed to the  $6s^2 - 6s^1p^1$ ,  $^1s_0 - ^3p_1$ , transition in the  $Pb^{2+}$  ion. LCAO calculations on the band structures of  $CsPbCl_3$  and  $CsPbBr_3$  have explained their optical properties in terms of a band structure isomorphous with that of the simple cubic thallium oxides, assuming an undistorted octahedral symmetry and neglecting the presence of the  $Cs^+$  ions, and are said to confirm the origins of the electronic spectra.<sup>(5,6)</sup> Since the absorption edges of  $CsPbCl_3$  and  $CsPbBr_3$  occur at only slightly lower energy than the first excited state any emission involving the conduction band would be obscured.

However, the caesium trihaloplumbates have distinct absorption edges rather than bands, which is more characteristic

of direct band-to-band transitions. It is possible that in addition to the intraionic transition a band-to-band transition also occurs. In contrast to the chloride and bromide where the emission and absorption features occur at the same energies, the emission maxima (1.73eV) and absorption edges (2.76eV) of  $\text{CsPbI}_3$  occur at very different energies. Hence, if they result from the same internal transition the Stokes shift would be 1.03eV, which is unreasonably large. Since the absorption edge must represent a band-to-band transition the maximum can only be attributed to either emission from a defect centre or relaxation from the conduction band. If the latter is true, there must be a quite considerable curvature in the band structure.

Following on from the caesium trihaloplumbates (II), cadmium was introduced into the  $\text{CsPbI}_3$  lattice. The  $\text{Cd}^{2+}$  ion is smaller than the  $\text{Pb}^{2+}$  ion (0.97Å and 1.21Å respectively) and has no lone pair of electrons to donate to the band system. It was hoped that the introduction of  $\text{Cd}^{2+}$  into  $\text{CsPbI}_3$  would provide evidence for the type of donation mechanism.

The absorption edges shifted to lower energies as the composition moved away from the pure phases to give a minimum of 2.46eV at  $\text{CsPb}_{.1}\text{Cd}_{.9}\text{I}_3$ . The initial red shift may be interpreted in terms of a progressive reduction in the optical band gap as lead ions are replaced by the smaller cadmium ions, with a concurrent lattice contraction. This

contraction will increase the self-overlap between the iodine d-states and any overlap of the non-bonding lead  $6s^2$  orbitals with the halide orbitals and thus give rise to lower energy transitions. All of the phases in the  $\text{CsPb}_x\text{Cd}_{1-x}\text{I}_3$  system gave emission maxima at  $\sim 1.73 - 1.68\text{eV}$ . When  $x = 0$  to  $0.5$  a single sharp emission at  $1.73\text{eV}$  was observed. The energy of this transition is virtually unaffected by changes in composition until  $x = 0.93$ . Consequently, the emission is attributed to the excitonic  $6s^2 \rightarrow 6s^1p^1$  transition of the  $\text{Pb}^{2+}$  ion. It seems likely from the optical data alone that the properties of the  $\text{CsPb}_x\text{Cd}_{1-x}\text{I}_3$  can be best explained in terms of lead  $ns^2$  electrons rather than iodine electrons populating the conduction band. To verify this postulate the  $\text{CsPb}_{.5}\text{Cd}_{.5}\text{X}_{3-x}\text{X}_x$  ( $X = \text{Cl}, \text{Br}, \text{I}$ ) system was investigated. As the larger iodide ions ( $2.2\text{\AA}$ ) were replaced by chloride ions ( $1.81\text{\AA}$ ) the absorption edges shifted to higher energies. The increased width of the optical band gap with increased chlorine can be explained in terms of reduced overlap of metal and halide orbitals. As iodine was replaced by bromine, however, the optical band gap decreased in energy. Although orbital overlap would be reduced by the presence of bromide ions, it is possible that orbital reorientation and lattice contraction more than compensate. The evidence from this system clearly indicates that cationic electrons and not anionic electrons are responsible for the observed properties.

Since the semiconducting properties of  $\text{CsSnBr}_3$  have

been described<sup>(7)</sup> the related system  $\text{CsSn}_x\text{Cd}_{1-x}\text{Br}_3$  was investigated. Again single sharp absorption edges as opposed to bands were observed. As the Sn:Cd ratio approached unity the edges shifted to higher energies. The initial increase in energy for phases containing less than 40% cadmium may result from more efficient overlap of the tin  $5s^2$ -orbital with the bromine 4d orbitals at low cadmium concentrations. The energy gap determined from emission spectra is the same as that calculated from absorption spectra, which indicates that a direct band-to-band transition is responsible for both processes. This conclusion agrees with the reported data on  $\text{CsSnBr}_3$  itself<sup>(7)</sup>.

To investigate the effects of two p-block elements in the same system, phases formed between the isomorphous compounds  $\text{CsSnI}_3$  and  $\text{CsPbI}_3$  were prepared. The optical band gap narrows progressively from the parent compounds to a minimum of 2.42eV between  $0.1 < x < 0.07$ . This differs from the  $\text{CsSn}_x\text{Pb}_{1-x}\text{Br}_3$  system<sup>(8)</sup>, in which the optical band gap narrows progressively as replacement of lead (II) by tin (II) contracts the lattice and reduces the average atomic distances, allowing increasing overlap between the tin-5s and bromine 4d-orbitals. Finally, a series of compounds of the type  $A^1_2A^1B^{III}X_6$  and  $A^1_2A^1B^{III}B^{III}_{1-x}I_6$  (where  $A^1 = \text{Cs, Rb or Na}$ ,  $B^{III} = \text{As, Sb or Bi}$ ,  $X = \text{Cl, Br}$ ) were investigated. None of the chlorides, which were all white, gave an absorption spectra over the spectral range 6.2 to

1.65eV. The bromides and iodides gave a single sharp absorption edge, the energies of the optical band gaps increasing with increasing size of the p-block element. The decrease in energy of the optical band gap observed on replacing bromide by iodine can be explained either in terms of the more diffuse nature of the iodine orbitals or by impurity levels. With the exceptions of  $\text{Rb}_2\text{NaBiBr}_6$ ,  $\text{Cs}_2\text{NaBiCl}_6$  and  $\text{Rb}_2\text{NaSbI}_6$  none of the phases produced an emission spectra at 80K. The band gaps determined from emission data are not the same as those determined from the absorption data, therefore the two processes arise from different transitions.

In the mixed metal system,  $\text{Cs}_2\text{NaSn}_x\text{Bi}_{1-x}\text{I}_6$ , the absorption edges became sharper as the percentage bismuth was increased. Structure was observed at shorter wavelengths to the absorption edge and this is attributed to interband transitions. The magnitudes of these energy bands follow the same pattern throughout the  $\text{Cs}_2\text{NaSb}_x\text{Bi}_{1-x}\text{I}_6$  series as the absorption edge.

The absorption spectra were repeated on the same samples nine months after preparation, and the absorption edges were found to have shifted to lower energies. The decrease in energy of the forbidden gap indicates that partial decomposition has resulted in impurity levels being formed within the forbidden gap.

Preliminary experiments were performed on 'simple iodides' and the caesium trihaloplumbates to investigate the effect of contact material and a.c., d.c. circuits on the electrical conductivities. The use of a.c. voltage overcomes certain problems inherent to d.c. measurements namely: polarization effects in ionic conductors and electrolytes; barriers at internal surfaces; and certain contact resistances. For those 'simple iodides' where it was possible to make a.c. and d.c. measurements it was found that the conductivities were the same within an order of magnitude. Therefore, it can be concluded that the type of voltage supply had no significant effect on the electrical conductivity in these materials. The results obtained with different contact materials do, however, show significant changes in electrical conductivity. For the 'simple iodides' it was found that tin foil gave the highest electrical conductivities for Group IV metal  $2^+$  iodides. While gold leaf gave the highest reading for Group V metal  $3^+$  iodides. This observation was confirmed in studies with  $\text{CsPbCl}_3$  where tin foil was the most effective contact material. The results obtained for  $\text{CsPbBr}_3$  and  $\text{CsPbI}_3$  show that gold leaf, silver loaded paint, tin foil and indium metal contacts were all within a half order of magnitude whilst the conductivities with aluminium foil, solder and no contact were lower by at

least a factor of ten. As a result of this investigation tin foil, gold leaf or silver loaded paint were used for all subsequent electrical measurements.

The emission spectra of the caesium trihaloplumbates, indicate an increase in band gap in the order Cl>Br>I, the opposite to that indicated by electrical measurements on the non-cubic phases. To resolve this anomaly it was necessary to accurately determine the band gaps. This was done by photoconductivity measurements. The photoconductivity data for CsPbCl<sub>3</sub> gave an energy gap of 2.79eV ( $\pm$ .5eV) while for CsPbBr<sub>3</sub> the value was 2.10eV ( $\pm$ .5eV). Although of lower energies to the band gaps determined by absorption data (2.93 and 2.29eV $\pm$ 0.03 respectively) the results were sufficiently close to assume that both properties arise from the same transition. It was not possible to obtain a positive photoconductive response for CsPbI<sub>3</sub> which implies that its photoconductivity maximum lies outside the range of the apparatus. However, it has been reported to photoconduct in the region of its absorption edge<sup>(9)</sup>. The positive photoconductivity data obtained for CsPbCl<sub>3</sub> and CsPbBr<sub>3</sub> are conclusive evidence for a direct optical band-to-band transition.

It was not possible to obtain photoconductivity data for any phase in the CsPb<sub>x</sub>Cd<sub>1-x</sub>I<sub>3</sub> series. However, bulk and four probe electrical conductivity measurements were made. The bulk conductivities are in the range 10<sup>-7</sup> to



$10^{-10} \Omega^{-1} \text{ cm}^{-1}$  while the surface conduction ranges from  $10^{-6}$  to  $10^{-7} \Omega^{-1} \text{ cm}^{-1}$ . Surface defects such as water and iodine vacancies may well account for the differing magnitudes of the two sets of data. The bulk and four probe conductivity data mirror the optical band gap across the series in that, as the band gap decreases in energy from  $x = 0.0$  to  $0.9$  the conductivity increases, and as it increases in energy from  $x = 0.9$  to  $1.0$  the conductivity falls. If the semiconducting properties in  $\text{CsPb}_x\text{Cd}_{1-x}\text{I}_3$  arise from the donation of lead 6s-electron density to a conduction band level, as was suggested by the optical data, then, as cadmium replaced lead, the lattice contraction would be paralleled by an increase in electrical conductivity until the lead concentration became too dilute to donate sufficient electrons into the band system. At the same time, a progressive reduction in the optical band gap would be observed as long as sufficient lead were present to produce an observable transition. The optical and electrical data all support this hypothesis. If, however, the semiconducting properties arise from the population of conduction band levels by iodine electrons themselves, the properties should be unaffected by the lead:cadmium ratio, while only changes in the lattice parameters would lead to changes in the semiconducting properties. Since only small variations in the x-ray data over most of the composition range have been observed, this hypothesis is less likely.

For the caesium trihaloplumbates the conductivities were in the order  $I > Cl > Br$ . Therefore, if iodine electrons are involved in population of the conduction band, the replacement of iodine by chlorine or bromine in the  $CsPb_{.5}Cd_{.5}X_{3-x}X_x$  system should reduce the conductivity. It was found that replacement by chlorine increased the conductivity despite the increasing energy of the optical band gap. While in the bromine containing phases the conductivity mirrors the optical band gap i.e. the conductivity rises with the decreasing energy of the optical band gap. When  $2/3$  of the iodine is replaced the conductivities are essentially the same, regardless of the second halide. This indicates that Pb-halide band overlap determines the conductivity and is strong evidence against any contribution of iodine electrons to the conduction mechanism.

The electrical conductivity data do not mirror changes in energy of the optical gap in the  $CsSn_xCd_{-x}Br_3$  system, which is evidence that the two processes arise from different transitions. The observed decrease in conductivity with reduced  $Sn^{2+}$  concentration, indicates that tin  $5s^2$ - electrons are responsible for electrical conduction in the bulk materials. Band gap calculations enable the conductance data to be explained in terms of the optical band gap, assuming a cationic transition is responsible for the observed properties. The  $^{119}Sn$

Mössbauer data indicate that as the proportion of cadmium is increased, the tin (II) becomes more ionic and the  $5s^2$  electrons are more localised and less labile. This would result in a decrease in electrical conductivity with increased cadmium content. The Mössbauer data therefore confirms the interpretation of the conductivity data in terms of donation of tin (II)  $5s^2$  electron density to a conduction band system.

In the  $\text{CsSnI}_3:\text{CsPbI}_3$  system it would be possible for either the lead (II) or tin (II)  $ns^2$  electrons to be donated to a conduction band system. The changes in conductivity are reflected in the optical band gap measurements from  $x = 0$  to 0.6, which suggests that the two processes arise from the same transition in these phases. A decrease in electrical conductivity is observed with reduced tin (II) content. Although, this fall is not exponential, it indicates that the tin  $5s^2$ - electrons play a vital role in the conduction mechanism. Again, the  $^{119}\text{Sn}$  Mössbauer data provide evidence for the loss of tin s-electron density. It is not surprising that the tin (II) and not the lead (II)  $ns^2$ -electrons are donated to the conduction band. Lead (II) is more ionic in character than tin (II) and thus the non-bonding electron pairs remain more tightly bound to the lead nucleus and so are less available for donation to a conduction band. The greater size of the  $\text{Pb}^{2+}$  ion will also contribute to these differences by reducing halide-

halide overlap and inhibiting the formation of the conduction band.

In the  $A_2^I Na B^{III} X_6$  series the electrical conductivities increase with increasing size of the p-block element and from chloride to iodide. This can be explained in terms of increased orbital overlap, which would facilitate the donation of electrons to a conduction band system. The replacement of caesium by rubidium increased the conductivity by a factor of ten in the chlorides and bromides but had little effect in the iodides. As the conductivities mirror the optical band gaps it seems likely that the same transition is responsible for both processes. Variable temperature conductivity measurements on  $Cs_2 Na Sb Cl_6$ ,  $Cs_2 Na Sb Br_6$ ,  $Rb_2 Na Sb Br_6$  and  $Cs_2 Na Bi Br_6$  show phase changes not detectable by D.T.A.. The band gaps calculated from these measurements are small,  $2.71 \times 10^{-1}$ ,  $2.28 \times 10^{-1}$ ,  $3.47 \times 10^{-1}$ , and  $1.28 \times 10^{-1}$  eV respectively. As the phase changes are not observed on cooling it is most probable that metastable phases have been formed and hence the small energy gaps. The surface conductivity measurements of  $Cs_2 Na Sb_x Bi_{1-x} I_6$  phases showed an increase in conductivity as Sb (III) was replaced by the larger Bi (III) ion, reaching a maximum at  $x = 0.6$ . As these results reflect the optical band gap it seems likely that the same transition is responsible for both processes. This was not, however, true of the bulk conductivities. Photoconductivity data were recorded for

those phases where  $x = 0$  to  $0.7$ , which is conclusive evidence for a direct band-to-band transition, and in addition gives an accurate value for the band gap. The optical band gaps are found to be of the same energy as those associated with photoconductivity, and therefore the optical properties arise from a direct-band-to-band transition. As an accurate value of the band gap was known the number of carriers could be calculated and their mobilities estimated. The results of the calculations show that the number and mobility of carriers has a direct effect on the changes in conductivity, and also that impurities such as hydroxyl ions, iodine vacancies or even sodium ions make a significant contribution to the conductivity.

#### 6.5.

#### Conclusion

In the foregoing discussion of optical and electrical properties of the iodide systems studied, the results have been indicative of a cationic mechanism. With the exception of the  $\text{Cs}_2\text{NaSb}_x\text{Bi}_{1-x}\text{I}_6$  system where impurities are definitely involved, all the other systems have been explained in terms of donation of main group  $ns^2$ -electron to a conduction band system. A mechanism involving population of empty solid state bands by iodine electrons themselves does not explain or account for any of the experimental data for compounds containing  $ns^2$  elements.

## References

1. M. J. Tricker, J. D. Donaldson, Inorganica Chimica Acta, (1978), 31, L445.
2. L. E. Orgel, Discuss. Faraday Soc., 1958, 26, 138.
3. J. D. Donaldson, personnel communication.
4. B. A. Belikovich, I. P. Pashchuk, N. S. Pidzyrailo, Opt. Spectrosc., 1977, 42, 62.
5. K. Heidrich, H. Künzel, J. Treusch, Solid State Commun., 1978, 25, 887.
6. D. Fröhlich, K. Heidrich, H. Künzel, G. Trendel, J. Treusch, J. Luminescence, 1979, 18/19, 385.
7. S. J. Clark, C. D. Flint, J. D. Donaldson, J. Phys. Chem. Solids, 1981, 42, 133.
8. S. J. Clark, Ph. D. Thesis, 1979, London.
9. C. K. Møller, Nature, 1958, 182, 1436.